UNIVERSITÀ DEGLI STUDI DI PADOVA

Head Office: Università degli Studi di Padova

Department of Civil, Environmental and Architectural Engineering

Ph.D. COURSE IN: Sciences of Civil, Environmental and Architectural Engineering
CURRICULUM: Materials, Structures, Complex systems and Architecture
SERIES: XXXVIII

INSIGHTS ON THE USE OF RECOVERED AGGREGATES FOR CONCRETE PRODUCTION

Coordinator: Prof. Massimiliano Ferronato
Supervisor: Prof. Flora Faleschini
Co-Supervisor: Prof. Vanesa Ortega-López

Ph.D. student: Daniel Trento

ABSTRACT

The construction industry is a great source of waste generated in the production and demolition phases. The most common type of waste generated on construction sites is Construction and Demolition Waste (C&DW), typically composed of concrete and bricks mixed with minor quantities of steel and timber, depending on the geographical area, site organization and local recycling practices. In addition to direct waste production generated in the construction phase, indirect waste, comprising by-products and materials produced during manufacturing and processing, also poses a significant environmental burden. Steel slags are an example of this kind of waste, which includes Blast Furnace Slags, Basic Oxygen Furnace Slags and Electric Arc Furnace Slags (EAFS). EAFS is generated in Electric Arc Furnaces, primarily used to recycle steel from scrap. Once cooled, the EAFS assumes a stone-like appearance with high-density. Batching plants are another significant source of waste, particularly through the accumulation of leftover concrete and washing residues, usually called Concrete Sludge Waste (CSW). At the same time, the construction industry is a great consumer of raw materials, and aggregates are the most consumed overall because of concrete production, which is the most produced and consumed substance on the planet after water. To save raw materials and limit the need for waste landfilling, recovered aggregates, e.g. those obtained from C&DW or EAFS, can effectively replace conventional gravel and sand for concrete production. However, landfilling is still quite common for most of this waste due to the reluctance of builders and stakeholders, absence of specific guidelines and insufficient information. The aim of this thesis is to address several mechanical challenges that may hinder the widespread adoption of recovered aggregates in concrete production. EAFS is here adopted to replace the coarse fraction of the natural aggregates, and to investigate specific mechanical properties which are unexplored in literature, i.e. the shear strength and the cyclic loading behavior. Furthermore, additional tests were performed on mortars with fine EAFS to evaluate and predict the yield stress in the fresh state. The results demonstrate usually superior performance than the conventional counterpart. Recycled concrete made with recycled aggregates recovered from C&DW shows some issues typically linked to higher shrinkage and inferior mechanical performance compared to the conventional counterparts. In this thesis, a method is proposed to enhance recycled concrete properties with the addition of Raw Crushed Wind Turbine Blade (RCWTB), a waste obtained from the recovery and crushing of decommissioned wind turbine blades. The results demonstrate substantial reductions in plastic shrinkage and notable enhancements in flexural strength. Finally, hardened leftover concrete (CSW) is also explored as both partial and total aggregate replacement, reporting satisfactory results.

SOMMARIO

L'industria delle costruzioni rappresenta una significativa fonte di rifiuti generati sia durante le fasi di produzione che di demolizione. Il tipo di rifiuto più comune prodotto nei cantieri è costituito dai Rifiuti da Costruzione e Demolizione (C&DW), generalmente composti da calcestruzzo e laterizio mescolati con quantità minori di acciaio e legno, a seconda dell'area geografica, dell'organizzazione del cantiere e delle pratiche locali di riciclo. Oltre alla produzione diretta di rifiuti nella fase costruttiva, anche la produzione indiretta di rifiuti, costituita da sottoprodotti e materiali generati durante le fasi di produzione, rappresenta un notevole onere ambientale. Le scorie siderurgiche sono un esempio di questa categoria, comprendendo le scorie di altoforno, le scorie da convertitore ad ossigeno e le scorie da forno ad arco elettrico (EAFS). Queste ultime sono prodotte in omonime fornaci, utilizzate principalmente per il riciclo dell'acciaio attraverso la fusione di rottami metallici. Una volta raffreddate, le EAFS assumono un aspetto simile ad una pietra e presentano un'elevata densità. Un'altra fonte rilevante di rifiuti è rappresentata dagli impianti di betonaggio, nei quali si accumulano residui di calcestruzzo indurito e fanghi di lavaggio, solitamente noti in letteratura come Concrete Sludge Waste (CSW). Parallelamente, l'industria delle costruzioni è una grande consumatrice di materie prime, in particolare degli aggregati, che risultano essere le materie prime più consumate a causa della massiccia produzione di calcestruzzo, la sostanza più prodotta e consumata dall'uomo dopo l'acqua. Al fine di preservare le risorse naturali e ridurre il ricorso allo smaltimento in discarica, gli aggregati recuperati, come quelli ottenuti da C&DW o EAFS, possono sostituire efficacemente la ghiaia e la sabbia convenzionali nella produzione del calcestruzzo. Tuttavia, il riciclo è ancora scarsamente praticato per la maggior parte di questi rifiuti, a causa della riluttanza degli operatori del settore, della mancanza di linee guida specifiche e della carenza di informazioni tecniche. L'obiettivo di questa tesi è affrontare alcune delle problematiche meccaniche che possono limitare l'adozione su larga scala degli aggregati recuperati nella produzione del calcestruzzo. Le scorie d'acciaieria EAFS sono qui impiegate per sostituire la frazione grossolana degli aggregati naturali e per studiare aspetti meccanici specifici non ancora esplorati in letteratura, come la resistenza a taglio e il comportamento sotto carichi ciclici. Inoltre, sono state condotte prove su malte contenenti scorie EAFS fini per valutare la tensione di attivazione dello scorrimento allo stato fresco. I risultati ottenuti mostrano generalmente prestazioni superiori rispetto al materiale convenzionale. Il calcestruzzo prodotto con aggregati provenienti da C&DW presenta alcune criticità, solitamente legate a maggiore ritiro e prestazioni meccaniche inferiori rispetto ai materiali convenzionali. In questa tesi viene proposta una metodologia per migliorare le proprietà del calcestruzzo riciclato mediante l'aggiunta di Raw Crushed Wind Turbine Blade (RCWTB), un rifiuto derivante dal recupero e dalla frantumazione di pale eoliche dismesse. I risultati evidenziano riduzioni significative del ritiro plastico e miglioramenti rilevanti nella resistenza a flessione. Infine, è stato esplorato anche l'utilizzo del calcestruzzo residuo indurito degli impianti di betonaggio (CSW) come sostituto parziale o totale degli aggregati, riportando risultati soddisfacenti.

INDEX

Abstract 3

Sommario 4

1 Introduction 17

1.1 Environmental issues 17

1.2 Organization of the Thesis 19

1.3 Recovered aggregates for concrete production: State-of-the-art 20

1.3.1 Recycled aggregates 21

1.3.1.1 Recovery processes 21

1.3.1.2 Recycled aggregate properties 22

1.3.1.3 Concrete with recycled aggregates 23

1.3.2 Metal slags 24

1.3.2.1 Electric Arc Furnace Slag (EAFS) 26

1.3.3 Raw Crushed Wind Turbine Blade (RCWTB) 32

1.3.3.1 Recovery of wind turbine blades and RCWTB production 32

Properties of RCWTB 36

1.3.3.2 Including RCWTB in concrete 38

1.3.4 Concrete Sludge Waste 40

1.3.4.1 Properties 41

1.3.4.2 Concrete sludge Waste Concrete and Mortar 42

1.3.5 Literature review: summary, research lacks and research directions 43

1.4 Regulatory framework for recycled aggregate and recycled concrete 45

1.4.1 Recovering aggregates for constructions: Regulation 45

1.4.1.1 Recovery as By-products 45

1.4.1.2 REACH Regulation and ECHA Registration 47

1.4.1.3 Recovery from waste 49

1.4.1.4 CE Marking 53

1.4.2 Current standards for recycled concrete: Limits and possible applications 54

1.4.2.1 Americas 54

1.4.2.2 Asia 54

1.4.2.3 Europe 55

1.4.2.4 Oceania 58

References 59
2 Electric Arc Furnace Slag in cementitious conglomerates 69
2.1 Motivations 69
2.2 Rheology: Yield Stress characterization 71
2.2.1 Introduction 71
2.2.2 Experimental methods 71
2.2.2.1 Materials 71
2.2.2.2 Mix design 73
2.2.2.3 Aggregate morphology 74
2.2.2.4 Mortar production and Yield stress measurement 74
2.2.3 Results 75
2.2.3.1 Aggregate morphology 75
2.2.3.2 Yield stress 76
2.2.4 Analytical prediction of the Yield stress 78
2.2.4.1 Prediction of the Loose Packing Fraction 78
2.2.4.2 Prediction of the Yield stress 79
2.2.5 Conclusions 82
2.3 Shear transfer behavior 83
2.3.1 Introduction 83
2.3.2 Unconfined shear transfer 85
2.3.2.1 Experimental methods 85
2.3.2.2 Results 89
2.3.3 Confined shear transfer 93
2.3.3.1 Experimental methods 93
2.3.3.2 Results 97
2.3.4 Discussion 102
2.3.4.1 Shear transfer: effect of the transverse reinforcement ratio 102
2.3.4.2 Comparison with analytical results 103
2.3.5 Conclusions 109
2.4 Axial cyclic loading 110
2.4.1 Introduction 110
2.4.2 Experimental methods 112
2.4.2.1 Aggregates 112

2.4.2.2 Mix design and preparation of the samples 113
2.4.2.3 Experimental plan and mechanical characterization 114
2.4.2.4 Cyclic loading 114
2.4.3 Results 115
2.4.3.1 Mechanical characterization 115
2.4.3.2 Cyclic loading behavior 117
2.4.4 Analytical stress-strain models for Electric Arc Furnace Concrete under cyclic loading 127
2.4.4.1 Constitutive relations under cyclic loading 127
2.4.4.2 Simplified model 130
2.4.5 Conclusions 132
References 133
3 Raw Crushed Wind Turbine Blades as effective addition for concrete production 139
3.1 Motivations 139
3.2 Rheology: Yield Stress characterization 140
3.2.1 Introduction 140
3.2.2 Experimental program 141
3.2.2.1 Materials 141
3.2.2.2 Mix design 142
3.2.2.3 Fabrication of the mixtures 142
3.2.2.4 Yield stress measurements 145
3.2.3 Results 146
3.2.3.1 Effect of GRFP and RCWTB 146
3.2.3.2 Effect of water/cement ratio 149
3.2.4 Analysis and discussion 151
3.2.4.1 Analysis of the cementitious paste 151
3.2.4.2 Analysis of the mortars 153
3.2.5 Conclusions 156
3.3 Improving recycled aggregate concrete with Raw Crushed Wind Turbine Blade 157
3.3.1 Introduction 157
3.3.2 Experimental methods 158
3.3.2.1 Materials 158
3.3.2.2 Mix design 160

3.3.2.3 Testing program 161
3.3.3 Results 161
3.3.3.1 Fresh properties 161
3.3.3.2 Hardened density 162
3.3.3.3 Plastic shrinkage 163
3.3.3.4 Mechanical properties 164
3.3.3.5 Flexural strength 166
3.3.3.6 Microstructural analysis 169
3.3.4 Analysis and discussion 171
3.3.4.1 Prediction of flexural strength 171
3.3.4.2 Economic analysis 173
3.3.5 Conclusions 174
References 175
4 Aggregates recovered from Concrete Sludge waste in cementitious conglomerates 179
4.1 Introduction 179
4.2 Experimental methods 180
4.2.1 Materials 180
4.2.1.1 Cement paste 180
4.2.1.2 Aggregates 180
4.2.2 Mix design 182
4.2.3 Testing program 183
4.3 Results 184
4.3.1 Set 1 184
4.3.1.1 Fresh properties and density 184
4.3.1.2 Mechanical properties 185
4.3.1.3 Microstructural analysis 187
4.3.2 Set 2 189
4.3.2.1 Improving mixture with 10% CSW 0-20 189
4.3.2.2 Improving mixture with 30% CSW 0-20 189
4.3.2.3 Improving mixture with 100% CSW 0-20 190
4.3.3 Leaching tests 191
4.3.3.1 Metals 194
4.3.3.2 Anions 194

4.3.3.3 Chemical Oxygen Demand 196
4.3.3.4 pH 196
4.4 Conclusions 198
References 199
5 Summary, conclusions and future developments 202
5.1 Summary 202
5.2 Conclusions 204
5.3 Future developments 206

LIST OF FIGURES

Figure 1-1. Global aggregate consumption: a) Global per-capita aggregate production in 2017; b) Quantities of sand, gravel, and stone in societal use. Source: [15]. 18
Figure 1-2. Recovered aggregates presented in this work: a) Recycled aggregates from Construction and Demolition Waste; b) Electric Arc Furnace Slag; c) Raw Crushed Wind Turbine Blade; d) Concrete Sludge Waste. 20
Figure 1-3. Recycled aggregate particles. 22
Figure 1-4. Crude steel production by process. The combination of Blast Furnace (BF) and Basic Oxygen Furnace (BOF) represents the integral cycle. The other option is the Electric Arc Furnace (EAF) which can be fed with steel scraps or briquettes produced with Direct Reduction Iron (DRI), an alternative process to Blast Furnace for processing the iron ore. CO_2 intensities are given in tons of CO_2 per ton of crude steel cast, based on 2022 calculation. Source: [55]. 25
Figure 1-5. EAFS in different fractions: a) 0-4 mm; b) 4-8 mm; c) 8-12 mm; d) 8-16 mm. 26
Figure 1-6. Applications of Electric Arc Furnace Concrete: a) KUBIK research building (Source: [102]); b) Port of Bilbao, Spain (Source: [101]). 31
Figure 1-7. Percentage of electricity demand covered by wind in Europe in 2023. Source: [104]. 33
Figure 1-8. European investments in the wind energy sector: a) New wind installations in 2024; b) Investment in new wind farms 2015-2024. Data from: [105]. 34
Figure 1-9. Wind turbine blade: a) view of the bolted connection (Source: [112]); b) blade section. 36
Figure 1-10. SEM images of the RCWTB: a)-b) fibers; c) balsa wood; d)-e) polyurethane; f) micro-fibers. Source: [112]. 37
Figure 1-11. Breaking surface in concrete including RCWTB. 39
Figure 1-13. Processing scheme of a plant for slag preparation [154]. 46
Figure 2-1. Materials employed in the experimental campaign: a) Sand A; b) Sand B; c) EAFS. 72
Figure 2-2. Grading curves of cement and aggregates. 73
Figure 2-3. Results: a) Yield stress; b) Relative yield stress. Error bars indicate the standard deviation. 77
Figure 2-4. Modelling of the parameter a varying the EAFS replacement. Black markers represent the values obtained from the experimental φ_m measurements. 78
Figure 2-5. Comparison between predicted values (Equation 2-1) and experimental measurements of the loose packing fraction. 79
Figure 2-6 Comparison between predicted and experimental mortar yield stress with: a) Quadratic and b) Linear regression of the parameter a for loose packing fraction modelling. 81
Figure 2-7. Aggregate grading curves. 86
Figure 2-8. Aggregates employed for this experimental campaign: a) EAFS 4-8; b) EAFS 8-12; c) EAFS 8-16. 86
Figure 2-9. Geometry and reinforcement details of push-off specimens. 88
Figure 2-10. Push-off test setup. 88
Figure 2-11. Failure patterns in selected push-off specimens: a) NAC; b) EAFC. 91
Figure 2-12. Crack surface in the shear transfer plane: a) NAC; b) EAFC. 91
Figure 2-13. Results of push-off tests: a) shear stress-slip curves; b) shear stress-crack opening curves. 92
Figure 2-14. Aggregates grading curves. 94
Figure 2-15. Geometry and reinforcement details of push-off specimens. 96

Figure 2-16. Push-off test setup: a) front; b) back. 96
Figure 2-17. Failure patterns in selected push-off specimens: a) NAC-2S; b) NAC-3S; c) NAC-4S; d) EAFC-2S; e) EAFC-3S; f) EAFC-4S. 99
Figure 2-18. Dimensionless shear strength for NAC and EAFC. Note: $\tau_u^* = \tau_u/f_c^{1/2}$; $\tau_u^+ = \tau_u/f_{ct}$. 99
Figure 2-19. Results of push-off tests: a) shear stress-slip curves; b) shear stress-crack opening curves. 101
Figure 2-20. Strains in the clamping steel. 102
Figure 2-21. Effect of the transverse reinforcement on the ultimate shear strength. 103
Figure 2-22. A hysteresis loop for concrete under cyclic loading and its characteristic points. U: Unloading point; R: Residual point; PR: Partial residual point; C: Common point; E: End point. 111
Figure 2-23. Grading curves of the aggregates. 112
Figure 2-24. Test setup of the cyclic compression test: a) scheme; b) photo. SG_l: Longitudinally-placed strain gauge; SG_tr: Transversally-placed strain gauge. 114
Figure 2-25. Loading protocol of the cyclic test. 115
Figure 2-26. Results of short-term cyclic compression tests: a-b) NAC1; c-d) EAF1. SG1 and SG2 stand for longitudinal SGs, SG3 and SG4 stand for transversal SGs. 118
Figure 2-27. Skeleton curves for cyclic compression tests. 118
Figure 2-28. Deformative properties of tested specimens under cyclic compression: a) Secant Modulus; b) Poisson's coefficient. 120
Figure 2-29. Results of short-term cyclic compression tests in terms of longitudinal, transverse, and volumetric mean strain: a-b) NAC1; c-d) EAF1. The subscript "sk" refers to the skeleton curve. 121
Figure 2-30. Skeleton curves of longitudinal, transverse, and volumetric mean strain for cyclic tests: a) first set of mixtures; b) second set of mixtures. 122
Figure 2-31. Evolution of damage: a) D_E; b) D_v. 124
Figure 2-32. Experimental vs. calculated skeleton curves. 128
Figure 2-33. Comparison between tested and calculated stress-strain relation in a loop of cyclic loading test for: a) NAC1; b) EAF1. 129
Figure 2-34. Comparison between experimental and simplified stress-strain relations for: a) NAC1; b) EAF1; c) NAC2; d) EAF2; e) BAR. 131
Figure 3-1. Materials employed in the experimental campaign: a) Sand; b) RCWTB; C) GFRP separated from RCWTB. 141
Figure 3-2. Granulometric distribution of cement and sand. 142
Figure 3-3. Yield stress for the cementitious pastes and mortars prepared for this experimental campaign: a) W/C=0.4; b) W/C=0.5. Error bars indicate the standard deviation. 147
Figure 3-4. Relative yield stress (i.e. ratio between the yield stress of the mixture containing fibers and the yield stress of the reference cement paste) for the cement pastes and mortars prepared in this work: a) W/C=0.4; b) W/C=0.5. Error bars indicate the standard deviation. 148
Figure 3-5. Effect of the W/C ratio for: a) Cement Paste+GFRP; b) Mortar+GFRP; c) Mortar+RCWTB. 150
Figure 3-6. Relative yield stress (i.e. ratio between the yield stress of the mixture containing fibers and the yield stress of the reference cement paste) as a function of the fiber relative packing fraction (i.e. ratio between the fiber volume fraction and the fiber maximum packing fraction) for cement pastes containing GFRP separated from RCWTB: a) GFRP fibers are considered as being deformed by the constitutive cement paste yield stress; b) GFRP fibers are considered as deformed by the overall mixture yield stress (paste and fibers). 152

Figure 3-7. Relative yield stress (i.e. ratio between the yield stress of the mortar containing fibers and the yield stress of the reference cement paste) as a function of the total relative packing fraction (i.e. the sum of the relative packing fraction of sand and fiber) for mortars containing GFRP separated from RCWTB: a) GFRP fibers are considered as being deformed by the constitutive cement paste yield stress; b) GFRP fibers are considered as deformed by the constitutive mortar yield stress (paste and sand); c) GFRP fibers are considered as deformed by the overall mixture yield stress (paste, sand and fibers). 154
Figure 3-8. Relative yield stress (i.e. ratio between the yield stress of the mortar containing fibers and the yield stress of the reference cement paste) as a function of the total relative packing fraction (i.e. the sum of the relative packing fraction of aggregate and fiber) for whole RCWTB inclusions: a) GFRP fibers are considered as deformed by the overall mixture yield stress (paste, aggregate and fibers), whereas RCWTB aggregate-like particles are considered as part of the sand; b) GFRP fibers are considered as deformed by the overall mixture yield stress, whereas RCWTB aggregate-like particles are not considered as part of the sand. 155
Figure 3-9. Granulometric distribution of the aggregates. 159
Figure 3-10. Materials employed in the experimental campaign: a) siliceous aggregate 12/22 mm; b) siliceous aggregate 4/12 mm; c) siliceous aggregate 0/4 mm; d) limestone aggregate 0/2 mm; e) CRA 4/22 mm; f) RCWTB. 159
Figure 3-11.Plastic shrinkage: evolution over three days. 163
Figure 3-12. Compressive strength test results: a) evolution under ambient curing; b) evolution under moist curing. 165
Figure 3-13. Flexural strength test results: a) evolution under ambient curing; b) evolution under moist curing. 167
Figure 3-14. Flexural strength test results: a) effect of RCWTB in 3-day flexural strength; b) effect of RCWTB in 7-day flexural strength. 168
Figure 3-15. SEM images of ITZs between RCWTB components and the cementitious matrix: a) GFRP-composite fiber; b) polymeric particle. Source: [81]. 169
Figure 3-16. EDX spectra of a GFRP-composite fiber. Source: [81]. 170
Figure 3-17. EDX spectra of a polymeric particle. Source: [81] 171
Figure 3-18. Comparison between experimental and predicted flexural strengths. 172
Figure 3-19. Cost of the concrete mixes. 173
Figure 4-1. Aggregates employed in this work: a) NA 0-4; b) NA 4-8; c) NA 8-16; d) CSW 0-20. 181
Figure 4-2. Aggregate grading curves. 181
Figure 4-3. Slump and densities of the Set 1 mixtures. 185
Figure 4-4. Compressive strength of the Set 1 mixtures. Error bars indicate the standard deviation. 186
Figure 4-5. Elastic Modulus E and splitting strength f_{ct} for Set 1 mixtures. Error bars indicate the standard deviation. 186
Figure 4-6. SEM images of the mixtures: a) REF; b) 20CSW; c) 30CSW; d) 100CSW. 188
Figure 4-7. Improvement recorded in the mixture optimization for 10% CSW 0-20. 189
Figure 4-8. Improvement recorded in the mixture optimization for 30% CSW 0-20. 190
Figure 4-9. Compressive strength (28-days) comparison between Set 1 and Set 2 for mixtures with the same replacement ratio. 191
Figure 4-10. Concentration of metals in the leachate. 195
Figure 4-11. Concentration of anions in the leachate. 195

Figure 4-12. Chemical Oxygen Demand (COD) in the leachate. 197
Figure 4-13. pH in the leachate. 197

LIST OF TABLES

Table 1-1. Main physical properties of EAFS. 28
Table 1-2. Average variations of EAFC fresh and hardened properties compared to those of NAC. 29
Table 1-3. Summary of the durability effects of EAFS incorporation in concrete. 29
Table 1-4. Properties of RCWTB. 37
Table 1-5. Average effect of the inclusion of RA recovered from returned concrete. 42
Table 1-6. Summary, research lacks and research directions for the recovered aggregates analyzed in this dissertation. 44
Table 1-7. Maximum percentage of replacement of coarse aggregates (% by mass). Source: EN 206 [179]. 56
Table 1-8. Maximum percentage of replacement of the coarse aggregate fraction (by mass) in concrete according to NTC 2018 [163]. 57
Table 2-1. Physical properties of the aggregates. 72
Table 2-2. Mixtures matrix. 73
Table 2-3. Morphology of the aggregates. 75
Table 2-4. Results of the packing fraction measurements. 76
Table 2-5. Physical properties of the aggregates. 85
Table 2-6. Mix design in kg/m^3. 86
Table 2-7. Steel bars mechanical properties. 88
Table 2-8. Fresh and hardened concrete properties 89
Table 2-9. Mean results of the push-off tests. 90
Table 2-10. Physical properties of the aggregates. 94
Table 2-11. Mix design in kg/m^3. 94
Table 2-12. Steel bars mechanical properties. 96
Table 2-13. Fresh and hardened concrete properties. 97
Table 2-14. Mean results of the push-off tests. 98
Table 2-15. Comparison between experimental and calculated ultimate shear strength for unconfined push-off samples. 105
Table 2-16. Comparison between experimental and calculated ultimate shear strength for confined push-off samples. 107
Table 2-17. Comparison between experimental and calculated residual shear strength for confined push-off samples. 108
Table 2-18. Physical properties of the aggregates. 112
Table 2-19. Concrete mix details (kg for 1 m^3). 113
Table 2-20. Test matrix of this experimental campaign. 115
Table 2-21. Mean fresh and hardened properties. 116
Table 2-22. Results of cyclic loading tests. 117
Table 3-1. Experimental matrix of the cast mixtures with water/cement ratio equal to 0.4 (in kg/m^3). 143
Table 3-2. Experimental matrix of the cast mixtures with water/cement ratio equal to 0.5 (in kg/m^3). 144
Table 3-3. Mix design (in kg/m^3). 160
Table 3-4. Results of fresh tests. 162
Table 3-5. Hardened density (in kg/m^3). 163

Table 3-6. Cost of the concrete constituents. 173
Table 4-1. Physical properties of the aggregates. 180
Table 4-2. Mix design for Set 1 (in kg/m^3). 182
Table 4-3. Mix design Set 2 (in kg/m^3). 183
Table 4-4. Results for fresh properties, density and compressive strength of the Set 1 mixtures. 184
Table 4-5. Results for fresh properties, density and compressive strength of the Set 2 mixtures. 184
Table 4-6. Comparison between Set 1 and Set 2 for mixtures with the same replacement ratio. 191
Table 4-7. Results of the leaching test on REF. 192
Table 4-8. Results of the leaching test on 10CSW2. 193

1 INTRODUCTION

1.1 ENVIRONMENTAL ISSUES

As the occurrence of extreme environmental events, e.g. rainfalls, droughts, hurricanes, has become more frequent in recent years [1], these natural calamities are continuously being worsened by climate change [2]. According to the World Meteorological Organization, the year 2024 is considered the hottest on record, with temperatures surpassing 1.5°C above pre-industrial levels [3]. According to recent reports on the climate change [4], there will be extensive and rapid changes on the ecosystems with unknown consequences for human and environmental health. The global warming may increase the evapotranspiration, and the severity of heat waves [5]; while rising land evaporation driven by a warming climate can intensify drought conditions, increasing the likelihood of wildfires and prolonging wildfire seasons [6]; and finally the heavy rain and snowstorms may become more frequent due to the air augmented capacity to hold moisture [5].

The global warming emergency is even worsened by the global population growth and the expansion of developing cities. Indeed, the construction sector plays a crucial role in economic growth significantly affecting the global environment. According to the 2023 Global status for building and construction [7], the buildings and construction sector plays a major role in global climate change, contributing approximately to 21% of worldwide greenhouse gas emissions. In 2022, buildings accounted for 34% of global energy consumption and 37% of energy- and process-related carbon dioxide emissions.

Concrete plays a major role for the building industry, because of its versatility, excellent performance and reduced prices. In fact, it is the most widely used construction material [8], and deemed to be the most extensively used substance on the planet after water [9,10]. Its great importance is related to the development of structures and infrastructure, e.g. bridges, roads, ports and airports. The concrete great demand in the construction industry is also an environmental concern linked to its components. A traditional concrete mixture typically consists of aggregates (about 60-75% of the total volume), cement , and water [11,12]. In such a conglomerate, cement is the primary source of carbon emission [10,13]: for each kilogram of cement, between 0.66 and 0.82 kg of CO_2 emissions are generated, accounting for about 7% of global anthropogenic CO_2 emissions [10,14]. However, the concrete supply even requires a large volume of aggregates, i.e. sand, gravel and crushed rocks. Global consumption of natural aggregates reached approximately 48.3 billion tons in 2015, with an estimated 5% growth every five years [11]. Such a consumption is mainly dominated by high production per capita in China and North America (Figure 1-1), although low- and medium-income countries are expected to experience the most significant relative growth in demand [15,16]. Despite its apparent simplicity, sand and gravel extraction carries significant environmental consequences due to the massive scale of its consumption in construction. These impacts include groundwater contamination [17], riverbed erosion leading to ecosystem damage and affecting livelihoods, and irreversible damage to river ecosystems when extraction exceeds natural replenishment rates [18]. In such a context, there is an urgent need to develop innovative construction materials that minimize reliance on natural resources, this involves reducing dependency on virgin resources and maximizing the use of by-products from various industries [12].

The construction industry is expected to continuously grow, playing a vital role in shaping our world, underpinning urbanization and economic progress. As society evolves, driven by technological innovation and the imperative for environmental sustainability, this sector remains poised for sustained evolution [19].

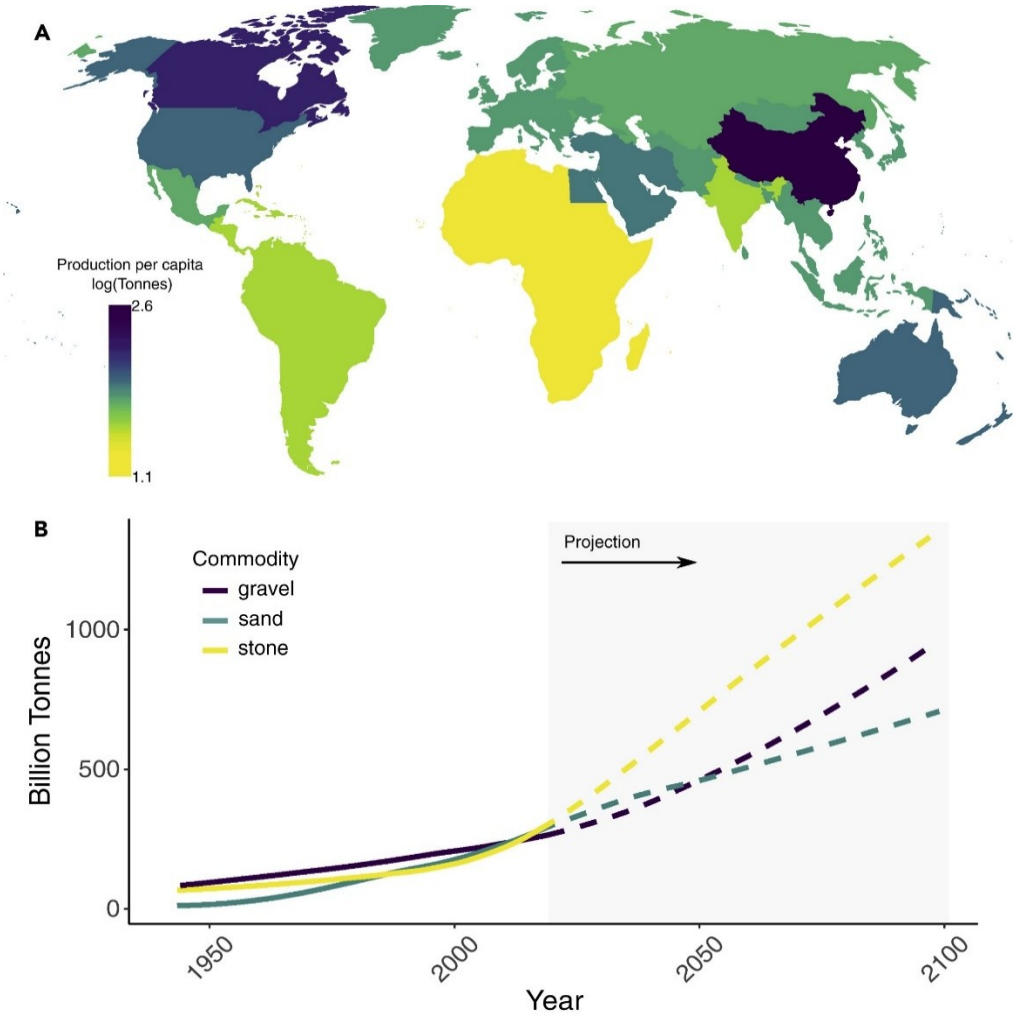

Figure 1-1. Global aggregate consumption: a) Global per-capita aggregate production in 2017; b) Quantities of sand, gravel, and stone in societal use. Source: [15].

1.2 ORGANIZATION OF THE THESIS

This PhD dissertation is organized into five chapters:

- Chapter 1 provides an introduction with the motivation and environmental issues linked to the exploitation of natural aggregates in the building industry. Subsequently, a state-of-the-art is presented focusing on the recovered aggregates analyzed in the following chapters. The recovery process, physical properties and effects of the replacement in concrete are outlined according to the literature survey.
- Chapter 2 provides insights on the use of Electric Arc Furnace Slag (EAFS), a by-product of the steel-making industry, as alternative aggregate. The results of experimental campaigns focusing on rheology, shear transfer and axial cyclic loading are shown.
- Chapter 3 provides insights on the use of Raw Crushed Wind Turbine Blade (RCWTB), a waste obtained from decommissioned wind turbines, as addition in concrete mix-design. Findings are presented on the rheology of cementitious conglomerates including RCWTB. Further, the results of an experimental campaign aiming to improve recycled concrete properties with RCWTB addition are presented.
- Chapter 4 deals with the use of Concrete Sludge Waste (CSW) as replacement of natural aggregate. Such waste is obtained from recovering leftover concrete and washing residues in Ready-Mix Concrete (RMC) plants.
- Chapter 5 summarizes the previous chapters, giving the fundamental outcomes with possible future developments.

1.3 RECOVERED AGGREGATES FOR CONCRETE PRODUCTION: STATE-OF-THE-ART

The growing demand for natural aggregates (NA) has been forcing industry to consider alternative materials. The possibility of using wastes and by-products as aggregates to reduce the environmental impact of concrete is well-documented [20]. Whereas research has been exploring this path extensively, large-scale applications of these practices remain a challenge.

This section presents a review of the current state-of-the-art regarding four promising alternative aggregates (Figure 1-2): Recycled Aggregates (RA), metal slags with particular attention to Electric Arc Furnace Slag (EAFS), Raw Crushed Wind Turbine Blades (RCWTB), and Concrete Sludge Waste (CSW). Their features, recovery processes, and the most relevant applications are deepened, highlighting both their potential advantages and any limitations. At the end of this section, research lacks and goals for the next sections are outlined.

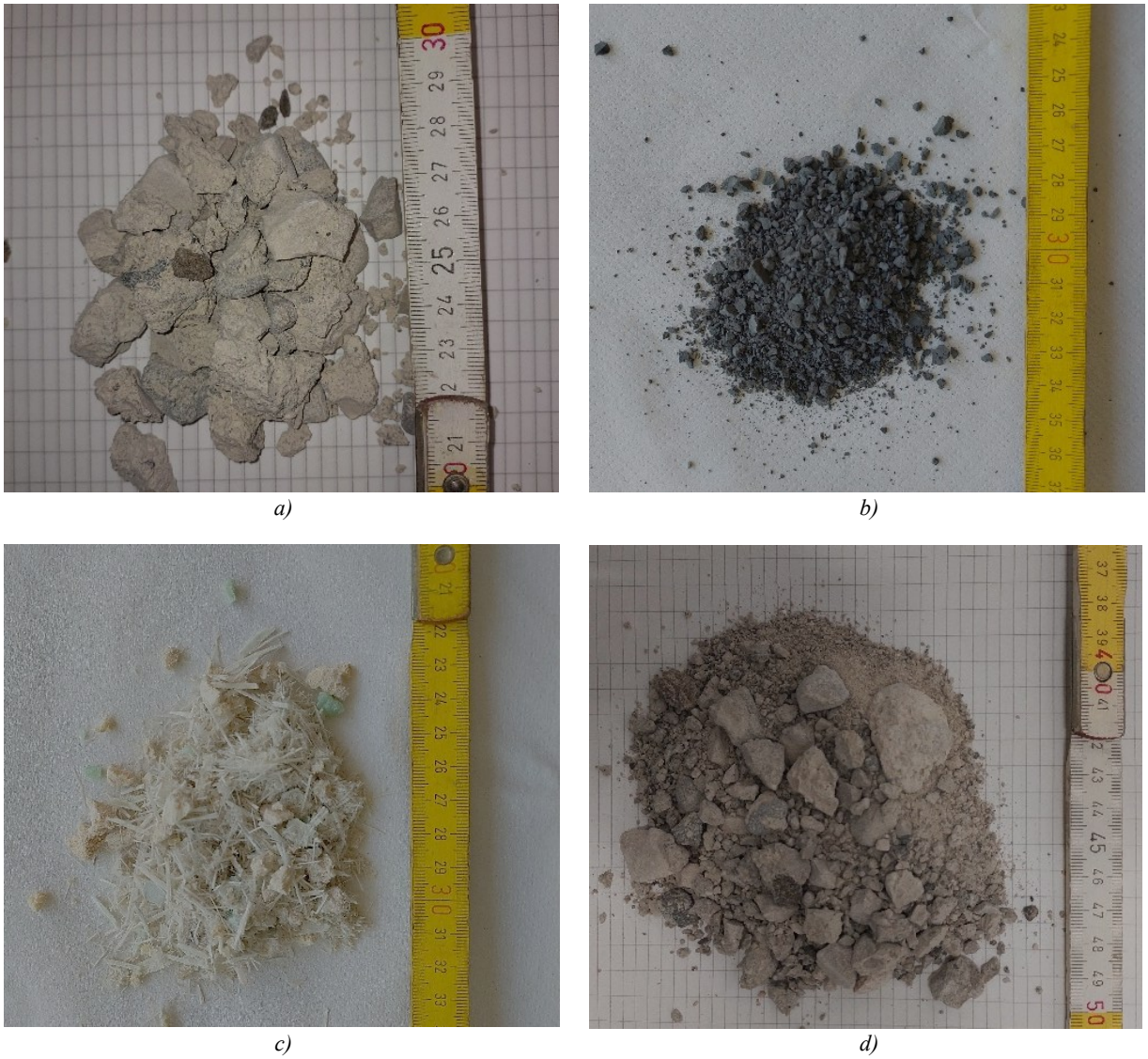

a) *b)* *c)* *d)*

Figure 1-2. Recovered aggregates presented in this work: a) Recycled aggregates from Construction and Demolition Waste; b) Electric Arc Furnace Slag; c) Raw Crushed Wind Turbine Blade; d) Concrete Sludge Waste.

1.3.1 Recycled aggregates

Talking about Recycled Aggregates (RA), the research community usually refers to recovered aggregates from Construction and Demolition Waste (C&DW).

C&DW is a combination of several materials, including inert and non-inert waste, hazardous and non-hazardous waste. They include concrete, steel, asphalt, bricks, metals, plastic, glass, wood, even counting those materials resulting from natural disaster, e.g. earthquakes, hurricanes, floods and tsunamis.

Globally, the production of C&DW is a huge burden. An estimated 2.1 billion tons of solid waste was generated worldwide in 2023 [21], which include at least 30% of C&DW [22,23], and is expected to grow due to the ongoing increase of world population. Though, such a waste generation is not equally distributed around the world, the largest waste producers are China, United States and the European Union [24]. The recovery rate varies from country to country [22]; nonetheless, it is estimated that roughly 35% of the world's C&DW is landfilled [22,23], despite its recyclability potential. According to this background, several governments, global organizations and academics have been acting on the recycling and reusing of C&DW to reduce its negative environmental and economic impacts. The European Union, for example, reached a C&DW recovery ratio of 89% in 2020, complying the target of 70% reuse and recycling aimed for 2020 [20]. Although this data includes reuse, recycling and backfilling operations, this goal was achieved mainly by backfilling and involving low-value recovery practices, reducing the potential to move towards effective waste management.

1.3.1.1 Recovery processes

The production process of RA has remained largely unchanged over the past years, despite advancements in C&DW recycling technologies. C&DW recycling facilities are generally classified into two types: stationery and mobile facilities. In stationary facilities, C&DW must be transported to the plant for processing. These facilities typically offer higher processing capacities and produce RA of superior quality compared to mobile units. Conversely, mobile facilities operate directly on-site, allowing immediate processing of C&DW and direct reuse of recycled aggregates in new construction projects, eliminating the need for additional transport [11].

The quality of RA is influenced by the type and number of crushing stages, which not only reduce size but also improve aggregate shape through collision and abrasion by making particles rounder [25] and removing some old adhered mortar [26]. The recycling process typically includes subsequent steps of crushing, screening, and impurity removal (e.g., steel, plastics, glass). Initially, a jaw crusher processes large debris and embedded steel, followed by magnetic separation and sieving. Oversized particles (typically >20 mm) undergo secondary crushing, which may be repeated if needed. Advanced variations of this method use equipment like eccentric rotors or screw crushers for better mortar removal and improved RA quality [27,28].

In addition to mechanical methods, thermal treatments are employed to weaken and remove adhered mortar. The heating and sorting method employs rotary kilns to warm the aggregates up to 700 °C, reducing mortar content to as low as 2% [29]. The heating and rubbing technique involves heating concrete to around 300 °C, followed by rubbing in a tube mill [30]. Newer adaptations replace kerosene furnaces with microwave ovens, achieving similar results with lower energy use [31]. However, temperatures above 500 °C can degrade RA quality, and thermal processes are energy-intensive with high CO_2 emissions [28]. Wet recycling techniques, such as thermal expansion, involve soaking C&DW in water, heating it, and then rapidly cooling to induce mortar-cracking stresses [32]. Another method, i.e. autogenous cleaning, uses

particle collision in a rotating drum, followed by washing and drying [33]. While these methods effectively clean aggregates, they require substantial water use, increasing operational costs.

1.3.1.2 Recycled aggregate properties

The assessment of RA effect in concrete mixtures requires a thorough assessment of its physical and mineralogical characteristics, which include particle shape, gradation, moisture content, specific gravity, bulk density, porosity, and mechanical resistance. These features influence performance parameters such as strength, workability, and durability [34–36].

RA particles generally exhibit angular shapes due to the fracturing pattern of crushed concrete. While the overall grain size distribution tends to be similar to Natural Aggregates (NA), RA contains more fines and a higher proportion of adhered mortar in smaller particles, which affects the mix design and increases paste demand [35,37]. The fineness modulus varies based on the crushing method and quality of the parent concrete [35]. Owing to the residual cement mortar on the particle surface, RA presents a rougher and more porous texture than NA. This rough surface can improve mechanical interlock but also increases water absorption. Indeed, the weak Interfacial Transition Zone (ITZ) created by the old mortar leads to reduced mechanical performance compared to natural aggregates [38,39].

RA in coarse fraction (>4 mm) typically exhibits lower specific gravity (2170-2630 kg/m^3) and bulk density (1178-2890 kg/m^3) than NA due to the presence of porous, low-density adhered mortar [40] as shown in Figure 1-3. This results in greater void content in concrete mixes, which must be compensated with additional cement paste or admixtures to maintain workability and strength [36,41]. Because of the porous nature of the bonded mortar (Figure 1-3), RA absorbs more water than NA. This leads to a decrease in fresh concrete density and an increase in air content, both of which adversely affect durability. A full replacement of aggregate coarse fraction with RA typically reduces concrete density by 5-6% [35,42]. RA shows higher crushing and impact values than NA, indicating weaker structural integrity. Los Angeles abrasion losses range from 36% to 65%, largely depending on the amount and quality of adhered mortar [35,43]. This high variability prevents the establishment of a universal performance model for RA, as the origin and composition of the source concrete play a significant role [36].

Fine fractions of RA (<4 mm) can also influence concrete performance, which is usually more detrimental than coarse RA. Their properties depend on the recycling technique and the number of crushing stages. The angularity and surface texture of fine RA further contributes to water absorption and affects the concrete fresh and hardened properties [36].

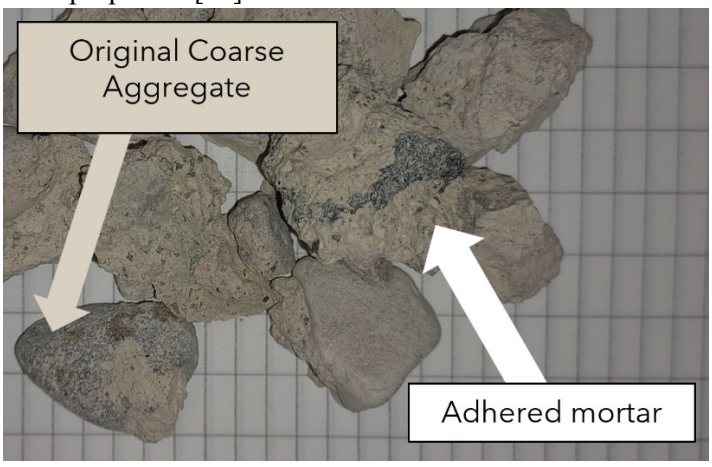

Figure 1-3. Recycled aggregate particles.

1.3.1.3 Concrete with recycled aggregates

To fully comprehend how recycled aggregate concrete (RAC) behaves, it is essential to compare its fresh and hardened properties with those of natural aggregate concrete (NAC). Workability, mechanical characteristics, physical and chemical properties, and long-term performance are typically affected by the percentage of recycled aggregate (RA) included in the mixture.

1.3.1.3.1 Workability and Density

Workability refers to how easily fresh concrete can be mixed, placed, and compacted. RAC typically exhibits reduced workability compared to NAC due to the higher water absorption and rougher texture of recycled aggregates [11,36,44]. To neutralize this effect, an higher water dosage, usually from 5% to 15% higher, is often adopted during mixing [36,45].

RAC tends to have lower density than NAC due to the attached mortar on recycled aggregates, which is more porous. Full replacement of natural aggregates commonly lowers density by about 5% [35]. This trend is also observed with recycled clay brick aggregates [46].

1.3.1.3.2 Mechanical Properties

A general deterioration of mechanical performance is typically observed as RA content increases [11]. Both recycled concrete aggregate and recycled clay brick aggregates reduce compressive strength. A 100% RA mix can reduce compressive strength by up to 40%. Some inconsistencies exist, e.g. Cachim [46] noted a strength increase at 15% recycled clay brick aggregate replacement due to pre-saturation, which can provide water for cement hydration during curing while unaffecting the initial water-to-cement ratio. Young's modulus also drops significantly with higher RA content. At 100% RA, the elastic modulus may decrease by around 23%. Flexural strength can lower by 11% and splitting tensile strength by up to 16%. These trends are generally consistent, though outliers exist also due to methodological variations [11].

1.3.1.3.3 Durability and long-term performance

RAC is more vulnerable to freeze-thaw damage because its higher porosity allows more water into the pores, increasing internal pressure during freezing. One study showed a 10.4% compressive strength loss in RAC compared to just 0.6% in NAC [47]. RAC may be more prone to Alkali-Silica reactions (ASR) due to residual reactive silica in recycled aggregates. Johnson and Shehata [48] found increasing RA content led to greater ASR-induced expansion. The reaction of calcium hydroxide with CO_2, called carbonations, reduces concrete pH and can corrode embedded steel. Due to higher porosity, RAC typically shows deeper carbonation than NAC. In fact, carbonation depth can be up to 2.5 times greater in RAC [49]. Chloride ingress, which accelerates rebar corrosion, is also greater in RAC due to its permeability. Guo et al. [50] found that total chloride penetration increased with the amount of RA, reaching up to twice the value of NAC when 100% RA was used.

Creep, or long-term deformation under load, increases with RA content due to higher porosity and water retention. Studies confirm a direct correlation between RA percentage and creep strain [51].

1.3.2 Metal slags

Over recent decades, global steel production has surged dramatically, resulting in a parallel rise in the generation of industrial by-products, particularly slags. As shown in Figure 1-4, steel can be manufactured primarily through two distinct methods: the traditional “integral cycle” and the more modern “electric arc cycle.” [52]. Each of these processes produces slag with varying physical, chemical, mineralogical, and mechanical properties, which in turn influence its potential for recycling and reuse.

One of the most well-known steelmaking techniques is the Linz-Donawitz process, a method that transforms pig iron into steel by blowing pure oxygen into the molten metal. This phase constitutes the second phase of the integral steelmaking cycle, where the initial stage involves melting iron ore in a blast furnace to yield pig iron. The Linz-Donawitz process, conducted in a basic oxygen furnace, is a milestone of this method. These two stages collectively produce substantial volumes of slag: approximately 290 kg of Blast Furnace Slag (BFS) per ton of pig iron [53] and around 110 kg of Basic Oxygen Furnace Slag (BOFS) per ton of steel [54]. According to global production data from the World Steel Association, pig iron production peaked at 1,963 million tons in 2021 and remained almost stable through 2023, reaching 1,892 million tons [55].

In contrast, the electric arc furnace process represents a more sustainable approach to steelmaking. This method allows for recycling steel and iron scrap in a streamlined, single-step process, with lower carbon emissions (Figure 1-4). Depending on operational parameters, e.g. furnace type, scrap composition, and additional materials used, the production of Electric Arc Furnace Slag (EAFS) ranges from 120 to 180 kg per ton of steel [56]. The Electric Arc Furnace process accounted for 28.6% of total global steel production in 2022 [55]. However, its share is significantly higher in several countries. In Europe, countries such as Poland (51.2%), Spain (71.9%), Italy (85.8%), Portugal (100%), Greece (100%), Croatia (100%), and Bulgaria (100%) rely heavily on electric arc furnaces; similarly, outside the EU, countries like Türkiye (71.6%), the United States (68.3%), Mexico (93.4%), Iran (92.1%), and Saudi Arabia (100%) also depend predominantly on this method according to 2023 world steel production [55]. Given its environmental advantages, the electric arc furnace process is gaining importance, and many nations are transitioning their steel sectors towards full electrification, suggesting a future increase in EAFS volumes.

Regardless of the production method, steel generally meets high-quality standards. Nevertheless, to satisfy increasing market demands for superior material performance, secondary refining operations, called secondary metallurgy, are frequently employed. Among these, there is the ladle furnace, a specialized form of electric arc furnace used for additional steel refining process. The refinement process in ladle furnace typically produces 30-50 kg of Ladle Furnace Slag (LFS) per ton of refined steel.

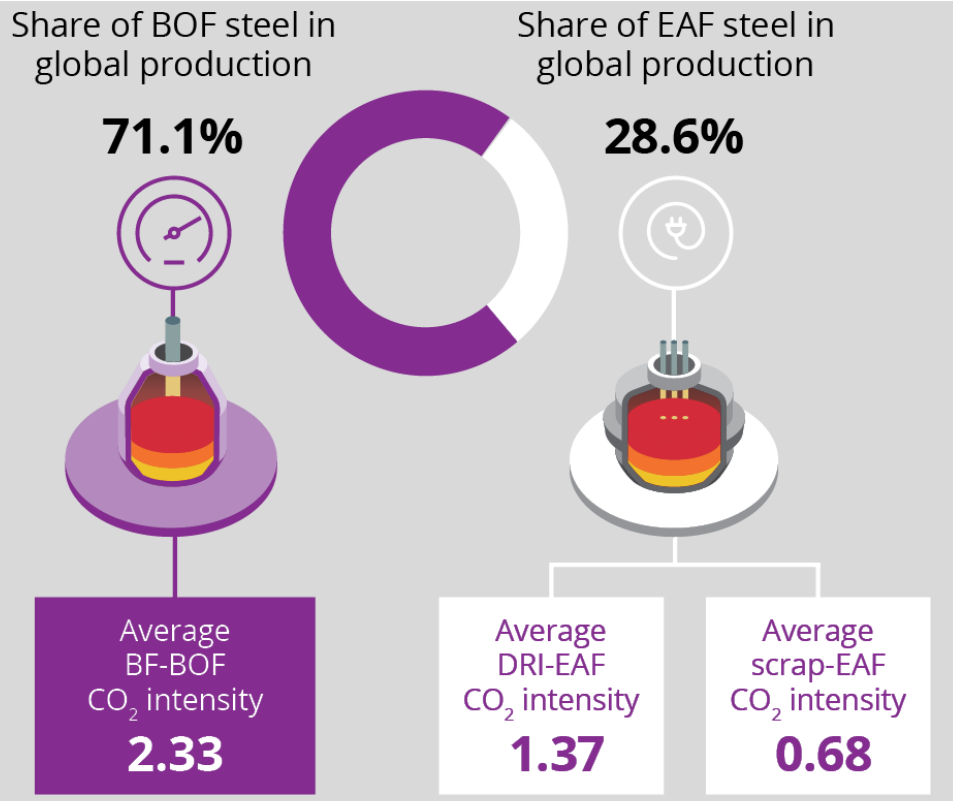

Figure 1-4. Crude steel production by process. The combination of Blast Furnace (BF) and Basic Oxygen Furnace (BOF) represents the integral cycle. The other option is the Electric Arc Furnace (EAF) which can be fed with steel scraps or briquettes produced with Direct Reduction Iron (DRI), an alternative process to Blast Furnace for processing the iron ore. CO_2 intensities are given in tons of CO_2 per ton of crude steel cast, based on 2022 calculation. Source: [55].

1.3.2.1 Electric Arc Furnace Slag (EAFS)

1.3.2.1.1 Properties

Electric Arc Furnace Slag (EAFS) is a by-product generated during the refining of molten steel in Electric Arc Furnace. This process involves the addition of fluxing agents like lime, limestone, and fluorspar. Due to density differences between slag and steel, EAFS can be easily separated from the molten metal. Electric Arc Furnace typically operates using steel scrap, sometimes supplemented by small quantities of pig iron, along with fluxes and carbon powder. The quality, density, and proportion of these input materials significantly influence the properties of both the steel and the resulting slag.

Two primary types of steel are produced with Electric Arc Furnace technology: carbon steel and stainless/high-alloy steel, each returning in distinct slags: EAFS-C and EAFS-S, respectively. The differences in composition between these types necessitate separate considerations in their processing and reuse. However, authors and research refer to EAFS as the one produced from carbon steel as it is the most abundant and common. For the same reason, EAFS-C is considered as EAFS in this work (Figure 1-5).

The final composition and characteristics of EAFS are shaped by a range of factors, including furnace type, steel grade, additives used, operating conditions, and post-cooling management. Typically, EAFS undergoes air cooling followed by weathering and physical treatments like crushing, sieving, magnetic separation, and controlled wetting/drying. These steps are essential to reduce the volumetric expansion of the slag, a basic factor for its safe reuse in construction [57–59].

Chemically, EAFS commonly contains CaO, SiO_2, Fe_2O_3, Al_2O_3, MgO, and MnO, [60]. The mineralogy is complex and varies with composition, featuring phases such as wustite, magnetite, brownmillerite, gehlenite, olivine, and various calcium silicates. Table 1-1 provides the main physical properties of electric arc furnace, demonstrating its suitability in construction applications as replacement of natural aggregates [52,60].

a) *b)* *c)* *d)*

Figure 1-5. EAFS in different fractions: a) 0-4 mm; b) 4-8 mm; c) 8-12 mm; d) 8-16 mm.

1.3.2.1.2 Electric Arc Furnace Concrete (EAFC)

Concrete incorporating Electric Arc Furnace Slag (EAFS) as aggregate has emerged as a promising alternative to the conventional one, capable of manufacturing not only normal strength concrete, but also High Strength Concrete (HSC), Self-Compacting Concrete (SCC), and Fiber-Reinforced Concrete (FRC).

In fresh state properties, concrete made with EAFS, known as Electric Arc Furnace Concrete (EAFC), generally shows reduced workability compared to natural aggregate concrete (NAC). This reduction is more important when EAFS replaces fine fraction, due to the angular shape of slag particles resulting from the crushing process [60]. The EAFS angular particles increase plastic viscosity and yield stress, lowering slump values [61]. High water absorption from some slags, depending on the cooling method, also increases water demand. However, the use of admixtures such as plasticizers and air entrainers can mitigate these effects and help achieve comparable workability to NAC. When EAFS is used in the coarse aggregate fraction, the slump reduction is more modest [62], and slump retention after 60 minutes remains high, with reductions between 9% and 16% [63]. Air content stays within the typical 1% to 1.6% range. The density of EAFC ranges from 2500 to 3100 kg/m^3, primarily due to the higher density of the slag [64], which is influenced by its intrinsic properties such as density and porosity. Because of this feature, EAFC has demonstrated effective radiation shielding capabilities [65,66], making it a sustainable alternative to traditional heavyweight concretes.

The compressive strength of EAFC is generally improved, especially when EAFS is used as coarse aggregate. This enhancement is attributed to the high strength of slag due to its iron oxide content, better bond with the cement matrix, and stronger Interfacial Transition Zone (ITZ) [67]. However, porous slags produce less evident improvements. Pellegrino and Gaddo [68] observed strength gain beyond 28 days for EAFC, while Manso et al. [69] found comparable strength with conventional mixes only after 90 days, emphasizing the impact of slag porosity and mineralogy. Özalp [70] produced concrete with EAFS and achieved results comparable to conventional concrete, without notable improvements in strength. In contrast, Faleschini et al. [71] reported an average compressive strength increase of about 35%-40%, based on tests conducted with both low-porosity and porous slags.

Tensile strength, strongly dependent on the testing method, also improves with EAFS replacement. Splitting tests showed increases of around 30% when EAFS replaces coarse aggregates [68], while uniaxial tests show negligible changes [72]. Enhanced ITZ contributes to this improvement, as failures occur through both paste and aggregate for EAFC, rather than along ITZ, unlike conventional concrete [62,73–75]. However, despite this improvement, EAFC tends to be more brittle, with splitting/compressive strength ratios of 2.3%-4.4%, below the typical 10% for NAC [63].

Shear strength, although less frequently studied, benefits from EAFS usage. Full-scale beam tests revealed increased shear capacity with EAFS, showing crack patterns similar to NAC [76]. The inclusion of metallic fibers further improved shear resistance [77]. Recent research has shown that EAFS enhances macro-level interlock and friction, contributing positively to shear transfer mechanisms [78].

Elastic modulus is particularly influenced by EAFS aggregate properties. When low-porosity slag is used, the elastic modulus can increase by up to 30% compared to NAC [73]. Rondi et al. [72] observed values around 46 GPa with total EAFS replacement, while Pellegrino and Gaddo [68] reported 31 GPa for EAFC versus 24 GPa for reference concrete. Pellegrino and Gaddo [68] also highlighted that Eurocode 2 provision formulas underestimate the elastic modulus for EAFC. In this context, Faleschini et al. [79] confirmed that aggregate type and content influence concrete stiffness more than cement content. In a more recent work on cyclic monoaxial loading, Trento et al. [80] measured 38 GPa of secant modulus for EAFC

and 28 GPa for the corresponding NAC after 28 days of curing. Table 1-2 provides the average variations of EAFC fresh and hardened properties compared to those of NAC.

Durability properties of EAFC, although less thoroughly studied, generally follow trends similar to mechanical performance (Table 1-3). Nonporous EAFS improve resistance to water absorption, chloride ingress, freeze-thaw cycles, and wet-dry cycles by 10%-20%, while porous slags show little to no effect. Despite lower workability without admixtures, proper mix design and compaction can resolve air content issues [73]. Chloride resistance measured via rapid chloride permeability test can be misleading due to increased conductivity from high iron content in EAFS, resulting in moderate to high permeability readings [63], although colorimetric tests with $AgNO_3$ indicate a reduced diffusion coefficient and improved durability [81]. Accelerated ageing tests according to ASTM D-4792 [82] revealed minor strength loss in EAFC (~5%) due to micro expansion from free oxides hydration, though strength and density stabilized after weather exposure [68,69]. EAFC shows better performance than NAC in the autoclave test according to ASTM C-151 [69]. In wet-dry cycles, EAFC shows susceptibility to expansion, sometimes exhibiting staining from iron products [83], however EAFS mixes typically performs better than other mixes containing conventional or other recovered aggregates [84]. Freeze-thaw resistance results varies: some studies reported lower strength for EAFC [68,69], others showed similar or better performance compared to NAC [69,83,85]. Regarding alkali-silica reaction, EAFS was found to be nonreactive, with expansion equal to 0.15% [69]. Results on carbonation resistance are inconclusive; some studies observed improved performance [86,87], while others reported significantly greater carbonation depth [83]. High-temperature resistance of EAFC is satisfactory, with limited spalling and lower strength loss up to 600°C compared to NAC [88].

Table 1-1. Main physical properties of EAFS.

Property	**Value**
Size (mm)	0-32
Apparent particle density (kg/dm^3)	2.84-4.02
Water absorption (%)	0.1-10
Porosity (%)	2-42
Pore dimension (μm)	0.2-8000
Los Angeles loss (%)	10-35
Crushing value (%)	10-22
Elongation index (%)	1-10
Flakiness index (%)	1-10
Volumetric expansion (%)	0.1-3.5

Table 1-2. Average variations of EAFC fresh and hardened properties compared to those of NAC.

Property	**Average Variation**	**Average Effect**
Workability	-	Slight decrease
Density	From +15% to +20%	Increase
Compressive strength	From +7% to +35%	Increase
Tensile strength	Up to +40%	Increase
Flexural strength	Up to +30%	Increase
Strength gain in time	-	Not affected
Secant Elastic Modulus	From +5% to +35%	Increase

Table 1-3. Summary of the durability effects of EAFS incorporation in concrete.

Property	**Average Effect**
Water absorption	Decrease
Chlorides penetration - Rapid chloride permeability test	Increase
Chlorides penetration - $AgNO_3$ colorimetric test	Decrease
Accelerated ageing resistance - ASTM D-4792	Slight increase
Autoclave test resistance - ASTM C-151	Increase
Wetting/drying resistance	Slight increase
Freezing/thawing resistance	Slight increase
Alkali-silica reaction	Not affected
Carbonation depth	Increase or decrease
High temperature resistance	Increase

1.3.2.1.3 Special concretes incorporating EAFS

High-Strength Concretes (HSC) are designed for enhanced strength, elasticity, and durability, typically achieved through optimized mix design involving high cement content, low water-to-cement ratio, superplasticizers, and high-quality aggregates. Their use in multistory buildings and long-span bridges helps reduce structural dimensions and extend service life, though they carry a higher environmental impact than conventional concrete. One promising solution to mitigate this impact is the use of EAFS as aggregate. Papayianni and Anastasiou [89] demonstrated that HSC incorporating EAFS can achieve compressive strengths exceeding 70 MPa at 28 days, with strength gains of 9.5% using EAFS as coarse aggregate and 21.3% when both fine and coarse EAFS are used. Faleschini et al. [81] confirmed improvements in compressive, tensile strength, and elastic modulus through full replacement of coarse aggregates with EAFS, even with relatively high water-to-cement ratios and no mineral fillers. Kim et al. [90] found that EAFS also enhances the performance of reinforced beams.

Despite these benefits, HSC tends to show brittle failure, lower tensile and impact strength, which can be addressed through fiber reinforcement. The inclusion of short fibers improves ductility, tensile resistance, and post-peak strength [91], effects also confirmed in EAFC [92]. However, fiber addition can complicate mixing and reduce workability, particularly in combination with the rough texture of EAFS, leading to variable results. Fuente-Alonso et al. [92] produced Fiber-Reinforced Concrete (FRC) with EAFS for pavements, observing mechanical improvements even with fibers. Metallic fibers overtook synthetic ones in terms of crack strength and post-crack behavior. Still, Ortega-López et al. [93] showed that in highly workable mixes, fiber addition might reduce mechanical performance due to the higher water-to-cement ratio needed for workability. A balance between mechanical and fresh properties is therefore necessary. Additionally, fibers in EAFS concretes contribute to durability, especially under freeze-thaw and wet-dry cycles, and improve residual strength after high-temperature exposure [85,94].

Regarding Self-Compacting Concretes (SCC), although EAFS slightly reduces slump values when replacing natural aggregates, successful SCC mixes can still be formulated. These mixes flow and fill formworks under their own weight without mechanical compaction, requiring careful control of viscosity, aggregate gradation, and use of superplasticizers. However, EAFS heavy and angular nature can affect workability and increase segregation risks [95,96]. Santamaria et al. [97] validated the use of EAFS as total coarse and partial fine aggregate replacement in SCC, reporting Abram's cone spread values between 520 and 680 mm, influenced by aggregate size and water-to-cement ratio. A follow-up study [98] found that cements incorporating fly-ash caused rapid slump loss, while mixes with only ordinary cement maintained better workability. Similarly, Sosa et al. [86] produced SCC with full aggregate replacement using EAFS and partial cement replacement with cupola slag powder, achieving slightly reduced slump flow but improved mechanical strength and elastic modulus.

1.3.2.1.4 Electric Arc Furnace Concrete: Applications

The outstanding properties of concrete incorporating EAFS have encouraged some applications in real structural elements. This section presents three case studies, two located in Spain and one in Italy.

Chronologically, the first example is the KUBIK research building developed by Tecnalia in Zamudio, Basque Country (Figure 1-6a). The building, inaugurated in 2010 and still fully active, covers a total surface area of approximately 500 m^2 across three floors. In this project, the basement walls and foundation slab were cast using concrete mixes with a high proportion of EAFS. Specifically, the foundation mix replaced 80% of the coarse aggregate with EAFS and used EAFS as a 100% replacement for the fine aggregate fraction [99].

The second case study is based in Vicenza, in Northeastern Italy, and involves the rehabilitation of a NATO-owned military infrastructure. Completed in 2009, the project employed approximately 11,455 m^3 of EAFS-containing concrete for various structural elements. The mixes were designed to achieve different strength classes, with compressive strengths ranging from 10 MPa to 32 MPa, and were used in both non-structural components and foundational elements such as slabs and piles. The overall use of EAFS represented about 10% of the total concrete volume cast for the project [52,64].

The final example comes from the Port of Bilbao (Spain), where EAFC was employed in the construction of heavy marine blocks for the Punta Lucero dock walls and for the development of the new Punta Sollana dock (Figure 1-6b). This marine application is particularly valuable for assessing the long-term durability of EAFS concrete, specifically its resistance to chloride ion penetration from seawater and coastal environmental exposure [100,101].

a) *b)*

Figure 1-6. Applications of Electric Arc Furnace Concrete: a) KUBIK research building (Source: [102]); b) Port of Bilbao, Spain (Source: [101]).

1.3.3 Raw Crushed Wind Turbine Blade (RCWTB)

The wind energy sector currently supplies 20% of Europe's electricity demand, with even higher provisions in certain countries: 56% in Denmark, 36% in Ireland, 31% in Germany, and 27% in both the Netherlands and Spain (Figure 1-7) [103,104]. The European Commission expects that by 2050, wind energy could provide half of Europe's electricity needs, with installed wind capacity expected to grow from 220 GW today to approximately 1,300 GW, mostly driven by onshore wind expansion [103]. To achieve this goal, WindEurope forecasts that the EU will install an average of 23 GW per year of new wind power capacity over 2025-2030, bringing the EU's installed wind capacity to 351 GW in EU and 450 GW in Europe by 2030 (Figure 1-8) [105]. This means that the EU wind energy target for 2030 is within reach. However, considering that wind turbines typically have a lifespan of around 25 years and that many wind farms will require repowering, a substantial amount of waste, mainly turbine blades and foundation materials, has been generating [106,107]. It is estimated that around 43 million tons of wind turbine blade will be cumulated by 2050 [12]. Even though approximately 80% of the turbine mass by weight is recyclable, a universally adopted recycling process has not yet been established, largely due to the complex composition dominated by Glass Fiber Reinforced Polymer (GFRP) and the high energy demands of many recycling technologies.

The basic recycling methods for wind turbine blades involve thermal or chemical treatments, such as pyrolysis or solvolysis, to separate the different material components for further processing [108]. Though, these methods are costly, energy-intensive, and associated with significant carbon emissions [109,110]. Another approach consists on mechanically crushing wind turbine blades without separating individual components, resulting in a composite material consisting mainly of GFRP, along with spherical-shaped particles of balsa wood and polyurethane [111,112]. Such a material is called Raw Crushed Wind Turbine Blade (RCWTB) from now on and is the one analyzed in the following sections. Reducing GFRP to a powder to use as filler has proven unsuitable, as it significantly increases concrete porosity, thereby greatly diminishing both its strength and stiffness [113]. Similarly, machining GFRP into aggregate-sized elements also leads to reduced mechanical performance, mainly due to poor adhesion to the cementitious matrix [114]. However, fibers produced through lighter crushing [115] or appropriate machining techniques [114] demonstrate adequate bond with the concrete matrix and can enhance flexural strength and load-bearing capacity [116].

1.3.3.1 Recovery of wind turbine blades and RCWTB production

Among the recycling methods proposed, most research to date has been focusing on crushing or machining the GFRP after separating it from other components [117]. A less extensively explored research line, i.e. the one hereafter analyzed, involves the use of the material obtained by simultaneously shredding the entire wind turbine blade without any separation of its components to obtain the so-called Raw Crushed Wind Turbine Blade (RCWTB) [118,119]. This process is simpler and more cost-effective, yielding a material composed of balsa wood and polyurethane particles along with GFRP fibers [112].

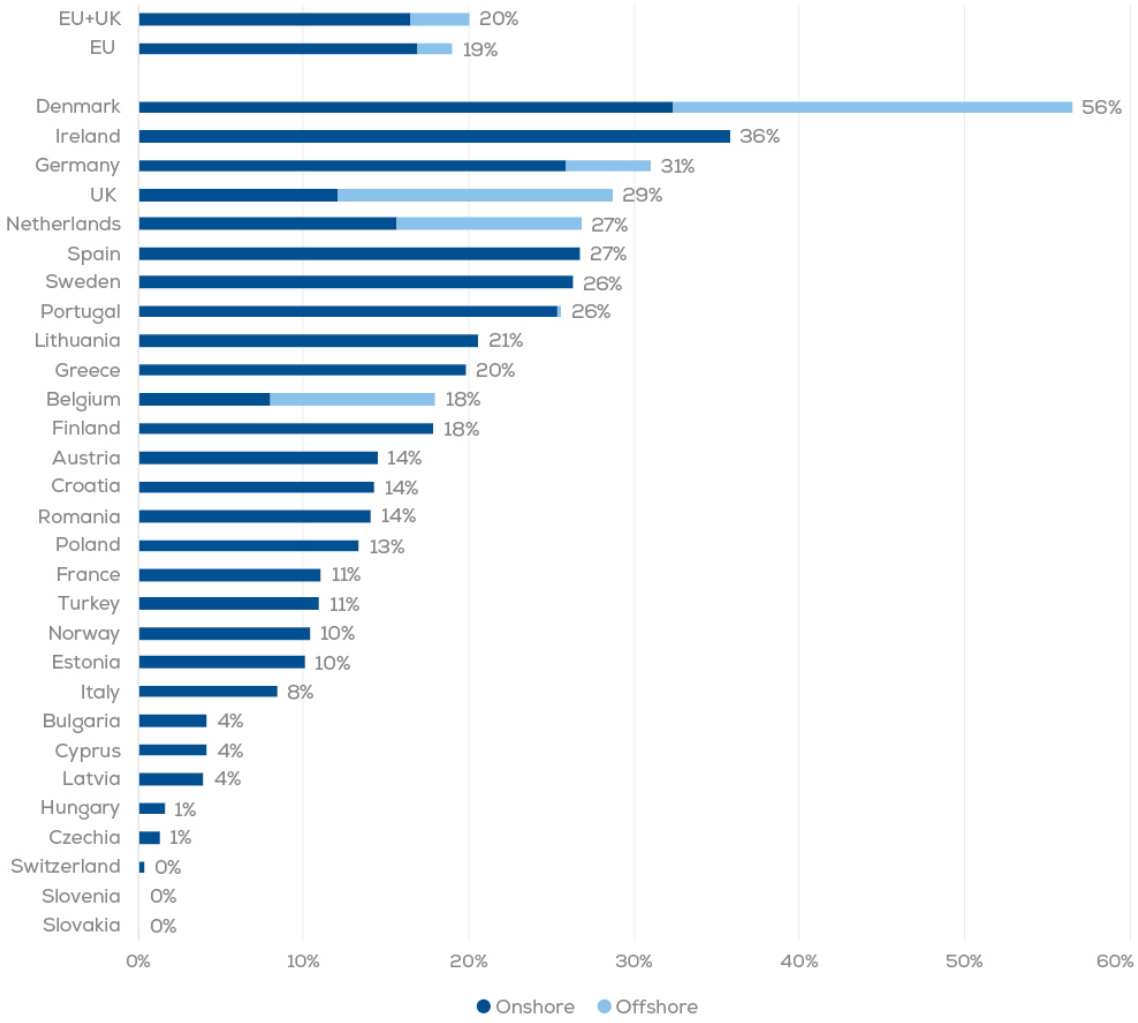

Figure 1-7. Percentage of electricity demand covered by wind in Europe in 2023. Source: [104].

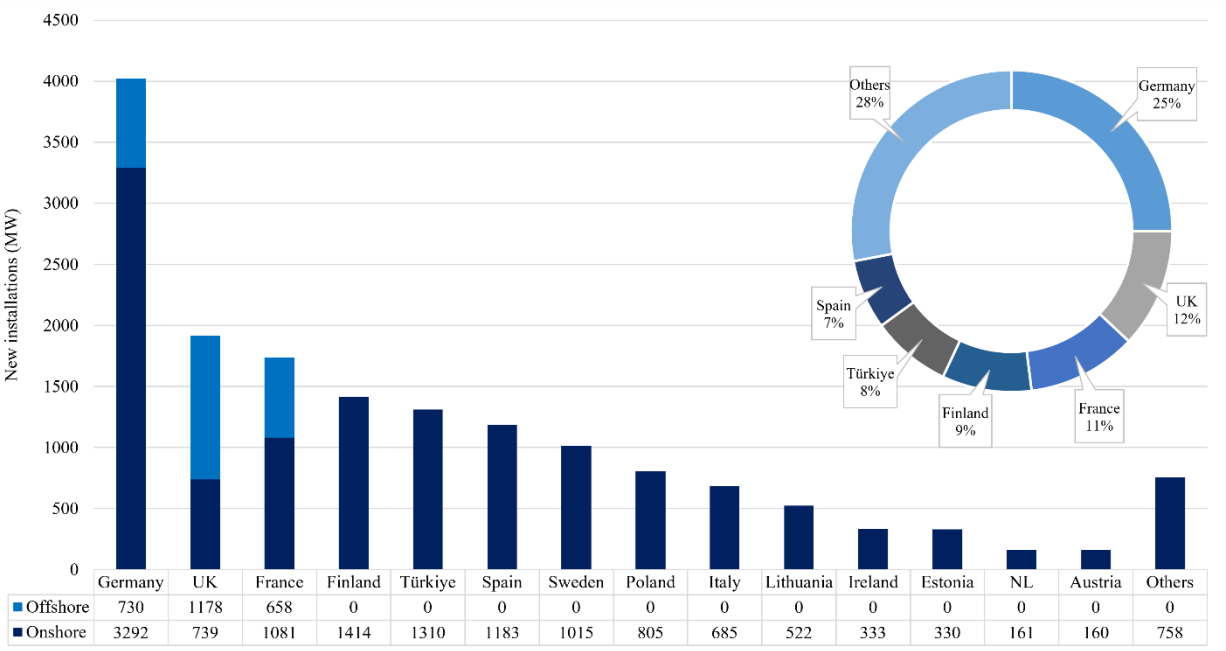

a)

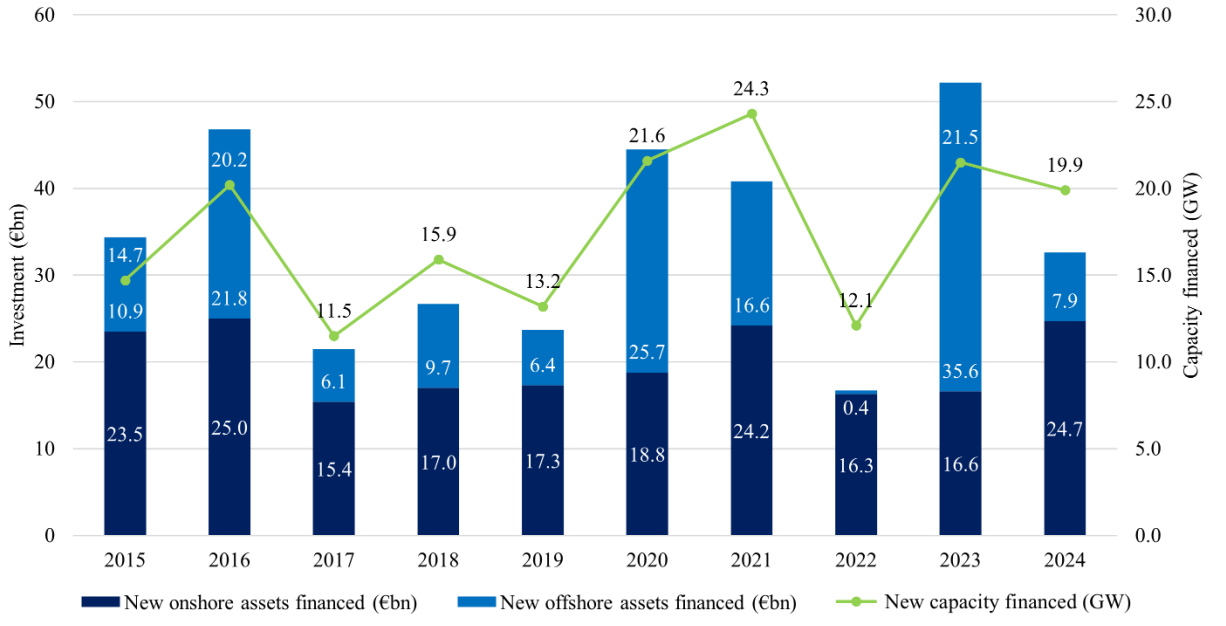

b)

Figure 1-8. European investments in the wind energy sector: a) New wind installations in 2024; b) Investment in new wind farms 2015-2024. Data from: [105].

Wind turbine blades are designed to minimize wind resistance, allowing the blades to rotate efficiently with minimal effort [120,121]. The first generations of wind turbines were equipped with blades measuring between 20 and 35 meters in length and weighing between 1.2 and 2 tons. It is this type of blade that will be dismantled and recycled in Europe until 2030 [112]. Over time, however, both the power output of wind turbines and the length of their blades have increased, with blades exceeding 55 meters now being quite common. The blades have a circular or slightly elliptical cross-section at the point of attachment to the nacelle, typically joined using a bolted connection (Figure 1-9a). This metallic section can be recycled through conventional metal recycling processes [122]. Moving outward from the attachment point, the blade profile becomes progressively slimmer and assumes an aerodynamic shape, as shown in Figure 1-9b. Structurally, the blade comprises a thin side wall reinforced with transverse stiffeners, designed to prevent both lateral and local buckling [120]. As the section approaches the blade tip, it narrows, and the side walls become thinner due to the decreasing structural demands (Figure 1-9b). Except for the metallic connection to the nacelle, wind turbine blades are primarily made of glass fiber composites embedded in polymeric resins (GFRP), which provide mechanical strength. Lightweight materials such as balsa wood and polyurethane are incorporated to enhance bending resistance while reducing overall blade weight [112]. Additionally, the blades are often coated with a protective resin layer, and some designs incorporate PVC stiffeners [112,123]. In sections closer to the tip, where less strength is required, the structure may consist predominantly of a single material. In contrast, areas requiring greater thickness are formed by sandwich panels composed of alternating layers of composite, balsa wood, and polyurethane, providing both strength and reduced weight [123].

The RCWTB production process involves the non-selective cutting of sandwich panels without separating composite, wood, or polyurethane followed by crushing and sieving. Initially, the blades are cut into 1-meter-long sections immediately after decommissioning, which are then transported to a dedicated facility for secondary cutting into sandwich panels suitable for crushing. This strategy is considered the most practical for transportation and processing efficiency [112]. Crushing is performed using a knife mill commonly employed for plastics, which is adjusted to produce fragments between 5 and 15 mm in size. During this process, the composite material is broken down into fibers, while approximately spherical particles of polyurethane and balsa wood are also produced. The final material, referred to as Raw Crushed Wind Turbine Blade (RCWTB), is shown in Figure 1-2c. According to Revilla-Cuesta et al. [112], the total energy consumption for cutting, crushing, and screening was estimated at 1.23 kWh/ton in the Spanish context, based on machine power ratings, operating time, and the volume of RCWTB produced. This value is approximately 0.75 kWh/ton lower than the typical energy consumption for producing crushed aggregate in a quarry [124]. Overall, this straightforward recycling process would require only the strategic integration of crushing facilities within the existing wind-energy sector waste-management infrastructure.

a) b)

Figure 1-9. Wind turbine blade: a) view of the bolted connection (Source: [112]); b) blade section.

Properties of RCWTB

The RCWTB material exhibits a real density of approximately 1.6 kg/dm^3, aligning with the characteristics of lightweight aggregates. In comparison, conventional aggregates typically have a density of around 2.4-2.6 kg/dm^3 [125]. The RCWTB bulk density is exceptionally low, approximately 250 kg/m^3, indicative of its porous and spongy nature [112].

Detailed material analysis identifies five distinct components within the RCWTB [112]: Glass Fiber Reinforced Polymer (GFRP), micro-fibers, polyurethane, balsa wood, and small non-separable particles. By weight, GFRP and micro-fibers are the most abundant due to their relatively higher density. These elements originated from the mechanical fragmentation of the GFRP. The GFRP fibers have an average length of approximately 13 mm and an equivalent diameter of 0.73 mm, i.e. dimensions comparable to certain commercial micro-fibers used in concrete reinforcement [126,127], and exhibits a tensile strength and Young's Modulus of around 270 MPa and 25 GPa, respectively [112,119]. The micro-fibers appear as thread-like clusters resulting from disintegration of both fiberglass and the surface resin coating. Balsa wood and polyurethane are present as roughly spherical particles, typically brown or green in color, with an average size of about 5 mm. Balsa wood shows extremely low density highlighting its value in lightweight blade construction [123]. The remaining small, non-separable particles consist of fragments too small to be mechanically separated, comprising primarily balsa wood, polyurethane, and fiberglass. Table 1-4 summarizes the properties and composition of RCWTB [112,119].

Overall, the physical characterization of RCWTB confirmed its dual functionality: it contains both fibers and particles that may act, respectively, as fiber reinforcement and lightweight aggregate in concrete. This dual role should be carefully considered in the design of concrete mixes incorporating RCWTB.

Figure 1-10 shows some Scanning Electron Microscope (SEM) images of the RCWTB main components: GFRP fibers, balsa wood, and polyurethane. The fibers (Figure 1-10a and b) show the typical morphology of fiberglass: thread-like strands bonded with polymer resin. However, the crushing process led to two distinct effects. First, the fiber ends appear irregular (Figure 1-10a), and second, in some areas, the fibers are coated with a thick polymer layer (Figure 1-10b). Rather than being detrimental, these features can be considered beneficial, as they increase surface roughness. The balsa wood exhibits a highly irregular surface topography, with numerous pores and a three-dimensional lamellar structure of varying orientations (Figure 1-10c). These features are considered beneficial for adhesion within the cementitious matrix, as the physical anchorage provided by surface protrusions could help mitigate the inherently weak bond caused by balsa wood low density in the interfacial transition zone. Polyurethane particles (Figure 1-10d and e), on the other hand, have relatively smooth and regular surfaces. Their bond with the cementitious matrix resembles that of other recycled plastics, typically forming less dense and less resistant interfacial zones

compared to natural aggregates [128]. In a final scan, the polymer matrix was entirely removed from GFRP, resulting in unbonded free glass fibers, thus resulting in the so-called micro-fibers (Figure 1-10f).

Table 1-4. Properties of RCWTB.

	Bulk density (kg/m^3)	**Appar. density (kg/m^3)**	**Composition (% wt.)**	**Length (mm)**	**Equivalent diameter (mm)**	**Aspect ratio (-)**	**Tens. strength (MPa)**	**Young's Modulus (GPa)**
Overall	1630	247	100	-	-	-	-	-
GFRP	2040*	-	66.8	13.07	0.73	17.90	270	25
Polyurethane		-	8.3	-	-	-	-	-
Balsa wood	330	-	6.3	-	-	-	-	-
Micro-fibers	-	-	13.8	-	-	-	-	-
Small non-separable particles	-	-	4.8	-	-	-	-	-

*Density measured in GFRP fibers and polyurethane together.

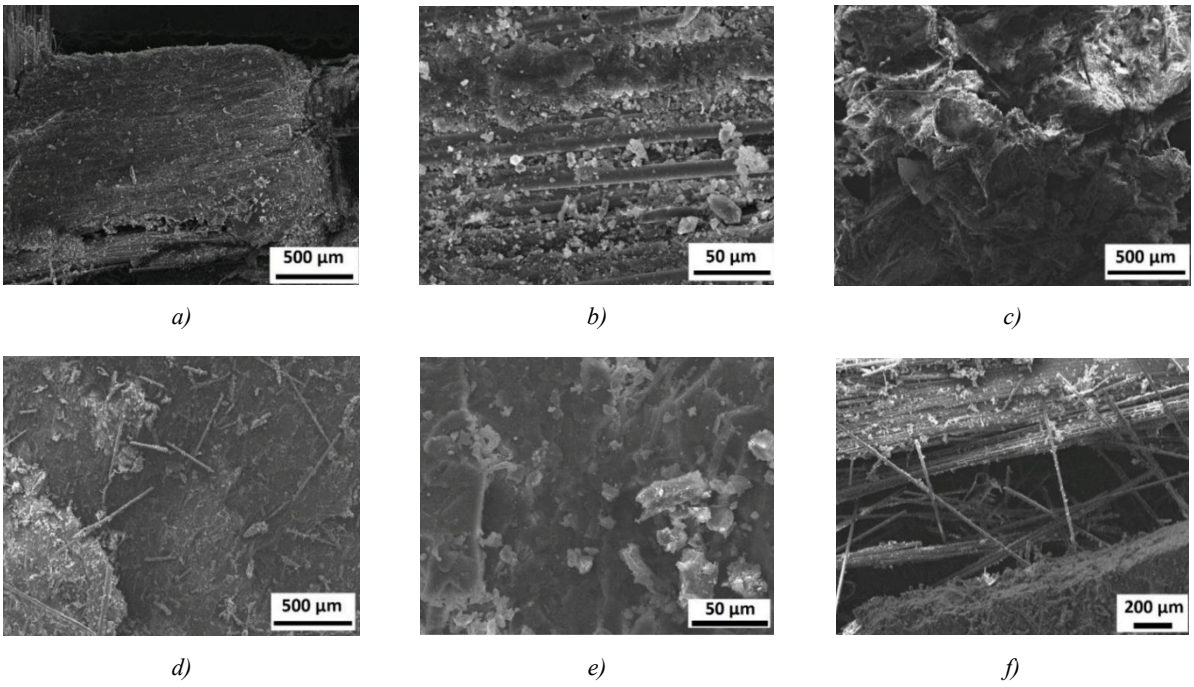

a) *b)* *c)*

d) *e)* *f)*

Figure 1-10. SEM images of the RCWTB: a)-b) fibers; c) balsa wood; d)-e) polyurethane; f) micro-fibers. Source: [112].

1.3.3.2 Including RCWTB in concrete

The inclusion of RCWTB in concrete conglomerates can serve as both fiber for GFRP and aggregate for balsa wood and polyurethane particles. Recent works demonstrates that RCWTB can be used in concrete production with a satisfactory fresh and mechanical performance [107,111,129].

1.3.3.2.1 Mechanical properties

The inclusion of RCWTB in concrete leads to a generally linear reduction in both compressive strength and Young's Modulus as the waste content increases. This decrease is primarily attributed to a higher water-to-cement ratio and reduced cement content associated with RCWTB addition, as well as the weaker bond between the cementitious matrix and the polyurethane and balsa wood particles. Nevertheless, small additions of RCWTB fibers (1.5% by volume) result in a slight increase in compressive strength. Moreover, a fiber content of 4.5% by volume appears to stabilize the compressive behavior of the concrete [111]. RCWTB fibers also contributed to a reduction in the concrete transverse deformability and Poisson's ratio, with each RCWTB content level showing a significant effect [129]. Regarding tensile performance, RCWTB additions do not show observable effect on the splitting tensile strength up to a volume content of 3.0%; beyond this threshold, strength begins to decrease. On the other hand, flexural strength is maintained, and even slightly improves, at higher RCWTB contents, likely due to the GFRP reinforcement [111], as shown in Figure 1-11.

1.3.3.2.2 Durability

RCWTB addition does not significantly affect concrete durability. Indeed, cyclic exposure to moisture and temperature variations, including wet-dry cycles and temperature-shock tests, induces micro-cracking within the cementitious matrix of concrete which is closely related to concrete porosity. Thus, increased micro-cracking is observed in more porous mixes, but this does not necessarily correlate directly with RCWTB content, since incorporating RCWTB did not always result in increased porosity [130]. The application of extreme thermal cycles, specifically alternating between sub-zero (-20 °C) and elevated temperatures (+70 °C), witnesses earlier beginning of both micro-cracking and RCWTB degradation compared to milder cycles. Notably, most of the damage occurs during the initial cycles, with little additional deterioration observed in subsequent cycles [130]. Compressive strength declines in response to both micro-cracking and damage to the RCWTB components. The results suggest that while RCWTB components, particularly balsa wood and polyurethane, are vulnerable to thermal deterioration, but the GFRP-composite fibers retain their bridging capacity within the cementitious matrix, helping mitigate strength loss in higher-RCWTB content concretes [130].

1.3.3.2.3 Sustainability

The inclusion of RCWTB contributes to a reduction in the overall carbon footprint of concrete (measured in $kgCO_2eq/m^3$). Additionally, when normalized per unit strength ($kgCO_2eq/(MPa \cdot m^3)$), a lower carbon footprint is observed in compression for mixes with low RCWTB contents and in flexure for those with higher contents. Therefore, the incorporation of RCWTB presents an opportunity to produce concrete with improved sustainability-performance balance [111].

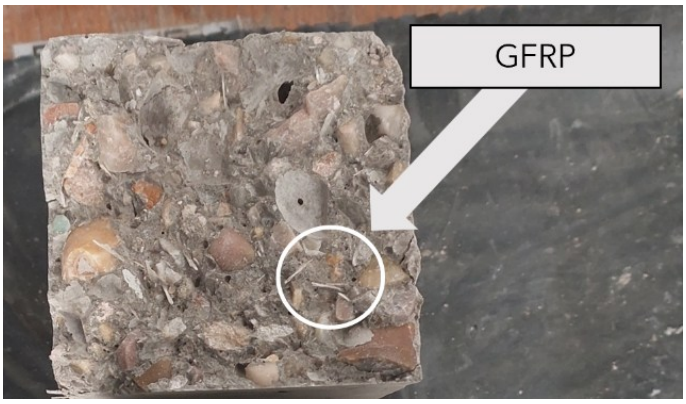

Figure 1-11. Breaking surface in concrete including RCWTB.

1.3.4 Concrete Sludge Waste

Concrete sludge waste (CSW), also known as returned or surplus concrete, refers to the leftover fresh concrete remaining in mixing trucks, typically in a workable state and containing a significant amount of cement mortar [131]. According to several concrete producers [132–134], approximately 4% of fresh concrete remains unused and is returned to production facilities, resulting in an estimated 500 million cubic meters of waste annually [132]. This surplus may be due to over-ordering, prolonged transport times, load rejection, or equipment failure [135]. Additionally, a considerable portion of CSW accumulates on the internal surfaces of transit mixer drums and requires washing to prevent hardening, which could otherwise cause damage and reduce equipment efficiency. Regular cleaning is essential to avoid operational disruptions, and overall, CSW at Ready-Mix Concrete (RMC) plants stems from three primary sources: returned fresh concrete, drum residues, and cleaning activities such as truck washing, batching plant maintenance, and dust control. To address this issue sustainably, four principal waste management strategies can be chosen, each focusing on maximizing resource recovery [136]:

- The first strategy involves redirecting excess fresh concrete to specialized factories to produce precast elements like paving and wall blocks or to serve in low-grade applications such as blinding or backfilling. This approach can substantially lower the resources required for waste processing; however, it may incur extra transportation costs associated with delivering fresh concrete waste to specialized facilities. The feasibility of this method also depends on the presence of suitable on-site or off-site plants capable of producing new concrete, as well as the distance involved in transportation, since the material must be reused before it loses its workability.
- The second approach aims to reuse fresh concrete in new batches, with or without chemical admixtures like retarders or activators [137,138]. This methodology minimizes the need to dispose of fresh concrete waste by incorporating it into new concrete batches. However, the absence of standardized guidelines or specifications introduces considerable uncertainty, making this method risky from a quality assurance and control perspective. Even when a particular project permits such reuse, it demands the involvement of trained staff with expertise in managing set retarders and activators. Moreover, implementation requires formal approval from all relevant stakeholders, including the client.
- The third strategy involves allowing the returned concrete to harden, followed by crushing to generate recycled aggregates (RA) or granular materials for use in construction; this method is widely adopted in countries like the United States, where around 60% of returned concrete waste is processed into RA [139].
- The fourth method employs a mechanical aggregate reclaiming system to wash out fresh concrete waste, separating aggregates and grey water, while the remaining cement slurry is either settled in pits or dewatered using filter presses. Although effective and already in use in certain facilities such as those in Norway [140], this method requires investment in equipment, staff training, and organizational changes, which can discourage widespread implementation.

Choosing a method rather than another is often a choice dictated from the company organization and standards. However, the third approach is currently the easiest to apply and scale, just requiring adequate storage, and crushing equipment. This dissertation focuses on CSW derived from hardened concrete waste, including residues generated during cleaning, which is processed to produce an all-in aggregate (0-20 mm) usable as both fine and coarse aggregate in new concrete, similarly to the third strategy. The main advantage of this recovery method lies in its simplicity and adaptability to any RMC plant equipped with basic

crushing and storage infrastructure. While previous research has mainly focused on fine CSW fractions for use as fillers to enhance packing [141], limited studies have examined the use of all-in CSW aggregate for new concrete production.

1.3.4.1 Properties

Research on the production of recycled aggregates (RA) from CSW is still limited, and existing findings are not yet exhaustive. However, certain consistent trends have emerged, largely influenced by the characteristics of the source material, i.e. the quality of the original concrete, and the specific recovery methods employed. In this section a review of the works dealing with recovery and management of concrete sludge waste according to the third strategy of the previous §1.3.4 is presented.

Zega and Di Maio [142] produced RA by crushing Ready-Mix Concrete (RMC) waste. Compared to natural granitic aggregate, the RA exhibited lower specific gravity, increased water absorption and abrasion loss, as well as a higher proportion of material passing the 75 μm sieve.

Kim and Goulias [143] crushed returned concrete to produce coarse RA. The RA demonstrates lower saturated surface dry specific gravity compared to the virgin aggregate, which indicates the higher porosity of the cementitious matrix encasing the aggregate particles. This increased porosity also contributes to the high-water absorption values. The results of the Los Angeles abrasion and soundness tests further highlight the fragility of the hydrated cementitious matrix surrounding the rigid aggregate.

Prado Vieira et al. [144] produced RA in fraction 0-19 mm by crushing hardened concrete. The recycled aggregates produced in this way demonstrated density ranging 2.50-2.71 kg/dm^3, compared to 2.60-2.79 kg/dm^3 for the original natural aggregates. This indicates that the RA is approximately 3% lighter than the NA, a difference attributed to the presence of adhered mortar on the RA particles, which increases porosity. In terms of particle grading, the RA showed a slightly lower fineness modulus compared to the NA, suggesting higher water demand for equivalent workability. This is confirmed by fines content, in fact the proportion of material passing the 0.150 mm sieve was 2% in NA and 5% in RA, indicating that RA is finer overall. This increase in fines is largely due to the crushing process, which produces a higher proportion of smaller particles. These findings confirms that both the adhered mortar and the crushing method influence the particle size distribution of RA [145].

Kim and Bentz [146] produced crushed returned concrete aggregate from different source concrete. In average, it was observed that the RA have a higher absorption capacity (relative to typical normal weight aggregates with absorptions in the range of 0% to 2% by mass) and a lower specific gravity, due to the mortar fraction that is combined with the virgin low absorption coarse aggregate.

Ferrari et al. [131] proposed a method to transform returned concrete into aggregate particles based on non-toxic superabsorbent polymer that are added directly into the drum of truck mixers. The aggregates produced using this technology are made of a composite mortar layer around the core of each recycled particle, affecting both particle size and various physical and chemical features. Producing aggregates in this way typically results in a reduction of particles smaller than 4 mm compared to original aggregates. This effect is attributed to the action of the additive, which binds fine components, e.g. cement, sand, and fillers, around the original aggregates, resulting in coarser overall grading. The density of the recycled aggregates is lower than that of natural aggregates, and it decreases with smaller particle sizes. This trend is due to the proportionally thicker mortar coating on smaller aggregates. Consequently, water absorption increases as particle size decreases, following the same logic.

Thus, recycled aggregates produced from returned concrete generally show lower density, higher water absorption, and increased fines content compared to natural aggregates, mainly due to the presence of

adhered mortar and increased porosity, similarly to RA produced from construction and demolition waste. These characteristics depend on both the original concrete properties and the crushing method. RA from returned concrete also tends to be finer and more variable in grading, which can increase water demand and affect workability.

1.3.4.2 Concrete sludge Waste Concrete and Mortar

Research on the properties of concrete containing recycled aggregates (RA) from returned concrete is even more limited.

Zega and Di Maio [142] manufactured structural concrete by replacing 25%, 50%, and 75% of the natural aggregate. Targeting a low strength level (17 MPa), the compressive strength of recycled concretes was similar to that of the source concrete for up to 50% replacement; whereas for the higher strength level (30 MPa), the compressive strength of the recycled concretes was found to be 16% lower than that of reference concrete across all replacement levels tested. Despite this moderate decrease, the durability performance, measured by water penetration under pressure, was comparable to, and in some cases even exceeded, that of the reference concrete.

Prado Vieira et al. [144] demonstrated that while RA can negatively affect workability and increase variability, the process can still be economically viable, particularly for concretes with compressive strength up to 30 MPa. Input to success is managing the age of the RA, with material used within 48 hours showing reduced cement demand. Pumpability was unaffected, highlighting the importance of tailored mix design. Although the crushing method is straightforward, careful stock management is necessary to control hydration levels.

Ferrari et al. [131] prepared concretes with 30% by weight of aggregate particles obtained adding a non-toxic superabsorbent polymer to the drum of truck mixers. The resulting concrete had the same compressive strength compared to reference concrete with only natural aggregates. Tests on water permeability, frost resistance, and chloride penetration resistance also confirmed that concretes incorporating the new aggregates exhibit durability comparable to that of conventional concretes made with natural aggregates.

Therefore, concrete made with aggregates from returned concrete can perform well, especially at moderate replacement levels and with proper handling. At lower strength levels, compressive strength remains comparable to conventional concrete, while at higher strengths, a slight reduction may occur. However, durability properties such as water permeability, frost resistance, and chloride penetration remain similar. With proper management, these aggregates offer a sustainable alternative for structural concrete.

Table 1-5. Average effect of the inclusion of RA recovered from returned concrete.

Property	**Average Effect**
Workability	Decrease
Density	Decrease
Compressive strength	Unaffected or slight reduction
Durability	Unaffected or improved

1.3.5 Literature review: summary, research lacks and research directions

The review of the state-of-the-art allowed for a deeper understanding of the advantages and limitations associated with each recovered aggregate. The physical properties of these materials offer valuable insights into their potential reuse applications. For instance, EAFS and CSW can be considered suitable for total or partial concrete replacement. In contrast, the heterogeneous nature of RCWTB prevents confirmation of similar suitability, instead suggesting more limited incorporation or partial replacement. These characteristics must be carefully considered during the mix design process.

Another aspect largely affecting the mix-design concerns the water demand, which is not always related to the water absorption itself. In the black-type EAFS employed for this dissertation, the water absorption is typically low, even lower than for most conventional counterparts. However, a slump decrease is observed in EAFS concrete due to the angular shape and rough surface of EAFS which hinders the concrete flowability. CSW physical properties strongly depend on the recovery process, however, the water absorption is at least the same, or much higher, than the one typically recorded for aggregates recovered from C&DW. For RCWTB, water absorption is not representative of the water demand, in fact the large presence of fibers hinders the concrete workability due to the bridge effect. These aspects should be considered adjusting water dosage, employing aggregate in their Saturated and Surface Dry (SSD) condition or adopting proper dosages of water-reducing admixtures.

The recovered aggregates here analyzed show distinctive properties and potential which reflect the mechanical properties of the final concrete. For example, the use of EAFS as partial or total aggregate replacement demonstrates strength gains due to the higher density and intrinsic strength of EAFS. Hence the potential of EAFS stands on those mechanical properties strongly affected by the aggregate nature, e.g. compressive strength and elastic modulus. Conversely, the mechanical properties which are more dependent on the cement matrix quality, e.g. tensile strength and flexural strength, remain equal or less affected. RCWTB demonstrates a totally different effect when included. Indeed, due to its heterogeneous composition mainly made of Glass Fiber Reinforced Polymer (GFRP), the RCWTB helps improve flexural and tensile strength thanks to the bridge effect that develops across cracks. However, the beneficial effect of RCWTB is more limited, or even absent, in compressive strength and those properties where the fiber tensile behavior cannot be exploited. As previously observed, the literature concerning CSW aggregate and concrete containing CSW is less abundant and uniform, though the effects of this recovered aggregate as concrete inclusion are expected to be quite similar to those observed for recycled aggregates from C&DW. The strong advantage of CSW stands on its extended availability, typically in each concrete batching plant, and limited cost for the recovery process, especially if the third strategy is adopted according to §1.3.4.

The previous points outline which aspects of each recovered aggregate should be deepened. Limited research is available on the fresh behavior and rheology of EAFS, RCWTB, and CSW. Many works are available on experimental workability typically measured with the slump test, but an analytical method useful to predict the flowability based on the aggregate physical properties is still missing. However, it should be noted that a single methodology cannot be considered for all the recovered aggregates explored in this dissertation. In fact, the physical properties and composition of EAFS are much more homogeneous than for RCWTB.

Concerning the mechanical properties, many results are already available from the literature for EAFS concrete, but research lacks involve some specific properties already explored for recycled concrete, e.g. the shear transfer and cyclic loading. RCWTB has been largely used as limited inclusion to conventional concrete since it cannot be used as full aggregate replacement. Thus, while employing RCWTB as concrete addition in limited volume percentage, sand and gravel can be replaced with other recovered aggregates.

This consideration opens new possibilities, but the interaction between RCWTB and other recovered aggregates needs to be deeply studied. Concerning the use of CSW aggregate as aggregate replacement, the literature is quite poor and heterogeneous due to the absence of a uniform recovery process and limited experimental experiences.

Considering the aspects so far outlined, the research insights developed in the following chapters were defined. Thus, concrete containing EAFS was deepened in the rheology with an analytical method to forecast the yield stress, which is the stress that activates the concrete flow in the fresh state. Further, mechanical performance was studied including shear transfer and cyclic axial loading, which are largely analyzed on recycled concrete in literature, but not for EAFC. Similarly, the rheology of concrete including RCWTB as concrete inclusion was studied, and an analytical procedure was followed for the yield stress modelling, which might be extended to other heterogeneous recovered aggregate. Given that RCWTB can just be used as partial aggregate replacement, an experimental campaign was carried out to study the interaction of RCWTB and recycled aggregate in concrete. Finally, an explorative experimental campaign involving mechanical characterization and environmental compatibility was performed on concrete with CSW as partial or total concrete replacement. This more general direction adopted for CSW concrete is justified by the overall poor literature.

Table 1-6 summarizes potential, research lacks and research direction defined in this chapter.

Table 1-6. Summary, research lacks and research directions for the recovered aggregates analyzed in this dissertation.

	Recovered aggregates for concrete production		
Recovered aggregate	Electric Arc Furnace Slags (EAFS)	Raw Crushed Wind Turbine Blade (RCWTB)	Concrete SludgeWaste (CSW)
Potential as aggregate replacement/Strengths	Mechanical properties: Compressive strength, Elastic Modulus	Mechanical properties: Flexural strength. It can be employed with other recovered aggregates	Extended availability (any batching plant)
Research lacks	Rheology, and some mechanical properties (e.g. shear strength and cyclic loading)	Rheology, and interaction with other recovered aggregates.	Poor and heterogeneous literature
Research direction	Rheology, shear transfer and cyclic loading	Rheology, behavior of recycled concrete including RCWTB	Explorative experimental campaign for a general characterization

1.4 REGULATORY FRAMEWORK FOR RECYCLED AGGREGATE AND RECYCLED CONCRETE

1.4.1 Recovering aggregates for constructions: Regulation

Recovered aggregates differ significantly in their physical, chemical, mineralogical, mechanical, and environmental characteristics, which directly affect their potential for reuse in various applications. Such differences mainly arise from the raw materials used and the specific operating conditions.

When defining a general regulatory framework for the recovery and reuse of these aggregates in the construction sector, the applicable environmental regulations and the technical standards relevant to each recovery route or end-use application must be considered simultaneously.

The first step is to address the legal classification of possible recovered aggregates. In Italy, materials which may become recovered aggregates are formerly classified as either:

- Waste, as defined in Legislative Decree 152/2006 (Art. 183, para. 1, letter a), intended for disposal or recovery operations (Arts. 182 and 184-ter) [147];
- By-product, as defined in Legislative Decree 152/2006 (Art. 183, para. 1, letter qq) and detailed in Art. 184-bis [147].

1.4.1.1 Recovery as By-products

To distinguish between waste and materials that should not be considered as such, the European Commission issued Communication COM(2007)59 [148], clarifying criteria based on rulings of the European Court of Justice. According to this guidance, a residue can be considered a by-product when it is not the primary purpose of a production process if the following conditions are met:

1) Its reuse is certain, not just potential;
2) It can be reused without additional processing;
3) Any preparation for reuse takes place within the production process itself.

To aid interpretation, the European Commission provided examples. A significant case is Blast Furnace Slag (BFS), which is generally produced under controlled conditions from the beginning, ensuring that it meets technical requirements for construction applications. BFS thus satisfies all three criteria, including certainty of reuse (criterion 1) and in-process preparation (criterion 3).

The EU's Directive 2008/98/EC [149], transposed in Italy through Legislative Decree 205/2010 [150], further refined the definition of by-products under Art. 184-bis. A substance qualifies as a by-product if:

1) It originates as part of a production process, where producing the substance itself is not the primary aim;
2) Its subsequent use is guaranteed, either by the producer or by third parties;
3) It can be used directly, without further treatment beyond "normal industrial practice";
4) Its intended use is legal, meeting all relevant product, environmental, and health requirements, without causing harmful impacts.

Once characterized, recovered aggregates must be registered with the European Chemicals Agency (ECHA) under the REACH Regulation and CE-marked, in accordance with Legislative Decree 106/2017 [151].

Steel slags, for example, can therefore be classified as by-products if these criteria are met. For example, Lombardy Region Resolution XI/5224 specifies the conditions under which electric arc furnace slag from

carbon steel production (EAFS-C) can qualify as a by-product [152]. If these conditions are not fulfilled, slags are instead classified as waste.

1.4.1.1.1 Normal Industrial Practice for steel slags

Article 6 of Ministerial Decree 13 October 2016, No. 264 [153] clarifies what constitutes "normal industrial practice" for by-products. In fact, treatments performed within the same production cycle and aimed at ensuring compliance with environmental and health standards are considered normal practice.

Because no universal legal definition exists, an essential reference is the Best Available Techniques Reference Document (BREF) for Iron and Steel Production [154]. This EU-level technical document outlines standard treatments applied to slags to prepare them for civil engineering and road construction use. For Electric Arc Furnace Slag (EAFS), examples of normal industrial practice include (Figure 1-12):

- Controlled slag cooling (e.g., water spraying);
- Crushing and screening to obtain suitable particle size;
- Magnetic separation of metallic particles for recycling;
- Storage and handling of processed slag in identified batches for testing and characterization.

In summary, "normal industrial practice" for EAFS primarily involves mechanical treatments to achieve the required size and quality for reuse.

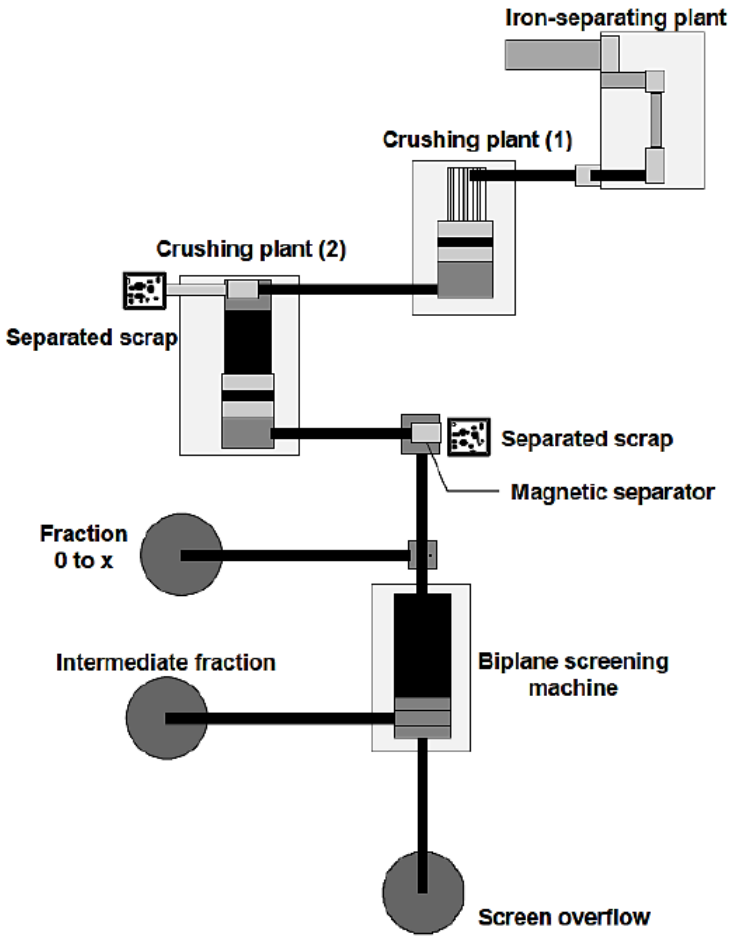

Figure 1-12. Processing scheme of a plant for slag preparation [154].

1.4.1.2 REACH Regulation and ECHA Registration

The REACH ("Registration, Evaluation, Authorisation and restrictions of CHemical substances") Regulation (EC No. 1907/2006), in force since 1 June 2007, aims to safeguard human health and the environment from risks posed by chemical substances [155]. REACH applies to all substances manufactured or imported in the EU (above 1 ton/year), whether used in industrial processes or consumer products, with certain exceptions.

Under REACH, companies bear the responsibility of proof: they must identify risks associated with substances, manage them, and communicate safe-use measures. ECHA ("European CHemical Agency") and Member States then evaluate compliance. The main roles defined under REACH are:

- Producers (manufacturing substances for use or sale);
- Importers (introducing substances or mixtures into the EU);
- Downstream users (industries or professionals using chemicals).

1.4.1.2.1 Substance Identification

Correct substance identification is essential for registration, risk assessment, and avoiding duplicate entries. For example, EAFS (black-type produced from carbon steel) is registered under:

- Name ("Slags, steelmaking, electric furnace (carbon steel production)");
- EC Number (932-275-6);
- Composition: determined by chemical analysis.

The principle of "one substance, one registration" (sameness principle) requires producers to demonstrate consistency in production processes and chemical/mineralogical composition, often illustrated through ternary diagrams [155].

1.4.1.2.2 REACH Procedures

REACH implementation involves four main steps [155]:

- Registration: companies submit dossiers on hazards, risks, and management measures;
- Evaluation: ECHA/Member States assess dossiers and may require additional data;
- Authorization: certain substances identified as Substances of Very High Concern (SVHC) can only be used with authorization;
- Restriction: limits or bans placed on hazardous substances.

Each EU Member State is responsible for imposing REACH through national legislation and sanctions.

1.4.1.2.3 CLP Regulation

The CLP ("Classification Labelling and Packaging") Regulation (EC No. 1272/2008) [156], in force since 20 January 2009, aligns EU legislation with the Globally Harmonised System of Classification and Labelling of Chemicals (GHS). It progressively replaced Directives 67/548/EEC [157] and 1999/45/EC [15] (both repealed on 1 June 2015) and amended the REACH Regulation (EC No. 1907/2006) [155]. Since June 2015, CLP has been the sole EU regulation governing the classification, labelling, and packaging of substances and mixtures.

The regulation applies to all industrial sectors and is legally binding for all Member States. Producers, importers, and downstream users must ensure that hazardous substances are classified, labelled, and packaged correctly before being placed in the market [156].

The main objective of CLP is to determine whether a substance or mixture should be classified as hazardous, assigning it to one or more hazard classes and categories (e.g., physical, health-related, or

environmental). Identified hazards must then be communicated along the supply chain, including to consumers.

For labelling, CLP sets strict requirements on content, including pictograms, signal words, hazard statements, and precautionary advice covering prevention, response, storage, and disposal. The regulation also provides the foundation for a wide range of other EU laws on chemical risk management. Additional provisions include harmonized classification and labelling processes, use of alternative chemical names in mixtures, and requirements for poison control centers.

1.4.1.2.4 REACH Regulation - Example: Safety Data Sheet

Within the scope of REACH, the characterization of recovered aggregates includes assessment of their physical, chemical, toxicological, and eco-toxicological properties to determine their impact on humans and the environment. Toxicological testing follows protocols developed by the Organization for Economic Co-operation and Development (OECD) and codified in internationally recognized guidelines. These tests also support the derivation of Predicted No Effect Concentration (PNEC) values, which define thresholds below which no adverse environmental effects are expected [155].

Although EAFS are not classified as hazardous substances and thus do not require a formal safety data sheet, information is made publicly available through the ECHA website. Each slag type has a dedicated "brief profile" containing:

- Substance identity;
- Hazard classification and labelling;
- Regulatory context (REACH compliance);
- CLP information;
- General substance information (consumer uses, industrial applications, formulation and re-packing, service life, precautionary measures, safe use);
- Registrant and supplier information;
- Identifiers (CAS names, IUPAC names, trade names, other identifiers);
- Scientific data (physico-chemical properties, environmental fate, eco-toxicological data, toxicological data).

1.4.1.3 Recovery from waste

Under Legislative Decree 152/2006 [147], Art. 183, paragraph 1, letter a) (as amended by Legislative Decree 205/2010 [150], Art. 10), waste is defined as any substance or object which the holder discards, intends to discard, or is required to discard.

In the case of steel slags, for example, steel plants often opt to classify slag as waste. In such a case, it must be assigned an EWC code (European Waste Catalogue, Commission Decision 2000/532/EC [158]). This six-digit code (three pairs of numbers) identifies the type of waste and, if hazardous, is followed by an asterisk (*):

- First pair ("Class"): identifies the sector of origin. For example, this is 10 for steel slags ("waste from thermal processes").
- Second pair ("Subclass"): identifies the process. For steelmaking, this includes: 02 ("waste from the steel industry") and 09 ("waste from casting of ferrous materials").
- Third pair ("Category"): specifies the waste description.

Assignment of an EWC code formally certifies the material status as waste, directing it to either recovery or disposal operations.

In practice, waste materials are sometimes classified as waste even when they might qualify as by-products. This choice may stem from business considerations such as:

- reliance on third-party recovery operators;
- insufficient in-house staff or storage capacity;
- limited production volumes that make direct by-product management uneconomical.

According to Legislative Decree 152/2006 [147], Art. 183, paragraph 1, letter a), recovery is defined as any operation whose principal result is to enable waste to serve a useful purpose, by replacing other materials that would otherwise be used to fulfil a particular function, or to prepare the waste to perform that function within the plant or in the wider economy.

Therefore, when construction and demolition waste or steel slags are classified as waste and sent to authorized recovery plants, those operators must ensure compliance with Legislative Decree 152/2006 [147], Art. 184-ter ("End of Waste"), which regulates the conditions under which waste ceases to be waste and becomes a reusable material.

1.4.1.3.1 End of waste

The concept of "End of Waste" refers to the point at which a material, originally classified as waste, ceases to hold that status and is instead considered a product. This approach originates from the revision of EU waste legislation: Directive 2006/12/EC [159] (now repealed) and its successor, Directive 2008/98/EC [149]. The latter broadened the perspective on waste management, shifting from a narrow focus on disposal and recovery to a more holistic life-cycle approach.

Directive 2008/98/EC [149] also introduced the waste hierarchy (Art. 4), establishing an order of priority in waste management:

- Prevention;
- Preparing for reuse;
- Recycling;
- Other recovery (e.g., energy recovery);
- Disposal.

According to Directive 2008/98/EC [149], Art. 6, waste loses its status when it has undergone recovery (including recycling) and meets specific conditions:

- The substance or object is commonly used for specific purposes;
- There is a market or demand for it;
- It meets the technical requirements for its intended use and complies with relevant legislation and product standards;
- Its use will not result in adverse impacts on human health or the environment.

In particular:

- the recovered material must be recognized and applied in established fields, fulfilling defined functions;
- the presence of a market reduces the likelihood of abandonment or illegal disposal;
- the material must guarantee performance and safety in line with applicable legal and technical standards.

The European Commission clarified in Communication COM(2007)59 [148] that while the ability to sell a material for profit increases the probability of its reuse, economic value alone is not sufficient. Thus, profitability is not an essential condition for "End of Waste" status, contrary to earlier national rules, such as Art. 181-bis of Legislative Decree 152/2006 [147], later repealed by Legislative Decree 205/2010 [150].

Italian legislation incorporated these EU provisions through Legislative Decree 152/2006 [147], as amended by Legislative Decree 205/2010 [150]. Article 184-ter ("End of Waste") directly adopts the conditions of Directive 2008/98/EC [149], Art. 6, and specifies in paragraph 2 that the recovery operation may consist simply of verifying whether the waste meets the criteria developed in accordance with the above conditions. This confirms that even the act of checking compliance can constitute a recovery operation, and therefore requires authorization under the procedures set out in Part Four of Legislative Decree 152/2006 [147].

At the EU level, Directive 2008/98/EC was later updated by Directive (EU) 2018/851 [23], transposed in Italy through Legislative Decree 116/2020 [160], which further refined the criteria for "End of Waste".

Further, the Ministerial Decree 28/06/2024, n. 127 [161] defines the criteria and conditions under which inert waste from construction/demolition (C&DW) and other mineral-origin inert waste ceases to be classified as waste and becomes recovered aggregate. Recovered aggregate must meet the specific criteria in Annex 1, including chemical/physical parameters, e.g. leaching limits, and ensure no adverse environmental or health impacts. Use is restricted to specific applications, such as road or railway embankments, foundations, and potentially concrete production in line with the previously mentioned UNI EN standards and national structural codes [162,163] according to section §1.4.2.

1.4.1.3.2 Recovery in ordinary regime

The ordinary regime for waste recovery is governed by Legislative Decree 152/2006 [147], Art. 208 (Single authorization for new waste disposal and recovery plants), as amended by Legislative Decree 205/2010 [150], Art. 22.

In practice, any party wishing to establish a new disposal or recovery facility (including those handling hazardous waste) must follow this procedure:

- Application submission: An application is filed with the Region, accompanied by the final plant design and supporting technical documentation.
- Procedure initiation (30 days): Within 30 days, the Region appoints the responsible officer and convenes a Services Conference to gather the necessary documents and information.

- Project evaluation (90 days): Within 90 days of its convocation, the Services Conference assesses the project, examines its overall compatibility (including environmental impact assessments, if required by law), and submits its conclusions to the Region.
- Final decision (30 days): Within 30 days of receiving the conclusions, the Region issues the authorization for construction and operation of the plant, provided the outcome is positive.

Overall, the process must be completed within 150 days from the initial application, resulting either in the granting of the single authorization or a reasoned refusal.

1.4.1.3.3 Recovery in simplified regime

The simplified regime for waste recovery is regulated by Legislative Decree 152/2006 [147], Art. 214 ("Determination of the activities and characteristics of waste for admission to simplified procedures"). This article establishes that a high level of environmental protection must always be guaranteed, achieved by:

- Defining the types and quantities of waste that may be treated.
- Setting the conditions under which non-hazardous waste recovery and disposal activities may follow simplified procedures.

Further details are provided in Legislative Decree 152/2006 [147], Art. 216 ("Recovery operations"), as amended by Legislative Decree 4/2008 [164], Art. 2, and Legislative Decree 205/2010 [150], Art. 30. The article states that:

- Start of activity: Waste recovery operations may begin 90 days after the notification of activity beginning is submitted to the Province with territorial jurisdiction, provided that the technical standards and specific conditions set out in Art. 214 are respected.
- Registration and verification: The Province records the company in a dedicated register and, within 90 days, verifies compliance with the requirements.

The notification of activity must include a technical report demonstrating compliance with:

- Applicable technical standards and specific conditions;
- Legal requirements for waste management;
- The type of recovery activities to be performed;
- Details of the facility, recovery capacity, and treatment or combustion cycle;
- Any use of mobile facilities;
- Characteristics of the recovered products.

The conditions and technical standards referenced are distinguished according to the type of waste:

- Non-hazardous waste: Defines maximum allowable quantities, origin, types, and characteristics, ensuring recovery without risks to human health and without harmful environmental impacts.
- Hazardous waste: Specifies maximum allowable quantities, origin, types, and characteristics, as well as limit values for hazardous substances, emission thresholds for each type of waste, activity, and facility, along with requirements ensuring safe recovery without risks to health or the environment.

Finally, the technical report must be renewed every five years or whenever there is a substantial modification in the recovery operations.

1.4.1.3.4 Producing and processing recycled aggregates

A key reference for processing Construction and Demolition Waste (C&DW) into Recycled Aggregates (RA) is the report issued by the European Joint Research Center [165].

Ideally, RA for use in concrete should be derived exclusively from concrete waste. In practice, however, C&DW is highly heterogeneous. It may contain various waste types and arrive at treatment plants with different levels of contamination from unintended materials.

Therefore, producing high-quality RA requires preliminary sorting both at the demolition site and at the C&DW management facility, ensuring that only suitable fractions are processed. C&DW not used for RA is either landfilled or diverted to other recovery routes outside the scope of this report (e.g., energy recovery from wood waste).

The main concepts for the valorization of C&DW into RA are:

- Material composition: RA with higher proportions of concrete and stone perform better than those with mixed materials.
- Contaminants: Clay, gypsum, asbestos, glass, wood, and plastics must be limited to trace amounts, especially when RA is used in bound applications (e.g., concrete).
- Metals: Residual metal content should be minimal. This is usually achieved via magnetic separation (for ferrous metals) and encouraged by the higher market value of recovered metals.
- Particle size: Small C&DW fractions often consist of soil and other undesirable materials, since weaker particles fragment more easily during demolition.
- Crushing: C&DW must be crushed to obtain smaller, usable aggregate sizes.
- Sieving: Necessary both to eliminate unwanted fine C&DW in early stages and to produce RA with consistent grading.
- Impurity distribution: As with C&DW, finer RA fractions contain more impurities than coarser fractions, because weaker constituents break down more readily during crushing.
- Washing: Washing RA improves quality by removing impurities and chemical contaminants (e.g., reducing chlorides). However, it requires significant investment and involves technical challenges in managing the washing water, due to variability in fines and soil content.

Typical equipment used for RA production is largely the same as that employed in demolition and natural aggregate (NA) processing. A standard RA production sequence is:

1) Preliminary sorting and fragmentation of C&DW at the demolition site, using conventional equipment. Material is then sent to a C&DW management plant or treated on-site.
2) Reception and storage at the plant according to waste type (e.g., mixed C&DW, concrete waste, ceramics, plastics, wood, metals, asbestos).
3) Selection for RA production: concrete waste or mixed C&DW (after contaminant removal, mostly concrete and masonry) enters the RA production line.
4) Initial screening: soils and small particles are removed by size separation; metals are removed using magnetic separators.
5) Processing: C&DW is crushed, sieved, passed through additional magnetic separators, and cleaned of lightweight materials (e.g., paper, plastics) using air sifters. Manual sorting is often applied to remove remaining contaminants such as wood and glass.
6) Final sieving: aggregates are graded and stockpiled for sale. RA intended for specific uses (e.g., backfilling) may skip sieving.
7) Storage: RA should preferably be stored under cover to limit moisture uptake.

1.4.1.4 CE Marking

The European Union has established specific regulations for construction products with the objective of creating a single market. Initially, this was done through Council Directive 89/106/EEC of 21 December 1988 ("Construction Products Directive" or CPD) [166], later repealed and replaced by Regulation (EU) No. 305/2011 (Construction Products Regulation or CPR) [167].

Annex I of the CPD defined the essential requirements for civil works, which are:

- Mechanical resistance and stability;
- Safety in case of fire;
- Hygiene, health, and environmental protection;
- Safety in use;
- Protection against noise;
- Energy efficiency and heat retention.

At the national level, the Ministerial Decree of 11 April 2007 issued by the Ministry of Infrastructure [168] implemented the CPD (previously transposed into Italian law by Presidential Decree No. 246 of 21 April 1993 [153]). Specifically:

- Annex 1 identifies construction products and the corresponding harmonized reference standards for aggregates.
- Annex 2 sets out the procedures for certifying aggregate conformity, depending on product category.
- Annex 3 lists the technical characteristics that producers must declare, based on the intended use of the aggregates.

1.4.2 Current standards for recycled concrete: Limits and possible applications

The use of recovered aggregates is regulated by specific national and supranational standards. Most standards provide specific requirements for recycled aggregates (RA) from construction and demolition waste concerning mainly physical properties and source material (e.g. just concrete, concrete and brick). However, most standards focus on the coarse fraction of RA, and consider neither RA fine fraction, nor other kinds of recovered aggregates. Concerning the possible uses, specific limitations are usually also given based on the grade of the final concrete and the expected exposure to degradation phenomena.

1.4.2.1 Americas

1.4.2.1.1 Brazil

Brazil's NBR 15116 [169] standard classifies construction and demolition waste into four classes (A-D), with Class A suitable for use as aggregates in concrete. Class A is further divided into Recycled Concrete Aggregate (composed of >90% concrete and natural resources) and Recycled Mixed Aggregate (composed of <90% concrete and natural resources). The standard sets strict requirements for water absorption and limits the use of materials with high masonry content to ensure the quality of recycled aggregates in concrete applications.

1.4.2.1.2 United States

The American Concrete Institute's ACI 555 [170] report provides an overview on the use of recycled aggregates in concrete. While it does not offer specific acceptance criteria, it discusses aggregate production, properties, and effects on concrete performance. The report emphasizes the importance of pre-soaking recycled aggregates to mitigate issues related to water absorption.

1.4.2.2 Asia

1.4.2.2.1 China

In China, the use of recycled aggregates in concrete is governed by several national standards, including GB/T 25177 [171] (for Recycled Coarse Aggregate for Concrete) and GB/T 25176 [172] (for Recycled Fine Aggregate for Concrete). These standards classify recycled aggregates into three classes based on properties such as crushing value, water absorption, and impurity content:

- Grade I is for recycled aggregates having the highest quality that can be used in structural concrete. The maximum allowed water absorption for Grade I coarse aggregate is 6.0%, and the crushing value should not exceed 20%.
- Grade II is suitable for non-structural applications.
- Grade III is restricted to use in road base layers and non-load-bearing elements.

Technical Code for the Application of Recycled Aggregates in Concrete (JGJ/T 240 [173]) further guides practical use, including mixing procedures, strength requirements, and curing practices. This code encourages the use of pre-soaking techniques and mixing adjustments to compensate for the higher absorption of recycled materials.

In major cities, e.g. Beijing and Shanghai, regional guidelines further support the integration of recycled aggregates into green building initiatives, aligning with national goals for carbon neutrality and sustainable development. Pilot projects have demonstrated successful use of up to 30% recycled coarse aggregate in structural concrete, contributing to construction waste reduction.

1.4.2.2.2 Hong Kong

Hong Kong's standards [174–176] mandate that recycled aggregates be pre-soaked before use. Concrete made with recycled aggregates must achieve a minimum compressive strength of 14 MPa at 7 days and 20 MPa at 28 days. Additionally, the slump of recycled aggregate concrete should be at least 75 mm at the time of casting to ensure adequate workability.

1.4.2.2.3 India

In India, the use of recycled aggregates is governed primarily by the Bureau of Indian Standards (BIS) under IS 383 [177]. The last version of this standard dates to 2016 and includes requirements for RA derived from construction and demolition waste.

The standard classifies recycled aggregates based on source and quality and permits their use up to a maximum of 100% in plain concrete, lean concrete, and non-structural applications. However, for structural concrete, IS 383 recommends using recycled coarse aggregate up to a maximum of 25% replacement by weight, and only when it meets specific physical property requirements such as water absorption ≤6%, aggregate impact value ≤45%, and flakiness and elongation index ≤35%.

1.4.2.2.4 Japan

The Japanese Industrial Standard JIS A 5021 [178] outlines specifications for Class H recycled aggregates manufactured by giving high level treatment such as crushing, grinding and classification to the concrete lumps generated because of, for example, demolition of a building. This standard emphasizes the importance of aggregate quality, including limitations on impurities and requirements for physical properties. Notably, the use of dry processing methods for recycled aggregates is currently under consideration, which could expand the applicability of recycled materials in concrete production.

1.4.2.3 Europe

In the European Union, only aggregates that comply with EN 12620 [162] can be used for concrete production, but each country reserves the right to impose stricter limits when deemed appropriate, whereas standard EN 206 [179] regulates the concrete production and performance, depending on the type of aggregate and the design concrete exposure class, while always excluding the fine fraction. The applicability limits of recycled aggregates are provided in Table 1-7, distinguishing between type A and B according to the nomenclature defined in EN 12620 [162]:

- Type A aggregates, composed mainly of crushed concrete with very limited amounts of contaminants.
- Type B aggregates, containing fractions of mortar and masonry with a low content of contaminants.

Table 1-7 shows the replacement limits for recycled aggregates based on the design exposure class. The values are justified by experimental observations which highlight a reduction in strength and durability as the proportion of recycled aggregate increases. Furthermore, Type B aggregates may be used for concrete mixes up to a maximum strength class of C30/37.

Table 1-7. Maximum percentage of replacement of coarse aggregates (% by mass). Source: EN 206 [179].

Recycled aggregate type	Exposure classes			
	X0	**XC1, XC2**	**XC3, XC4, XF1, XA1, XD1**	**All other exposure classes**
Type A*: (Rc90, Rcu95, Rb10-, Ra1-, FL2-, XRg1-)	50%	30%	30%	0%
Type B*: (Rc50, Rcu70, Rb30-, Ra5-, FL2-, XRg2-)	50%	20%	0%	0%

* Aggregate classification based on EN 12620 [162].

In the European and global context, other supranational organizations may provide specific guidelines and recommendations. This is the case of RILEM (International Union of Laboratories and Experts in Construction Materials, Systems and Structures) that proposes a classification system for recycled aggregates based on material composition according to Technical Committees 121 [180] and 217 [181]. This system guides the acceptable use of recycled aggregates in concrete concerning environmental exposure classes and strength requirements. For instance, RCA Type 1 (recycled concrete aggregate made of 100% crushed concrete) aggregates can replace up to 100% natural coarse aggregates in concrete with strength classes up to C50/60.

1.4.2.3.1 Belgium

Belgium's PTV 406 [182] standard allows for the use of recycled aggregates derived from construction and demolition waste, provided they meet specific quality criteria. These criteria include limitations on contaminants and requirements for mechanical properties to ensure suitability for concrete applications.

1.4.2.3.2 Denmark

Denmark's DS 2426 [183] standard, aligned with EN 206 [179], allows the use of recycled concrete aggregates in reinforced and non-reinforced concrete with compressive strengths up to 40 MPa in moderate and passive environmental conditions. Recycled masonry aggregates are allowed in non-reinforced concrete with strengths up to 20 MPa in passive conditions. For fine aggregates (0-4 mm), a maximum of 20% recycled content is allowed, with the remaining 80% being natural sand.

1.4.2.3.3 Finland

In Finland, crushed concrete aggregates are classified into four categories based on their origin and technical properties [184]. Category 1 includes raw materials from unused concrete elements, while categories 2-4 concern demolition waste, differentiated by factors such as grain size distribution and frost resistance. RA used in road construction must possess a CE certificate, ensuring compliance with European standards.

1.4.2.3.4 Germany

Germany's DIN 1045-2 [185] standard has expanded the scope for using recycled aggregates in concrete. It introduces concrete quality classes BK-N (normal), BK-E (enhanced), and BK-S (special), each with specific requirements for recycled aggregate content and properties. For instance, concrete containing 25% coarse RA by volume falls in BK-N class, while for higher replacement percentages the BK-E class

must be considered, with more strict requirements. Use of recycled aggregates in prestressed and lightweight concrete remains forbidden, and certain exposure classes (e.g., XA2, XA3, XM) are excluded due to insufficient data.

1.4.2.3.5 Italy

Italy's NTC 2018 (Norme Tecniche per le Costruzioni 2018) [163] standard references the harmonized European standard EN 12620 [162] for the qualification of recycled aggregates in concrete. While specific substitution percentages are not explicitly stated, guidelines give limitations based on the source of the recycled material and the desired concrete strength class (Table 1-8). For example, aggregates from pure concrete demolition may be used up to 20% for concrete classes ≤C45/55.

The use of recycled aggregate in the Italian context is particularly pressing, as according to the Italian Green Public Procurement criteria for construction referred to as CAM ("Criteri Ambientali Minimi") in Italian Standard [186], ready-mixed concrete and pre-mixed concrete in public works must include a minimum of 5% by weight of recycled materials, recovered materials, or by-products, based on the combined total of these components. This percentage is determined by calculating the ratio of the dry weight of these materials to the total weight of the concrete, excluding both free and absorbed water. Only the portion of recycled, recovered, or by-product materials that remain in the final product should be counted in this calculation.

Table 1-8. Maximum percentage of replacement of the coarse aggregate fraction (by mass) in concrete according to NTC 2018 [163].

Origin of recycled material	**Final concrete strength class***	**Usage percentage (%)**
Building demolitions (rubble)	= C8/10	Up to100%
	≤ C20/25	Up to 60%
Demolitions of unreinforced and reinforced concrete	≤ C30/35	Up to 30%
	≤ C45/55	Up to 20%
Reuse of internal concrete in qualified precast plants - from any class	Lower class than the original concrete	Up to 15%
	Same class as the original concrete	Up to 10%

*According to Eurocode 2 (EC2) and NTC2018.

1.4.2.3.6 Norway

Norwegian guidelines [187] permit to include more than 90% of crushed concrete, bricks, and natural aggregates. For applications with specific material property requirements, it is recommended that the combined content of concrete and natural aggregates is at least 80%.

1.4.2.3.7 Portugal

Portugal's LNEC E 471 [188] standard outlines requirements for recycled concrete aggregates, distinguishing between RCA1 and RCA2 based on composition. Both types must meet criteria for density and water absorption, with RCA2 potentially containing higher amounts of mortar or masonry. The standard also specifies environmental exposure classes and limits for contaminants to ensure the durability and performance of concrete incorporating recycled aggregates.

1.4.2.3.8 Spain

Spain's Structural Code [189] permits the use of recycled aggregates in both mass and reinforced concrete, provided the compressive strength does not exceed 40 MPa. The content of recycled aggregates is limited to 20% of the total coarse aggregate weight, and they must originate from sound or high-strength structural concrete. Additionally, water absorption limits are set at 7% for recycled aggregates and 4.5% for natural aggregates.

1.4.2.3.9 Switzerland

Switzerland's standards [190] differentiate between classified and unclassified concrete made with recycled aggregates. Classified concrete allows up to 100% replacement of virgin aggregates with recycled materials, provided quality requirements are met. Unclassified concrete, suitable for plain applications, also permits full replacement but is limited to non-structural uses. The standards encourage the preferential use of recycled materials, even if they are slightly more expensive, to promote sustainability.

1.4.2.3.10 United Kingdom

The UK has updated its standards with BS 8500-1 [191] and BS 8500-2 [192] in 2023. These revisions expand the range of lower-carbon concretes and allow for the inclusion of supplementary cementitious materials. Regarding recycled aggregates, the standards specify requirements for coarse recycled aggregates, including limitations on contaminants and guidance on their use in various concrete applications.

1.4.2.4 Oceania

1.4.2.4.1 Australia

In Australia, the Cement, Concrete & Aggregates Australia (CCAA) continues to classify recycled aggregates into five types: Recycled Concrete Aggregates, Recycled Concrete and Masonry, Reclaimed Aggregate, Reclaimed Asphalt Pavement, and Reclaimed Asphalt Aggregate. Recycled concrete aggregates recovered from construction and demolition waste remain the most used recycled aggregate in concrete production. While the Commonwealth Scientific and Industrial Research Organization (CSIRO) previously categorized recycled coarse aggregates into Class 1A and 1B (CSIRO HB 155 [193]).

REFERENCES

[1] T. Frederikse, M.K. Buchanan, E. Lambert, R.E. Kopp, M. Oppenheimer, D.J. Rasmussen, R.S.W. van de Wal, Antarctic Ice Sheet and emission scenario controls on 21st-century extreme sea-level changes, Nat Commun 11 (2020) 390. https://doi.org/10.1038/s41467-019-14049-6.

[2] M.L. Nehdi, A. Marani, L. Zhang, Is net-zero feasible: Systematic review of cement and concrete decarbonization technologies, Renewable and Sustainable Energy Reviews 191 (2024) 114169. https://doi.org/10.1016/j.rser.2023.114169.

[3] Record carbon emissions highlight urgency of Global Greenhouse Gas Watch, World Meteorological Organization (2024). https://wmo.int/media/news/record-carbon-emissions-highlight-urgency-of-global-greenhouse-gas-watch (accessed January 20, 2025).

[4] Climate change: a threat to human wellbeing and health of the planet. Taking action now can secure our future — IPCC, (n.d.). https://www.ipcc.ch/2022/02/28/pr-wgii-ar6/ (accessed January 23, 2025).

[5] S. Bolan, L.P. Padhye, T. Jasemizad, M. Govarthanan, N. Karmegam, H. Wijesekara, D. Amarasiri, D. Hou, P. Zhou, B.K. Biswal, R. Balasubramanian, H. Wang, K.H.M. Siddique, J. Rinklebe, M.B. Kirkham, N. Bolan, Impacts of climate change on the fate of contaminants through extreme weather events, Science of The Total Environment 909 (2024) 168388. https://doi.org/10.1016/j.scitotenv.2023.168388.

[6] N.J. Abram, B.J. Henley, A. Sen Gupta, T.J.R. Lippmann, H. Clarke, A.J. Dowdy, J.J. Sharples, R.H. Nolan, T. Zhang, M.J. Wooster, J.B. Wurtzel, K.J. Meissner, A.J. Pitman, A.M. Ukkola, B.P. Murphy, N.J. Tapper, M.M. Boer, Connections of climate change and variability to large and extreme forest fires in southeast Australia, Commun Earth Environ 2 (2021) 1–17. https://doi.org/10.1038/s43247-020-00065-8.

[7] United Nations Environment Programme, 2023 Global Status Report for Buildings and Construction: Beyond foundations - Mainstreaming sustainable solutions to cut emissions from the buildings sector, United Nations Environment Programme, 2024. https://doi.org/10.59117/20.500.11822/45095.

[8] F. Belaïd, How does concrete and cement industry transformation contribute to mitigating climate change challenges?, Resources, Conservation & Recycling Advances 15 (2022) 200084. https://doi.org/10.1016/j.rcradv.2022.200084.

[9] J. Watts, Concrete: the most destructive material on Earth, The Guardian (2019). https://www.theguardian.com/cities/2019/feb/25/concrete-the-most-destructive-material-on-earth (accessed September 3, 2024).

[10] O. Felipe Arbeláez Pérez, V. Senior Arrieta, J. Hernán Gómez Ospina, S. Herrera Herrera, C. Ferney Rodríguez Rojas, A. María Santis Navarro, Carbon dioxide emissions from traditional and modified concrete. A review, Environmental Development 52 (2024) 101036. https://doi.org/10.1016/j.envdev.2024.101036.

[11] B. Wang, L. Yan, Q. Fu, B. Kasal, A Comprehensive Review on Recycled Aggregate and Recycled Aggregate Concrete, Resources, Conservation and Recycling 171 (2021) 105565. https://doi.org/10.1016/j.resconrec.2021.105565.

[12] A. Hasheminezhad, D. King, H. Ceylan, S. Kim, Comparative life cycle assessment of natural and recycled aggregate concrete: A review, Science of The Total Environment 950 (2024) 175310. https://doi.org/10.1016/j.scitotenv.2024.175310.

[13] K. Robalo, H. Costa, R. do Carmo, E. Júlio, Experimental development of low cement content and recycled construction and demolition waste aggregates concrete, Construction and Building Materials 273 (2021) 121680. https://doi.org/10.1016/j.conbuildmat.2020.121680.

[14] E. Aprianti, P. Shafigh, S. Bahri, J.N. Farahani, Supplementary cementitious materials origin from agricultural wastes – A review, Construction and Building Materials 74 (2015) 176–187. https://doi.org/10.1016/j.conbuildmat.2014.10.010.

[15] M. Bendixen, L.L. Iversen, J. Best, D.M. Franks, C.R. Hackney, E.M. Latrubesse, L.S. Tusting, Sand, gravel, and UN Sustainable Development Goals: Conflicts, synergies, and pathways forward, One Earth 4 (2021) 1095–1111. https://doi.org/10.1016/j.oneear.2021.07.008.

[16] D. Ioannidou, G. Sonnemann, S. Suh, Do we have enough natural sand for low-carbon infrastructure?, Journal of Industrial Ecology 24 (2020) 1004–1015. https://doi.org/10.1111/jiec.13004.

[17] E.D. Marques, D. Tubbs, O.V.O. Gomes, E.V. Silva-Filho, Influence of acid sand pit lakes in surrounding groundwater chemistry, Sepetiba sedimentary basin, Rio de Janeiro, Brazil, Journal of Geochemical Exploration 112 (2012) 306–321. https://doi.org/10.1016/j.gexplo.2011.10.002.

[18] A. Torres, J. Brandt, K. Lear, J. Liu, A looming tragedy of the sand commons, Science 357 (2017) 970–971. https://doi.org/10.1126/science.aao0503.

[19] Why Construction Aggregates Will Always Be a Growing Industry - Mineralocity, (2023). https://mineralocity.com/2023/09/05/why-construction-aggregates-will-always-be-a-growing-industry/ (accessed January 27, 2025).

References

[20] S. Dias, J. Almeida, A. Tadeu, J. de Brito, Alternative concrete aggregates - Review of physical and mechanical properties and successful applications, Cement and Concrete Composites 152 (2024) 105663. https://doi.org/10.1016/j.cemconcomp.2024.105663.

[21] U.N. Environment, Global Waste Management Outlook 2024 | UNEP - UN Environment Programme, (2024). https://www.unep.org/resources/global-waste-management-outlook-2024 (accessed February 3, 2025).

[22] J. Soto-Paz, O. Arroyo, L.E. Torres-Guevara, B.A. Parra-Orobio, M. Casallas-Ojeda, The circular economy in the construction and demolition waste management: A comparative analysis in emerging and developed countries, Journal of Building Engineering 78 (2023) 107724. https://doi.org/10.1016/j.jobe.2023.107724.

[23] K. Kabirifar, M. Mojtahedi, C. Wang, V.W.Y. Tam, Construction and demolition waste management contributing factors coupled with reduce, reuse, and recycle strategies for effective waste management: A review, Journal of Cleaner Production 263 (2020) 121265. https://doi.org/10.1016/j.jclepro.2020.121265.

[24] J. Hao, F.D. Maria, Z. Chen, S. Yu, W. Ma, L.D. Sarno, Comparative Study of Construction and Demolition Waste Management in China and the European Union, Detritus (2020) 114. https://doi.org/10.31025/2611-4135/2020.14029.

[25] R.V. Silva, J. de Brito, R.K. Dhir, Properties and composition of recycled aggregates from construction and demolition waste suitable for concrete production, Construction and Building Materials 65 (2014) 201–217. https://doi.org/10.1016/j.conbuildmat.2014.04.117.

[26] Z.H. Duan, C.S. Poon, Properties of recycled aggregate concrete made with recycled aggregates with different amounts of old adhered mortars, Materials & Design 58 (2014) 19–29. https://doi.org/10.1016/j.matdes.2014.01.044.

[27] M. Behera, S.K. Bhattacharyya, A.K. Minocha, R. Deoliya, S. Maiti, Recycled aggregate from C&D waste & its use in concrete – A breakthrough towards sustainability in construction sector: A review, Construction and Building Materials 68 (2014) 501–516. https://doi.org/10.1016/j.conbuildmat.2014.07.003.

[28] F. de Andrade Salgado, F. de Andrade Silva, Recycled aggregates from construction and demolition waste towards an application on structural concrete: A review, Journal of Building Engineering 52 (2022) 104452. https://doi.org/10.1016/j.jobe.2022.104452.

[29] E. Mulder, T.P.R. de Jong, L. Feenstra, Closed Cycle Construction: An integrated process for the separation and reuse of C&D waste, Waste Management 27 (2007) 1408–1415. https://doi.org/10.1016/j.wasman.2007.03.013.

[30] H. Shima, H. Tateyashiki, R. Matsuhashi, Y. Yoshida, An Advanced Concrete Recycling Technology and its Applicability Assessment through Input-Output Analysis, Journal of Advanced Concrete Technology 3 (2005) 53–67. https://doi.org/10.3151/jact.3.53.

[31] A. Akbarnezhad, K.C.G. Ong, M.H. Zhang, C.T. Tam, T.W.J. Foo, Microwave-assisted beneficiation of recycled concrete aggregates, Construction and Building Materials 25 (2011) 3469–3479. https://doi.org/10.1016/j.conbuildmat.2011.03.038.

[32] M.S. de Juan, P.A. Gutiérrez, Study on the influence of attached mortar content on the properties of recycled concrete aggregate, Construction and Building Materials 23 (2009) 872–877. https://doi.org/10.1016/j.conbuildmat.2008.04.012.

[33] M. Pepe, R.D. Toledo Filho, E.A.B. Koenders, E. Martinelli, Alternative processing procedures for recycled aggregates in structural concrete, Construction and Building Materials 69 (2014) 124–132. https://doi.org/10.1016/j.conbuildmat.2014.06.084.

[34] A. Hanif, Y. Kim, Z. Lu, C. Park, Early-age behavior of recycled aggregate concrete under steam curing regime, Journal of Cleaner Production 152 (2017) 103–114. https://doi.org/10.1016/j.jclepro.2017.03.107.

[35] R.V. Silva, J. de Brito, R.K. Dhir, Fresh-state performance of recycled aggregate concrete: A review, Construction and Building Materials 178 (2018) 19–31. https://doi.org/10.1016/j.conbuildmat.2018.05.149.

[36] K.P. Verian, W. Ashraf, Y. Cao, Properties of recycled concrete aggregate and their influence in new concrete production, Resources, Conservation and Recycling 133 (2018) 30–49. https://doi.org/10.1016/j.resconrec.2018.02.005.

[37] S. Seara-Paz, B. González-Fonteboa, F. Martínez-Abella, I. González-Taboada, Time-dependent behaviour of structural concrete made with recycled coarse aggregates. Creep and shrinkage, Construction and Building Materials 122 (2016) 95–109. https://doi.org/10.1016/j.conbuildmat.2016.06.050.

[38] S. Ismail, M. Ramli, Engineering properties of treated recycled concrete aggregate (RCA) for structural applications, Construction and Building Materials 44 (2013) 464–476. https://doi.org/10.1016/j.conbuildmat.2013.03.014.

[39] R. Wang, N. Yu, Y. Li, Methods for improving the microstructure of recycled concrete aggregate: A review, Construction and Building Materials 242 (2020) 118164. https://doi.org/10.1016/j.conbuildmat.2020.118164.

[40] F. Muhammad, M. Harun, A. Ahmed, N. Kabir, H.R. Khalid, A. Hanif, Influence of bonded mortar on recycled aggregate concrete properties: A review, Construction and Building Materials 432 (2024) 136564. https://doi.org/10.1016/j.conbuildmat.2024.136564.

[41] I. González-Taboada, B. González-Fonteboa, F. Martínez-Abella, J.L. Pérez-Ordóñez, Prediction of the mechanical properties of structural recycled concrete using multivariable regression and genetic programming, Construction and Building Materials 106 (2016) 480–499. https://doi.org/10.1016/j.conbuildmat.2015.12.136.

[42] J. Lavado, J. Bogas, J. de Brito, A. Hawreen, Fresh properties of recycled aggregate concrete, Construction and Building Materials 233 (2020) 117322. https://doi.org/10.1016/j.conbuildmat.2019.117322.

[43] S.A. Memon, Z. Bekzhanova, A. Murzakarimova, A Review of Improvement of Interfacial Transition Zone and Adherent Mortar in Recycled Concrete Aggregate, Buildings 12 (2022). https://doi.org/10.3390/buildings12101600.

[44] R. Kurda, J. de Brito, J.D. Silvestre, Influence of recycled aggregates and high contents of fly ash on concrete fresh properties, Cement and Concrete Composites 84 (2017) 198–213. https://doi.org/10.1016/j.cemconcomp.2017.09.009.

[45] A.M. Wagih, El-Karmoty ,Hossam Z., Ebid ,Magda, S.H. and Okba, Recycled construction and demolition concrete waste as aggregate for structural concrete, HBRC Journal 9 (2013) 193–200. https://doi.org/10.1016/j.hbrcj.2013.08.007.

[46] P.B. Cachim, Mechanical properties of brick aggregate concrete, Construction and Building Materials 23 (2009) 1292–1297. https://doi.org/10.1016/j.conbuildmat.2008.07.023.

[47] S. Lotfi, J. Deja, P. Rem, R. Mróz, E. van Roekel, H. van der Stelt, Mechanical recycling of EOL concrete into high-grade aggregates, Resources, Conservation and Recycling 87 (2014) 117–125. https://doi.org/10.1016/j.resconrec.2014.03.010.

[48] R. Johnson, M.H. Shehata, The efficacy of accelerated test methods to evaluate Alkali Silica Reactivity of Recycled Concrete Aggregates, Construction and Building Materials 112 (2016) 518–528. https://doi.org/10.1016/j.conbuildmat.2016.02.155.

[49] R.V. Silva, R. Neves, J. de Brito, R.K. Dhir, Carbonation behaviour of recycled aggregate concrete, Cement and Concrete Composites 62 (2015) 22–32. https://doi.org/10.1016/j.cemconcomp.2015.04.017.

[50] H. Guo, C. Shi, X. Guan, J. Zhu, Y. Ding, T.-C. Ling, H. Zhang, Y. Wang, Durability of recycled aggregate concrete – A review, Cement and Concrete Composites 89 (2018) 251–259. https://doi.org/10.1016/j.cemconcomp.2018.03.008.

[51] Z. He, H. Hu, I. Casanova, C. Liang, S. Du, Effect of shrinkage reducing admixture on creep of recycled aggregate concrete, Construction and Building Materials 254 (2020) 119312. https://doi.org/10.1016/j.conbuildmat.2020.119312.

[52] F. Faleschini, D. Trento, M.A. Zanini, 8 - Steel slag aggregate in concrete, in: J. de Brito, F. Agrela, R.V. Silva (Eds.), The Path to Green Concrete, Woodhead Publishing, 2024: pp. 241–265. https://doi.org/10.1016/B978-0-443-19165-7.00006-X.

[53] S.Z. Carvalho, F. Vernilli, B. Almeida, M. Demarco, S.N. Silva, The recycling effect of BOF slag in the portland cement properties, Resources, Conservation and Recycling 127 (2017) 216–220. https://doi.org/10.1016/j.resconrec.2017.08.021.

[54] M. Jawad Ahmed, W. Franco Santos, H.J.H. Brouwers, Air granulated basic Oxygen furnace (BOF) slag application as a binder: Effect on strength, volumetric stability, hydration study, and environmental risk, Construction and Building Materials 367 (2023) 130342. https://doi.org/10.1016/j.conbuildmat.2023.130342.

[55] World Steel in Figures 2024, Worldsteel.Org (n.d.). https://worldsteel.org/data/world-steel-in-figures/world-steel-in-figures-2024/ (accessed April 23, 2025).

[56] A. Piemonti, A. Conforti, L. Cominoli, S. Sorlini, A. Luciano, G. Plizzari, Use of Iron and Steel Slags in Concrete: State of the Art and Future Perspectives, Sustainability 13 (2021) 556. https://doi.org/10.3390/su13020556.

[57] H. Kumar, S. Varma, A review on utilization of steel slag in hot mix asphalt, Int. J. Pavement Res. Technol. 14 (2021) 232–242. https://doi.org/10.1007/s42947-020-0025-0.

[58] J.-Y. Lee, J.-S. Choi, T.-F. Yuan, Y.-S. Yoon, D. Mitchell, Comparing Properties of Concrete Containing Electric Arc Furnace Slag and Granulated Blast Furnace Slag, Materials 12 (2019) 1371. https://doi.org/10.3390/ma12091371.

[59] A. Santamaria, F. Faleschini, G. Giacomello, K. Brunelli, J.-T. San José, C. Pellegrino, M. Pasetto, Dimensional stability of electric arc furnace slag in civil engineering applications, Journal of Cleaner Production 205 (2018) 599–609. https://doi.org/10.1016/j.jclepro.2018.09.122.

[60] C. Pellegrino, F. Faleschini, Sustainability Improvements in the Concrete Industry: Use of Recycled Materials for Structural Concrete Production, Springer, 2016.

[61] N. Roussel, Correlation between Yield Stress and Slump: Comparison between Numerical Simulations and Concrete Rheometers Results, Mater Struct 39 (2006) 501–509. https://doi.org/10.1617/s11527-005-9035-2.

[62] F. Faleschini, K. Brunelli, M.A. Zanini, M. Dabalà, C. Pellegrino, Electric Arc Furnace Slag as Coarse Recycled Aggregate for Concrete Production, J. Sustain. Metall. 2 (2016) 44–50. https://doi.org/10.1007/s40831-015-0029-1.

[63] S.I. Abu-Eishah, A.S. El-Dieb, M.S. Bedir, Performance of concrete mixtures made with electric arc furnace (EAF) steel slag aggregate produced in the Arabian Gulf region, Construction and Building Materials 34 (2012) 249–256. https://doi.org/10.1016/j.conbuildmat.2012.02.012.

[64] F. Faleschini, D. Trento, M.A. Zanini, C. Pellegrino, V. Ortega-López, A. Santamaria, Mechanical strength and environmental sustainability of EAF concrete, in: Life-Cycle of Structures and Infrastructure Systems, CRC Press, 2023: pp. 2455–2462. https://doi.org/10.1201/9781003323020-299.

[65] M. Papachristoforou, I. Papayianni, Radiation shielding and mechanical properties of steel fiber reinforced concrete (SFRC) produced with EAF slag aggregates, Radiation Physics and Chemistry 149 (2018) 26–32. https://doi.org/10.1016/j.radphyschem.2018.03.010.

[66] B. Pomaro, F. Gramegna, R. Cherubini, V. De Nadal, V. Salomoni, F. Faleschini, Gamma-ray shielding properties of heavyweight concrete with Electric Arc Furnace slag as aggregate: An experimental and numerical study, Construction and Building Materials 200 (2019) 188–197. https://doi.org/10.1016/j.conbuildmat.2018.12.098.

[67] N. Rojas, M. Bustamante, P. Muñoz, K. Godoy, V. Letelier, Study of properties and behavior of concrete containing EAF slag as coarse aggregate, Developments in the Built Environment 14 (2023) 100137. https://doi.org/10.1016/j.dibe.2023.100137.

[68] C. Pellegrino, V. Gaddo, Mechanical and durability characteristics of concrete containing EAF slag as aggregate, Cement and Concrete Composites 31 (2009) 663–671. https://doi.org/10.1016/j.cemconcomp.2009.05.006.

[69] J.M. Manso, J.A. Polanco, M. Losañez, J.J. González, Durability of concrete made with EAF slag as aggregate, Cement and Concrete Composites 28 (2006) 528–534. https://doi.org/10.1016/j.cemconcomp.2006.02.008.

[70] F. Özalp, Effects of electric arc furnace (EAF) slags on mechanical and permeability properties of paving stone, kerb and concrete pipes, Construction and Building Materials 329 (2022) 127159. https://doi.org/10.1016/j.conbuildmat.2022.127159.

[71] F. Faleschini, M.A. Zanini, K. Toska, Seismic reliability assessment of code-conforming reinforced concrete buildings made with electric arc furnace slag aggregates, Engineering Structures 195 (2019) 324–339. https://doi.org/10.1016/j.engstruct.2019.05.083.

[72] L. Rondi, G. Bregoli, S. Sorlini, L. Cominoli, C. Collivignarelli, G. Plizzari, Concrete with EAF steel slag as aggregate: A comprehensive technical and environmental characterisation, Composites Part B: Engineering 90 (2016) 195–202. https://doi.org/10.1016/j.compositesb.2015.12.022.

[73] L. Coppola, A. Buoso, D. Coffetti, P. Kara, S. Lorenzi, Electric arc furnace granulated slag for sustainable concrete, Construction and Building Materials 123 (2016) 115–119. https://doi.org/10.1016/j.conbuildmat.2016.06.142.

[74] F. Faleschini, A. Santamaria, M.A. Zanini, J.-T. San José, C. Pellegrino, Bond between steel reinforcement bars and Electric Arc Furnace slag concrete, Mater Struct 50 (2017) 170. https://doi.org/10.1617/s11527-017-1038-2.

[75] A. Sekaran, M. Palaniswamy, S. Balaraju, A Study on Suitability of EAF Oxidizing Slag in Concrete: An Eco-Friendly and Sustainable Replacement for Natural Coarse Aggregate, The Scientific World Journal 2015 (2015) 972567. https://doi.org/10.1155/2015/972567.

[76] C. Pellegrino, F. Faleschini, Experimental behavior of reinforced concrete beams with Electric arc furnace slag as recycled aggregate., ACI Materials Journal 110 (2013).

[77] A. Santamaría, J.M. Romera, I. Marcos, V. Revilla-Cuesta, V. Ortega-López, Shear strength assessment of reinforced concrete components containing EAF steel slag aggregates, Journal of Building Engineering 46 (2022) 103730. https://doi.org/10.1016/j.jobe.2021.103730.

[78] F. Faleschini, D. Trento, V. Ortega-López, M.A. Zanini, Shear transfer in fly ash concrete with electric arc furnace aggregates, Magazine of Concrete Research 75 (2023) 906–918. https://doi.org/10.1680/jmacr.22.00280.

[79] F. Faleschini, L. Hofer, M.A. Zanini, M. dalla Benetta, C. Pellegrino, Experimental behavior of beam-column joints made with EAF concrete under cyclic loading, Engineering Structures 139 (2017) 81–95. https://doi.org/10.1016/j.engstruct.2017.02.038.

[80] D. Trento, V. Ortega-Lopez, M.A. Zanini, F. Faleschini, Stress-strain behavior of electric arc furnace slag concrete under uniaxial compression: Short- and long-term evaluation, Construction and Building Materials 422 (2024) 135837. https://doi.org/10.1016/j.conbuildmat.2024.135837.

[81] F. Faleschini, M. Alejandro Fernández-Ruíz, M.A. Zanini, K. Brunelli, C. Pellegrino, E. Hernández-Montes, High performance concrete with electric arc furnace slag as aggregate: Mechanical and durability properties, Construction and Building Materials 101 (2015) 113–121. https://doi.org/10.1016/j.conbuildmat.2015.10.022.

[82] ASTM D4792-13 - Standard Test Method for Potential Expansion of Aggregates from Hydration Reactions, (2019).

[83] M.A. González-Ortega, S.H.P. Cavalaro, G. Rodríguez de Sensale, A. Aguado, Durability of concrete with electric arc furnace slag aggregate, Construction and Building Materials 217 (2019) 543–556. https://doi.org/10.1016/j.conbuildmat.2019.05.082.

[84] V. Revilla-Cuesta, J. Manso-Morato, N. Hurtado-Alonso, A. Santamaría, J.T. San-José, Degradation under cyclic wet-dry aging of full-scale high-workability concrete maximizing sustainable raw materials, Case Studies in Construction Materials 20 (2024) e03334. https://doi.org/10.1016/j.cscm.2024.e03334.

[85] V. Ortega-López, J.A. Fuente-Alonso, A. Santamaría, J.T. San-José, Á. Aragón, Durability studies on fiber-reinforced EAF slag concrete for pavements, Construction and Building Materials 163 (2018) 471–481. https://doi.org/10.1016/j.conbuildmat.2017.12.121.

[86] I. Sosa, C. Thomas, J.A. Polanco, J. Setién, P. Tamayo, High Performance Self-Compacting Concrete with Electric Arc Furnace Slag Aggregate and Cupola Slag Powder, Applied Sciences 10 (2020). https://doi.org/10.3390/app10030773.

[87] H.D. Andrade, J.M.F. de Carvalho, L.C.B. Costa, F.P. da F. Elói, K.D. do C. e Silva, R.A.F. Peixoto, Mechanical performance and resistance to carbonation of steel slag reinforced concrete, Construction and Building Materials 298 (2021) 123910. https://doi.org/10.1016/j.conbuildmat.2021.123910.

[88] A.-L. Beaucour, P. Pliya, F. Faleschini, R. Njinwoua, C. Pellegrino, A. Noumowé, Influence of elevated temperature on properties of radiation shielding concrete with electric arc furnace slag as coarse aggregate, Construction and Building Materials 256 (2020) 119385. https://doi.org/10.1016/j.conbuildmat.2020.119385.

[89] I. Papayianni, E. Anastasiou, Production of high-strength concrete using high volume of industrial by-products, Construction and Building Materials 24 (2010) 1412–1417. https://doi.org/10.1016/j.conbuildmat.2010.01.016.

[90] S.-W. Kim, Y.-J. Lee, Y.-H. Lee, K.-H. Kim, Flexural Performance of Reinforced High-Strength Concrete Beams with EAF Oxidizing Slag Aggregates, Journal of Asian Architecture and Building Engineering 15 (2016) 589–596. https://doi.org/10.3130/jaabe.15.589.

[91] V. Guerini, A. Conforti, G. Plizzari, S. Kawashima, Influence of Steel and Macro-Synthetic Fibers on Concrete Properties, Fibers 6 (2018) 47. https://doi.org/10.3390/fib6030047.

[92] J.A. Fuente-Alonso, V. Ortega-López, M. Skaf, Á. Aragón, J.T. San-José, Performance of fiber-reinforced EAF slag concrete for use in pavements, Construction and Building Materials 149 (2017) 629–638. https://doi.org/10.1016/j.conbuildmat.2017.05.174.

[93] V. Ortega-López, A. García-Llona, V. Revilla-Cuesta, A. Santamaría, J.T. San-José, Fiber-reinforcement and its effects on the mechanical properties of high-workability concretes manufactured with slag as aggregate and binder, Journal of Building Engineering 43 (2021) 102548. https://doi.org/10.1016/j.jobe.2021.102548.

[94] M. Papachristoforou, E.K. Anastasiou, I. Papayianni, Durability of steel fiber reinforced concrete with coarse steel slag aggregates including performance at elevated temperatures, Construction and Building Materials 262 (2020) 120569. https://doi.org/10.1016/j.conbuildmat.2020.120569.

[95] Y.-N. Sheen, D.-H. Le, T.-H. Sun, Innovative usages of stainless steel slags in developing self-compacting concrete, Construction and Building Materials 101 (2015) 268–276. https://doi.org/10.1016/j.conbuildmat.2015.10.079.

[96] S. Tomasiello, M. Felitti, EAF slag in self-compacting concretes, Facta Universitatis - Series: Architecture and Civil Engineering 8 (2010) 13–21.

[97] A. Santamaría, A. Orbe, M.M. Losañez, M. Skaf, V. Ortega-Lopez, J.J. González, Self-compacting concrete incorporating electric arc-furnace steelmaking slag as aggregate, Materials & Design 115 (2017) 179–193. https://doi.org/10.1016/j.matdes.2016.11.048.

[98] A. Santamaría, V. Ortega-López, M. Skaf, J.A. Chica, J.M. Manso, The study of properties and behavior of self compacting concrete containing Electric Arc Furnace Slag (EAFS) as aggregate, Ain Shams Engineering Journal 11 (2020) 231–243. https://doi.org/10.1016/j.asej.2019.10.001.

[99] J.A. Chica, I. Apraiz, P. Elguezabal, M.O. Rrips, V. Sánchez, B. Tellado, Kubik: Open Building Approach For The Construction of an Unique Experimental Facility Aimed to Improve Energy Efficiency in Buildings, Open House International 36 (2011) 63–72. https://doi.org/10.1108/OHI-01-2011-B0008.

[100] Bilbaoport, Puesta en servicio de las obras del proyecto de prolongación del dique de Punta Sollana, Bilbaoport (2016). https://www.bilbaoport.eus/noticias/puesta-servicio-las-obras-del-proyecto-prolongacion-del-dique-punta-sollana/ (accessed April 26, 2025).

[101] Bilbaoport, Cien profesionales de la obra pública analizarán en el Puerto de Bilbao el uso y valorización de hormigones reciclados, Bilbaoport (2016). https://www.bilbaoport.eus/noticias/cien-profesionales-la-obra-publica-analizaran-puerto-bilbao-uso-valorizacion-hormigones-reciclados/ (accessed April 26, 2025).

[102] KUBIK experimental building, Tecnalia (n.d.). https://www.tecnalia.com/en/infrastructure/kubik-experimental-building (accessed May 2, 2025).

[103] Wind energy today | WindEurope, (n.d.). https://windeurope.org/about-wind/wind-energy-today/ (accessed March 12, 2025).

[104] Wind energy in Europe: 2023 Statistics and the outlook for 2024-2030 | WindEurope, (n.d.). https://windeurope.org/intelligence-platform/product/wind-energy-in-europe-2023-statistics-and-the-outlook-for-2024-2030/ (accessed April 28, 2025).

[105] Wind energy in Europe: 2024 Statistics and the outlook for 2025-2030 | WindEurope, (n.d.). https://windeurope.org/intelligence-platform/product/wind-energy-in-europe-2024-statistics-and-the-outlook-for-2025-2030/ (accessed May 2, 2025).

[106] N. Tazi, J. Kim, Y. Bouzidi, E. Chatelet, G. Liu, Waste and material flow analysis in the end-of-life wind energy system, Resources, Conservation and Recycling 145 (2019) 199–207. https://doi.org/10.1016/j.resconrec.2019.02.039.

[107] N. Hurtado-Alonso, J. Manso-Morato, V. Revilla-Cuesta, M. Skaf, Strength-based RSM optimization of concrete containing coarse recycled concrete aggregate and raw-crushed wind-turbine blade, Composite Structures 356 (2025) 118895. https://doi.org/10.1016/j.compstruct.2025.118895.

[108] Y. Wei, S.A. Hadigheh, Development of an innovative hybrid thermo-chemical recycling method for CFRP waste recovery, Composites Part B: Engineering 260 (2023) 110786. https://doi.org/10.1016/j.compositesb.2023.110786.

[109] R. Fonte, G. Xydis, Wind turbine blade recycling: An evaluation of the European market potential for recycled composite materials, Journal of Environmental Management 287 (2021) 112269. https://doi.org/10.1016/j.jenvman.2021.112269.

[110] A.S. Al-Fatesh, N.Y.A. AL-Garadi, A.I. Osman, F.S. Al-Mubaddel, A.A. Ibrahim, W.U. Khan, Y.M. Alanazi, M.M. Alrashed, O.Y. Alothman, From plastic waste pyrolysis to Fuel: Impact of process parameters and material selection on hydrogen production, Fuel 344 (2023) 128107. https://doi.org/10.1016/j.fuel.2023.128107.

[111] V. Revilla-Cuesta, J. Manso-Morato, N. Hurtado-Alonso, M. Skaf, V. Ortega-López, Mechanical and environmental advantages of the revaluation of raw-crushed wind-turbine blades as a concrete component, Journal of Building Engineering 82 (2024) 108383. https://doi.org/10.1016/j.jobe.2023.108383.

[112] V. Revilla-Cuesta, M. Skaf, V. Ortega-López, J.M. Manso, Raw-crushed wind-turbine blade: Waste characterization and suitability for use in concrete production, Resources, Conservation and Recycling 198 (2023) 107160. https://doi.org/10.1016/j.resconrec.2023.107160.

[113] K. Pławecka, J. Przybyła, K. Korniejenko, W.-T. Lin, A. Cheng, M. Łach, Recycling of Mechanically Ground Wind Turbine Blades as Filler in Geopolymer Composite, Materials 14 (2021) 6539. https://doi.org/10.3390/ma14216539.

[114] A. Yazdanbakhsh, L.C. Bank, K.-A. Rieder, Y. Tian, C. Chen, Concrete with discrete slender elements from mechanically recycled wind turbine blades, Resources, Conservation and Recycling 128 (2018) 11–21. https://doi.org/10.1016/j.resconrec.2017.08.005.

[115] G.-T. Xu, M.-J. Liu, Y. Xiang, B. Fu, Valorization of macro fibers recycled from decommissioned turbine blades as discrete reinforcement in concrete, Journal of Cleaner Production 379 (2022) 134550. https://doi.org/10.1016/j.jclepro.2022.134550.

[116] H. Rodin, S. Nassiri, K. Englund, O. Fakron, H. Li, Recycled glass fiber reinforced polymer composites incorporated in mortar for improved mechanical performance, Construction and Building Materials 187 (2018) 738–751. https://doi.org/10.1016/j.conbuildmat.2018.07.169.

[117] Y. Tao, S.A. Hadigheh, Y. Wei, Recycling of glass fibre reinforced polymer (GFRP) composite wastes in concrete: A critical review and cost benefit analysis, Structures 53 (2023) 1540–1556. https://doi.org/10.1016/j.istruc.2023.05.018.

[118] D. Baturkin, R. Masmoudi, A. Tagnit-Hamou, S. Metiche, L. Massicotte, "Feasibility Study on the Recycling of FRP Materials from Wind Turbine Blades in Concrete," in: A. Ilki, M. Ispir, P. Inci (Eds.), 10th International Conference on FRP Composites in Civil Engineering, Springer International Publishing, Cham, 2022: pp. 1729–1742.

[119] J. Manso-Morato, N. Hurtado-Alonso, V. Revilla-Cuesta, R. Serrano-López, V. Ortega-López, Deformational and energy-absorption performance of low-strength structural concrete with joint additions of raw-crushed wind-turbine blade and coarse recycled aggregate, Emergent Mater. (2025). https://doi.org/10.1007/s42247-025-01060-5.

[120] P.U. Haselbach, X. Chen, P. Berring, Place smart, load hard - structural reinforcement of the trailing edge regions of a wind turbine blade strengthening the buckling resistance, Composite Structures 300 (2022) 116068. https://doi.org/10.1016/j.compstruct.2022.116068.

[121] R. Özkan, M.S. Genç, Aerodynamic design and optimization of a small-scale wind turbine blade using a novel artificial bee colony algorithm based on blade element momentum (ABC-BEM) theory, Energy Conversion and Management 283 (2023) 116937. https://doi.org/10.1016/j.enconman.2023.116937.

[122] Y. Zhao, Y. Zhang, Q. Zhou, X. Bian, W. Lyu, Lightning damage on GFRP materials of wind turbines under positive first return stroke, Electric Power Systems Research 215 (2023) 108978. https://doi.org/10.1016/j.epsr.2022.108978.

[123] J. Joustra, B. Flipsen, R. Balkenende, Structural reuse of wind turbine blades through segmentation, Composites Part C: Open Access 5 (2021) 100137. https://doi.org/10.1016/j.jcomc.2021.100137.

[124] A. Petit, G. Cordoba, C.I. Paulo, E.F. Irassar, Novel air classification process to sustainable production of manufactured sands for aggregate industry, Journal of Cleaner Production 198 (2018) 112–120. https://doi.org/10.1016/j.jclepro.2018.07.010.

[125] M. Bravo, J. de Brito, J. Pontes, L. Evangelista, Mechanical performance of concrete made with aggregates from construction and demolition waste recycling plants, Journal of Cleaner Production 99 (2015) 59–74. https://doi.org/10.1016/j.jclepro.2015.03.012.

[126] Ortega-López Vanesa, Revilla-Cuesta Víctor, Santamaría Amaia, Orbe Aimar, Skaf Marta, Microstructure and Dimensional Stability of Slag-Based High-Workability Concrete with Steelmaking Slag Aggregate and Fibers, Journal of Materials in Civil Engineering 34 (2022) 04022224. https://doi.org/10.1061/(ASCE)MT.1943-5533.0004372.

[127] J. Manso-Morato, N. Hurtado-Alonso, V. Revilla-Cuesta, M. Skaf, V. Ortega-López, Fiber-Reinforced concrete and its life cycle assessment: A systematic review, Journal of Building Engineering 94 (2024) 110062. https://doi.org/10.1016/j.jobe.2024.110062.

[128] A.A. Omar, M.Z.H.A. Sabri, K.N. Ismail, Interfacial Transition Zone (ITZ) Study of Concrete with Polyethylene Terephthalate (PET) Plastic, Key Engineering Materials 908 (2022) 639–644. https://doi.org/10.4028/p-t74yg2.

[129] V. Ortega-López, F. Faleschini, N. Hurtado-Alonso, J. Manso-Morato, V. Revilla-Cuesta, Analysis of raw-crushed wind-turbine blade as an overall concrete addition: Stress–strain and deflection performance effects, Composite Structures 340 (2024) 118170. https://doi.org/10.1016/j.compstruct.2024.118170.

[130] V. Revilla-Cuesta, N. Hurtado-Alonso, J. Manso-Morato, R. Serrano-López, J.M. Manso, Effects of temperature and moisture fluctuations for suitable use of raw-crushed wind-turbine blade in concrete, Environ Sci Pollut Res 31 (2024) 37757–37776. https://doi.org/10.1007/s11356-024-33720-0.

[131] G. Ferrari, M. Miyamoto, A. Ferrari, New sustainable technology for recycling returned concrete, Construction and Building Materials 67 (2014) 353–359. https://doi.org/10.1016/j.conbuildmat.2014.01.008.

[132] Returned Concrete, Stories Sika Group (n.d.). https://reports.sika.com/stories/en/returned-concrete (accessed April 3, 2025).

[133] Use of returned concrete aggregate as replacement of virgin aggregate - Smartcrete, SmartCrete CRC (2023). https://smartcretecrc.com.au/projects/use-of-returned-concrete-aggregate-as-replacement-of-virgin-aggregate/ (accessed April 3, 2025).

[134] Returned Concrete Treatment, Master Builders Solutions (n.d.). https://master-builders-solutions.com/en-us/products/mastersuna/returned-concrete-treatment/ (accessed April 3, 2025).

[135] L. de B.P. Vieira, A.D. de Figueiredo, T. Moriggi, V.M. John, Waste generation from the production of ready-mixed concrete, Waste Management 94 (2019) 146–152. https://doi.org/10.1016/j.wasman.2019.05.043.

[136] D. Xuan, C.S. Poon, W. Zheng, Management and sustainable utilization of processing wastes from ready-mixed concrete plants in construction: A review, Resources, Conservation and Recycling 136 (2018) 238–247. https://doi.org/10.1016/j.resconrec.2018.04.007.

[137] C. Lobo, W.F. Guthrie, R. Kacker, A Study on the Reuse of Plastic Concrete Using Extended Set-Retarding Admixtures, J Res Natl Inst Stand Technol 100 (1995) 575–589. https://doi.org/10.6028/jres.100.043.

[138] M. Paolini, R. Khurana, Admixtures for recycling of waste concrete, Cement and Concrete Composites 20 (1998) 221–229. https://doi.org/10.1016/S0958-9465(97)00066-8.

[139] K. Obla, H. Kim, C. Lobo, Crushed Returned Concrete as Aggregates for New Concrete, National Ready Mixed Concrete Association, 2007. https://trid.trb.org/View/1485308 (accessed April 3, 2025).

[140] S. Adomako, C.J. Engelsen, L.T. Døssland, T. Danner, R.T. Thorstensen, Technical and environmental properties of recycled aggregates produced from concrete sludge and excavation materials, Case Studies in Construction Materials 19 (2023) e02498. https://doi.org/10.1016/j.cscm.2023.e02498.

[141] J.V. Martins, D.C.S. Garcia, M.T.P. Aguilar, W.J. dos Santos, Influence of replacing Portland cement with three different concrete sludge wastes, Construction and Building Materials 303 (2021) 124519. https://doi.org/10.1016/j.conbuildmat.2021.124519.

[142] Zega Claudio Javier, Di Maio Angel Antonio, Recycled Concretes Made with Waste Ready-Mix Concrete as Coarse Aggregate, Journal of Materials in Civil Engineering 23 (2011) 281–286. https://doi.org/10.1061/(ASCE)MT.1943-5533.0000165.

[143] Kim Haejin, Goulias Dimitrios G., Shrinkage Behavior of Sustainable Concrete with Crushed Returned Concrete Aggregate, Journal of Materials in Civil Engineering 27 (2015) 04014204. https://doi.org/10.1061/(ASCE)MT.1943-5533.0001166.

[144] L. de Brito Prado Vieira, A. Domingues de Figueiredo, V.M. John, Evaluation of the use of crushed returned concrete as recycled aggregate in ready-mix concrete plant, Journal of Building Engineering 31 (2020) 101408. https://doi.org/10.1016/j.jobe.2020.101408.

[145] M.S. Rashwan, S. Abourizk, The Properties of Recycled Concrete, CI 19 (1997) 56–60.

[146] H. Kim, D.P. Bentz, Internal Curing with Crushed Returned Concrete Aggregates for High Performance Concrete, in: 2008. https://trid.trb.org/View/919743 (accessed May 3, 2025).

[147] Decreto Legislativo 3 aprile 2006, n. 152. Norme in materia ambientale, n.d.

[148] COM(2007)59. Comunicazione della Commissione al Consiglio e al Parlamento Europeo relativa alla Comunicazione interpretativa sui rifiuti e sui sottoprodotti., Commissione delle Comunità Europee, Bruxelles, 2007.
[149] Directive 2008/98/EC. Directive 2008/98/EC of the European Parliament and of the Council of 19 November 2008 on waste and repealing certain Directives, n.d.
[150] Decreto Legislativo 3 dicembre 2010. n. 205. Disposizioni di attuazione della Direttiva 2008/98/EC del Parlamento Europeo e del Consiglio del 19 Novembre 2008 relativa ai rifiuti e che abroga alcune direttive., n.d.
[151] Decreto Legislativo 16 giugno 2017, n. 106. Adeguamento della normativa nazionale alle disposizioni del regolamento (UE) nr. 305/2011, che fissa condizioni armonizzate per la commercializzazione dei prodotti da costruzione e che abroga la Direttiva 89/106/CEE., n.d.
[152] Risoluzione del Consiglio della Regione Lombardia n. XI/5224 del 13 settembre 2021. Approvazione linee guida per la gestione delle scorie nere di acciaieria a forno elettrico., Regione Lombardia, n.d.
[153] Decreto del Presidente della Repubblica 21 aprile 1993, n. 246. Regolamento di attuazione della direttiva 89/106/CEE relativo ai prodotti da costruzione., Presidente della Repubblica, n.d.
[154] Commission of the European Union. Joint Research Centre. Institute for Prospective Technological Studies., Best available techniques (BAT) reference document for iron and steel production: industrial emissions Directive 2010/75/EU : integrated pollution prevention and control., Publications Office, LU, 2013. https://data.europa.eu/doi/10.2791/97469 (accessed August 21, 2025).
[155] REACH. “Registration, Evaluation, Authorisation and restrictions of CHemical substances,” ECHA (European CHemical Agency), 2007.
[156] CLP Regulation (EC) n. 1272/2008, ECHA (European CHemical Agency), n.d.
[157] Council Directive 67/548/EEC. Council Directive of 27 June 1967 on the approximation of laws, regulations and administrative provisions relating to the classification, packaging and labelling of dangerous substances., 2022.
[158] Commission Decision 2000/532/EC. Commission Decision of 3 May 2000 replacing Decision 94/3/EC establishing a list of wastes pursuant to Article 1(a) of Council Directive 75/442/EEC on waste and Council Decision 94/904/EC establishing a list of hazardous waste pursuant to Article 1(4) of Council Directive 91/689/EEC on hazardous waste., n.d.
[159] Directive 2006/12/EC. Directive 2006/12/EC of the European Parliament and of the Council of 5 April 2006 on waste., n.d.
[160] Decreto Legislativo 3 settembre 2020, n. 116. Attuazione della Direttiva (UE) 2018/851 che modifica la Direttiva 2008/98/CE relativa ai rifiuti e attuazione della Direttiva (UE) 2018/852 che modifica la Direttiva 1994/62/CE sugli imballaggi e i rifiuti da imballaggio., n.d.
[161] Decreto Ministeriale 28 giugno 2024, n. 127. Regolamento recante disciplina della cessazione della qualifica di rifiuto dei rifiuti inerti da costruzione e demolizione, altri rifiuti inerti di origine minerale, ai sensi dell’articolo 184-ter, comma 2, del decreto legislativo 3 aprile 2006, n. 152/2006. (24G00144) (GU Serie Generale n.213 del 11-09-2024), Ministero dell’Ambiente e della Sicurezza Energetica, Rome, 2024.
[162] EN 12620:2013 - Aggregates for Concrete, (2013).
[163] Norme Tecniche per le Costruzioni (NTC 2018), (2018). https://www.gazzettaufficiale.it/do/atto/serie_generale/caricaPdf?art.codiceRedazionale=18A00716&art.dataPubblicazioneGazzetta=2018-02-20&art.num=1&art.tiposerie=SG&cdimg=18A00716001000101100 01&dgu=2018-02-20.
[164] Decreto Legislativo 16 gennaio 2008, n. 4. Ulteriori disposizioni correttive ed integrative del decreto legislativo 3 aprile 2006, n. 152, recante norme in materia ambientale., n.d.
[165] P. J, D.B. J, L.T. M, Use of recycled aggregates in concrete: opportunities for upscaling in Europe, Publications Office of the European Union, Luxembourg (Luxembourg), 2023. https://doi.org/10.2760/144802%2520(online).
[166] Council Directive 21 December 1988. Council Directive of 21 December 1988 on the approximation of laws, regulations and administrative provisions of the Member States relating to construction products (89/106/CEE)., 1988.
[167] Regulations (UE) No 305/2011. Regulation (UE) No 305/2011 of the European Parliament and of the Council of 9 March 2011 laying down harmonized conditions for the marketing of construction products and repealing Council Directive 89/106/EEC., 2011.
[168] Decreto Ministeriale 11 Aprile 2007. Applicazione della Direttiva 89/106/CE sui prodotti da costruzione, recepita con Decreto del Presidente della Repubblica 21 Aprile 1993, n. 246, relativa all’individuazione dei prodotti e dei relativi metodi di controllo della conformità di aggregati, Ministero delle Infrastrutture, 2007.
[169] ABNT NBR 15116:2021 - Recycled Aggregates for Use in Mortar and Concrete - Requirements and Test Methods, (2021). https://www.dinmedia.de/en/standard/abnt-nbr-15116/343808631.
[170] ACI 555R-01 - Removal and Reuse of Hardened Concrete, (2001).
[171] GB/T 25177-2010 - Recycled Coarse Aggregate for Concrete, (2010).
[172] GB/T 25176-2010 - Recycled Fine Aggregate for Concrete and Mortar, (2010).

[173] JGJ/T 240-2011 - Technical Specification for Application of Recycled Aggregate, (2011). https://www.chinesestandard.net/PDF/English.aspx/JGJT240-2011.
[174] CS3:2013 - Aggregates for Concrete, (2013).
[175] HKBD 2009 - Code of Practice for Site Supervision (2024 Edition), (2024).
[176] Works Bureau Technical Circular 12:2002 (WBTC No. 12/2002) - Specifications Facilitating the Use of Recycled Aggregates, (2002).
[177] IS 383:2016 - Coarse and Fine Aggregate for Concrete - Specification (Third Revision), (2016). https://www.services.bis.gov.in/php/BIS_2.0/bisconnect/knowyourstandards/Indian_standards/isdetails_mnd/10425.
[178] JIS A 5021:2005 - Recycled Aggregate for Concrete - Part 1: Recycled Coarse Aggregate, (2005).
[179] EN 206:2013 - Concrete - Specification, performance, production and conformity, (2013).
[180] E.K. Lauritzen, RILEM Technical Committee 121-DRG. Demolition and Reuse of Concrete and Masonry: Guidelines for Demolition and Reuse of Concrete and Masonry, 1993.
[181] E. Vázquez, RILEM Technical Committee 217-PRE. Progress of Recycling in the Built Environment, 2013.
[182] PTV 406 - Classification of Recycled Aggregates, (2003).
[183] DS 2426:2011 - Concrete - Specification, Performance, Production and Conformity, (2011).
[184] BY-43:2008 - Betonin kiviainekset, (2008).
[185] DIN 1045-2:2012 - Concrete, Reinforced and Prestressed Concrete Structures - Part 2: Concrete - Specification, Properties, Production and Conformity, (2012).
[186] Decreto Ministeriale 23 giugno 2022, n. 254. Criteri ambientali minimi per l'affidamento del servizio di progettazione ed esecuzione dei lavori di interventi edilizi, Ministero della Transizione Ecologica, Rome, 2022.
[187] RESIBA – Recycled Aggregates for Construction and Building (1999-2002), (2002).
[188] LNEC E 471:2006 - Specifications for the Use of Recycled Aggregates in Concrete, (2006).
[189] EHE-08 Instrucción de Hormigón Estructural, (2008).
[190] SIA 162/4:1994 - Recycled Concrete, (1994).
[191] BS 8500-1:2015 - Concrete - Complementary British Standard to BS EN 206 - Part 1: Method of Specifying and Guidance for the Specifier, (2015).
[192] BS 8500-2:2023 - Concrete - Complementary British Standard to BS EN 206 - Specification for Constituent Materials and Concrete, (2023).
[193] CSIRO HB 155-2002 - Guide to the Use of Recycled Concrete and Masonry Materials, (2002).

2 ELECTRIC ARC FURNACE SLAG IN CEMENTITIOUS CONGLOMERATES

2.1 MOTIVATIONS

At the beginning of the Ph.D. program, the author carried out a wide literature review, focusing on the most recent and advanced contributions on the use of Electric Arc Furnace Slag (EAFS) as aggregate replacement for concrete. At the end of this phase, some research lacks that may currently limit an extensive use of EAFS in the concrete market were identified. These gaps include:

1. Rheology
   Several works have already measured the workability of Electric Arc Furnace Concrete (EAFC). However, there are no available models to predict analytically EAFC flowability and its yield stress which activates the motion.
2. Shear transfer
   Shear behavior is a crucial point in structural analysis. Shear collapses are particularly dangerous and difficult to predict. Furthermore, shear stress is difficult to isolate, as it usually acts with bending moments. A study on the shear transfer for EAFC including assessment of each shear transfer mechanism compared to reference concrete would be of great practical interest.
3. Axial cyclic loading
   When conducting structural analysis, it is essential to characterize the mechanical performance of construction materials. Numerous studies have focused on monotonic axial compression. However, many structural elements are subjected to cyclic loading, e.g. traffic, wind, or earthquake. According to the author's knowledge, at the beginning of the Ph.D. program there were no studies on EAFC cyclic behavior.

The following subsections present results intended to address these identified research gaps.

The following papers concerning this topic have been already published by the Ph.D. candidate:

F. Faleschini, D. Trento, V. Ortega-López, M.A. Zanini, Shear transfer in fly ash concrete with electric arc furnace aggregates, Magazine of Concrete Research 75 (2023) 906–918. https://doi.org/10.1680/jmacr.22.00280.

F. Faleschini, D. Trento, V. Ortega-López, Behavior of EAF Concrete Under Cyclic Axial Loading, in: A. Ilki, D. Çavunt, Y.S. Çavunt (Eds.), Building for the Future: Durable, Sustainable, Resilient, Springer Nature Switzerland, Cham, 2023: pp. 768–777. https://doi.org/10.1007/978-3-031-32519-9_75.

D. Trento, F. Faleschini, Short-and long-term deformative properties of concrete containing Electric Arc Furnace slags, in: M. Del Zoppo, D.A. Talledo, S. Bianchi, P. Castaldo, I.G. Colombo, D. Gino, G. Ferrara, S. Labò, S. Spagnuolo (Eds.), Proceedings of the 3rd *fib* Italy YMG Symposium on Concrete and Concrete Structures, Turin, 2023: pp. 331–338. ISBN 978-2-940643-22-6

D. Trento, V. Ortega-Lopez, M.A. Zanini, F. Faleschini, Stress-strain behavior of electric arc furnace slag concrete under uniaxial compression: Short- and long-term evaluation, Construction and Building Materials 422 (2024) 135837. https://doi.org/10.1016/j.conbuildmat.2024.13583

2.2 RHEOLOGY: YIELD STRESS CHARACTERIZATION

2.2.1 Introduction

In the past, several works proved excellent properties of concrete including EAFS as replacement of the conventional gravel [1–4]. Even if the studies concerning the hardened properties are numerous, there is still a research lack for the rheology of concretes including EAFS, particularly about the yield stress at the fresh state.

Yield stress in fresh concrete denotes a threshold in the material rheology, in fact a solid viscoelastic behavior is usually observed for lower stress, but once the yield stress is surpassed the material flows more like a liquid with its steady-state flow behavior typically modelled using either the Bingham or Herschel-Bulkley models [5,6].

The performance of fresh cementitious conglomerates is affected by both the rheological properties of the cementitious paste and the aggregate particles [7,8]. The cement paste yield stress is mainly governed by the Van der Waals forces and the number of contact points among the cement particles according to the Yodel model [9,10]. Focusing on mortars, the effect of aggregates on yield stress is generally associated to the ratio between the sand volume fraction within the mixture and its loose packing fraction [11,12]. A ratio of 0.8 is recognized as a fundamental threshold, marking the shift from rheological behavior dominated by cement pastes (below 0.8) to that influenced by direct contact between sand particles (above 0.8) [13]. The loose packing fraction is typically governed by the particle granulometric distribution and morphology [14,15], such a parameter typically spans in the range 0.5-0.6 for sand [16] and reaches higher values for wider sieving distribution and roundish shape of the particles [17,18].

In this chapter, morphology properties of EAFS and natural sand are measured and linked to the loose packing fraction. Consequently, the yield stress for mortars containing EAFS and conventional sand is measured experimentally and modelled considering the loose packing fraction as an input parameter.

2.2.2 Experimental methods

2.2.2.1 Materials

2.2.2.1.1 Cement paste

The mortars formulated in this work were designed to be the mortar phase or the concrete equivalent mortar of a reference concrete. The reference conglomerate is a concrete containing cement CEM II/B-LL 32.5 R according to EN 197-1 [19] as a binder. The granulometric curve of the cement is displayed in Figure 2-2. The effective water to cement ratio is equal to 0.54. To achieve adequate workability, a polycarboxylate superplasticizer was also employed with a dosage of 0.85% over the total cement mass.

2.2.2.1.2 Aggregates

Two natural sands, called A and B, were employed in this experimental campaign. They are commercial sands 0-4 supplied by quarries in the northwestern France. The Electric Arc Furnace Slag (EAFS) was provided in the fraction 0/4 by a steel-making company in the Northeast of Italy.

Figure 2-1 depicts the aggregates chosen for this work, whereas Figure 2-2 displays the grading curves. Physical properties are summarized in Table 2-1 for all aggregates, further measurements were carried out on washed EAFS ($EAFS_w$) to eliminate the particles passing throw 63 μm sieve. The diameters corresponding to 10%, 30%, 60% and 90% of cumulative passing mass, labeled D_{10}, D_{30}, D_{60} and D_{90}, are

specified, as well as the water absorption w_{abs} and particle density ρ measured according to EN 1097-6 [20]. A uniformity coefficient C_u was also calculated as the ratio between D_{90} and D_{10} [16,21]. The specific surface S_{spe} computed from the particle size distribution was estimated considering spherical particle shape as done in a previous work [16].

Different from natural sand, EAFS has a sharp-pointed shape and rough surface. The content of fine particles (finer than 63 μm) is equal to 4.15%. As observed in previous studies, the particle density is quite higher than for conventional aggregates, and water absorption is slightly higher than for the conventional aggregates employed in this work [22,23]. However, it is worth to mention that EAFS in fine fraction has water absorption significantly lower than most recovered aggregates, indeed such a parameter might reach values up to ten times higher in fine recycled aggregates [24].

Table 2-1. Physical properties of the aggregates.

	Shape (-)	**D_{10} (mm)**	**D_{30} (mm)**	**D_{60} (mm)**	**D_{90} (mm)**	**C_u (-)**	**w_{abs} (%)**	**ρ (kg/m^3)**	**S_{spe} (m^2/kg)**
Sand A	Roundish	0.16	0.29	0.63	1.55	9.70	0.10	2640	7.23
Sand B	Roundish	0.50	1.05	1.17	2.56	5.10	0.20	2630	4.04
EAFS	Sharp	0.20	0.96	2.14	3.62	18.10	1.61	3780	4.53
EAFS$_w$	Sharp	0.20	0.99	2.25	3.50	17.50	1.61	3780	2.10

a) *b)* *c)*

Figure 2-1. Materials employed in the experimental campaign: a) Sand A; b) Sand B; c) EAFS.

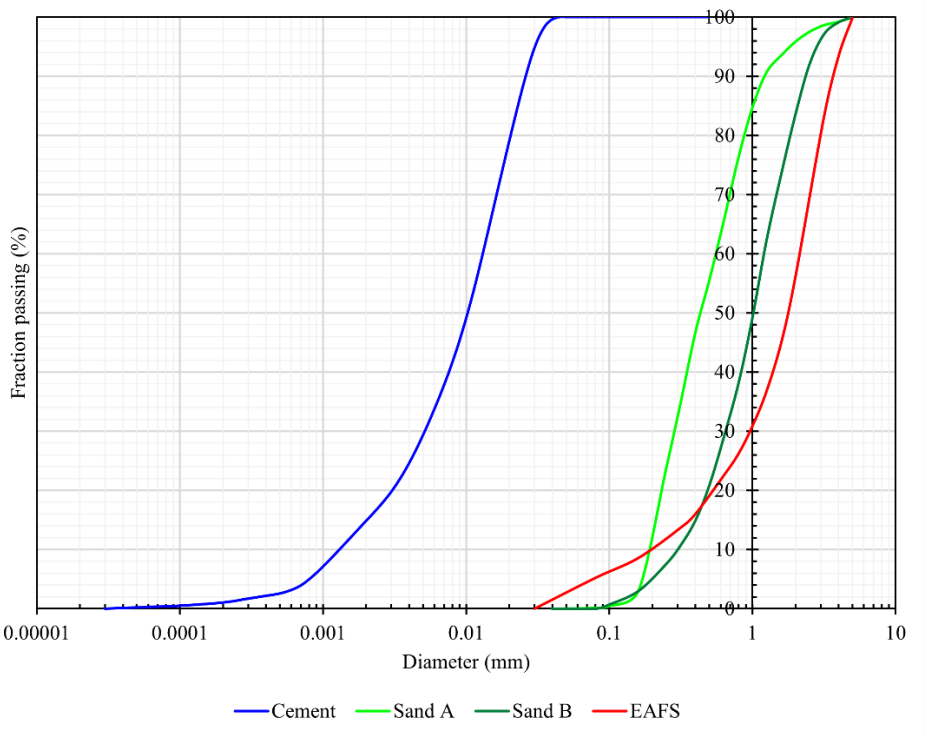

Figure 2-2. Grading curves of cement and aggregates.

2.2.2.2 Mix design

As previously stated, the mortars prepared in this work were prepared as the mortar phase or the concrete equivalent mortar of a reference concrete.

The mortar phase of this concrete contains a mixture of 50% sand A and 50% sand B, with a sand to cement ratio equal to 2.83, whereas the concrete contains coarse aggregates with gravel to sand mass ratio equal to 1.13. The gravel is a combination of 6.3-16 (36%) and 11.2-22.4 (64%) commercial gravel supplied by the same quarry. The concrete equivalent mortar of the reference concrete was considered according to the procedure described in Schwartzentruber & Catherine [25] considering the particles as spherical. As an outcome, the resulting sand to cement ratio for the concrete equivalent mortar is 3.24.

In this experimental campaign, both methods, i.e. mortar phase and concrete equivalent mortar, were considered for yield stress measurements. For each mix-design approach a total of six mixtures were cast with EAFS replacement ratio equal to 0%, 20%, 40%, 60%, 80% and 100% in volume. The mixtures matrix is shown in Table 2-2 for the sake of clarity.

Table 2-2. Mixtures matrix.

	Mix-design method	
	Mortar phase	**Concrete equivalent mortar**
Water/Cement	0.54	0.54
Superplasticizer/Cement	0.85%	0.85%
Aggregate/Cement	2.83	3.24
Natural Sand	0.5A + 0.5B	0.5A + 0.5B
EAFS volume replacement	0%, 20%, 40%, 60%, 80%, 100%	0%, 20%, 40%, 60%, 80%, 100%

2.2.2.3 Aggregate morphology

In this section, a protocol is defined to relate the shape and particle distribution of the aggregates with their loose packing fraction, which is essential to predict the yield stress of fresh cementitious conglomerates.

2.2.2.3.1 Particle shape analysis

A representative quantitative description of the particles was carried out by scanning. After sieving, the particles of each fraction were kept separately (4 mm, 3.15 mm, 2 mm, 1.6 mm, 1.25 mm, 1 mm, 0.8 mm, 0.63 mm, 0.4 mm, 0.315 mm, 0.16 mm, 0.08 mm). Consequently, samples with at least 100 particles were chosen for image scanning. A high-resolution image scanner was employed to get high-quality two-dimensional (2D) pictures of the particles.

The image analysis was run with the ImageJ® software. After greyscaling and thresholding calibration, each 2D scanned particle was modelled as an ellipse thanks to an automatic tool, with the long axis called length (L) and the short axis called width (W).

Particles with diameters larger than 0.315 mm were also weighted, in such a way the average thickness (T) was calculated considering each particle as an ellipsoid with the longest axis equal to L, the medium axis equal to W and particle density of the considered aggregate. Finally, the average flatness r_f is calculated as the ratio L/T.

2.2.2.3.2 Packing fraction measurement

Packing fraction strongly depends on the compaction energy [26], hence two different protocols are defined to measure loose and dense packing fractions.

The loose packing was considered as the natural random loose packing found through gravity flowing in a 4 liters funnel with an 8 cm long and 4 cm diameter orifice positioned 5 cm above the top of the test container, which consisted of a 2 liters cylinder. After completely filling the container, the exceeding material was eliminated by leveling smoothly the surface, carefully avoiding any kind of compaction. The dense packing fraction was determined with the same equipment, but the sample was compacted in three layers by applying 25 hits with a 1 kg steel ram. The samples were then weighed, and the packing fractions were calculated considering the particle density.

Loose and dense packing fractions are measured for all aggregates and mixtures of aggregates required for mortar casting according to Table 2-2.

2.2.2.4 Mortar production and Yield stress measurement

2.2.2.4.1 Mortar production

Mortars were prepared using a two-step mixing procedure. Initially, the dry ingredients were combined in the mixer for 1 minute. Water and superplasticizer were then added to the dry mix, hence mixing was performed at a low speed (120 rpm) for 1 minute. The mixing speed was then increased to 250 rpm for additional 2 minutes. After this 4-minutes blending phase, the mixer was stopped, and the bowl was scraped. Finally, the mixture underwent a high speed (250 rpm) mixing phase for 1 minute.

2.2.2.4.2 Yield stress measurement

The yield stress measurements were performed using the Anton Paar Rheolab QC rheometer available at the University of Southern Brittany. The adopted procedure was analogous to the one used in previous works [16,27]. Torque stress was applied at a constant strain rate of 0.01 s^{-1}, at this low shear rate, the

effects of plastic viscosity are negligible, allowing the yield stress to be determined from the measured maximum torque. The test duration was not set; instead, testing was stopped upon the torque peak was attained to ensure the yield stress was reached, as suggested by Nerella et al. [28]. The Vane geometry consisted of four blades, with overall dimensions of 40 mm and 22 mm for height and diameter, respectively; leading to a Vane constant of 3.6×10^4 mm^3.

For each mixture a total of at least four measurements were taken, the average yield stress was then calculated removing the outliers.

2.2.3 Results

2.2.3.1 Aggregate morphology

2.2.3.1.1 Particle shape analysis

Table 2-3 shows the results concerning the image analysis of the particles. The length L, the length over width ratio (L/W) and the flatness ratio r_f are specified for each size, in the last row the average values are also shown. The parameters L/W and r_f are not dependent on the particle size for all aggregates tested, hence the average values can be considered reliable to represent the whole particle size distribution.

It is worth mentioning that EAFS 0-4 demonstrated much lower average r_f than the conventional counterparts. Such a result proves dimensional uniformity and isotropic behavior of the EAFS among the three dimensions, which usually lead to better mechanical properties.

Table 2-3. Morphology of the aggregates.

	Sand A			**Sand B**			**EAFS**		
Sieve diameter (mm)	***L* (mm)**	***L/W* (-)**	**r_f (mm)**	***L* (mm)**	***L/W* (-)**	**r_f (mm)**	***L* (mm)**	***L/W* (-)**	**r_f (mm)**
4	7.53	1.34	6.16	6.66	1.30	4.87	6.07	1.38	1.56
3.15	5.81	1.39	4.92	5.33	1.30	5.05	5.04	1.43	1.55
2	4.73	1.37	5.46	4.64	1.36	5.33	3.97	1.50	1.84
1.6	3.76	1.37	5.44	3.81	1.38	5.88	2.65	1.53	1.76
1.25	2.94	1.11	6.49	2.86	1.32	4.87	2.17	1.55	1.95
1	2.42	1.38	5.35	2.32	1.40	5.36	1.53	1.48	1.41
0.8	1.92	1.35	7.07	1.92	1.42	5.17	1.36	1.58	1.73
0.63	1.42	1.34	-	1.44	1.36	-	1.02	1.49	1.42
0.4	1.02	1.27	-	1.01	1.18	-	0.69	1.55	1.19
0.315	0.71	1.28	-	0.73	1.42	-	0.52	1.58	1.59
0.16	0.40	1.36	-	0.41	1.39	-	0.33	1.70	-
0.08	0.21	1.34	-	0.22	1.37	-	0.16	1.77	-
Average	-	1.33	5.84	-	1.35	5.22	-	1.55	1.60

2.2.3.1.2 Packing fraction measurement

The experimental loose and dense packing fractions of the aggregates and their blends are shown in Table 2-4.

The EAFS and conventional sand 0.5A + 0.5B show the same loose packing fraction, but higher values were attained in mixtures of them, such a result is typically due to a reciprocal void filling, indeed the maximum loose packing was obtained for 40% EAFS. The dense packing fraction is greater than the loose one for any aggregate type and blend, as expected. This observation agrees with the compressible packing theory, as the packing strongly depends on the compaction energy [16,18]. The loose to dense packing fraction ratio is roughly equal to 0.9, with higher values in those mixtures with higher loose packing, such a result proves the compaction is less effective in mixtures which already show a greater compaction in the random loose condition.

The loose and dense packing fractions are also determined for washed EAFS, resulting in values equal to 0.581 and 0.643, respectively. The same parameters attain higher values for the unwashed material, and this is due to the presence of fine particles (smaller than 63 μm) that help fill micro-voids.

Please note that loose and dense packing fractions depend on the granulometric distribution and particle shape, this means that they might change for any natural sand and EAFS.

Table 2-4. Results of the packing fraction measurements.

		Natural sand volume (%)	**EAFS volume (%)**	**Loose packing fraction (-)**	**Dense packing fraction (-)**	**Dense/Loose packing fraction (-)**
EAFS		0	100	0.612	0.681	0.899
Natural sand	0.5A+0.5B	100	0	0.612	0.675	0.907
		80	20	0.630	0.687	0.917
		60	40	0.632	0.692	0.913
		40	60	0.621	0.691	0.899
		20	80	0.617	0.680	0.907
	A	100	0	0.597	0.652	0.916
	B	100	0	0.585	0.649	0.902

2.2.3.2 Yield stress

The results of the yield stress measurements are displayed in Figure 2-3.

The mortar phase method led to lower yield stress for all replacement ratios than the counterparts designed according to the concrete equivalent mortar approach. Such a result is mainly due to larger presence of aggregates in concrete equivalent mortar method when maintaining the same cementitious paste. However, the relative increase remained almost constant, as shown in Figure 2-3b.

As expected, higher EAFS replacements correspond to higher yield stress. The total replacement of conventional sand with EAFS led to yield stress values roughly 4.5 times higher. Such a result is mainly due to rough surface and sharp-pointed shape of EAFS [29], which lead to mortars with increased bond in the Interfacial Transition Zone (ITZ), resulting in greater intrinsic viscosity and resistance to flow.

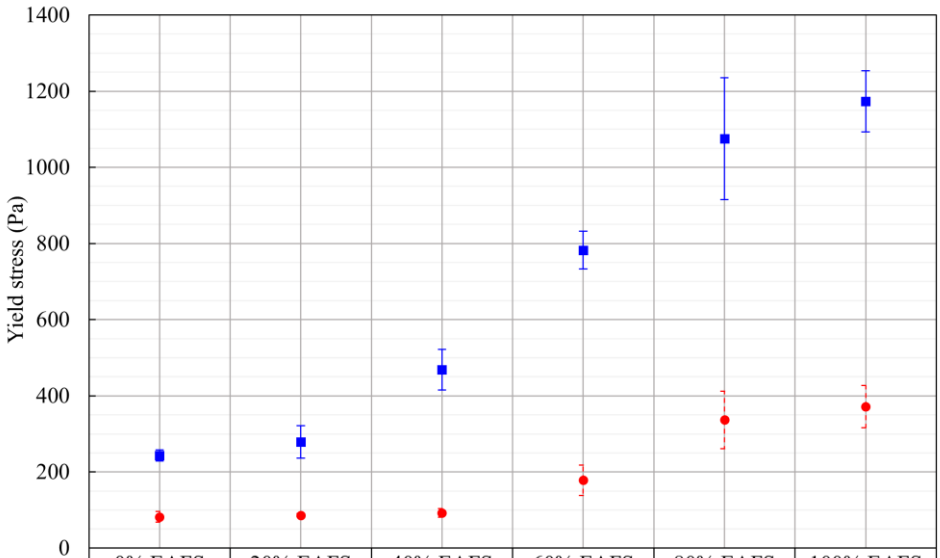

	0% EAFS	20% EAFS	40% EAFS	60% EAFS	80% EAFS	100% EAFS
● Mortar Phase	82	86	92	178	337	372
■ Concrete Eq. Mortar	243	278	468	783	1075	1174

a)

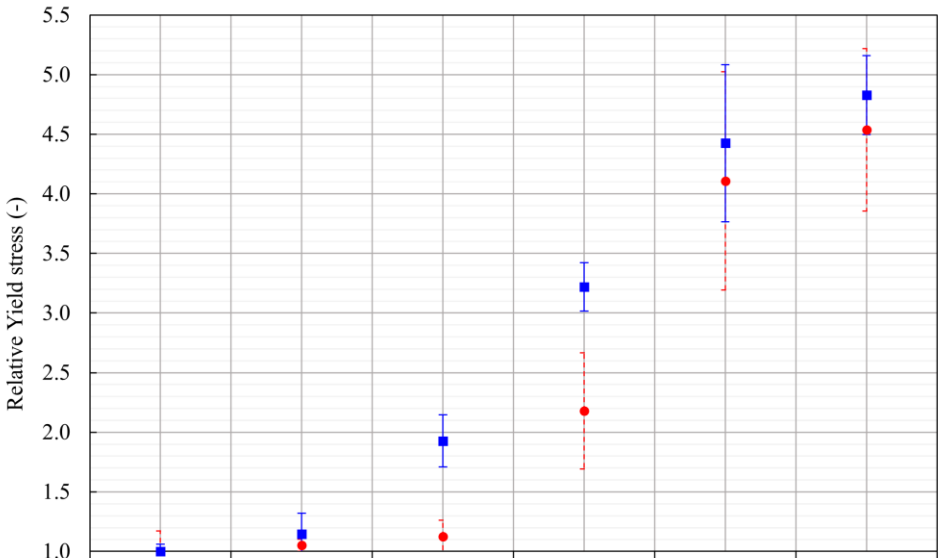

	0% EAFS	20% EAFS	40% EAFS	60% EAFS	80% EAFS	100% EAFS
● Mortar Phase	1.00	1.05	1.12	2.18	4.11	4.54
■ Concrete Eq. Mortar	1.00	1.15	1.93	3.22	4.42	4.83

b)

Figure 2-3. Results: a) Yield stress; b) Relative yield stress. Error bars indicate the standard deviation.

2.2.4 Analytical prediction of the Yield stress

2.2.4.1 Prediction of the Loose Packing Fraction

To predict the loose packing fraction, it is worth remembering that such a parameter depends on the granulometric distribution and the shape of the particles [30,31]. In a previous study [16], a linear relationship was found between the logarithm of C_u/r_f and the loose packing fraction φ_m, where C_u reflects the broadness of the particle size distribution, and r_f refers to the particle shape. Therefore, the loose packing fraction can be modelled using Equation 2-1:

$$\varphi_m = a + b \log\frac{C_u}{r_f} \qquad 2\text{-}1$$

Where the parameter b assumes constant value equal to 0.041 as experimentally observed by Barry et al. [16] for natural and manufactured crushed sand, whereas a depends on the sand type. This means that the linear relationship has constant slope b and intercept a, with the last one depending on the aggregate type and blend.

In this work, Equation 2-1 was employed to predict the loose packing fraction. The best fit with the experimental data was found for a that changes according to the EAFS replacement with a quadratic trend (Figure 2-4), this relationship shows a great agreement with the experimental data giving a coefficient of determination R^2 and Root Mean Square Error (RMSE) equal to 0.938 and 3.869×10^{-3}, respectively. A linear model is also proposed (Figure 2-4) and considered to follow a simpler approach, in this case the R^2 and the RMSE are equal to 0.755 and 7.682×10^{-3}. The comparison between the experimental and the predicted loose packing fractions is shown in Figure 2-5 for both regression methods. As expected, the quadratic regression demonstrates a more accurate prediction of the experimental data, however the difference remains lower than 0.012 for all computed values.

Please note that the modelling shown in Figure 2-4 is valid for the loose packing fraction obtained in this experimental campaign, and cannot be automatically extended to any natural aggregate and EAFS.

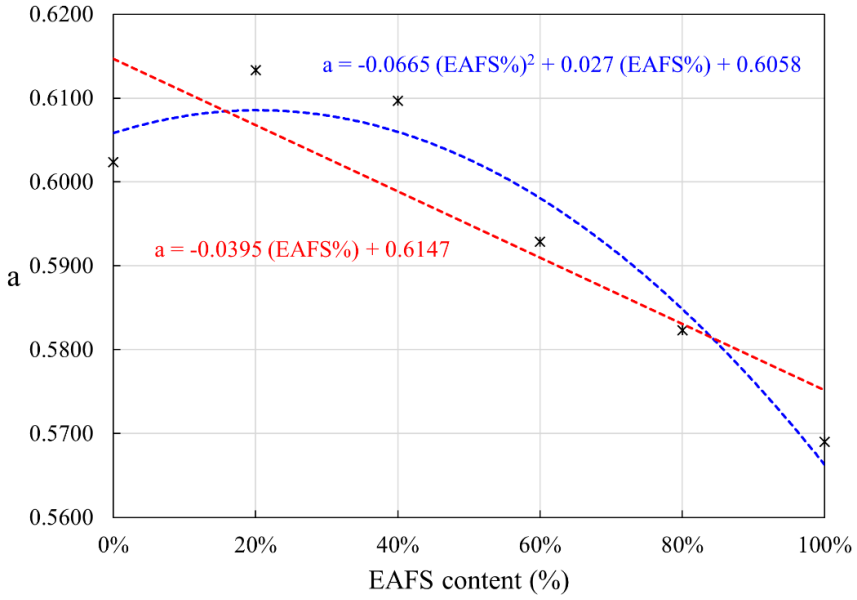

Figure 2-4. Modelling of the parameter a varying the EAFS replacement. Black markers represent the values obtained from the experimental φ_m measurements.

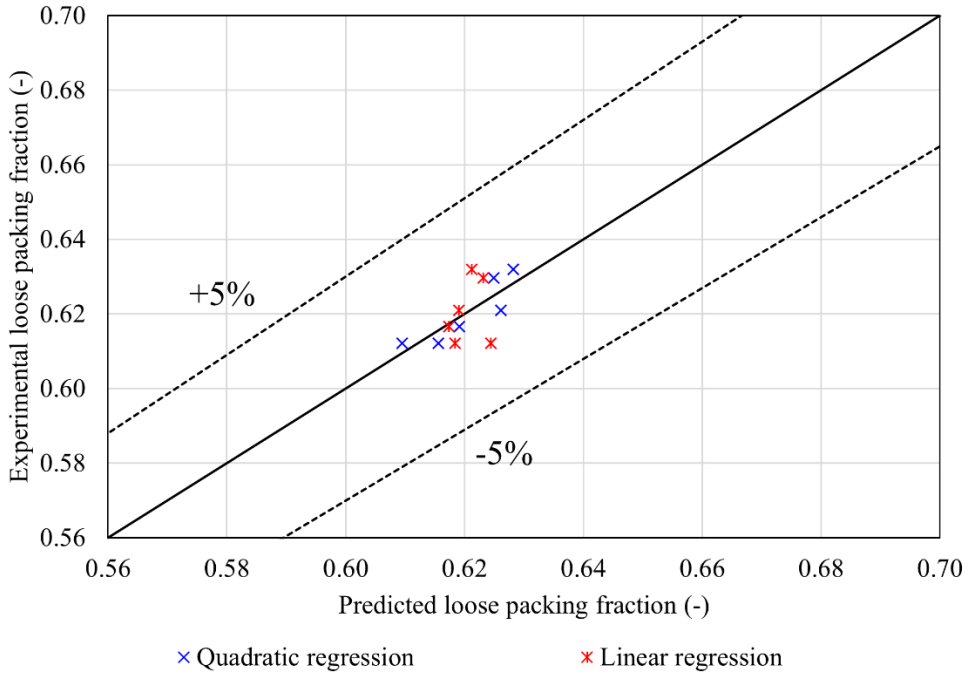

Figure 2-5. Comparison between predicted values (Equation 2-1) and experimental measurements of the loose packing fraction.

2.2.4.2 Prediction of the Yield stress

The yield stress of cementitious mortars can be modelled with a two-steps approach through the yield stress estimation of the cementitious paste and consequent extension for sand particles presence.

The yield stress of the cementitious paste was modelled with the Yodel model [9,10], which is confirmed to be effective for cement pastes [27,32]. The Yodel model relates the yield stress of cement pastes to the strength of interactions between cement particles, which are governed by Van der Waals forces and the number of particle contacts, with this last one influenced by the volume fraction of the cement solids. The Yodel model is depicted by Equation 2-2:

$$\tau_{cp} = m\frac{A_0 a^*}{d^2 H^2}\frac{\varphi_{cem}^2(\varphi_{cem}-\varphi_{per})}{\varphi_{m,cem}(\varphi_{m,cem}-\varphi_{cem})} \qquad 2\text{-}2$$

Where m is a pre-factor depending on the cement particle size distribution, a^* is the radius of curvature at the "contact points", H represents the surface-to-surface separation distance at these points, A_0 corresponds to the non-retarded Hamaker constant, d is the average diameter of the cement particles, φ_{cem} represents the cement volume fraction in the paste, $\varphi_{m,cem}$ represents the loose packing fraction of the cement particles, and φ_{per} is the percolation volume fraction of the cement particles. The cement volume fraction in the paste φ_{cem} was calculated from the mix-design data, $\varphi_{m,cem}$ was evaluated experimentally as for the aggregates and assumes a value of 0.610, as typically observed for cements [16,33]. Instead, the percolation volume fraction φ_{per} was measured experimentally by adding progressively small amounts of cement to water and superplasticizer until reaching a yield stress different from 0, this experiment led to φ_{per} equal to 0.397. Please note that the parameters here presented are typical for each cement matrix, hence they need to be calibrated for each cement type and superplasticizer.

At the mortar scale, it is important to consider that the effective water/cement ratio may slightly differ due to the presence of aggregates. Since aggregates were adopted dry as exposed to room environment, the

resulting cement paste contained less water. The absorbed water was considered proportional to the water absorption and the specific surface of the aggregate according to Equation 2-3:

$$m_{abs} \propto w_{abs} \times S_{spe} \quad 2\text{-}3$$

Where m_{abs} represents the absorbed water and S_{spe} is the specific surface. This formula (Equation 2-3) can be adopted and extended for natural aggregates and EAFS (Equation 2-4):

$$m_{abs} = a_{NAT}\,(1 - EAFS\%)\,w_{abs,NAT}\,S_{spe,NAT} + a_{EAFS}\,(EAFS\%)\,w_{abs,EAFS}\,S_{spe,EAFS} \quad 2\text{-}4$$

Where a_{NAT} and a_{EAF} are calibration coefficients that depend on the aggregate nature and need adjustment for each aggregate type. In this way, Equation 2-4 defines the amount of water which is subtracted from the cement paste due to the aggregate presence, and should be considered for the calculation of φ_{cem} in Equation 2-2.

The mortar yield stress was then calculated according to the Trung-Ovarlez-Chateau model (Equation 2-5) [34], which demonstrates to be reliable for mortars [8,14,16]:

$$\tau_{mortar} = \tau_{cp}\sqrt{\frac{1-\varphi}{(1-\varphi/\varphi_m)^{\eta\varphi_m}}} \quad 2\text{-}5$$

Where φ and φ_m are the volume fraction and the loose packing fraction of the aggregate, respectively, whereas η is an intrinsic viscosity coefficient that depends on the aggregate nature. The parameter η assumes value equal to 2.5 for spherical inclusions, but for real aggregates ranges between 2.5 and 5 [14].

Equations 2-1, 2-2, 2-4, 2-5 were employed to predict the yield stress of the mortars tested experimentally. The intrinsic viscosity η was regarded as equal to 3.7 for conventional mortar (0%EAFS), but a higher value was adopted for mortars containing EAFS. For this purpose, η was considered linearly increasing as the EAFS replacement ratio increases, with a maximum of 4.2 for 100% EAFS content. This is justified by the sharp-pointed shape and rough surface of the EAFS that increase intrinsic viscosity. The intrinsic viscosity might need calibration for each aggregate type and blend, however the value of 3.7 is quite typical for mortars with conventional aggregates.

The comparison between the experimental and the predicted yield stresses are displayed in Figure 2-6 considering quadratic and linear regression for the parameter *a* in loose packing density prediction. The results show that the predicted values agree well with the measured ones, however much greater accuracy can be achieved with a quadratic regression rather than a linear one for the parameter *a*.

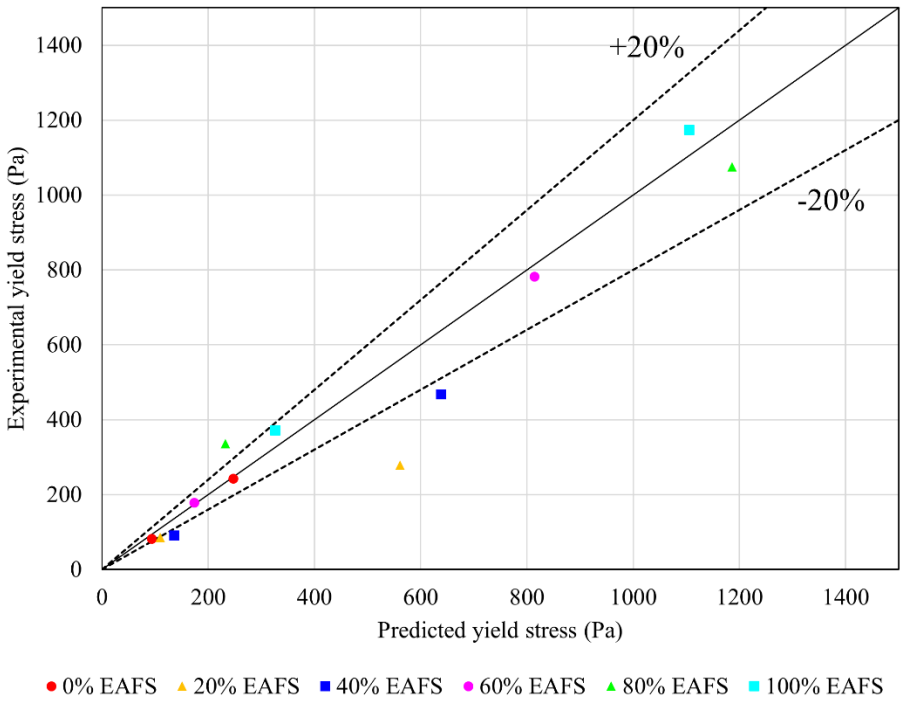

a)

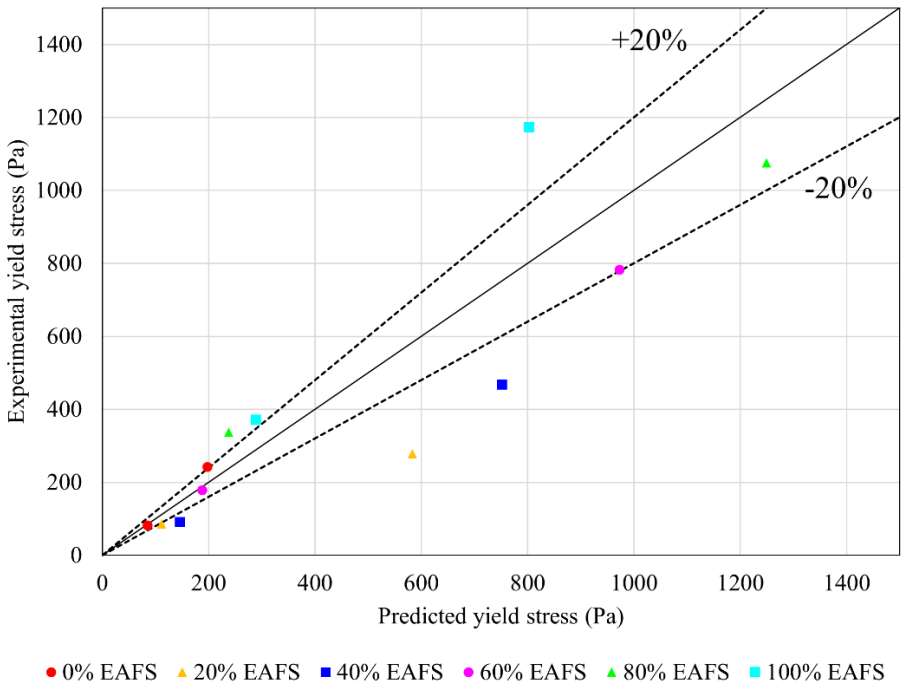

b)

Figure 2-6 Comparison between predicted and experimental mortar yield stress with: a) Quadratic and b) Linear regression of the parameter a for loose packing fraction modelling.

2.2.5 Conclusions

In this study, the yield stress of mortars incorporating Electric Arc Furnace Slag (EAFS) as aggregate replacement was experimentally measured, analyzed, and modeled. EAFS was used to replace conventional aggregate at replacement levels of 0%, 20%, 40%, 60%, 80%, and 100%. Based on the results, the following conclusions can be drawn:

- EAFS particles exhibit lower flatness compared to the conventional aggregates adopted in this experimental campaign, indicating more uniform and isotropic dimensions across the three axes.
- Yield stress increased with higher EAFS content. This was primarily attributed to the rough surface texture and angular geometry of EAFS particles, which contributed to greater intrinsic viscosity and flow resistance in the mortar mixtures.
- A linear relationship was observed between the logarithm of the ratio C_u/r_f and the loose packing fraction φ_m, where C_u represents the particle size distribution broadness and r_f denotes the shape factor. The slope of this relationship remained constant at 0.041, while the intercept a varies with the EAFS replacement ratio. To model this variation, both linear and quadratic regressions were applied. Although both provided satisfactory fits, the quadratic regression yields more accurate predictions of parameter a.
- The Yodel and Trung-Ovarlez-Chateau models were employed to estimate the yield stress using the calculated loose packing fraction. Predicted values closely match the experimental results, with the quadratic regression for parameter a again offering greater accuracy over the linear approach.

2.3 SHEAR TRANSFER BEHAVIOR

2.3.1 Introduction

Previous studies have proven that replacing the coarse fraction of natural aggregates (NA) with EAFS in concrete can lead to excellent properties [35–37]. In this type of concrete, mechanical properties are generally improved due to several factors, including the greater intrinsic strength of EAFS particles compared to NA, their rough surface, which promotes a strong bond with the cementitious paste, and their slight hydraulic activity [22,38]. Some real-scale tests were also carried out on beams [39–41], columns [42] and beam-column joints [43,44] demonstrating in all cases the same, or even better performance than conventional counterparts.

The shear behavior of Reinforced Concrete (RC) members is critical in structural engineering, affecting the design and safety of infrastructures and buildings [45]. Shear forces may induce internal stresses that can lead to diagonal cracking and potential brittle shear failure, which is considered generally among the most unsafe ones for RC members. The main mechanisms responsible for shear transfer include cohesion effect, aggregate interlock, dowel action, arch mechanism, and stirrups contribution [46–48]. Among these, aggregate interlock is one of the major mechanisms of shear transfer across cracks [49]. However, the study of each shear resistant mechanism separating it from the others is challenging from the experimental point of view, also because shear solicitation usually occurs in co-presence with bending moment for most common structural elements, such as beams and columns. For this reason, several experimental setups were developed to investigate shear strength directly, reducing the bending solicitation as much as possible. Among them, it is worth mentioning the single notched FIP-Type specimen [50], the double-notched push-through specimens [51], and the S-shape push-off specimen proposed by Hofbeck et al. [52], which is the most common. In this test method [52], a vertical load is applied on the sample, which transfers as shear stress along a middle shear plane.

Shear strength is also a crucial point when investigating unconventional aggregates to substitute traditional sand and gravel. Indeed, the shear transfer resulting from aggregate replacement is different from the one observed for conventional concretes. According to the knowledge of the author, limited literature is available on the shear transfer mechanism with recovered or unconventional aggregates.

Fonteboa et al. [53] examined the shear strength of Recycled Aggregate Concrete (RAC) and observed a decline in shear friction capacity, specifically in specimens without transverse reinforcement. Similar results were found by Xiao et al. [54], who attributed the strength loss to microcracks and internal damage in the attached mortar of the Recycled Aggregate (RA). Fakitsas et al. [55] additionally confirmed these outcomes, demonstrating that in high-strength RAC, shear planes tend to pass through the aggregates rather than around them, leading to reduced shear strength. For normal-strength concrete, Rahal and Hassan [56] demonstrated that failure surfaces in Natural Aggregate Concrete (NAC) are generally rougher than those in RAC due to crack formation along the old Interfacial Transition Zone (ITZ) of the recycled aggregate, which is more vulnerable than the new ITZ. Nevertheless, when confined, shear strength increases significantly, as confirmed numerically by Sun et al. [57]. This improvement is attributed to the compression force applied at the interface, developing aggregate interlock and friction similarly in both RAC and NAC. Waseem and Singh [58] performed shear stress-slip tests on RAC with unconfined and confined push-off samples. When reinforcement was present and crossed the shear interface, aggregate interlock and dowel actions played a significant role in shear strength development. They also checked existing strength prediction models, getting acceptable results. Trindade et al. [59] analyzed the shear transfer mechanism in recycled concrete beams varying the longitudinal and transverse reinforcement ratio,

some push-off specimens were also tested to analyze the failure surface and hence the aggregate interlock contribution. Imjai et al. [60] suggested a new semi-empirical equation to calculate the shear strength of specimens with different RA replacement ratios. Clerici et al. [61] evaluated in a recent work the aggregate interlock and dowel action adopting the double-notched push-through setup for concretes containing EAFS as partial aggregate replacement. Mixtures containing EAFS demonstrated increased stress transfer due to aggregate interlock. Furthermore, dowel action gave just a minor contribution, about 8-10%, to the total shear strength, thus confirming that aggregate interlock is the primary mechanism responsible for shear transfer.

2.3.2 Unconfined shear transfer

The aim of this study is to provide an analysis on the shear transfer mechanism in the pre-cracking phase, i.e. when cohesion contribution plays a dominant role.

2.3.2.1 Experimental methods

2.3.2.1.1 Materials

The physical features of the aggregates are listed in Table 2-5, whereas Figure 2-7 shows the aggregates grading curves: note that three fractions of EAFS were adopted to replace the 4-16 mm NA fraction, in different amounts. The EAFS aggregates are depicted in Figure 2-8. All mixtures were cast with a cement CEM IV/A (V) 42.5 R, according to EN 197-1 [19]: choosing such a pozzolanic cement, with about 30% of fly ash replacing clinker, allows to achieve a more sustainable mix with a lower carbon footprint, which however shows a rapid-strength gain. To cast the concrete mixes, tap water from Padova's water supply system (in Italy) was employed, which does not contain any harmful substances, and a sulphonated naphthalene water-reducing admixture was added at different percentages of the cement weight to reach the required workability.

2.3.2.1.2 Mix design

Two concrete mixes were realized: a Natural Aggregate Concrete (NAC) and an Electric Arc Furnace Concrete (EAFC). The former contained natural aggregates only, whereas in the latter EAFS replaced the natural gravel. The aggregates fine fraction (0-4 mm) is the same for both the mixes, and it is made with river sand. Table 2-6 shows the mix design of the two concretes realized for this experimental campaign.

2.3.2.1.3 Mechanical characterization

For each mix, a series of cylinders 100×200 mm was cast to evaluate compressive strength f_c at 14 and 28 days, indirect tensile strength f_{ct} and elastic modulus E_c at 28 days. Together with cylindrical samples, three push-off specimens were prepared for each mixture.

Table 2-5. Physical properties of the aggregates.

Aggregate type	Shape	Surface	Apparent particle density (kg/dm^3)	Water absorption (%)
NA 0-4	Roundish	Smooth	2.644	2.72
NA 4-16	Roundish	Smooth	2.769	1.37
EAFS 4-8	Sharp	Smooth	3.840	0.89
EAFS 8-12	Sharp	Smooth	3.800	1.01
EAFS 8-16	Sharp	Smooth	3.784	0.82

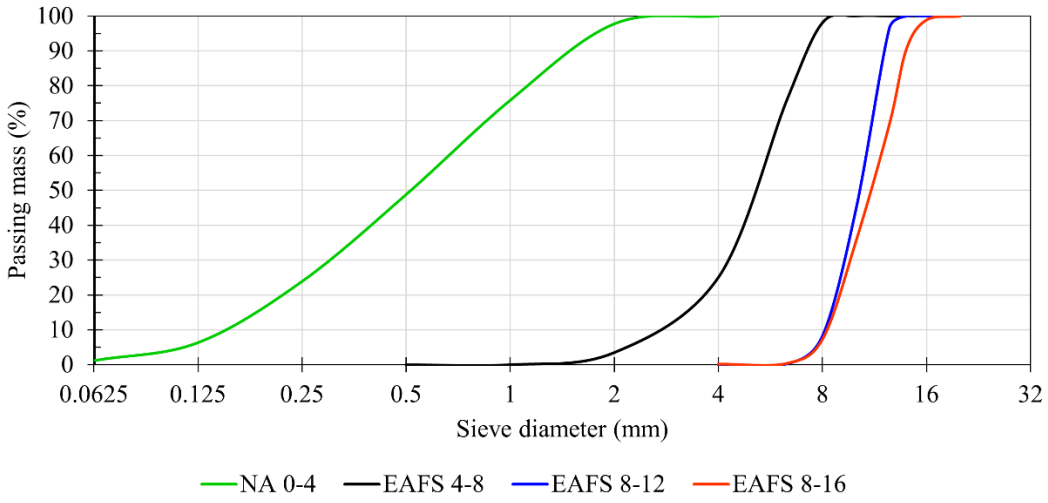

Figure 2-7. Aggregate grading curves.

a) *b)* *c)*

Figure 2-8. Aggregates employed for this experimental campaign: a) EAFS 4-8; b) EAFS 8-12; c) EAFS 8-16.

Table 2-6. Mix design in kg/m³.

	NAC	***EAFC***
Cement IV/A (V) 42.5 R	400	400
W/C ratio	0.5	0.5
Water	200	200
NA 0-4	863	863
NA 4-16	1027	-
EAFS 4-8	-	502
EAFS 8-12	-	359
EAFS 8-16	-	563
Superplasticizer	3.2 (0.8%)	4.8 (1.2%)

2.3.2.1.4 Push-off test setup

The push-off test method was employed to study the shear transfer mechanism in EAFC. The specimen geometry and reinforcement details are displayed in Figure 2-9. The geometry is similar to that assumed in a previous study [62]. The height of each specimen is 260 mm, with a rectangular cross-section of $b \times h = 140 \times 100\ mm^2$. The specimens feature two intermediate notches, formed directly within the formwork, designed to control stress flow and ensure that shear stress develops primarily along the contact plane between the two halves of the specimen. This region of the specimen is the shear transfer plane, where both normal and tangential stresses act simultaneously. Four L-shaped longitudinal bars having diameter of 10 mm were placed in the samples to prevent possible flexural failure outside the investigated shear plane region; these bars were joined with six transverse bars of 6 mm diameter. The main mechanical properties of the steel bars are displayed in Table 2-7. No transverse reinforcement crossing the shear plane was installed, as done by Fonteboa et al. [53], for the condition of $\rho_t = A_{st}/A_c = 0$, where A_{st} is the transverse steel area, A_c is the concrete area in the sliding plane and ρ_t is the transverse reinforcement ratio. The same arrangement was used by Barragan et al. [63], Mathews et al. [64], Rahal and Al-Khaleefi [65] and Waseem and Singh [58]. In this way, the pure effect of the friction contribution to the shear strength can be analyzed without focusing, at this stage, on the reinforcement contribution. Indeed, it is worth recalling that non-ordinary concretes, such as concretes made with recycled or lightweight aggregates or high-strength concretes, face different aggregate interlock mechanisms owing to different crack kinematics [66].

The specimens were loaded with a 600 kN servo-testing machine, with monotonic loading under displacement control, fixed at 0.3 mm/min, similarly to the experience of Yusuf et al. [62]. A push-off sample before loading is shown in Figure 2-10. The test setup consists of four linear voltage displacement transducers (LVDTs) and two displacement and strain transducers (DSTs). A pair of LVDTs was used on two faces of the specimen and the displacement recorded by each instrument (D_1 and D_2) was used to calculate the relative vertical slip s between the two L-shaped halves according to Equation 2-6:

$$s_i = D_{1,i} - D_{2,i} \qquad 2\text{-}6$$

Where i indicates the face of the specimen. The DSTs directly measured the crack opening in the transverse direction as they were placed crossing the shear plane, as for the research of da Cunha et al. [67]. In the loading machine, a hinge connection was positioned on the top of the actuator: the aim of this was to keep the applied load as axial as possible, thus minimizing bending emerging from possible irregularities present in the specimens and maintaining pure shear action in the analyzed region. With the same goal, i.e. minimizing the effect of irregularities and discontinuities on the surfaces, a steel plate and a thin layer of high-strength mortar were placed on the top and bottom of the sample.

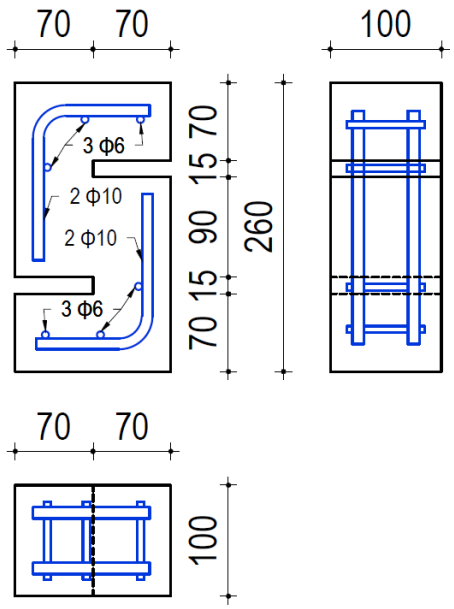

Figure 2-9. Geometry and reinforcement details of push-off specimens.

Table 2-7. Steel bars mechanical properties.

	φ6 mm	***φ10 mm***
Yield Strength (MPa)	546	516
Ultimate Strength (MPa)	680	602
Ultimate Strain (%)	9.67	9.79

Figure 2-10. Push-off test setup.

2.3.2.2 Results

In this subsection, results of the experimental campaign are presented and discussed including fresh behavior and mechanical properties at 14 and 28 days, shear strength and failure modes of push-off specimens, shear stress-slip curves and shear stress-crack opening curves.

2.3.2.2.1 Fresh behavior

The fresh density d_{fc} and Abram's cone slump are given in Table 2-8. In this study, the EAFC demonstrated adequate workability. The fresh EAFC achieved the same slump class (S3) as the NAC mix, according to EN 206 [68]. Compared to the NAC, the EAFC exhibited only a slight decrease in slump. This minor reduction is attributed to the shape characteristics of EAFS, which tend to make fresh EAFC less workable [69]. Typically, this issue can be mitigated by adjusting the fine particle content in the mix. Additionally, no sudden loss of workability was observed during casting, confirming that the use of slag aggregates with pozzolanic cement is feasible from a workability standpoint.

2.3.2.2.2 Mechanical characterization

Regarding mechanical properties, the findings of this study align with existing knowledge on EAFC (Table 2-8). Compared to the NAC mix, the EAFC demonstrated increases in compressive strength of approximately 44% and 37% after 14 and 28 days of curing, respectively. Additionally, the tensile strength and elastic modulus were enhanced by 28% and 36%, respectively. These results highlight the effective interaction between EAFS and the blended cement, leading to faster strength development and continued strength gain beyond 56 days. The improvements in strength over NAC are due to several factors: the intrinsic higher strength of EAFS aggregates due to their high iron oxide content [70], the strong bond between the EAFS and the cement matrix promoted by the slag angular shape [71], and the improved Interfacial Transition Zone (ITZ) enriched by hydration products forming in the aggregate boundary zone during later stages of curing [38].

Table 2-8. Fresh and hardened concrete properties

	NAC	***EAFC***
Slump (cm)	12	10
d_{fc} (kg/m^3)	2407	2824
d_c (kg/m^3)	2431	2828
$f_{c,14}$ (MPa)	32.48	46.98
f_c (MPa)	38.96	53.34
f_{ct} (MPa)	3.56	4.56
E_c (GPa)	28.142	38.289

2.3.2.2.3 Shear transfer strength

Table 2-9 presents the key findings from the push-off tests. It includes the ultimate loads (P_u), the ultimate shear strengths τ_u, calculated as P_u divided by the shear plane area (A_c = 9000 mm²), the average ultimate slips s_u measured at P_u, and the average ultimate crack widths w_u, also evaluated at P_u.

Table 2-9. Mean results of the push-off tests.

	NAC	***EAFC***
P_u (kN)	52.81	68.38
τ_u (MPa)	5.86	7.60
s_u (mm)	0.427	0.319
w_u (mm)	0.039	0.038
τ_u^* (-)	0.94	1.04
τ_u^+ (-)	1.65	1.67

As shown in Table 2-9, the EAFC shear strength proved to be higher than for the conventional counterpart, with an average increase of 30%. To understand more effectively the shear behavior, shear strengths were normalized using both $f_c^{1/2}$ and f_{ct}, resulting in the dimensionless parameters τ_u^* and τ_u^+, respectively. Previous studies have established a sound relationship between concrete mechanical properties and shear strength [72], with $f_c^{1/2}$ often serving as a simplified representation for f_{ct}, as indicated by ACI 318-19 [73]. However, as noted earlier, this relationship may not work consistently for non-conventional concretes like EAFC, where the correlation between compressive and tensile strength differs from that in NAC. This divergence is largely due to the interaction between EAFS and the cement matrix, which influences the characteristics of the Interfacial Transition Zone (ITZ), including its thickness and bond quality. The dimensionless shear strengths presented in Table 2-9 confirm that both τ_u^* and τ_u^+ are higher for EAFC than NAC. Specifically, EAFC exhibited an average increase of 10% in τ_u^*, emphasizing the positive impact of EAFS on mechanical properties and, consequently, shear performance. In contrast, the increase in τ_u^+ was slight, just 1%, indicating that splitting tensile strength was closely aligned with shear strength for both concrete types. The enhanced shear strength of EAFC may also be attributed to the angular shape of the slag aggregates, which improves tensile behavior, increases contact surface area, and enhances friction between the two L-shaped blocks, an observation consistent with Yang et al. [74].

2.3.2.2.4 Failure modes

Figure 2-11 shows representative NAC and EAFC specimens after testing. No visible cracking was observed until 90% of the peak load. Cracks started to form just before reaching the maximum load, followed by a sudden brittle failure. This was initiated by a prominent vertical crack, typically emerging at one notch edge, and was followed by a secondary sub-vertical crack that quickly developed across the shear plane, forming a compressed strut. The initial vertical crack, the most pronounced, extended across the specimen, while subsequent cracks assumed inclined paths up to 30° from the shear plane. Failure was primarily governed by tensile splitting. Because no transverse reinforcement intersected the shear plane, the load capacity fell abruptly after the peak, leading to complete separation of the two L-shaped parts.

Figure 2-12 presents the post-failure shear surfaces of both NAC and EAFC specimens. Two failure mechanisms were observed: cracks directly crossing the aggregates, and cracks propagating around aggregates within the Interfacial Transition Zone (ITZ). While both modes occurred in each mix, EAFC was dominated by aggregate fracture, whereas NAC showed both mechanisms with roughly equal frequency. These observations were validated by failure surfaces from splitting tests. EAFC failed at loads approximately 29% higher than NAC, and the cementitious matrix had high strength due to elevated cement content. This suggests that the quality of the ITZ in EAFC delayed the onset of cracking. However, once shear stress exceeded a critical threshold, failure occurred through aggregate cracking, i.e. a behavior

typical of high-strength concretes. The resulting EAFC fracture surfaces exhibited pronounced angularity and roughness, which increased the contact area and contributed to the improved shear performance.

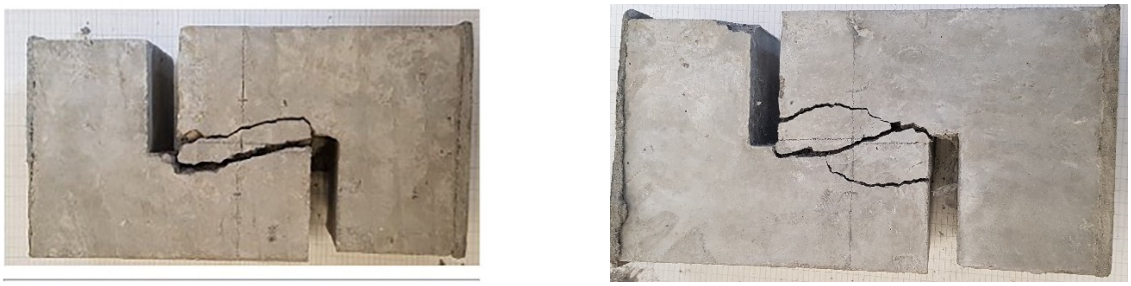

a) b)

Figure 2-11. Failure patterns in selected push-off specimens: a) NAC; b) EAFC.

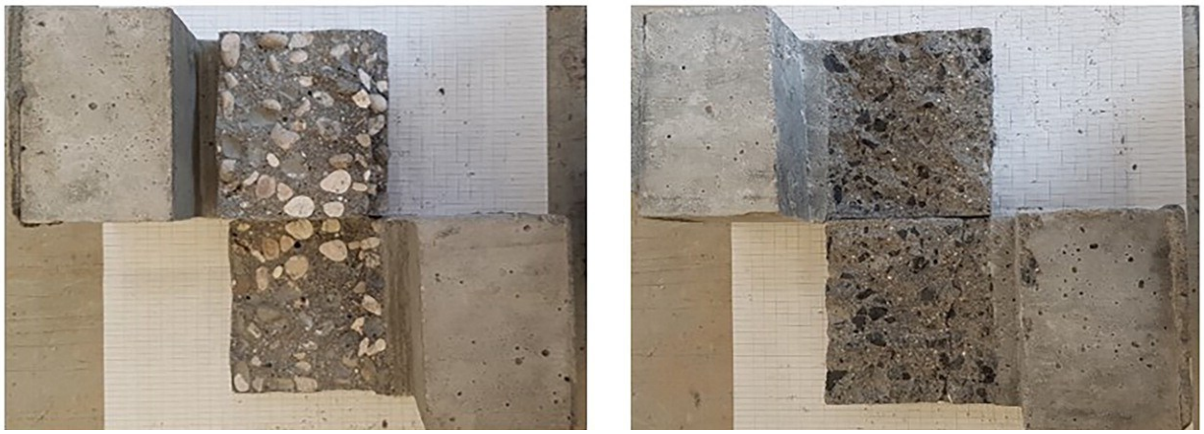

a) b)

Figure 2-12. Crack surface in the shear transfer plane: a) NAC; b) EAFC.

2.3.2.2.5 Shear stress-slip curves

Figure 2-13a displays the shear stress-slip curves for both NAC and EAFC specimens, with values representing the average of four LVDT measurements per specimen. After reaching the peak shear strength, a sudden drop in the curves was observed, but this post-peak behavior is not shown, as slip measurements became meaningless and exceeded the device limits, resulting in unreliable data.

The ultimate slip values s_u reported in Table 2-9 were obtained from these curves. On average, EAFC specimens exhibited 26% less slip than NAC specimens, indicating reduced deformation capacity. These outcomes demonstrate a more brittle failure behavior in EAFC, which aligns with the general trend that higher-strength concretes tend to exhibit increased brittleness [75]. This is further supported by the steeper slopes of the EAFC curves in Figure 2-13a, reflecting higher shear stiffness compared to NAC. Nonetheless, the overall deformation behavior of both concrete types remained broadly similar.

2.3.2.2.6 Shear stress-crack opening curves

Figure 2-13b shows the shear stress-crack opening curves, based on the average readings from the two DSTs placed on opposite faces of each specimen. For sample EAFC-2, the full curve could not be recorded due to crack-induced detachment of the instrumentation. For all other specimens, the curves are drawn up to the point of ultimate shear strength, following the same approach used for the stress-slip curves.

The ultimate crack widths w_u listed in Table 2-9 were found from these curves. At peak shear stress, the average w_u values for NAC and EAFC were nearly the same, differing by only about 2%. All measured w_u values were below 0.1 mm, which is consistent with the brittle nature of the failure mode observed.

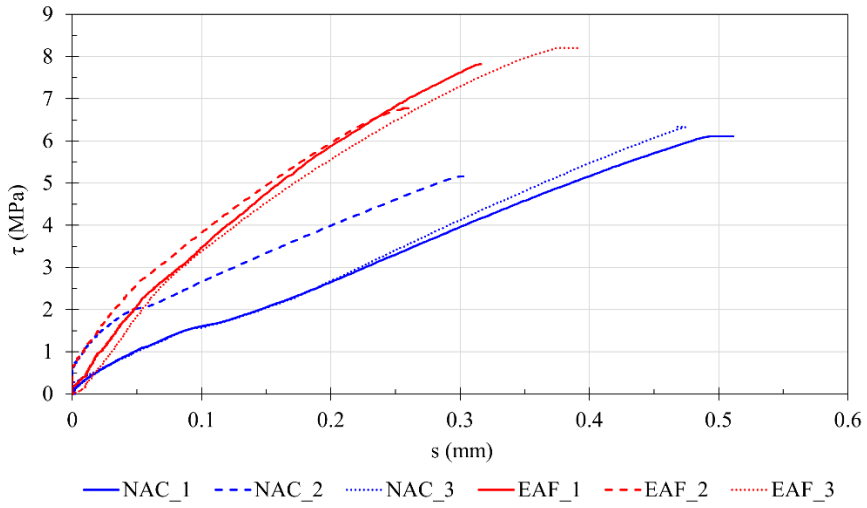

a)

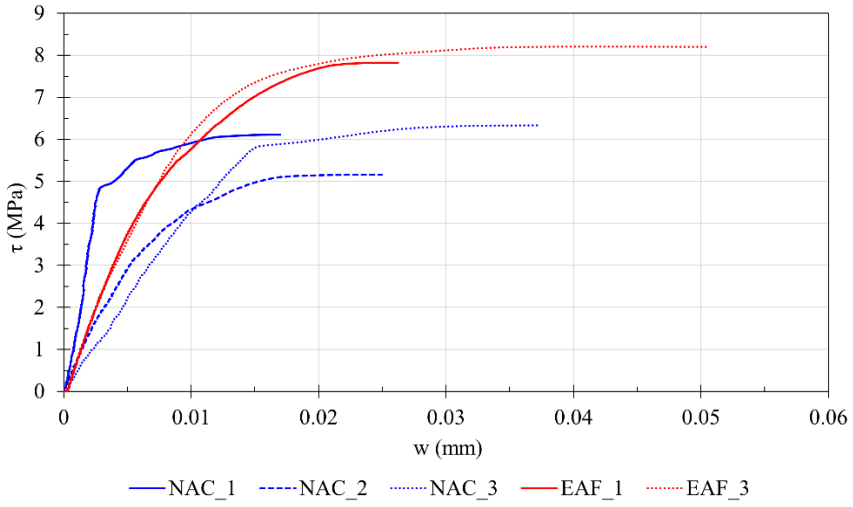

b)

Figure 2-13. Results of push-off tests: a) shear stress-slip curves; b) shear stress-crack opening curves.

2.3.3 Confined shear transfer

The aim of this study is to offer a step forward from the work presented in the previous section §2.3.2. In that case, the absence of clamping steel allowed to isolate the cohesion contribution, focusing on the pre-cracking behavior. In this work, similar specimens are prepared with the addition of confining pressure through transverse reinforcement, allowing for the recording of post-crack behavior and a more complete analysis of the resulting shear transfer mechanism.

2.3.3.1 Experimental methods

2.3.3.1.1 Materials

The cement adopted in this work is a CEM IV/A (V) 42.5 R containing 65-89% clinker and 11-35% fly ash according to EN 197-1 [19]. The mixing was carried out with tap water from the water supply system of Padova (Italy), free from harmful substances. A formaldehyde-free superplasticizer for concrete based on non-sulphonated acrylic polymers was also included to achieve the desired consistency.

Many aggregate types were used to properly adjust the mix-design: a natural sand (NA 0-4), two conventional gravels (NA 4-8 and NA 4-16), and three EAFS fractions (EAFS 4-8; EAFS 8-12; EAFS 8-16). The main physical properties are listed in Table 2-10, while the grading curves are shown in Figure 2-14. The EAFS features rough surface and sharp-pointed shape due to the recovering process which consists of crushing and grinding, and its mineralogy is mainly made of wustite, hematite, magnetite, merwinite (Figure 2-8). Instead, a smooth surface and roundish shape is generally observed in natural aggregates, as for NA 0-4 and NA 8-16 which are river sand and gravel, respectively. Instead, the intermediate natural aggregate fraction NA 4-8 was obtained from crushed rocks, hence it showed smooth surface and sharp shape. It is worth observing the difference in particle density and water absorption between EAFS and conventional counterparts. Particle density is roughly 40% higher in EAFS, whereas water absorption exhibits lower values than for conventional aggregates.

2.3.3.1.2 Mix design

Two concrete mixes were made according to the mix-design shown in Table 2-11: a Natural Aggregate Concrete (NAC), and an Electric Arc Furnace Concrete (EAFC) including just EAFS for the coarse aggregate fraction. The mixture proportion is equivalent, the effective water/cement ratio is 0.5, considering that the aggregates were mixed in saturated surface-dry conditions. The aggregates were graded with the Bolomey curve of the total solid mass of the mixture (therefore considering cement + aggregates). To attain adequate consistency, the water reducing admixture was incorporated in dosage 1.0% and 1.2% on the cement weight for NAC and EAFC, respectively. The target slump is in the range 20-25 cm. With this aim, an higher superplasticizer dosage was adopted for EAFC to limit workability losses [76].

Table 2-10. Physical properties of the aggregates.

Aggregate type	Shape	Surface	Particle density (kg/dm³)	Water absorption (%)
NA 0-4	Roundish	Smooth	2.644	2.72
NA 4-8	Sharp	Smooth	2.782	1.37
NA 8-16	Roundish	Smooth	2.690	1.21
EAFS 4-8	Sharp	Rough	3.840	0.89
EAFS 8-12	Sharp	Rough	3.800	1.01
EAFS 8-16	Sharp	Rough	3.784	0.82

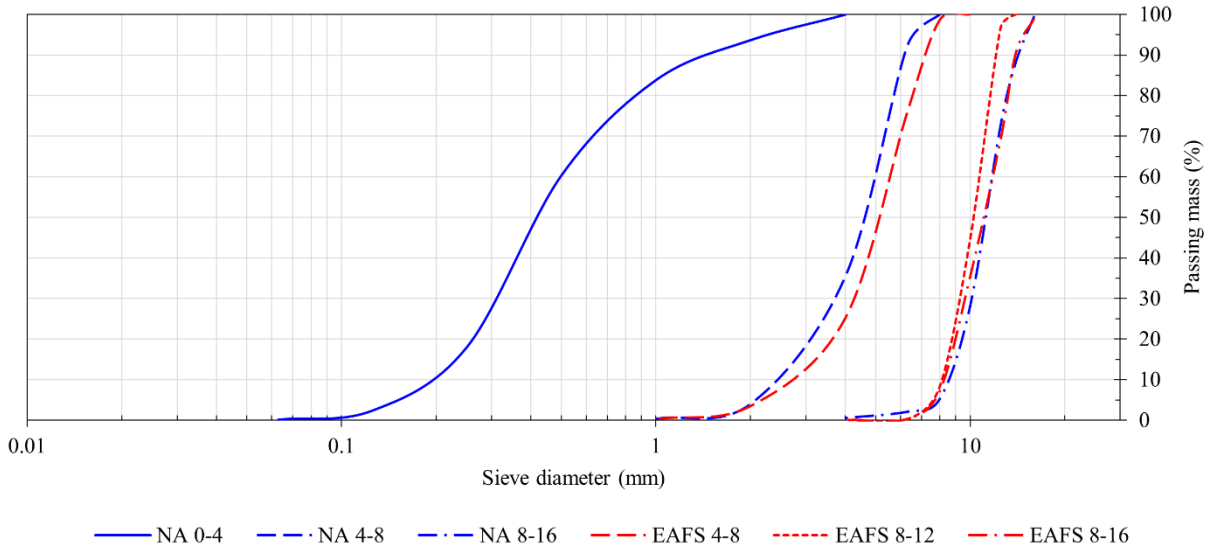

Figure 2-14. Aggregates grading curves.

Table 2-11. Mix design in kg/m³.

	NAC	***EAFC***
Cement IV/A (V) 42.5 R	384	384
W/C ratio	0.5	0.5
Water	192	192
NA 0-4	517	517
NA 4-8	725	-
NA 8-16	541	-
EAFS 4-8	-	1001
EAFS 8-12	-	372
EAFS 8-16	-	370
Superplasticizer	3.84 (1.0%)	4.61 (1.2%)

2.3.3.1.3 Mechanical characterization

A series of cylindrical samples 100×200 mm and push-off samples were cast for each mixture, i.e. NAC and EAFC. Compressive strength, splitting strength and Young's Modulus were evaluated on cylindrical samples according to the European Standards EN 12390-3 [77], EN 12390-6 [78] and EN 12390-13 [79], respectively. Instead, direct shear strength was tested on push-off samples according to the procedure presented in the next subsection.

2.3.3.1.4 Push-off test setup

The push-off test method was adopted to examine the shear transfer mechanism in EAFC. The geometry and reinforcement details of the push-off samples are shown in Figure 2-15. Each sample measured 450 mm in height with a rectangular cross-section of 300×150 mm^2. Two intermediate notches were formed directly by the shape of the formwork to control stress distribution and guarantee proper concentration of shear stresses along the contact plane between the two specimen halves. The shear transfer plane, which measures 210×150 mm^2, is the critical zone where both shear and normal stresses act concurrently. Each specimen holds a steel cage composed of six φ12 L-shaped longitudinal bars and variable number of φ8 closed stirrups, the reinforcement detail and properties are given in Figure 2-15 and Table 2-12. The transverse reinforcement crossing the shear plane is measured with the transverse reinforcement ratio $\rho_t=A_{st}/A_c$, where A_{st} is the transverse steel area and A_c is the concrete area in the sliding plane. This ratio is equal to 0.64%, 0.96% and 1.28% for 2, 3 and 4 closed stirrups, respectively. It is important to note that unconventional concretes, e.g. those incorporating lightweight or recycled aggregates or high-strength mixtures, exhibit different aggregate interlock behaviors due to modifications in crack kinematics [58,66].

The push-off samples were tested in a universal testing machine with a 600 kN capacity under monotonic displacement-controlled loading, set at 0.5 mm/min. As shown in Figure 2-16, a Linear Potentiometer Sensor (LPS) and a Displacement and Strain Transducer (DST) were attached to the front and back of each sample prior to testing. Some Strain Gauges (SGs) were also placed on the transverse reinforcement. In this way, LPSs and DSTs provided directly the slip and crack opening across the shear plane, respectively, while SGs measure the strain on the φ8 closed stirrups. To ensure axial load application and minimize involuntary bending due to specimen irregularities, a hinge connection was placed at the top of the actuator. Additionally, two steel plates were placed at the specimen top and bottom to limit the force application area to 150×120 mm^2, this solution was needed to limit the bending solicitation on the specimen extremities, otherwise these portions might work as cantilever beams.

The shear stress τ was calculated as the applied compressive force divided by the nominal area of the shear friction transfer plane of 210×150 mm^2 according to Equation 2-7:

$$\tau = \frac{P}{A_c} \qquad 2\text{-}7$$

where P is the measured load, and A_c is the shear plane area, i.e. 31,500 mm^2 in this case.

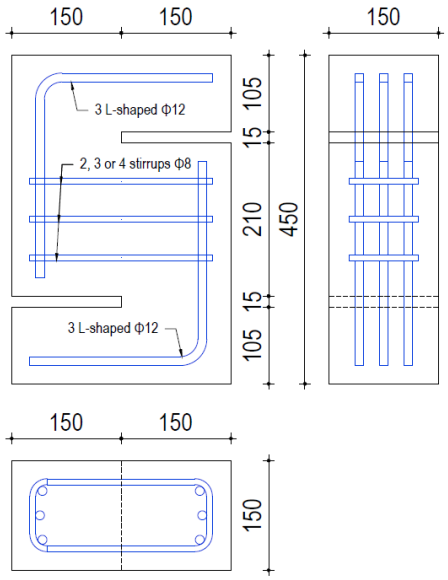

Figure 2-15. Geometry and reinforcement details of push-off specimens.

Table 2-12. Steel bars mechanical properties.

	φ8 mm	***φ12 mm***
Yield Strength (MPa)	558	523
Ultimate Strength (MPa)	607	615
Ultimate Strain (%)	4.96	11.14

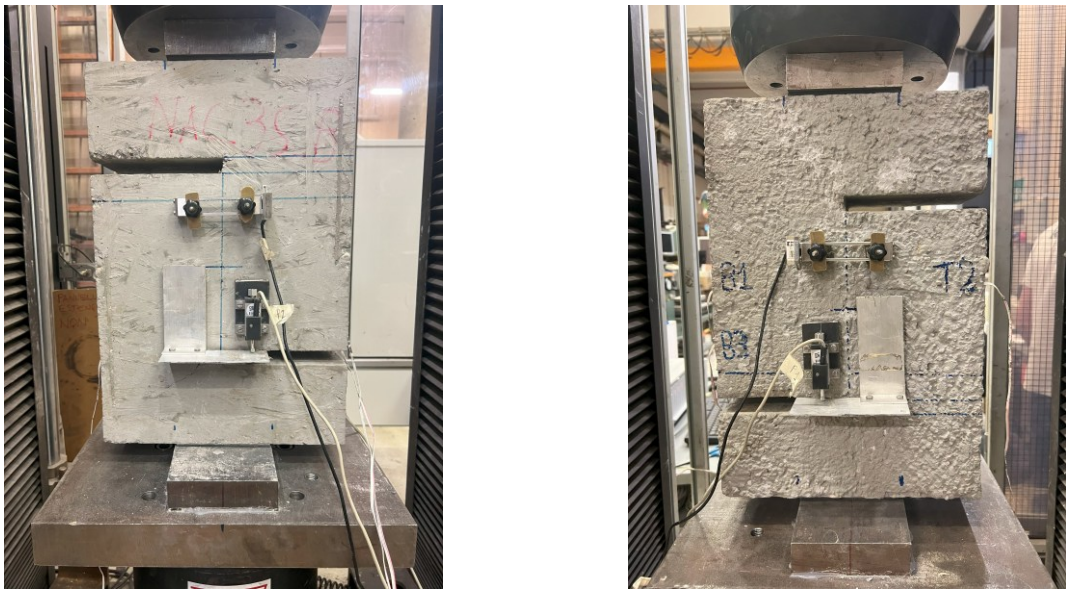

a) *b)*

Figure 2-16. Push-off test setup: a) front; b) back.

2.3.3.2 Results

2.3.3.2.1 Fresh properties and mechanical characterization

Table 2-13 presents the fresh and hardened concrete properties including Abram's cone slump, average fresh density (d_{fc}), hardened density (d_c), compressive strength at 14 ($f_{c,14}$) and 28 days of curing (f_c), splitting strength (f_{ct}) and Young's modulus (E_c) at 28 days.

A workability loss was observed for EAFC compared to the conventional counterparts. Such a behavior is typical for concrete containing EAFS, as experimentally proven by previous works [80].

About mechanical properties, results confirm existing knowledge on EAFC. Compared to NAC, the EAFC exhibited compressive strength increases of approximately 30% and 31% after 14 and 28 days of curing, respectively. Additionally, Young's modulus enhanced by 19%, while splitting strength remained almost unchanged. This observation is primarily attributed to the fact that splitting tensile strength is more directly affected by the quality of the cement matrix and ITZ rather than just the compressive strength [70]. The strength improvement of EAFC over NAC has been attributed in literature to the excellent strength of EAFS aggregates due to their high iron oxide content [70], the greater bond between slag and cementitious matrix [71], and the improved ITZ quality, resulting from the accumulation of late hydration products in the ITZ [38].

Table 2-13. Fresh and hardened concrete properties.

	NAC	***EAFC***
Slump (cm)	25	19
d_{fc} (kg/m^3)	2428	2984
d_c (kg/m^3)	2371	2938
$f_{c,14}$ (MPa)	32.92	42.64
f_c (MPa)	38.58	50.56
f_{ct} (MPa)	3.28	3.18
E_c (GPa)	32.07	38.21

2.3.3.2.2 Shear strength

The average test results are outlined in Table 2-14, which shows the ultimate loads P_u, ultimate shear strengths τ_u, ultimate slips s_u and ultimate crack widths w_u measured at P_u: each homogeneous class is identified with the mixture name followed by a tag indicating the number of closed stirrups, i.e. 2S, 3S and 4S. The failure patterns for each sample class are given in Figure 2-17. As expected, shear strength improved with an increased transverse reinforcement ratio and when EAFS replaced NA. Remarkably, greater transverse reinforcement enhances confinement, leading to a higher normal force on the shear plane. Among the shear transfer mechanisms, friction and aggregate interlock are particularly influenced by normal force, increasing with higher normal stress. Concerning the enhancements observed in EAFC, these are due to several reasons already mentioned. Among them the most important to mention are: higher intrinsic strength of EAFS particles compared to NA, their rough surface and sharp shape, which leads to stronger ITZ and higher friction [22]. The failure paths of some selected samples are shown in Figure 2-17. The failure took place similarly for all samples, regardless of the mixture type and reinforcement ratio. In fact, a vertical or subvertical crack appeared in all samples at approximately 0.5-0.7 P_u. This crack

progressively expanded and, in some cases, was accompanied by the formation of additional nearby cracks. In some cases, concrete spalling also occurred, but this phenomenon was mainly observed in the post-peak phase and did not depend on either the reinforcement ratio or the aggregate type.

Then, shear strengths were normalized dividing them by $f_c^{1/2}$ and f_{ct} to obtain τ_u^* and τ_u^+, respectively. Previous studies have confirmed a strong correlation between concrete mechanical properties and shear strength [72], however, the relationship between f_c and f_{ct} may deviate from standard NAC models when dealing with non-conventional concretes. In the case of EAFC, this discrepancy appears due to the unique interaction between EAFS and the cementitious matrix, which alters interface properties, ITZ thickness, and adhesion strength [29]. Having a look at the results in Figure 2-18, both dimensionless shear stress parameters confirm the observation already made for τ_u, i.e. higher shear strength for higher ρ_t and EAFS replacement, with a more certain trend for τ_u^+.

2.3.3.2.3 Cracking strength and residual strength

The cracking shear stress τ_{cr} that started the first surface crack is detailed in Table 2-14. As already mentioned, these cracks formed along the shear transfer plane, typically appearing as vertical fractures, and led to slight softening in the shear stress-deformation response. Additionally, the ratio τ_{cr}/τ_u is given, demonstrating that this parameter is not affected by the aggregate type.

The residual stress τ_r was also determined and considered as the average stress where a significant plateau was attained, usually observed for slip values in the range between 2.5 mm and 5 mm (Table 2-14). Residual strength demonstrates rough proportionality with the ultimate strength, hence assuming typically higher value for higher ultimate strength. The ratio τ_{cr}/τ_u is specified in the last row of Table 2-14 and assumes a value in the range 0.5-0.6 for all homogeneous classes.

Table 2-14. Mean results of the push-off tests.

	NAC-2S	***NAC-3S***	***NAC-4S***	***EAFC-2S***	***EAFC-3S***	***EAFC-4S***
P_u (kN)	249.00	251.79	276.67	307.43	341.56	332.69
τ_u (MPa)	7.91	7.99	8.78	9.76	10.84	10.56
s_u (mm)	0.195	0.245	0.160	0.210	0.218	0.170
w_u (mm)	0.4470	0.3814	0.2695	0.4856	0.3387	0.3531
τ_{cr} (MPa)	5.40	5.07	5.09	5.65	6.01	6.71
τ_r (MPa)	4.36	4.13	4.45	5.01	6.30	6.16
τ_{cr}/τ_u (-)	0.684	0.635	0.58	0.579	0.554	0.635
τ_r/τ_u (-)	0.552	0.517	0.507	0.513	0.581	0.583

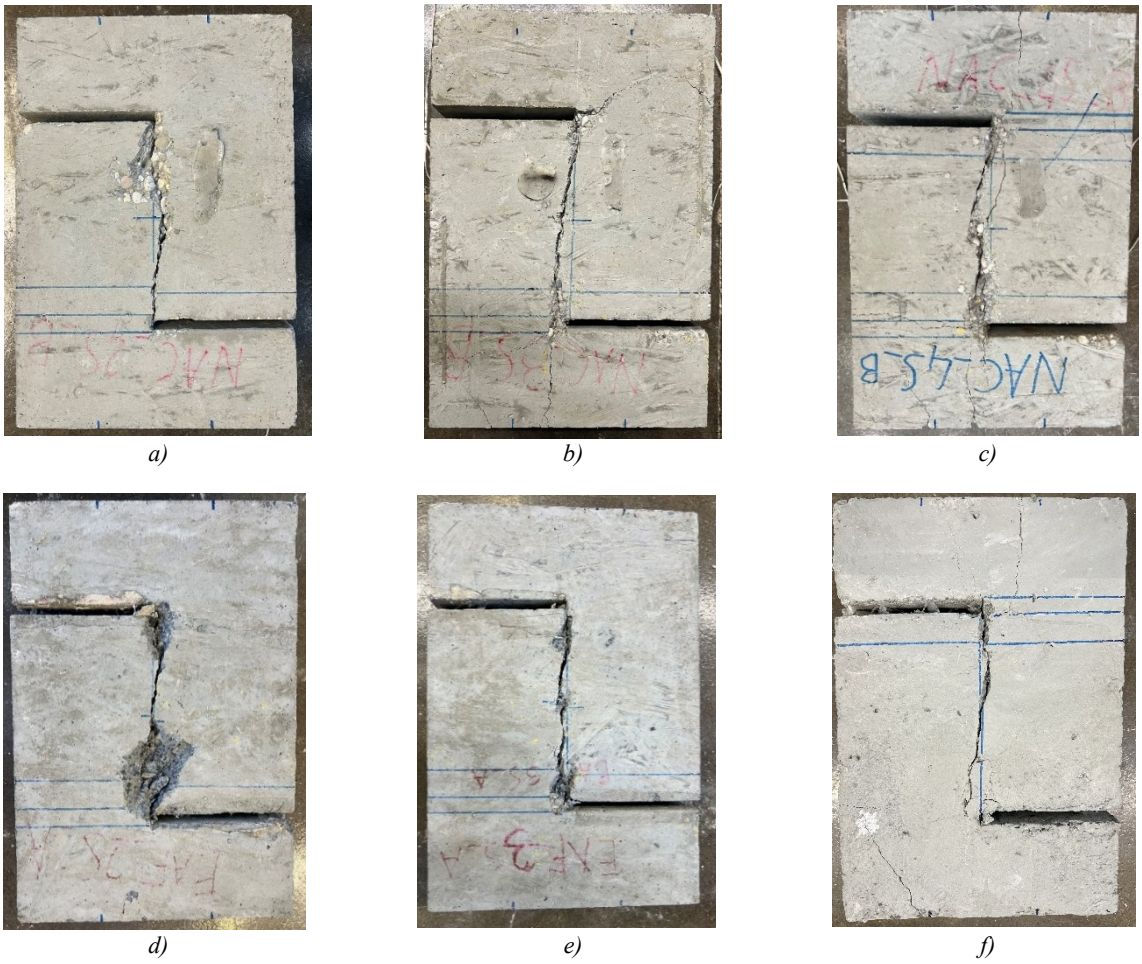

Figure 2-17. Failure patterns in selected push-off specimens: a) NAC-2S; b) NAC-3S; c) NAC-4S; d) EAFC-2S; e) EAFC-3S; f) EAFC-4S.

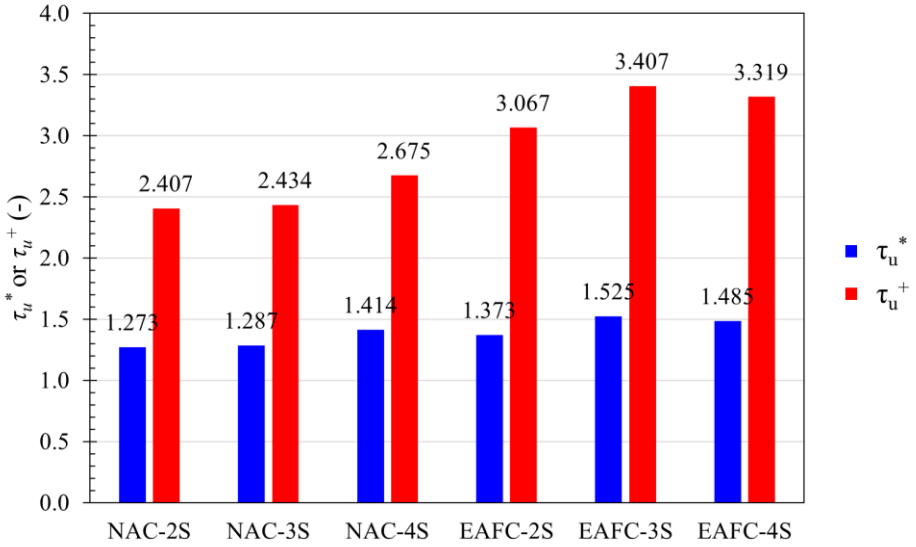

Figure 2-18. Dimensionless shear strength for NAC and EAFC. Note: $\tau_u^* = \tau_u/f_c^{1/2}$; $\tau_u^+ = \tau_u/f_{ct}$.

2.3.3.2.4 Shear stress-slip curves

A selection of the measured shear stress-slip relationships is given in Figure 2-19a, demonstrating that the development and degradation of shear friction in NAC and EAFC concrete push-off specimens follows a fundamentally similar trend. The measured relationships highlight three distinct stages of shear behavior:

1) Elastic Stage: At the beginning, the material displays linear-elastic behavior with no visible cracking along the slip plane. The ascending branch holds a nearly linear trend up to approximately 70-80% of the peak load, where shear resistance primarily depends on cohesion and, to a lesser extent, dowel action.
2) Crack Development and Friction Mobilization: As cracking starts on the slip plane, friction mobilizes due to the normal force induced by transverse reinforcement straining. At this stage, the shear stress-slip relationship becomes nonlinear, showing a more modest increase in shear resistance. The applied load then reaches a small plateau corresponding to the peak load, P_u. Beyond this stage, additional displacement leads to a change in slope, accompanied by irreversible slip and crack dilation, ultimately causing aggregate interlock breakdown. At the maximum load, the main shear transfer contributions are aggregate interlock, residual tensile stresses in fracture zone and, with a minor function, dowel action.
3) Post-Peak and Residual Phase: In the descending branch, the shear resistance stabilizes at a residual plateau, where dowel action from transverse reinforcement bridging the shear plane becomes the primary contributor to shear strength.

In previous works [58,65] and in the experimental campaign focusing on unconfined push-off specimens §2.3.2, a sharply ascending linear branch followed by a linear descending branch was detected for transversally unreinforced samples, indicating unstable crack propagation and brittle failure. In those samples, stage 3 was not noticeable due to the absence of confining pressure.

2.3.3.2.5 Shear stress-crack opening curves

Similar observations can be made for the shear stress-crack opening relationships (Figure 2-19b). However, during Phase 2 (Crack Development and Friction Mobilization), crack development was more evident, with cracks propagating faster than slips. In Phase 3 (Post-Peak and Residual Phase), the post-peak branch displayed a softer decline, with a lower slope than the slip curve, while the residual plateau was less distinct, indicating a more gradual decrease in shear resistance as crack opening augmented.

2.3.3.2.6 Stirrup strain

Figure 2-20 gives the shear stress versus the tensile strain in the clamping bars for each homogeneous class. At the beginning, all curves demonstrated a rapid increase in stress with strain, followed by a peak and subsequent softening. EAFC curves attained higher stress over a higher strain compared to NAC, which could indicate improved post-peak behavior and better resistance to shear degradation. Increasing the number of closed stirrups (2S to 4S) generally leads to improved shear stress resistance. This result is more evident for NAC specimens, but their overall performance continues to be lower than EAFC counterparts. The curves, particularly for NAC, displayed some irregularities in their paths, which might be due to experimental alterations or microcracking behavior. At lower ρ_t values, stirrups typically reach higher deformation, hence showing less brittle behavior.

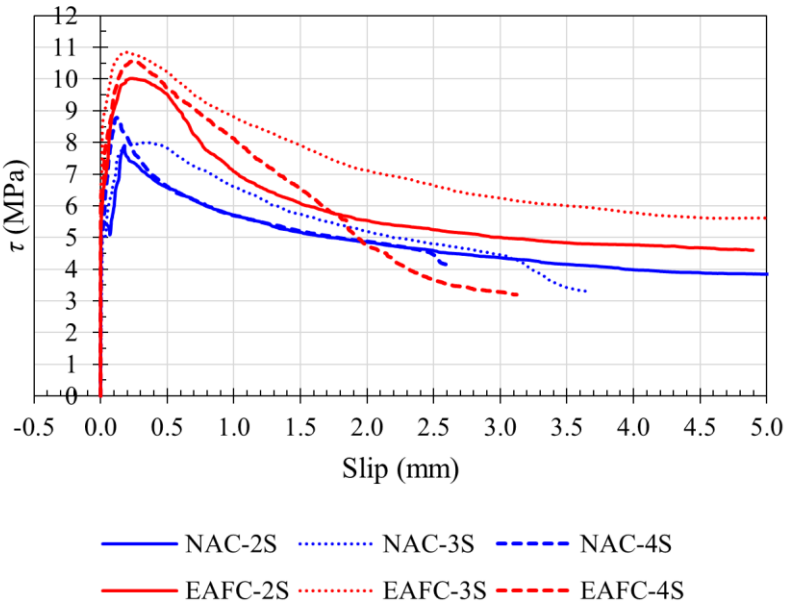

a)

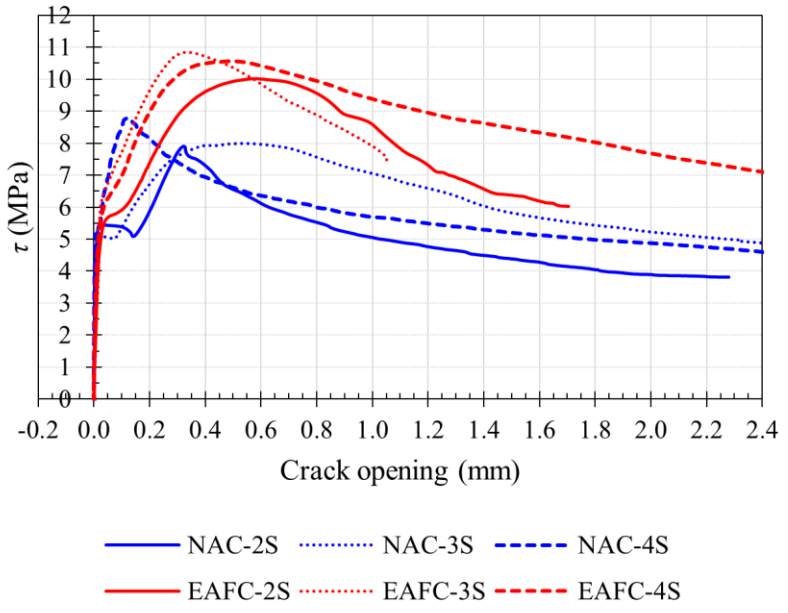

b)

Figure 2-19. Results of push-off tests: a) shear stress-slip curves; b) shear stress-crack opening curves.

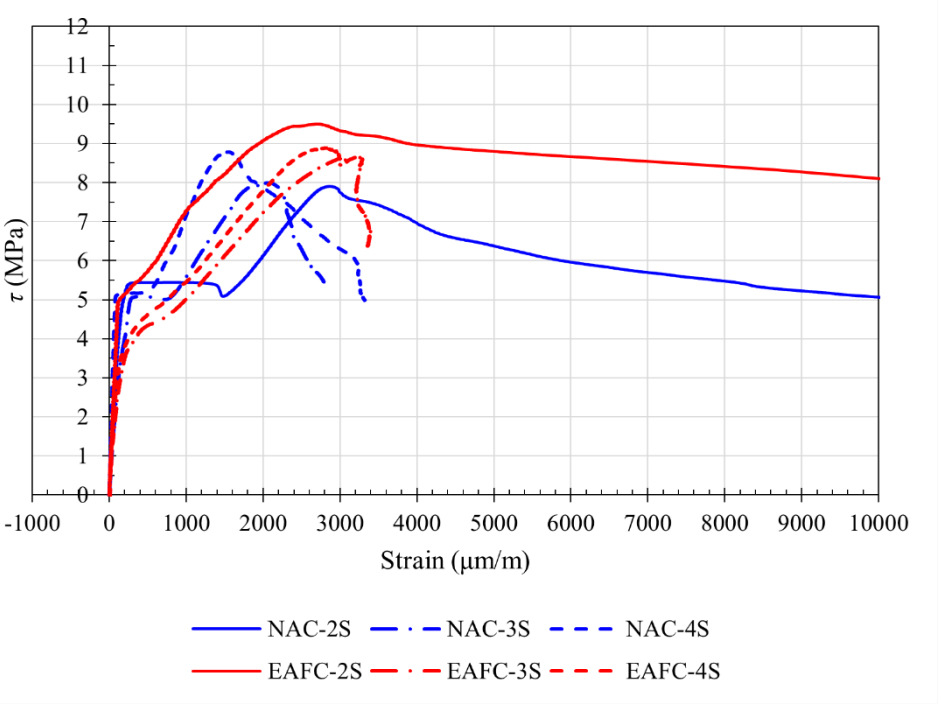

Figure 2-20. Strains in the clamping steel.

2.3.4 Discussion

In this subsection, the results obtained for the experimental campaigns presented in §2.3.2 and §2.3.3 are analyzed and discussed.

2.3.4.1 Shear transfer: effect of the transverse reinforcement ratio

Figure 2-21 displays the effect of the transverse reinforcement ratio ρ_t on shear strength, considering values of 0.64%, 0.96%, and 1.28%, which correspond to the use of 2, 3, and 4 closed stirrups with a diameter of 8 mm distributed across the shear transfer area, as explained in §2.3.3. Data for the unconfined condition ρ_t = 0% are also considered from §2.3.2. Please note that the same cement type and water-to-cement ratio were adopted, allowing for an effective comparison.

The figure clearly establishes that shear strength is significantly influenced by both the clamping force provided by transverse reinforcement and the compressive strength of the concrete. These findings are consistent with those reported by Xiao et al. [54] and Rahal and Al-Khaleefi [65], who found that increasing the amount of transverse reinforcement improves ultimate shear strength regardless of the concrete type or grade. For example, in the NAC specimens, shear strength increased by 35%, 36%, and 50% as ρ_t increased from 0% to 0.64%, 0.96%, and 1.28%, respectively.

Moreover, Figure 2-21 suggests that the cohesion component of shear resistance, approximated as the Y-intercept of the trend lines, contributes substantially to the total shear strength in reinforced specimens. In the case of NAC, this cohesion accounted for approximately 74%, 73%, and 67% of the total shear resistance for reinforcement ratios of 0.64%, 0.96%, and 1.28%, respectively.

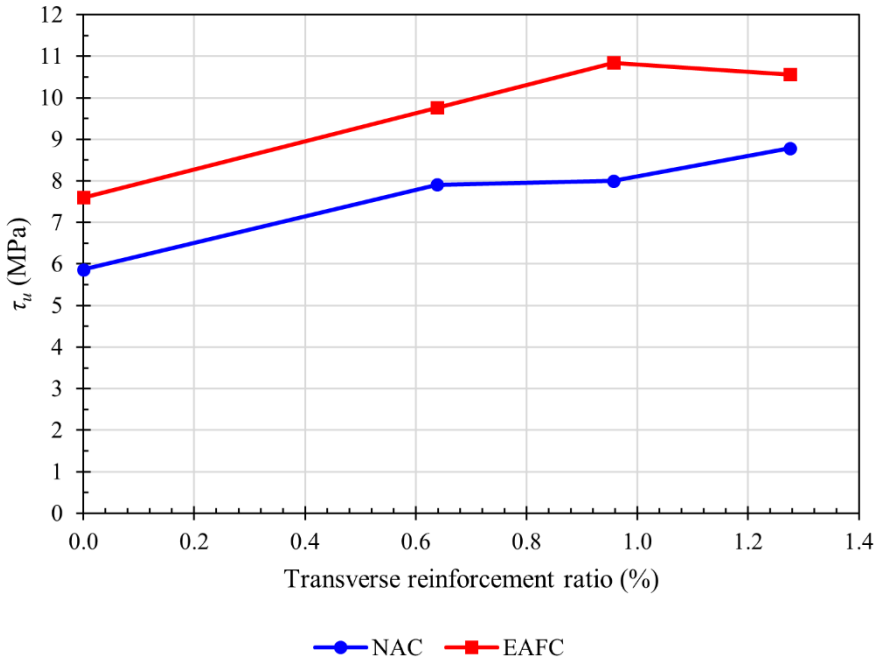

Figure 2-21. Effect of the transverse reinforcement on the ultimate shear strength.

2.3.4.2 Comparison with analytical results

2.3.4.2.1 Unconfined shear transfer

Several formulas are available in design codes and literature to estimate shear transfer strength, most of them were originally developed for evaluating concrete construction joints. These equations are usually based on the Mohr-Coulomb failure criterion. Equation 2-8 is a common expression for this:

$$\tau = c + \mu\sigma_n \qquad 2\text{-}8$$

where:

- c represents cohesion, typically expressed as a percentage of the splitting tensile strength.
- μ is the coefficient of friction along the shear plane, which depends on the interface roughness.
- σ_n is the normal stress on the shear plane, related to the level of confinement provided by transverse reinforcement crossing the interface.

For unconfined push-off samples, Equation 2-8 simplifies because no transverse reinforcement is present. As a result, the second term is removed, making τ a constant that depends just on the roughness of the surface, as defined by the considered design code or publication.

It is important to note that most formulas derived from this equation were originally developed for conventional concrete, where cracks typically propagate around aggregates rather than through them. In this subsection some recommended values for c and μ are considered from design codes for reinforced concrete and literature. The selected formulas are presented hereafter and considered consistent for unconfined push-off samples when presented in the Mohr-Coulomb failure criterion form (allowing to isolate the cohesion) and coefficients are available for monolithic concrete, which is the case experienced for the experimental campaign presented in §2.3.2.

The ACI 318-11 [81] shear-friction strength is given by Equation 2-9:

$$\tau_{u,ACI11} = c + 0.8\rho_t f_{yt} \leq \begin{bmatrix} 0.2f_c \\ 3.3 + 0.08f_c \\ 11\ MPa \end{bmatrix} \quad 2\text{-}9$$

Where f_{yt} is the yield stress of the transverse reinforcement, ρ_t is the transverse reinforcement ratio, and μ is the friction coefficient assuming values depending on the surface conditions:

- Normalweight concrete: c= 2.8 MPa;
- Lightweight concrete: c= 1.4 MPa;
- Sand-lightweight concrete: c= 1.7 MPa.

The AASHTO LRFD [82] nominal shear strength is displayed in Equation 2-10:

$$\tau_{u,AASHTO} = c + \mu\rho_t f_{yt} \leq \begin{bmatrix} 0.25f_c \\ 10.3\ MPa \end{bmatrix} \quad 2\text{-}10$$

Where the cohesion coefficient c and μ depend on the surface condition:

- Monolithic concrete: c= 2.8 MPa, μ= 1.4;
- Roughened hardened concrete: c= 1.7 MPa, μ= 1.0.

Sagaseta and Vollum [83] carried out a linear regression on the results of push-off tests to calculate the best fit for Equation 2-8. At the end of the study, they proposed the following coefficients depending on the aggregate type:

- Gravel: c= 0.57 $f_{ctk,0.05}$, μ= 1.06;
- Limestone: c= 0.91 $f_{ctk,0.05}$, μ= 0.91.

Where $f_{ctk,0.05}$ is calculated as for Equation 2-11:

$$f_{ctk,0.05} = \begin{cases} 0.2\ {f_{ck}}^{2/3} & for\ \leq C50/60 \\ 1.5\ln\left(1 + (f_{cm}/10)\right) & for\ > C50/60 \end{cases} \quad 2\text{-}11$$

Where f_{ck} and f_{cm} are the characteristic and average compressive strength respectively.

Table 2-15 presents a comparison between the experimentally observed shear strengths τ and the predictions from three methods: the methods ACI 318-11 [81], AASHTO LRFD [82] and Sagaseta and Vollum [83]. For all samples, calculations are intended for monolithic concrete and compressive strength is considered as the average one for a more reliable comparison, as done by Sagaseta and Vollum [83]. Additionally, coefficients for normalweight concrete and gravel are considered for ACI 318-11 [81] and Sagaseta and Vollum [83], respectively. The same factors are selected for EAFC as well, since other coefficients for heavyweight aggregates like EAFS are not provided.

The results show that all models offer conservative strength estimates. Among them, the ACI 318-11 [81] and AASHTO LRFD [82] models exhibit the same prediction in this case, this is because they give the same cohesion coefficient, which is the only contribution for unconfined push-off samples. In comparison, the Sagaseta and Vollum [83] model is even more conservative than the others. The accuracy of the predictions is rough and very conservative for both NAC and EAFC, with slightly better predictions for NAC. The reason behind these inaccurate predictions probably stands in the calibration mode, in fact all these formulas were proposed for shear transfer with confining pressure in the shear transfer plane. In such a case, the part of the formulas related to the friction μ assumes values not equal to zero. Furthermore, the formulas provided by design codes are presented for design purposes, and removing the safety coefficient factors as done here might not be sufficient for reliable forecasting.

The next chapter overcomes these issues presenting comparison with predictions for confined push-off samples.

Table 2-15. Comparison between experimental and calculated ultimate shear strength for unconfined push-off samples.

	NAC	***EAFC***
τ_u (MPa)	5.86	7.60
$\tau_{u,ACI11}$ (MPa)	2.8	2.8
$\tau_{u,AASHTO}$ (MPa)	2.8	2.8
$\tau_{u,SAG}$ (MPa)	1.31	2.51
$\tau_u/\tau_{u,ACI11}$ (-)	0.478	0.368
$\tau_u/\tau_{u,AASHTO}$ (-)	0.478	0.368
$\tau_u/\tau_{u,SAG}$ (-)	0.224	0.330

2.3.4.2.2 Confined shear transfer

The experimental ultimate strengths at §2.3.3 are here evaluated against predictions from five models: the ACI 318-19 shear-friction model [73], the AASHTO LRFD modified shear-friction model [82], Mattock's modified shear-friction model [84], Rahal's simplified SMCS model [85] and Sagaseta and Vollum's model [83]. Additionally, the experimental residual strengths were compared with predictions from the ACI 318-19 [73], AASHTO [82], and Mattock's model [84], as well as Eurocode 2 (EC2) provisions [86].

The fundamental equations for these models are outlined below under the following assumptions: the clamping reinforcement is perpendicular to the shear transfer plane; no external forces act perpendicular to this plane; and both resistance and material reduction factors are assumed to be equal to one. Please note that, differently from the ones given in the previous subsection §2.3.4.2.1, not all equations here proposed are based on the Mohr-Coulomb failure criterion.

For the calculation of ultimate strength, the code-based models assume monolithically cast concrete. In contrast, residual strength predictions are based on surfaces that have been intentionally roughened. This assumption is supported by findings from Mattock et al. [87] and Kahn and Mitchell [88], who observed that after reaching the ultimate shear strength, non-precracked push-off specimens retained a residual strength comparable to that of precracked specimens. Rahal and Al-Khaleefi [65] also noted that precracking lowers the ultimate strength to a level between that of non-precracked specimens and the residual strength, depending on the grade of the precracking.

The ACI 318-19 [73] shear-friction strength is chosen in this case rather than the older version ACI 318-11 [81]. The equation proposed in ACI 318-19 [73] is given by Equation 2-12:

$$\tau_{ACI19} = \mu\rho_t f_{yt} \leq \begin{bmatrix} 0.2f_c \\ 3.3 + 0.08f_c \\ 11\ MPa \end{bmatrix} \qquad 2\text{-}12$$

Where f_{yt} is the yield stress of the transverse reinforcement, and μ is the friction coefficient, taken as 1.4 for monolithically cast concrete, 1.0 for concrete cast against roughened hardened concrete. For the specimens in this study, μ=1.4 and μ=1.0 are used for ultimate strength and residual strength calculation, respectively. In the previous subsection §2.3.4.2.1 the older version of this model was chosen because a term related to the cohesion was present (Equation 2-9), but in the newer version (Equation 2-12) it was removed.

The AASHTO LRFD [82] nominal shear strength is displayed in Equation 2-10.

For monolithic concrete and roughened hardened interfaces, Mattock's modified shear-friction model [84] provides Equation 2-13:

$$\tau_{MAT} = \begin{bmatrix} 2.25\rho_t f_{yt} & for\ \ \rho_t f_{yt} \leq K_1/1.45 \\ K_1 + 0.8\rho_t f_{yt} & for\ \ \rho_t f_{yt} > K_1/1.45 \end{bmatrix} \qquad 2\text{-}13$$

Which can assume maximum values of 0.3 f_c and 16.5 MPa. The factor K_1 is taken as 0.1 f_c, but not exceeding 5.5 MPa, for monolithic concrete and 2.8 MPa for roughened surfaces. For unroughened hardened concrete, Mattock's model aligns with the ACI 318-19 [73] provisions.

The nominal shear strength in Rahal's simplified model for combined stress-resultants (SMCS) [85] is given by Equation 2-14:

$$\frac{\tau_{SMCS}}{f_c} = \sqrt{\omega_l \times \omega_t} \leq k \qquad 2\text{-}14$$

Where reinforcement indexes are $\omega_l = \rho_l f_{yl}/f_c \leq k$ and $\omega_t = \rho_t f_{yt}/f_c \leq k$, and the upper limit k is defined as $\frac{1}{3} - \frac{f_c\,[MPa]}{900}$. In push-off specimens [85], ω_l is considered as k.

The Sagaseta and Vollum's model [83] is presented in the previous subsection §2.3.4.2.1. In this model, cohesion c and friction μ are proposed to be applied in Equation 2-8. As for the subsection §2.3.4.2.1, coefficients for gravel are considered.

Eurocode 2 (EC2) [86] provides shear transfer estimates for interfaces between concretes cast at different times. The general strength equation is Equation 2-15:

$$\tau_{EC2} = c_{v1}\sqrt{f_{ck}} + \mu\rho_t f_{yt} \leq 0.3 f_{cd} \qquad 2\text{-}15$$

Where f_{ck} and f_{cd} are the characteristic and design compressive strength, which are here considered equal to the mean compressive strength for a more reliable comparison with the experimental results. The factors c_{v1} and μ depend on the roughness of the interface, in this case they are assumed equal to 0.19 and 0.9 as for very rough surfaces, respectively, considering that this method is applied just for residual strength prediction. No coefficients for monolithic surfaces are provided.

The ACI 318-19 [73], AASHTO LRFD [82], Mattock's model [84], SMCS model [85] and Sagaseta and Vollum's model [83] are developed for monolithic concrete structures, where the critical shear transfer plane is assumed to remain uncracked. These models are adopted to estimate the ultimate strength of all tested specimens. In contrast, the EC2 [86] equation is intended for interfaces between concrete cast at different times and is therefore unsuitable for directly predicting ultimate strength in monolithic specimens.

Table 2-16 presents the calculated strengths based on these five models, along with the corresponding ratios of experimentally observed to predicted values. The results show that most models provide conservative strength estimates. Among them, the AASHTO LRFD [82] and Mattock's model [84] exhibit the best overall agreement with the experimental results. In comparison, the ACI 318-19 [73] model is notably more conservative than the others. Sagaseta and Vollum's model [83] coefficients provide good estimations as well for higher transverse reinforcement ratio. The accuracy of the predictions is roughly the same for NAC and EAFC, with no significant differences observed between the two concrete types.

Table 2-16. Comparison between experimental and calculated ultimate shear strength for confined push-off samples.

	NAC-2S	***NAC-3S***	***NAC-4S***	***EAFC-2S***	***EAFC-3S***	***EAFC-4S***
τ_u (MPa)	7.91	7.99	8.78	9.76	10.84	10.56
$\tau_{u,ACI19}$ (MPa)	5.00	6.39	6.39	5.00	7.34	7.34
$\tau_{u,AASHTO}$ (MPa)	7.8	9.65	9.65	7.8	10.3	10.3
$\tau_{u,MAT}$ (MPa)	8.04	8.14	9.57	7.91	9.34	10.77
$\tau_{u,SMCS}$ (MPa)	6.33	11.21	11.21	7.07	8.66	14.01
$\tau_{u,SAG}$ (MPa)	5.09	6.98	8.87	5.33	7.22	9.11
$\tau_u/\tau_{u,ACI19}$ (-)	1.58	1.251	1.375	1.952	1.476	1.438
$\tau_u/\tau_{u,AASHTO}$ (-)	1.013	0.828	0.91	1.251	1.052	1.025
$\tau_u/\tau_{u,MAT}$ (-)	0.983	0.981	0.917	1.233	1.16	0.981
$\tau_u/\tau_{u,SMCS}$ (-)	1.249	0.713	0.783	1.38	1.251	0.754
$\tau_u/\tau_{u,SAG}$ (-)	1.554	1.145	0.990	1.831	1.501	1.159

Table 2-17 compares the experimentally measured residual strengths with predictions from four methods: ACI 318-19 [73], AASHTO LRFD [82], Mattock's model [84], and Eurocode 2 (EC2) [86]. For all specimens, the ACI 318-19 [73], AASHTO LRFD [82], and Mattock's model [84] are adopted with equations intended for intentionally roughened surfaces, while the EC2 [86] method is applied with the "very rough" surface coefficient. As demonstrated in first part of Table 2-17, the ACI 318-19 [73] model commonly yields conservative predictions. Nevertheless, it tends to slightly overestimate residual strength when assuming a rough surface at higher reinforcement ratios. This can be explained by the fact that high-strength concrete typically develops smoother shear crack interfaces [72]. Overall, the ACI 318-19 [73] and EC2 [86] models demonstrate the closest agreement with the experimental results, as reflected in the first part of Table 2-17. Both the AASHTO LRFD [82] and Mattock's [84] models tend to overpredict residual strength for the tested concretes. Rahal et al. [72] suggested that these predictions could be improved by excluding the cohesion term, since push-off specimens without transverse reinforcement tend to fail once the ultimate strength is reached and do not retain significant residual strength [65,89]. Hence, this correction is proposed for AASHTO LRFD [82] and Mattock's [84] models in the second part of Table 2-17. Please note that removing the cohesion term in the AASHTO LRFD [82] method, the resulting equation corresponds to the one proposed by ACI 318-19 [73]. The correction through removal of the cohesion term gives an overall closer prediction, however results remain quite overestimated for low transverse reinforcement ratio. Thus, this correction should be adopted in AASHTO LRFD [82] and Mattock's [84] models for residual strength predictions to get more reliable results.

Table 2-17. Comparison between experimental and calculated residual shear strength for confined push-off samples.

	NAC-2S	***NAC-3S***	***NAC-4S***	***EAFC-2S***	***EAFC-3S***	***EAFC-4S***
τ_r (MPa)	4.36	4.13	4.45	5.01	6.30	6.16
$\tau_{r,ACI}$ (MPa)	3.57	5.36	6.39	3.57	5.36	7.14
$\tau_{r,AASHTO}$ (MPa)	5.27	7.06	8.84	5.27	7.06	8.84
$\tau_{r,MAT}$ (MPa)	5.66	7.09	8.51	5.66	7.09	8.51
$\tau_{r,EC2}$ (MPa)	4.39	6.00	7.61	4.57	6.17	7.78
$\tau_r/\tau_{r,ACI}$ (-)	1.221	0.771	0.698	1.403	1.177	0.862
$\tau_r/\tau_{r,AASHTO}$ (-)	0.827	0.585	0.504	0.95	0.893	0.697
$\tau_r/\tau_{r,MAT}$ (-)	0.771	0.583	0.523	0.886	0.89	0.724
$\tau_r/\tau_{r,EC2}$ (-)	0.992	0.688	0.586	1.097	1.021	0.792
	Predictions without the cohesion term					
$\tau_{r,AASHTO}$ (MPa)	3.57	5.36	7.14	3.57	5.36	7.14
$\tau_{r,MAT}$ (MPa)	2.86	4.29	5.71	2.86	4.29	5.71
$\tau_r/\tau_{r,AASHTO}$ (-)	1.221	0.771	0.623	1.403	1.175	0.863
$\tau_r/\tau_{r,MAT}$ (-)	1.524	0.963	0.779	1.752	1.469	1.079

2.3.5 Conclusions

This section experimentally investigated the influence of Electric Arc Furnace Slag (EAFS) as a recycled coarse aggregate on the mechanical properties and shear strength of plain concrete. Shear transfer mechanisms were assessed through push-off tests, providing new insights into this relatively unexplored area. A novelty of this research stands on the combined use of EAFS and fly ash-blended cement, resulting in a workable concrete mix with promising mechanical performance.

The main conclusions regarding the shear strength of EAFS concrete (EAFC) are summarized as follows:

- EAFC exhibited higher shear strength than conventional natural aggregate concrete (NAC) in push-off tests, even without the presence of transverse reinforcement or confinement. All specimens experienced a brittle failure upon reaching peak load. Although the global failure modes were similar between NAC and EAFC, differences were noted in the crack paths along the shear interfaces.
- Two distinct failure mechanisms were observed depending on the aggregate type. In EAFC, aggregate crushing was prevalent under the given cement dosage and water-to-cement ratio, indicating stronger bond and interfacial resistance. In contrast, cracks in NAC either crossed the aggregates or propagated around them. The fracture surfaces in EAFC were notably rough, featuring angular and irregular textures that eased multiple contact points and enhanced shear resistance through macro-scale aggregate interlock.
- Shear friction formulas, traditionally developed for natural aggregate concrete, were found to be quite conservative when applied to EAFC, especially when transverse reinforcement was not present. While these models aligned more closely with the NAC results, the predictions for EAFC were significantly underestimated. Thus, the safety margin provided by these models was greater for EAFC than for NAC.

2.4 AXIAL CYCLIC LOADING

2.4.1 Introduction

When conducting a structural analysis, it is essential to characterize the mechanical performance of the construction materials involved. Additionally, to accurately predict the service life of a structure, durability-related properties must also be evaluated. Understanding the behavior of construction materials under cyclic loading, i.e. alternating loading and unloading, is vital for a range of applications, such as the design of bridges, offshore systems, nuclear containment structures, and other reinforced concrete (RC) systems subjected to seismic actions. Beyond earthquakes, cyclic loading can also arise from wind, waves, and traffic.

Cyclic loads can be categorized into two types: fatigue loading, which involves many cycles of relatively low stress, and incremental loading, where fewer cycles are applied but at higher stress levels. While earlier research focused on the cyclic response of plain and reinforced concrete under these types of loading [90,91], recent years have seen a growing interest in alternative, more sustainable concretes. Among these, Recycled Aggregate Concrete (RAC) produced with Construction and Demolition Waste (C&DW) has attracted particular attention. Previous studies [92–94] examined the fatigue performance of RAC, while others [95–97] explored its behavior under incremental cyclic loading. In one of these studies, Hu et al. [95] observed similar failure modes for both RAC and natural aggregate concrete (NAC) under monotonic and cyclic loading. Though, RAC specimens exhibited more numerous and inclined post-failure surface cracks, whereas NAC samples typically failed with a single, near-vertical crack. Interestingly, the authors noted that partial replacement of natural aggregates (NAs) with recycled aggregates (RAs) may be more detrimental than full replacement. González-Fonteboa et al. [98,99] further analyzed damage evolution in RAC, finding that the critical stress, i.e. the stress level at which concrete begins to expand volumetrically instead of contracting, decreases with increasing RA content. For a given stress level, damage intensity rose with higher RA replacement ratios, attributed to microcrack propagation. According to several authors [100,101], concrete initially contains microcracks that remain stable up to 30-40% of its compressive strength. Beyond this threshold, cracks begin to propagate, especially within the interfacial transition zone. Rapid crack growth occurs once concrete starts to expand under increasing load. This transition point, marked by the minimum volumetric strain $\varepsilon_{v,min}$, corresponds to the critical stress σ_{cr} [100].

Regarding the stress-strain behavior of concrete under cyclic loading, Sinha et al. [90] introduced the uniqueness hypothesis, proposing that a set of stress-strain curves could reliably predict the response of plain concrete to arbitrary axial loading histories. Their experimental results, based on both complete and partial unloading, confirmed this concept. Shah and Winter [102], using prismatic specimens, observed a shakedown effect approaching a critical load, characterized by accelerated microcrack growth.

Karsan and Jirsa [103], testing rectangular columns under various cyclic regimes, challenged the uniqueness concept by proposing non-uniqueness: loading-unloading curves are not solely determined by stress level but also depend on the prior loading history. Bahn and Hsu [104] validated this idea using randomly generated cycles. Working on this, Palermo and Vecchio [105] developed a model consistent with the compression field theory, linking unloading and reloading curves to the monotonic envelope curve. Sima et al. [106] offered a detailed analysis of strength and stiffness degradation under repeated loads and proposed a constitutive model that accounts for crack opening and closing behavior. Similarly, Aslani et al. [107,108] developed comprehensive stress-strain models for both compressive and tensile states, incorporating independent damage parameters derived from previous studies.

The typical hysteresis loop observed in cyclic loading includes unloading and reloading paths that define a skeleton curve, connecting the peak points of each cycle. This skeleton curve generally resembles the stress-strain curve from monotonic loading. Four main points can be identified on a hysteresis loop:

- Unloading point (U) where unloading phase starts.
- Residual (R) or partial residual point (PR) where unloading stops.
- Common point (C), which is the intersection of unloading and reloading paths.
- End point (E) where the reloading branch rejoins the skeleton curve.

Many studies [103,104] have found that the unloading curve is typically concave with initially high stiffness, while the reloading path often resembles the monotonic envelope. Thus, power-type functions are often used to model the unloading phase, while reloading paths can be approximated by linear or power-type functions [95,108]. Figure 2-22 shows a typical loop recorded during a cyclic loading test.

A confirm of these observations was obtained by Hu et al. [95], who demonstrated that RAC skeleton curves closely align with those from monotonic tests, much like NAC behavior [103,104]. They applied the skeleton curve model proposed by Guo [109] and extended by Xiao et al. [110] to both RAC and NAC, achieving strong agreement with experimental data. Yang et al. [111] later confirmed the applicability of these models to RAC, suggesting that existing NAC-based models can be successfully extended to sustainable alternatives.

According to the best knowledge of the authors, there were no published works on EAFS concrete subject to uniaxial cyclic loading at the beginning of the Ph.D. program. Thus, this chapter aims to address this research gap by presenting experimental results from five distinct concrete mixtures, which vary in aggregate type and curing duration. Specifically, the analysis includes specimens cured under standard conditions for 28 days (one NAC and one EAFS concrete) as well as long-term specimens, i.e. cylinders cured for six years, comprising a NAC, an EAFS concrete, and a mix incorporating barite aggregates.

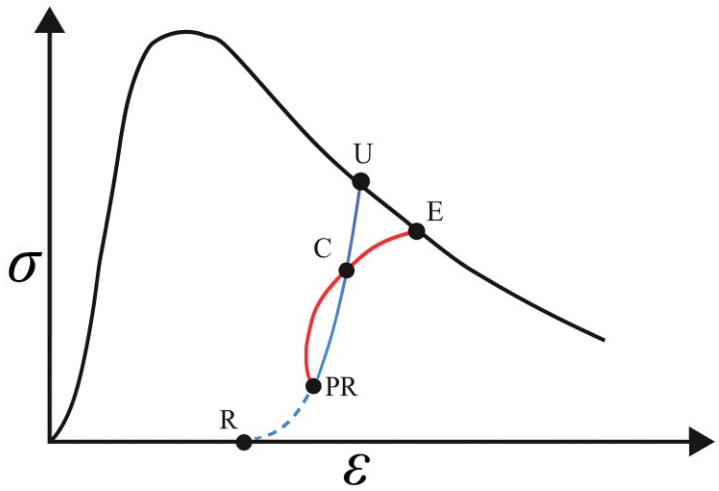

Figure 2-22. A hysteresis loop for concrete under cyclic loading and its characteristic points. U: Unloading point; R: Residual point; PR: Partial residual point; C: Common point; E: End point.

2.4.2 Experimental methods

2.4.2.1 Aggregates

Table 2-18 presents the physical properties of the aggregates, including particle density and water absorption, which were determined in accordance with EN 1097-6 [20]. It is noteworthy that barite (BAR 4-14) and EAFS (EAFS 4-16) exhibit similar characteristics in terms of shape, surface texture, and density (Table 2-18). The particle size distribution curves for the aggregates used in this experimental study are displayed in Figure 2-23.

Table 2-18. Physical properties of the aggregates.

Aggregate type	Shape	Particle density (kg/dm^3)	Water absorption (%)
NA 0-4	Roundish	2.644	2.71
NA 4-16	Roundish	2.690	1.37
EAFS 4-16	Sharp	3.808	0.91
BAR 4-14	Sharp	3.817	1.90

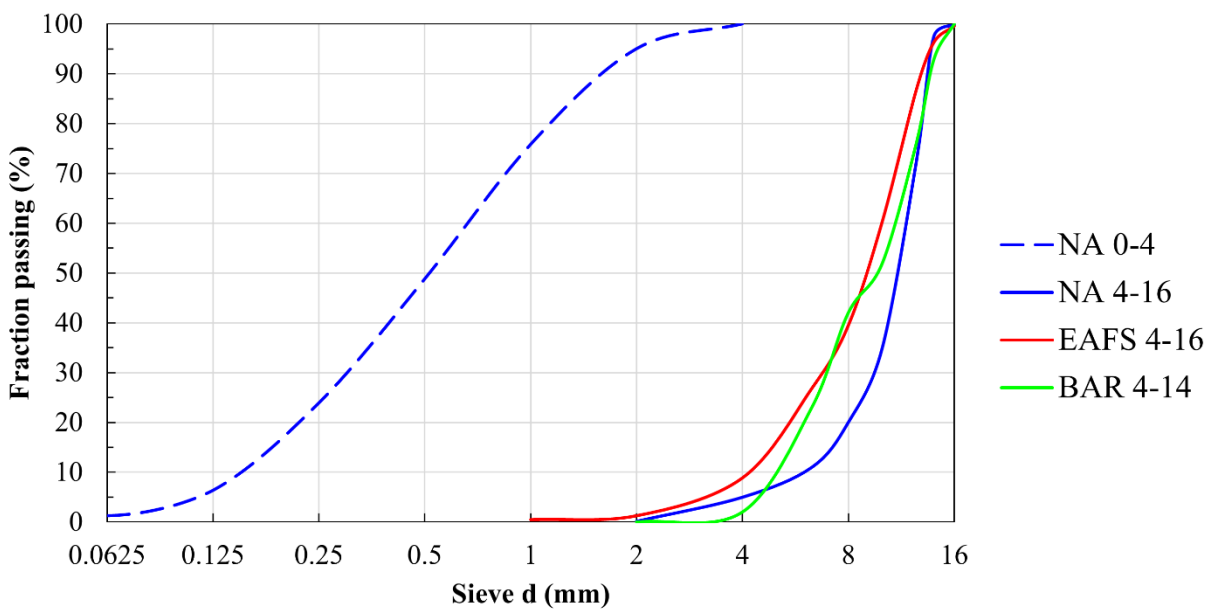

Figure 2-23. Grading curves of the aggregates.

2.4.2.2 Mix design and preparation of the samples

Five concrete mixtures were investigated: NAC1, EAF1, NAC2, EAF2 and BAR. The mixtures can be grouped in two sets, according to the mix details shown in Table 2-19. The first set aims to investigate the cyclic behavior of concrete in the short term, i.e. after 28 days, in addition to the main mechanical properties. This group of concretes is made of a conventional (NAC1) and an EAFC mix (EAF1), and there a cement type CEM IV/A (V) 42.5 R was used, according to EN 197-1 [19], with water-to-cement ratio equal to 0.5. This binder, currently very used in the Italian market context, contains about 30% of fly ash (FA) replacing clinker, allowing to limit the environmental footprint compared to the concretes belonging to the second group.

Instead, the second set purpose is investigating the cyclic behavior of concrete in the long term, i.e. after six years since casting, other than the main mechanical properties, which were evaluated at 28 days. This group is made again by a conventional (NAC2), an EAFS concrete (EAF2), and additionally one with barite aggregates (BAR). These mixes were prepared using a Portland cement CEM I 52.5 R, according to EN 197-1 [19] with a reduced water dosage, resulting in a W/C ratio equal to 0.4. At the age of these concretes casting, CEM IV/A (V) 42.5 R was instead not very common, and for laboratory practices, Portland cement was very often adopted as done in the present case. The choice of investigating barite concrete had the aim to produce a heavyweight concrete with similar density to that made with EAFS. This comparison is particularly interesting considering the applications of heavyweight concrete as shielding against radiation in the eventuality of exposing them to cyclic loading, as in nuclear plants. Indeed, Pomaro et al. [112] established that the shielding properties of EAFS concretes are similar or even higher than those measured for barite concrete.

In both sets, the EAFS concrete was produced using EAFS as 100% of the coarse aggregate fraction, while the fine aggregate portion remained consistent with that of the natural aggregate concrete (NAC), using natural sand. All concrete mixtures included a sulphonated naphthalene-based water-reducing admixture (WRA) to ensure adequate workability. It is generally observed, as supported by previous studies [53], that slag-based concretes require a higher WRA dosage due to the reduced workability associated with EAFS. Tap water from the municipal supply of Padova (Italy), which is free from harmful substances, was used in all mixes.

Table 2-19. Concrete mix details (kg for 1 m^3).

	NAC1	***EAF1***	***NAC2***	***EAF2***	***BAR***
Cement dosage	400	400	400	400	400
Cement type	IV/A (V) 42.5 R	IV/A (V) 42.5 R	I 52.5 R	I 52.5 R	I 52.5 R
W/C ratio	0.5	0.5	0.4	0.4	0.4
Water	200	200	160	160	160
NA 0-4	863	863	913	966	897
NA 4-16	1027	-	971	-	-
EAFS 4-16	-	1424	-	1270	-
BAR 4-14	-	-	-	-	1371
Superplasticizer	3.2	4.8	3.2	4.0	4.0

2.4.2.3 Experimental plan and mechanical characterization

For each mixture, a series of cylinders with dimensions d×h = 100×200 mm was cast to evaluate the compressive strength f_c, the indirect tensile strength f_{ct} and the overall cyclic compressive behavior.

Compressive f_c and tensile strength f_{ct} were tested according to EN 12390-3 [77] and EN 12390-6 [78], respectively, under force control at a speed rate of 0.5 MPa/s and 0.05 MPa/s, respectively.

2.4.2.4 Cyclic loading

Concerning the cyclic loading protocol, there are no specific standards that can be considered, hence the adopted setup is based on EN 12390-3 [77] with some modifications. First, samples were equipped with four strain gauges (SGs): two were placed transversally, and the others longitudinally (Figure 2-24). Figure 2-25 shows instead the applied loading history: it consists of several alternate cycles of loading and unloading. The first part was performed under a force-control mode, at a speed of about 0.1 MPa/s. After a brief stabilization phase, three stress levels were applied, being 0.1, 0.3 and 0.5f_c, with two loading cycles per applied stress level. In the second part, the load was increased under a displacement-control mode at speed 0.3 mm/min, with single loading cycles, increasing the displacement of +0.3 mm per cycle. Between each loading and unloading cycles, and vice versa, there was a 10 second stabilization phase. The load application stopped after reaching the peak load as no post-peak branch was visible for any sample. As stated, two curing times were chosen for the cyclic compressive strength: 28 days strength f_{cc} and a prolonged time, here selected as six years strength $f_{cc,6y}$. Table 2-20 shows the test matrix of this experimental campaign, i.e. the number and type of tests performed per each mixture.

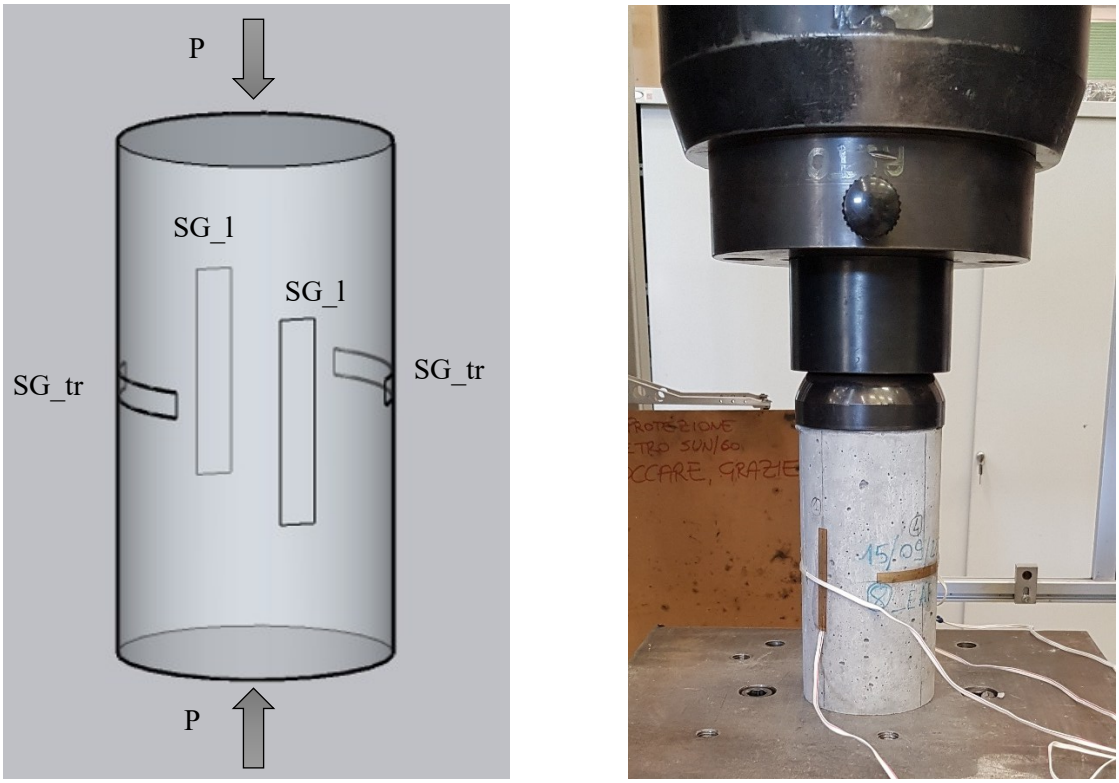

a) *b)*

Figure 2-24. Test setup of the cyclic compression test: a) scheme; b) photo. SG_l: Longitudinally-placed strain gauge; SG_tr: Transversally-placed strain gauge.

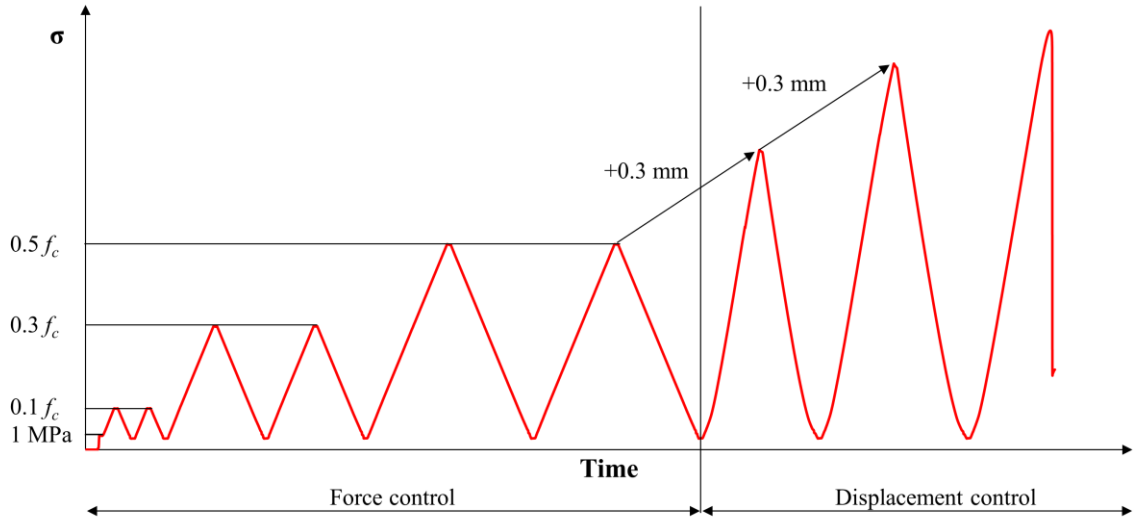

Figure 2-25. Loading protocol of the cyclic test.

Table 2-20. Test matrix of this experimental campaign.

	NAC1	***EAF1***	***NAC2***	***EAF2***	***BAR***
Fresh density ρ_{fc}	3	3	3	3	3
Hardened density at 28 days ρ_c	3	3	3	3	3
Compressive strength at 28 days f_c	3	3	3	3	3
Splitting strength at 28 days f_{ct}	3	3	3	3	3
Cyclic compressive strength at 28 days f_{cc}	2	2	-	-	-
Cyclic compressive strength at 6 years $f_{cc,6y}$	-	-	2	2	2

2.4.3 Results

2.4.3.1 Mechanical characterization

Table 2-21 lists the fresh and hardened concrete properties in terms of: Abram's cone slump according to EN 12350-2 [113], fresh density ρ_{fc}, hardened density ρ_c at 28 days of curing, compressive strength f_c and tensile strength f_{ct} at 28 days of curing.

The workability of the mixtures was slightly reduced when EAFS was used as aggregate, primarily due to the shape-related effects of EAFS particles [37]. A similar reduction in workability was also observed in the mixture containing barite aggregates. To offset this effect, a higher superplasticizer dosage was adopted in concretes incorporating EAFS. According to EN 206 [68], mixtures NAC1, EAF1, and BAR fall within the S3 consistency class (100-150 mm slump), while the remaining mixtures are classified as S4 (160-210 mm).

Both fresh and hardened densities were higher in the EAFS and barite concretes compared to the NAC mixtures, reflecting the greater particle density of these aggregates. Specifically, density increased by

approximately 15% in the EAFS mix and 20% in the barite mix. The differences between fresh and hardened densities were negligible for all batches, a result attributed to effective curing that minimizes water loss.

Concerning mechanical performance, experimental results confirm the beneficial effects of replacing natural aggregates (NAs) with EAFS. In the first series of mixtures, compressive and splitting tensile strengths increased by approximately 37% and 28%, respectively, compared to the reference NAC. A similar trend was observed in the second series, where the EAF2 mix exhibited compressive strengths 41% and 46% higher than those of the NAC and barite concretes, respectively. These improvements are likely due to several advantageous characteristics of EAFS, including strong bond with the cement matrix [22], intrinsic higher aggregate strength [29], and the improved quality of the Interfacial Transition Zone (ITZ) [38].

Conversely, replacing NAs with barite aggregates was not beneficial from a mechanical perspective: although density increased, there was no corresponding gain in strength, making the substitution less favorable if mechanical performance is prioritized.

Comparing the two sets of mixtures, it is noteworthy that concrete produced with CEM IV/A 42.5 R exhibited similar strength to that made with CEM I 52.5 R. This outcome is particularly significant considering the less successful results reported by other studies using alternative cement types, such as CEM IV/B [114]. These findings suggest that the interaction between EAFS and pozzolanic cement necessitates further investigation.

Another important observation concerns the relationship between compressive and splitting strength. Despite the higher compressive strength of the second series, it displayed lower tensile strength than the first. Though, it should be noted that the relationship between these two properties is nonlinear [115]. While tensile strength generally increases with compressive strength, it does so at a slower rate and is also influenced by factors such as the W/C ratio, cement type, and curing conditions. In particular, the composition of the cementitious matrix (including cement, fillers, and supplementary cementitious materials) plays a crucial role. For instance, partial replacement of clinker with pozzolanic materials, e.g. fly ash or silica fume, may enhance tensile strength more significantly than compressive strength when used in moderate amounts (up to 10%) [116]. In this study, the first series was made using pozzolanic cement containing fly ash, while the second series employed ordinary Portland cement. This difference likely explains the lower tensile strength in the second series, despite its higher compressive strength. Additionally, greater variability was observed in the splitting tensile strength results of the second series, which should be considered in further analysis.

Table 2-21. Mean fresh and hardened properties.

	NAC1	***EAF1***	***NAC2***	***EAF2***	***BAR***
Slump (cm)	12	10	19	21	15
Fresh density ρ_{fc} (kg/m^3)	2407	2824	2390	2817	2884
Hardened density at 28 days ρ_c (kg/m^3)	2431	2828	2404	2830	2828
Compressive strength at 28 days f_c (MPa)	38.96	53.34	41.24	58.00	39.70
Splitting strength at 28 days f_{ct} (MPa)	3.56	4.56	3.32	4.24	3.36

2.4.3.2 Cyclic loading behavior

2.4.3.2.1 First set of concretes: short-term cyclic tests

Figure 2-26 presents the complete stress-strain curves for the first set of concrete mixtures conducted at 28 days of curing. Strain measurements are reported such that positive values indicate expansion and negative values indicate contraction. Hence, the strain data from transversely oriented strain gauges appear on the right side of the graph, while those from longitudinal strain gauges are shown on the left.

Table 2-22 summarizes average results obtained from the short-term cyclic tests: the cyclic compressive strength f_{cc}, the ultimate longitudinal strain $\varepsilon_{l,u}$, and the ultimate transverse strain $\varepsilon_{tr,u}$. Notably, the cyclic compressive strength f_{cc} closely matches the values obtained under monotonic loading f_c, indicating that the cyclic loading history does not significantly affect this parameter. This observation is consistent with findings from previous studies [95,106].

All specimens exhibited brittle failure immediately when reaching the peak load. On average, the EAF1 concrete samples demonstrated a higher peak longitudinal strain (+31%) and a slightly lower peak transverse strain (-4%) compared to the NAC specimens, suggesting enhanced ductility in the axial direction and slightly reduced lateral expansion at failure.

The skeleton curves shown in Figure 2-27 were derived from the cyclic stress-strain data by connecting the peak points of each loading cycle, using the average longitudinal strain recorded by the two strain gauges. These curves closely resemble those obtained under monotonic loading conditions, as noted by Hu et al. [95].

Table 2-22. Results of cyclic loading tests.

	NAC1	***EAF1***	***NAC2***	***EAF2***	***BAR***
Cyclic compressive strength at 28 days f_{cc} (MPa)	38.12	52.53	-	-	-
Cyclic compressive strength at 6 years $f_{cc,6y}$ (MPa)	-	-	59.02	76.00	63.10
Ultimate longitudinal strain $\varepsilon_{l,u}$ (με)	-1992	-2620	-1599	-1870	-2451
Ultimate transversal strain $\varepsilon_{tr,u}$ (με)	1345	1297	1075	914	1460
Minimum volumetric strain $\varepsilon_{v,min}$ (με)	-622	-828	-523	-574	-835
Critical stress σ_{crit} (MPa)	33.04	49.70	49.54	64.01	52.94
Dimensionless critical stress σ_{crit}/f_{cc} (-)	0.867	0.947	0.840	0.845	0.825

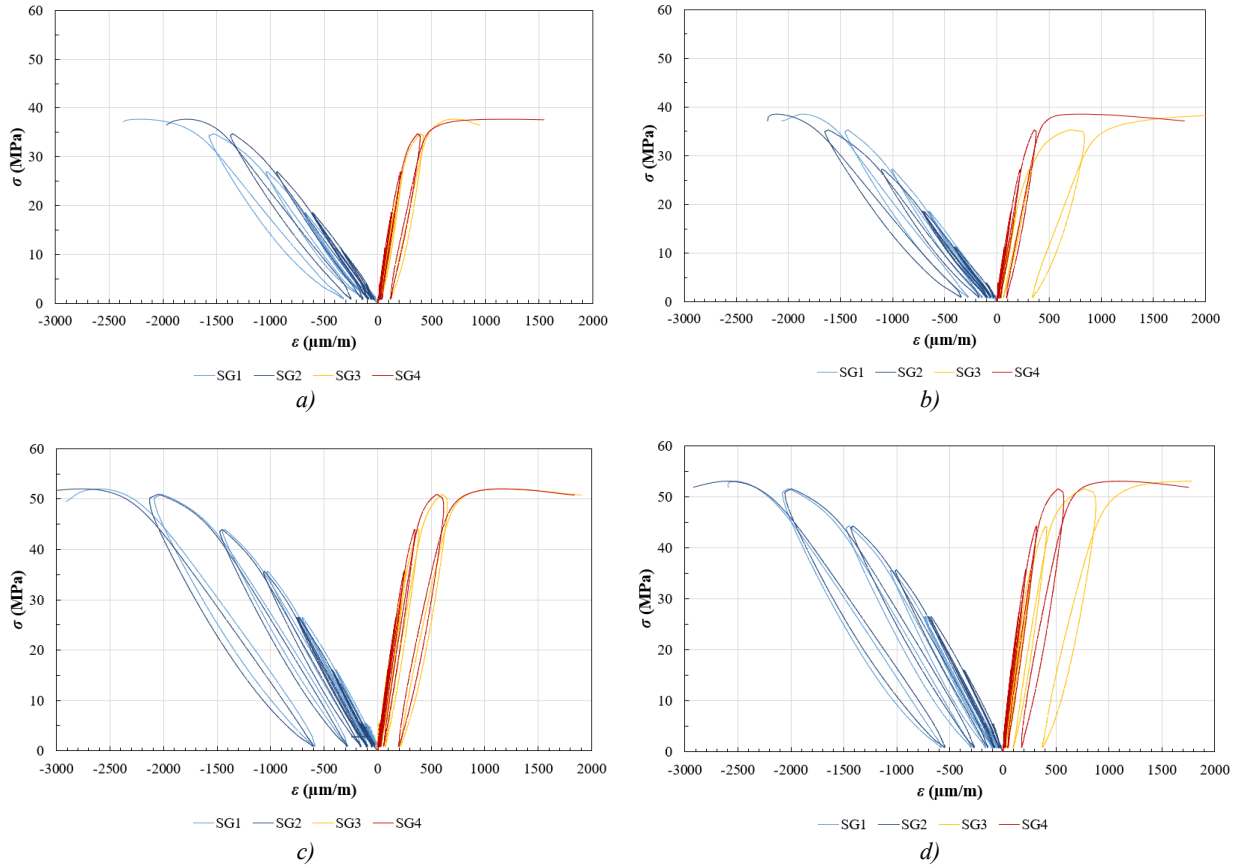

Figure 2-26. Results of short-term cyclic compression tests: a-b) NAC1; c-d) EAF1. SG1 and SG2 stand for longitudinal SGs, SG3 and SG4 stand for transversal SGs.

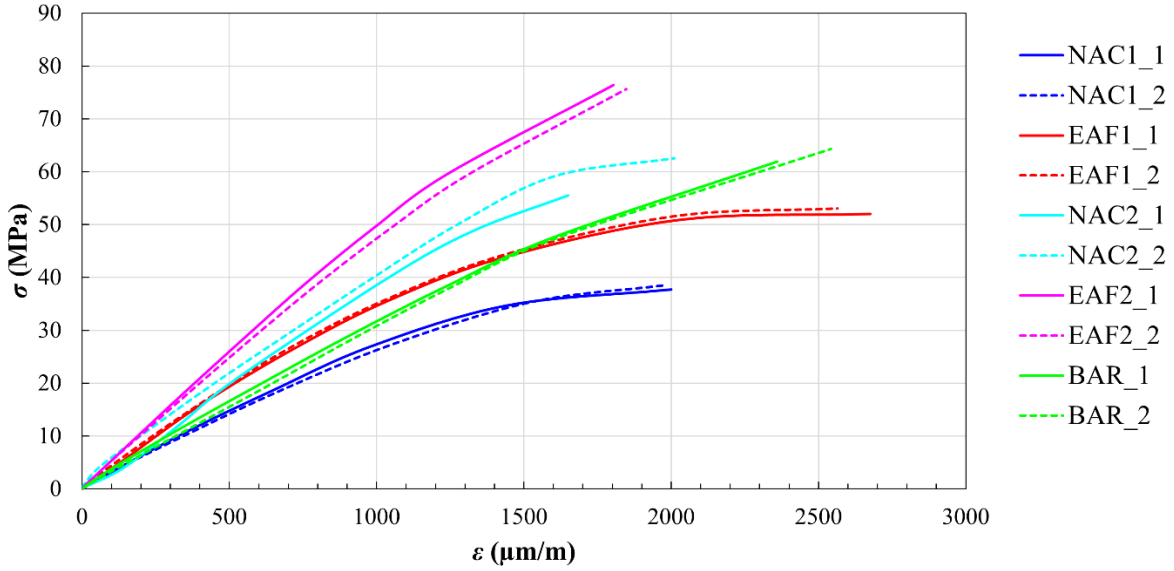

Figure 2-27. Skeleton curves for cyclic compression tests.

A comparison between the skeleton curves of the different concrete types reveals that the EAF1 concrete exhibits a slightly steeper initial slope compared to NAC1. However, as the stress approaches its peak, the slope decreases for both mixtures and becomes similar. As outlined in [95,117,118], the secant modulus E at various stress levels can be analytically determined from the skeleton curves using Equation 2-16:

$$E = \frac{\sigma_2 - \sigma_1}{\varepsilon_{l2} - 0.005\%} \quad 2\text{-}16$$

Where σ_1 represents the stress corresponding to a longitudinal strain of 0.005%, while σ_2 is the stress associated with a given longitudinal strain ε_{l2}. Using these values, the secant modulus E was calculated at various stress levels and is graphically presented in Figure 2-28a.

For the short-term cyclic tests, EAF1 concrete exhibits a significantly higher secant modulus at lower stress levels. Specifically, at 0.4 f_c, the average E reaches 38.289 GPa for EAF1, compared to 28.142 GPa for NAC1. However, at peak load, the difference in secant modulus between the two mixtures tightens considerably, with only an 877 MPa difference. These findings highlight the importance of thoroughly characterizing the full stress-strain response to capture differences in mechanical performance across the complete loading range.

Regarding the transverse behavior of concrete, the Poisson's ratio v is typically evaluated at 0.4 f_c in accordance with Eurocode 2 (EC2) [86]. Therefore, Equation 2-17 is applied to determine v, following the approach used in [86,117]:

$$\nu = \frac{\varepsilon_{tr2} - \varepsilon_{tr1}}{\varepsilon_{l2} - 0.005\%} \quad 2\text{-}17$$

where ε_{tr2} is the transverse strain at a given stress level, ε_{l2} is the corresponding longitudinal strain, and ε_{tr1} is the transverse strain corresponding to a longitudinal strain of 0.005%. As with the secant modulus E, Poisson's coefficient was evaluated at multiple stress levels to gain deeper insight into the deformational response of the concretes.

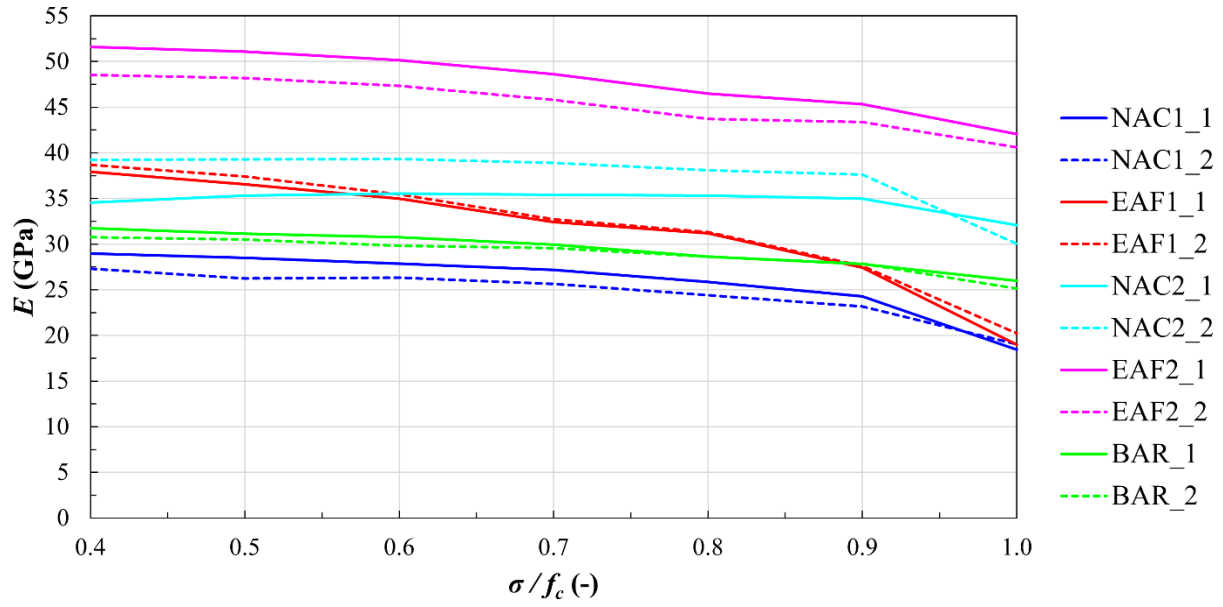

a)

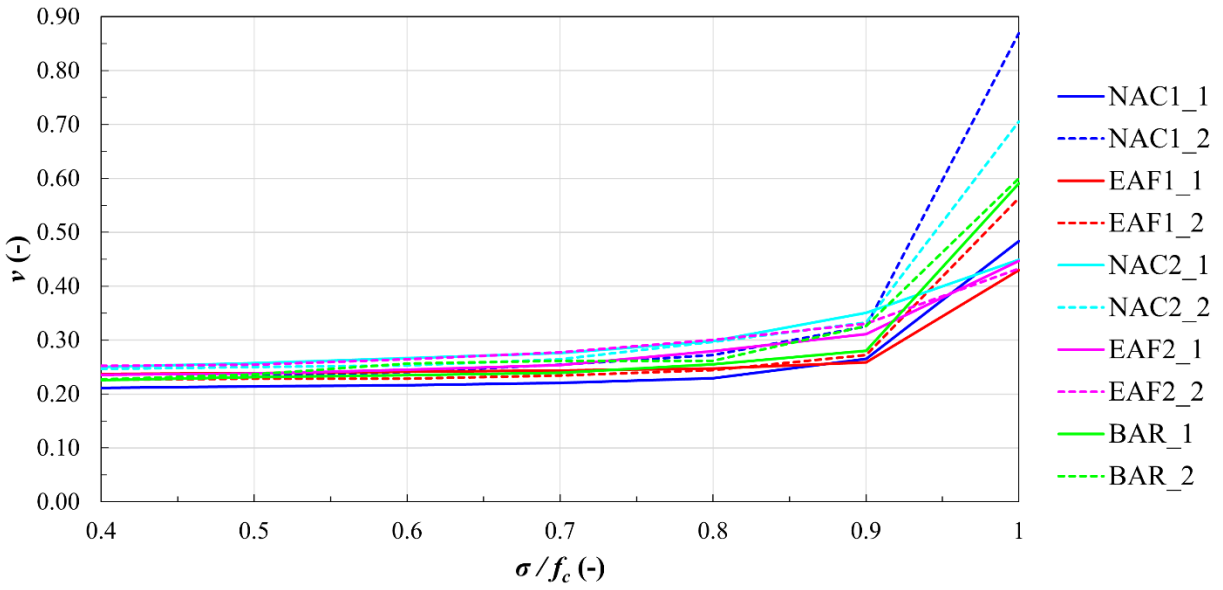

b)

Figure 2-28. Deformative properties of tested specimens under cyclic compression: a) Secant Modulus; b) Poisson's coefficient.

At 0.4 f_c, EAF1 concrete exhibits a Poisson's ratio approximately 6% higher than that of NAC1 (Figure 2-28b), although for all tested specimens, ν remains within the typical range of 0.20-0.30 up to 0.8 f_c. Beyond this point, NAC1 displays significantly greater transverse deformation: at peak load, the average maximum ν reaches 0.676 for NAC1 compared to 0.496 for EAF1. However, it is important to note that the scatter in Poisson's ratio values increases distinctly at higher stress levels (between 0.8 fc and f_c), which reduces the reliability of the data in this range.

Figure 2-29 illustrates the evolution of longitudinal, transverse, and volumetric strains versus the dimensionless stress level (σ/f_{cc}) for each specimen subjected to cyclic loading. The plotted strain values represent the average readings from the corresponding strain gauges. Additionally, skeleton curves are included by connecting the peak points of each respective strain curve. The volumetric strain ε_v is calculated using Equation 2-18:

$$\varepsilon_v = \varepsilon_l + 2\varepsilon_{tr} \qquad 2\text{-}18$$

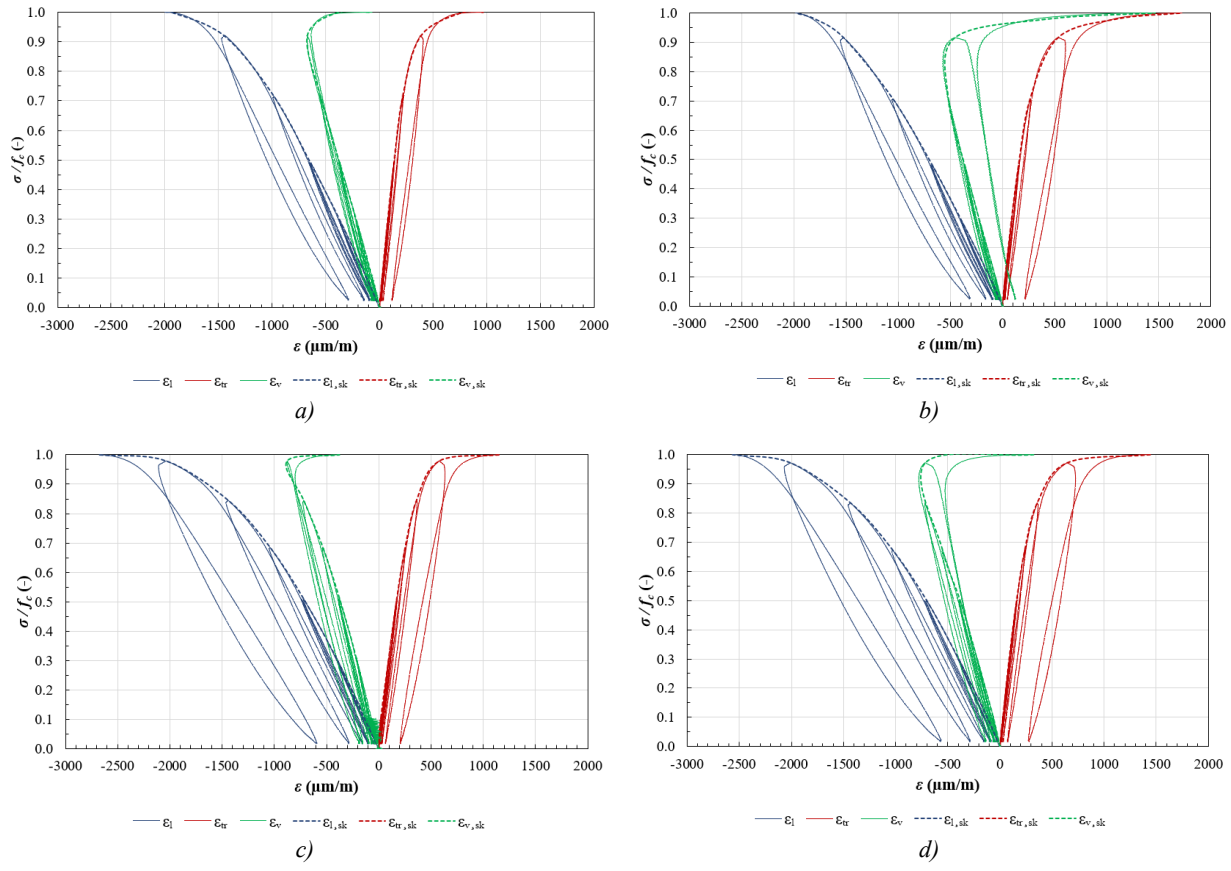

Figure 2-29. Results of short-term cyclic compression tests in terms of longitudinal, transverse, and volumetric mean strain: a-b) NAC1; c-d) EAF1. The subscript "sk" refers to the skeleton curve.

Figure 2-30a presents a summarized graphical comparison of the skeleton curves based on the average longitudinal ε_l, transverse ε_{tr}, and volumetric ε_v strains. Within this plot, the minimum volumetric strain points were identified, and their corresponding coordinates (namely $\varepsilon_{v,min}$, σ_{crit}, and the dimensionless value σ_{crit}/f_{cc}) are listed in Table 2-22. It is important to note that the critical stress σ_{crit} indicates the onset of rapid and continuous crack propagation, which occurs when the volumetric strain reaches its minimum value, as described in previous works [100,117].

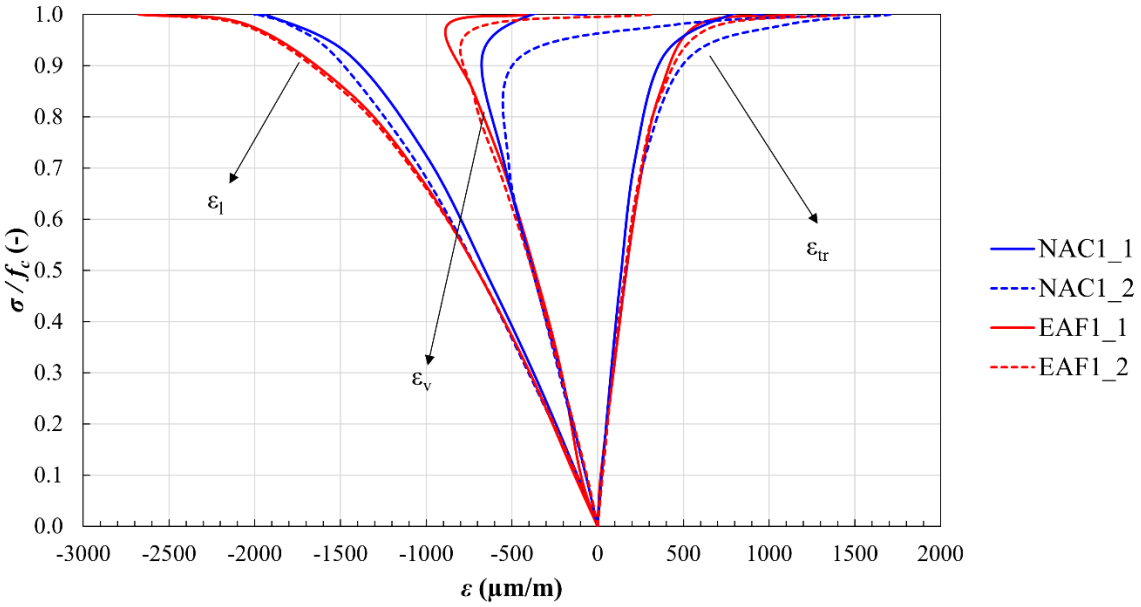

a)

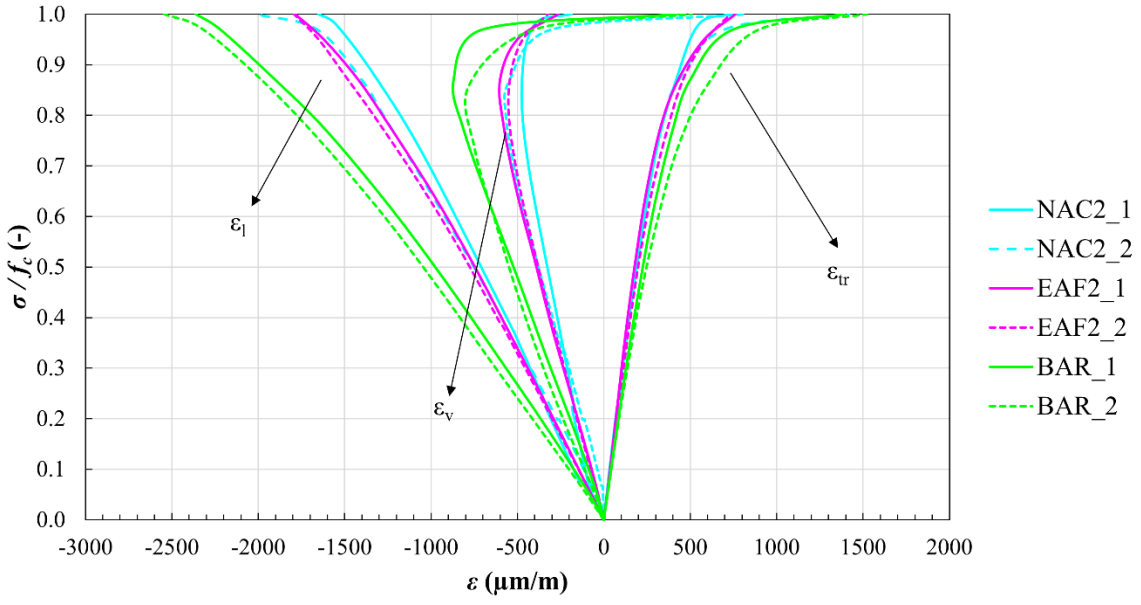

b)

Figure 2-30. Skeleton curves of longitudinal, transverse, and volumetric mean strain for cyclic tests: a) first set of mixtures; b) second set of mixtures.

EAF1 concrete exhibits higher values of both minimum volumetric strain $\varepsilon_{v,min}$ and critical stress σ_{crit}. On a microscopic level, critical stress appears to be influenced not only by the material compressive strength but also by additional factors. Particularly, the ratio σ_{crit}/f_{cc} is greater in EAFS concrete compared to NAC. EAFS concrete, characterized by a stronger Interfacial Transition Zone (ITZ), tends to initiate cracks later under compressive loading. This delay may be attributed to the improved bond between the cement matrix and the EAFS particles, facilitated by the slag features [22,38].

Conversely, NAC1 concrete shows a more substantial post-critical stress reserve compared to EAFS concrete. The relatively small difference between σ_{crit} and the peak stress in EAFS specimens highlights their more brittle behavior, which is commonly observed in high-strength concretes.

As loading proceeds, the internal structure of the concrete undergoes progressive degradation. This deterioration can be quantified by tracking changes in the secant modulus E, considered as material damage [119]. For this purpose, the dimensionless damage parameter D_E is computed using Equation 2-19:

$$D_E = 1 - \frac{E_d}{E_{ini}} \qquad 2\text{-}19$$

Where, E_d is the secant modulus at a given stress level, and E_{ini} is the initial modulus, assumed to be the value of E at $0.4\,f_c$, based on the observation that the stress-strain curve remains approximately linear up to this point. This assumption aligns with findings from Sima et al. [106], who noted that concrete under compression typically exhibits linear behavior until about half of its peak strength. Figure 2-31a displays the evolution of dimensionless damage. Focusing on the short-term test results (First set), the damage patterns within each concrete type are coherent and similar. EAFS concrete shows the most pronounced increase in damage: although the modulus E at peak stress is nearly the same for both EAF1 and NAC1, EAF1 starts from a significantly higher modulus at lower stress levels. Between $0.7\,f_c$ and $0.9\,f_c$, a noticeable inflection appears in the damage curves, i.e. likely a result of cyclic loading. This behavior diverges from the smooth progression typically seen under monotonic compression [98], suggesting that cyclic loading introduces a distinct damage evolution pathway.

An alternative method for assessing damage progression involves tracking changes in Poisson's ratio v. In this approach, damage D_v is quantified using Equation 2-20:

$$D_v = \frac{v_d}{v_{ini}} - 1 \qquad 2\text{-}20$$

Where v_d is the Poisson's coefficient at a given stress level, and v_{ini} represents its initial value, taken at $0.4\,f_c$. The resulting damage evolution, based on this definition, is shown in Figure 2-31b. Considering the short-term results, the conventional concrete (NAC) displays a higher average damage even at medium to low stress levels, indicating a greater tendency to undergo transverse deformation. As stress approaches the peak load, the damage increases sharply, especially beyond $0.9\,f_c$, due to the significant expansion in the transverse direction.

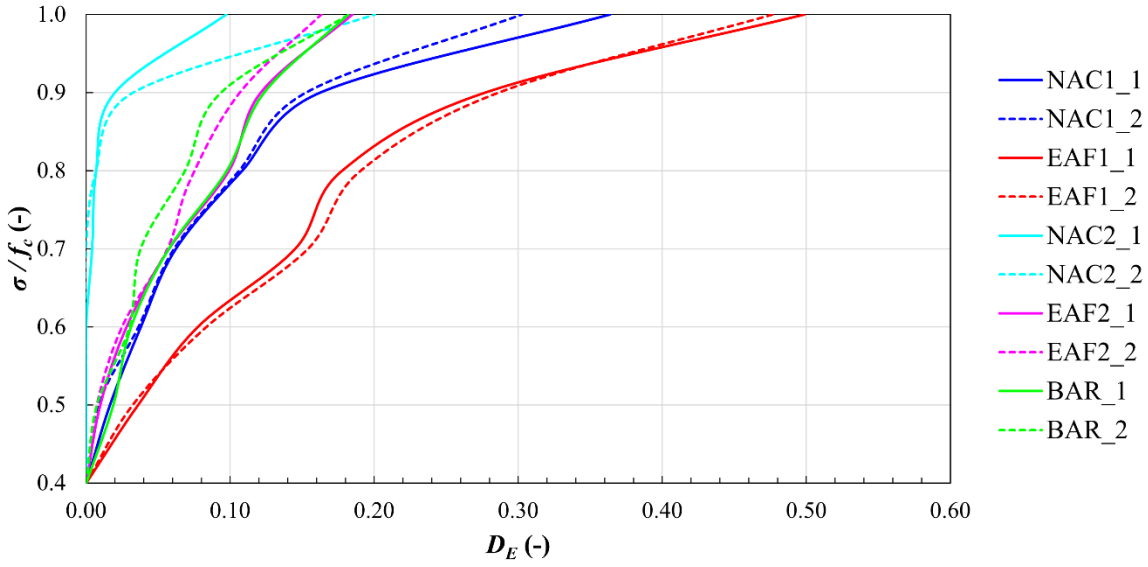

a)

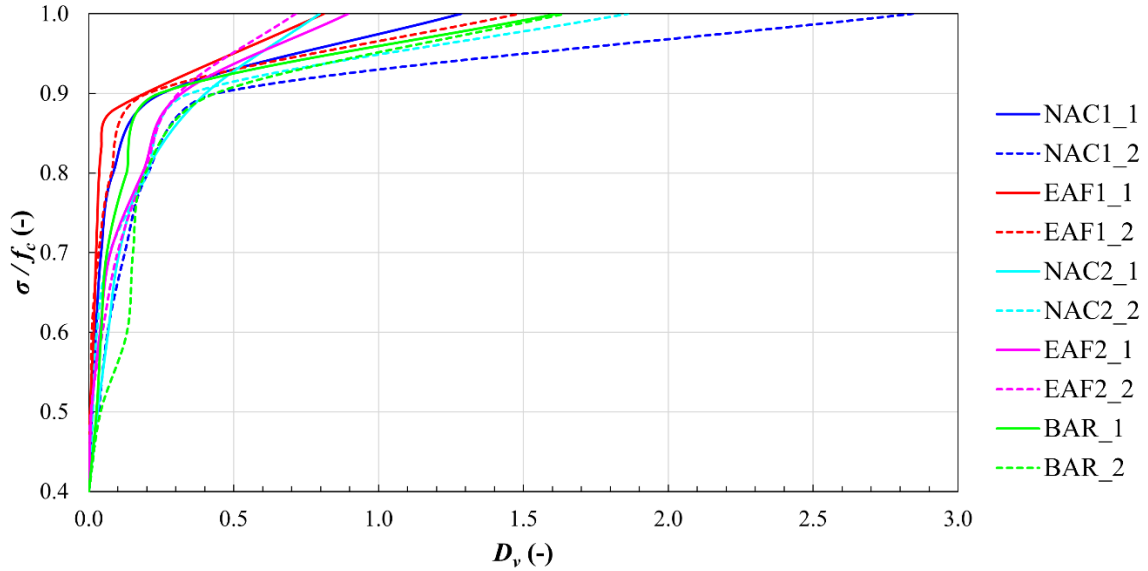

b)

Figure 2-31. Evolution of damage: a) D_E; b) D_v.

2.4.3.2.2 Second set of concretes: long-term cyclic tests and comparison

This section presents the results of cyclic tests performed on specimens cured for six years, with the aim of expanding the findings discussed earlier using a different set of samples. Table 2-22 summarizes the main outcomes, reporting the cyclic compressive strength after 6 years of curing $f_{cc,6y}$, along with the corresponding ultimate longitudinal $\varepsilon_{l,u}$ and transversal $\varepsilon_{tr,u}$ strains. Figure 2-30b illustrates the evolution of average longitudinal, transverse, and volumetric strains, calculated as described in the previous section.

Among all tested specimens, concrete containing EAFS showed the highest cyclic strength: $f_{cc,6y}$ was 29% and 20% greater than those of NAC and BAR concretes, respectively. Like high-strength concretes, EAF2 reached peak stress with minimal transverse deformation, whereas NAC2 exhibited the lowest ultimate longitudinal strain. As noted previously and supported by the literature [95], cyclic and monotonic compressive strengths are generally comparable, making these outcomes directly interpretable based on the strength differences between NAC2, BAR, and EAF2.

According to this statement, the strength gain Δ over time for the second set of mixtures can be calculated, comparing values at 28 days and after 6 years. BAR showed the greatest relative strength increase (59%) from 39.70 MPa to 63.10 MPa, while EAFS concrete exhibited the lowest (31%) raising from 58.00 MPa to 76.00 MPa. These findings align with Rondi et al. [120], who observed that EAFS-based concrete (with 100% replacement of natural aggregates) reaches its strength plateau after about 120 days of curing, with little gain afterward.

A full comparison of the secant modulus E across all specimens is shown in Figure 2-28a. Within the second group, EAF2 had the highest elastic modulus, while BAR had the lowest, a contrast more pronounced than in the first set of tests. This is consistent with the known deformability of barite concrete, attributed to the soft nature of barium sulfate and the presence of microcracks filled with powdery materials such as barite, iron oxide, and clay [121]. Furthermore, NAC2 and EAF2 demonstrated greater stiffness compared to their counterparts from the first series, directly correlated with their higher compressive strengths. The reduction in E from $0.4f_c$ to f_c was also more limited in this set: approximately -16%, -17%, and -18% for NAC2, EAF2, and BAR, respectively, compared to -33% and -51% in NAC1 and EAF1.

Poisson's ratio ν comparisons are presented in Figure 2-28b. All tested concretes maintained ν values within the 0.20-0.30 range up to $0.8f_c$. Beyond this stress level, the data became more scattered, making meaningful comparisons unreliable. However, up to $0.8f_c$, NAC2 and EAF2 generally showed higher average ν values.

Figure 2-30b illustrates the evolution of mean longitudinal, transverse, and volumetric strains, and Table 2-22 reports the coordinates of the minimum volumetric strains $\varepsilon_{v,min}$, along with the corresponding critical stress σ_{crit} and normalized ratio σ_{crit}/f_{cc}. The trends observed in short-term tests are mostly applicable here as well, with some variations. EAF2 concrete again reached higher σ_{crit} and σ_{crit}/f_{cc} values than the other mixes, though the differences were less significant, indeed σ_{crit}/f_{cc} is just 0.005 and 0.020 higher than NAC2 and BAR, respectively. These findings strengthen the conclusion that EAFS concrete achieves rapid strength development at early ages. Among all, BAR exhibited the highest volumetric strain, further reflecting its relatively soft and deformable nature. Consistent with the first test series, EAF2 displayed higher $\varepsilon_{v,min}$ values than NAC2. Particularly, the post-critical stress reservoir was generally larger in this second set of specimens, likely due to the prolonged curing period.

The influence of aggregate type on σ_{crit}/f_{cc} is well-documented. Gonzalez-Fonteboa et al. [98] reported σ_{crit}/f_{cc} values above 0.90 for limestone-based concretes at 28 days, but the ratio declined with increased use of recycled aggregates. Harder aggregates, like EAFS, allow higher critical stresses, a conclusion supported by the high σ_{crit}/f_{cc} values observed in this study. Additionally, the age of curing appears to influence this

parameter: both the present results and those from Gonzalez-Fonteboa et al. [98] show σ_{crit}/f_{cc} values exceeding 0.85 at 28 days, but below 0.85 after long-term curing. This suggests that extended curing may reduce the σ_{crit}/f_{cc} ratio, although further evidence is needed to confirm this trend.

Damage evolution, calculated as in previous sections, is shown in Figure 2-31. The damage index D_E displayed similar patterns for EAF2 and BAR, while NAC2 remained mostly undamaged until $0.9\,f_c$. Compared to short-term specimens, long-term specimens exhibited less pronounced damage progression. The curves in Figure 2-31a include several inflection points, indicating a non-linear accumulation of damage likely influenced by the cyclic loading regime, contrarily to the smoother trends observed under monotonic loading [98].

Damage based on Poisson's ratio D_v for the second group was also calculated using Equation 2-20, with results shown in Figure 2-31b. On average, NAC2 and BAR showed higher D_v values, especially near peak load. As with D_E, the curves contain noticeable inflections, again suggesting that cyclic loading induces a distinct pattern of damage development. Near peak stress, D_v values for NAC1 and EAF1 (short-term specimens) were generally higher than those for NAC2 and EAF2.

2.4.4 Analytical stress-strain models for Electric Arc Furnace Concrete under cyclic loading

2.4.4.1 Constitutive relations under cyclic loading

This section introduces an analytical model developed to predict the stress-strain (σ-ε) behavior of concrete containing EAFS under cyclic loading. While several studies have proposed constitutive models for cement-based materials subjected to cyclic or fatigue loads, including those incorporating various slags [122,123], no specific model has been formulated for EAFS-based concrete. The modeling approach adopted here is based on the methodology presented by Hu et al. [95] for Recycled Aggregate Concrete (RAC) produced with construction and demolition waste.

In this framework, the dimensionless strain x and stress y are defined according to Equations 2-21 and 2-22:

$$x = \frac{\varepsilon}{\varepsilon_u} \qquad 2\text{-}21$$

$$y = \frac{\sigma}{f_{cc}} \qquad 2\text{-}22$$

where ε_u is the ultimate strain and f_{cc} is the cyclic compressive strength.

Each hysteresis loop, as outlined in section §2.4.1 and illustrated in Figure 2-22, is characterized by four points. The cyclic behavior of concrete is typically modeled as a combination of a skeleton curve and corresponding unloading/reloading branches. As noted earlier, the skeleton curve under cyclic loading aligns well with that of monotonic loading. Therefore, this study employs the model proposed by Guo [109], later extended by Xiao et al. [110], to represent the skeleton curve for EAFC. This model is expressed by Equation 2-23:

$$y = \begin{cases} px + (3-2p)x^2 + (p-2)x^3, & 0 \le x < 1 \\ x/[q(x-1)^2 + x], & x \ge 1 \end{cases} \qquad 2\text{-}23$$

Here, p and q are empirical parameters determined through experimental calibration. In the current investigation, all specimens failed in a brittle manner at peak load, meaning the post-peak segment ($x \ge 1$) is not observed and is thus excluded from the analysis.

Figure 2-32 shows the experimental skeleton curves with those predicted using Equation 2-23. The theoretical curve shows a closer fit for NAC than for EAFS or BAR mixes. This outcome is expected, given that the original model was calibrated specifically for conventional concrete.

After establishing the skeleton curve, it is necessary to define the strain values at each characteristic point (x_u, x_r, x_c, x_e) to accurately describe the cyclic response. Prior to reaching the peak load, the unloading branch typically intersects the strain axis slightly above the origin, indicating a small residual strain. Accordingly, the residual strain x_r can be determined based on the unloading strain x_u, as expressed in Equation 2-24:

$$x_r = a x_u^b \qquad 2\text{-}24$$

where x_u is considered an input parameter, defined in advance when implementing the model.

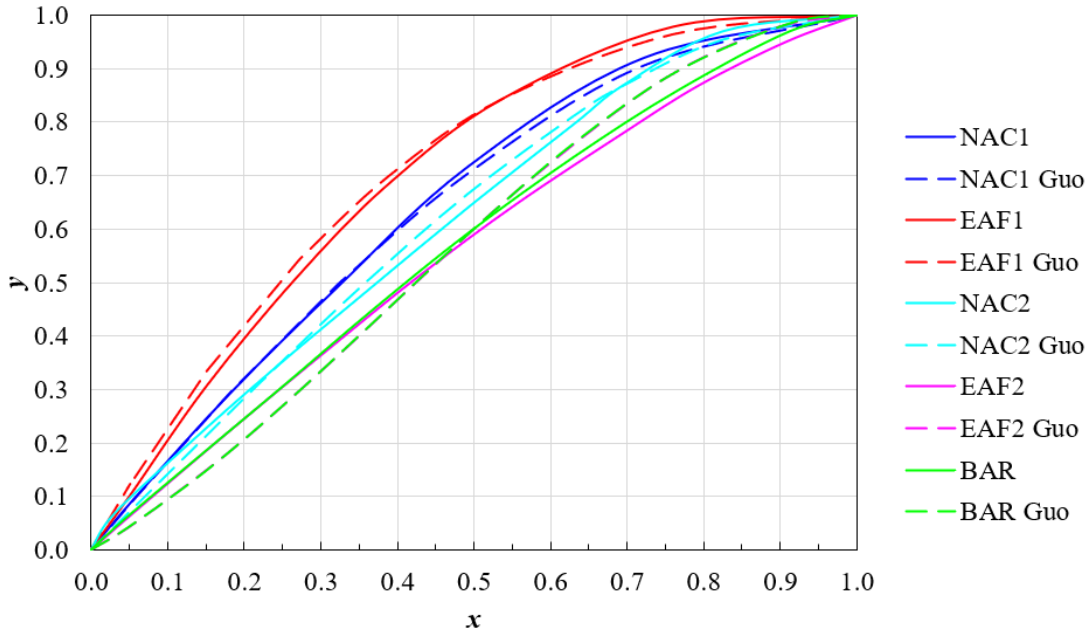

Figure 2-32. Experimental vs. calculated skeleton curves.

The intersection point between the unloading and reloading curves, commonly named common point, is defined in relation to the unloading point, as expressed in Equation 2-25:

$$x_c = cx_u + d \qquad 2\text{-}25$$

Similarly, the end point of the reloading branch is also related to the unloading point, using the same functional form as that employed for the residual strain, as shown in Equation 2-26:

$$x_e = gx_u^h \qquad 2\text{-}26$$

In Equations 2-24, 2-25, and 2-26, the coefficients *a*, *b*, *c*, *d*, *g*, and *h* represent regression parameters, which must be calibrated based on experimental data.

After identifying the characteristic points, the unloading and reloading branches of the cyclic stress-strain curve can be made. As proposed by Hu et al. [95], the unloading path is described by the expression given in Equation 2-27:

$$y = u \cdot y_u \left(\frac{x - x_r}{x_u - x_r}\right)^v \qquad 2\text{-}27$$

The reloading path is divided into two segments: the first extends from the reloading point to the common point, while the second spans from the common point to the end point. As defined in Equation 2-28, the initial segment is modeled using a power function, whereas the latter is assumed to be linear:

$$y = \begin{cases} r \cdot y_c \left(\dfrac{x - x_r}{x_u - x_r}\right)^s, & x < x_c \\ \dfrac{y_e - y_c}{x_e - x_c} \cdot (x - x_c) + y_c, & x \geq x_c \end{cases} \qquad 2\text{-}28$$

In these equations, *u*, *v*, *r*, and *s* are calibration parameters derived from experimental data.

Using the set of equations 2-23 through 2-28, it is possible to analytically define a complete stress-strain relationship for concrete under cyclic loading. A validation of this theoretical model is presented in Figure 2-33, which shows its application to a single cycle, i.e. the final loop of the experimental loading path. This loop is typically the most challenging to predict due to the accumulation of plastic deformations at high stress levels. As shown in Figure 2-33, the model yields reasonably accurate results, with a better fit

observed for the NAC1 concrete compared to EAF1. The agreement is especially strong in the initial portion of the reloading branch, while deviations become more evident beyond the common point. This discrepancy is likely due to the assumption of linearity in the latter segment of the reloading path.

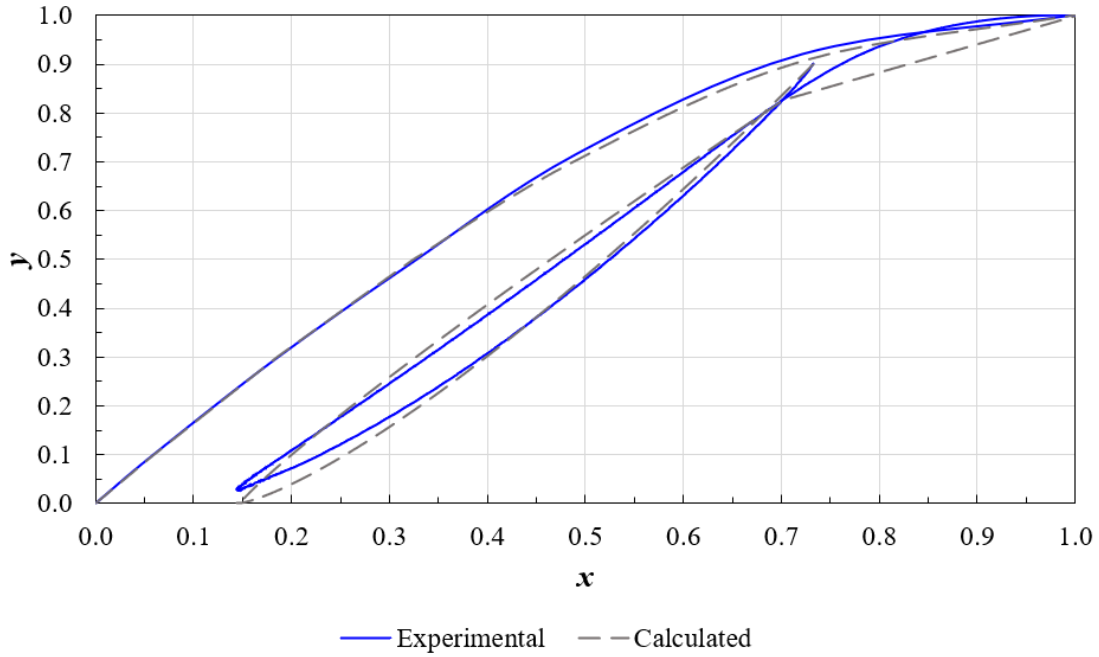

a)

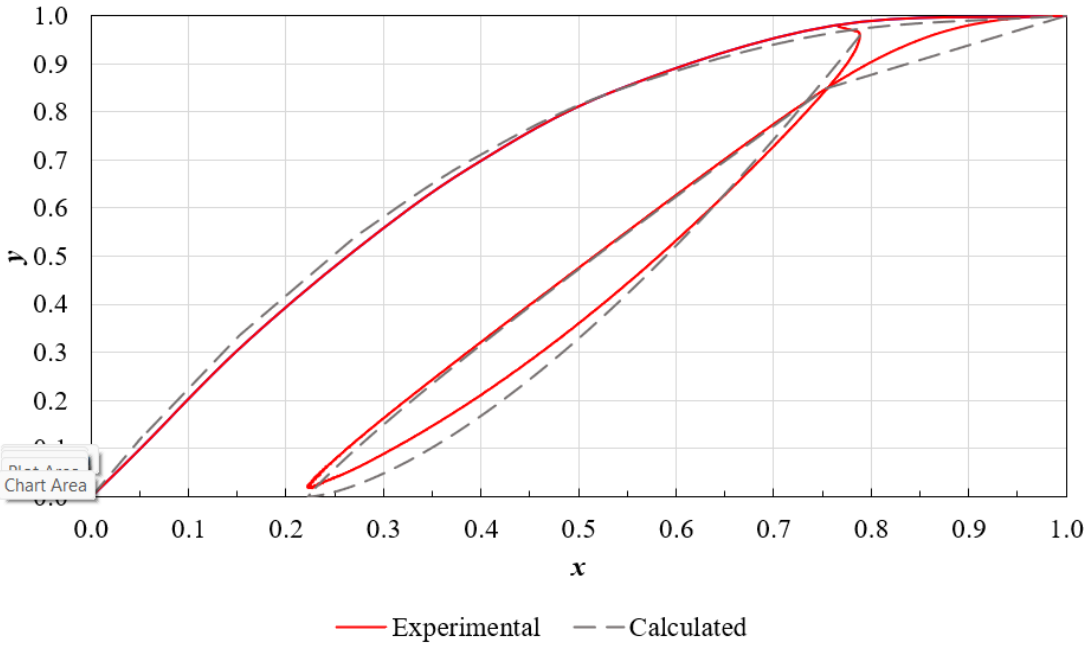

a)

Figure 2-33. Comparison between tested and calculated stress-strain relation in a loop of cyclic loading test for: a) NAC1; b) EAF1.

2.4.4.2 Simplified model

The model presented in section §2.4.4.1 for predicting the full cyclic stress-strain response of NAC and EAFS concretes shows good alignment with experimental results. However, due to its complexity, it may not always be convenient for practical engineering applications. As an alternative, a simplified method can be adopted, where both the unloading and reloading branches are assumed to be linear and overlapping, as expressed by Equation 2-29:

$$y = y_u \cdot \frac{x - x_r}{x_u - x_r} \qquad 2\text{-}29$$

To complete this approach, the skeleton curve remains defined by Equation 2-23. Figure 2-34 compares experimental data with the results from this simplified model. The comparison indicates a satisfactory level of agreement, suggesting that this simplified formulation is suitable for representing the hysteresis behavior, especially for concretes of the second set.

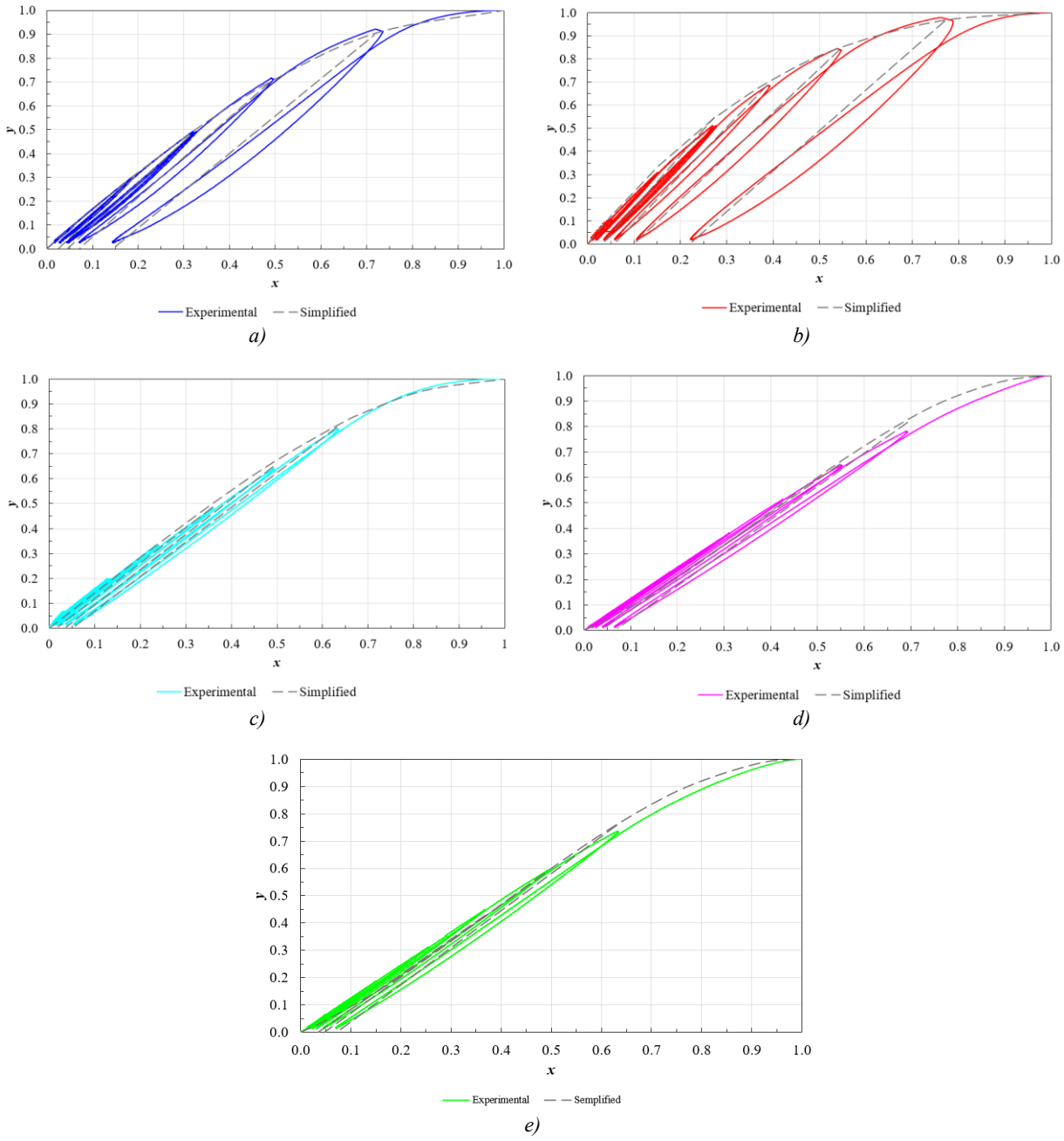

Figure 2-34. Comparison between experimental and simplified stress-strain relations for: a) NAC1; b) EAF1; c) NAC2; d) EAF2; e) BAR.

2.4.5 Conclusions

This subsection presents an investigation on the cyclic behavior and deformative characteristics of concrete incorporating Electric Arc Furnace Slag (EAFS) as coarse aggregate. The complete stress-strain relation under cyclic loading was analyzed and compared with that of conventional natural aggregate concrete (NAC). Experimental testing was performed on both short-term specimens cured for 28 days and long-term specimens stored for six years under standard curing conditions since casting. Deformative parameters were derived from the experimental data, and damage evolution was assessed. Analytical constitutive models were developed to describe the cyclic response, including both a detailed and a simplified version.

Based on the findings, the following conclusions can be drawn:

- EAFS concrete (EAFC) exhibited a more pronounced strength gain at early ages compared to NAC. However, this strength advantage diminished over time, although the substitution of natural gravel with EAFS still resulted in higher overall compressive strength.
- Under the cyclic loading protocol used in this study, no significant differences in compressive strength were observed between cyclic and monotonic loading for any of the concrete types tested.
- In short-term tests, EAFS concrete displayed a notably higher secant modulus than NAC at lower stress levels, although this advantage decreased near peak load. In contrast, long-term results showed that EAFS concrete consistently maintained a steeper stress-strain curve than NAC, regardless of the stress level applied.
- Across all concrete types, Poisson's ratio remained within the typical range of 0.20-0.30 up to approximately 80% of the compressive strength ($0.8 f_c$). Beyond this point, the scatter of data increased significantly.
- EAFC exhibited a more brittle failure mode than NAC, as indicated by higher normalized critical stress values (σ_{crit}/f_c). On the other hand, BAR concrete (with barite aggregates) recorded the largest volumetric strains under cyclic loading, attributable to the deformability of its heavy aggregates.
- The constitutive models proposed in this work effectively predict the stress-strain behavior under cyclic loading for both NAC and EAFS concrete. Furthermore, the simplified model, i.e. assuming linear and overlapping unloading/reloading branches, proved to be effective for practical applications, offering comparable predictive performance with reduced complexity.

REFERENCES

[1] L. Coppola, A. Buoso, D. Coffetti, P. Kara, S. Lorenzi, Electric arc furnace granulated slag for sustainable concrete, Construction and Building Materials 123 (2016) 115–119. https://doi.org/10.1016/j.conbuildmat.2016.06.142.

[2] A. Piemonti, A. Conforti, L. Cominoli, S. Sorlini, A. Luciano, G. Plizzari, Use of Iron and Steel Slags in Concrete: State of the Art and Future Perspectives, Sustainability 13 (2021) 556. https://doi.org/10.3390/su13020556.

[3] A.M. Rashad, Behavior of steel slag aggregate in mortar and concrete - A comprehensive overview, Journal of Building Engineering 53 (2022) 104536. https://doi.org/10.1016/j.jobe.2022.104536.

[4] L.C.B. Costa, M.A. Nogueira, H.D. Andrade, J.M.F. de Carvalho, F.P. da F. Elói, G.J. Brigolini, R.A.F. Peixoto, Mechanical and durability performance of concretes produced with steel slag aggregate and mineral admixtures, Construction and Building Materials 318 (2022) 126152. https://doi.org/10.1016/j.conbuildmat.2021.126152.

[5] F. De Larrard, C.F. Ferraris, T. Sedran, Fresh concrete: A Herschel-Bulkley material, Mat. Struct. 31 (1998) 494–498. https://doi.org/10.1007/BF02480474.

[6] J.E. Wallevik, Rheology of Particle Suspensions: Fresh Concrete, Mortar and Cement Paste with Various Types of Lignosulfonates, Doctoral thesis, Fakultet for ingeniørvitenskap og teknologi, 2003. https://ntnuopen.ntnu.no/ntnu-xmlui/handle/11250/236410 (accessed February 25, 2025).

[7] F. Mahaut, S. Mokéddem, X. Chateau, N. Roussel, G. Ovarlez, Effect of coarse particle volume fraction on the yield stress and thixotropy of cementitious materials, Cement and Concrete Research 38 (2008) 1276–1285. https://doi.org/10.1016/j.cemconres.2008.06.001.

[8] F. Mahaut, X. Chateau, P. Coussot, G. Ovarlez, Yield stress and elastic modulus of suspensions of noncolloidal particles in yield stress fluids, Journal of Rheology 52 (2008) 287–313. https://doi.org/10.1122/1.2798234.

[9] R.J. Flatt, P. Bowen, Yodel: A Yield Stress Model for Suspensions, Journal of the American Ceramic Society 89 (2006) 1244–1256. https://doi.org/10.1111/j.1551-2916.2005.00888.x.

[10] R.J. Flatt, P. Bowen, Yield Stress of Multimodal Powder Suspensions: An Extension of the YODEL (Yield Stress mODEL), Journal of the American Ceramic Society 90 (2007) 1038–1044. https://doi.org/10.1111/j.1551-2916.2007.01595.x.

[11] Z. Toutou, N. Roussel, Multi Scale Experimental Study of Concrete Rheology: From Water Scale to Gravel Scale, Mater Struct 39 (2006) 189–199. https://doi.org/10.1617/s11527-005-9047-y.

[12] H. Hafid, G. Ovarlez, F. Toussaint, P.H. Jezequel, N. Roussel, Effect of particle morphological parameters on sand grains packing properties and rheology of model mortars, Cement and Concrete Research 80 (2016) 44–51. https://doi.org/10.1016/j.cemconres.2015.11.002.

[13] J. Yammine, M. Chaouche, M. Guerinet, M. Moranville, N. Roussel, From ordinary rhelogy concrete to self compacting concrete: A transition between frictional and hydrodynamic interactions, Cement and Concrete Research 38 (2008) 890–896. https://doi.org/10.1016/j.cemconres.2008.03.011.

[14] I. Ivanova, V. Mechtcherine, Effects of Volume Fraction and Surface Area of Aggregates on the Static Yield Stress and Structural Build-Up of Fresh Concrete, Materials 13 (2020) 1551. https://doi.org/10.3390/ma13071551.

[15] O. Ahmadah, H. Bessaies-Bey, A. Yahia, N. Roussel, A new mix design method for low-environmental-impact blended cementitious materials: Optimization of the physical characteristics of powders for better rheological and mechanical properties, Cement and Concrete Composites 128 (2022) 104437. https://doi.org/10.1016/j.cemconcomp.2022.104437.

[16] M. Barry, M. Clément, D. Rangeard, Y. Jacquet, A. Perrot, Manufactured crushed sand: packing fraction prediction and influence on mortar rheology, Mater Struct 56 (2023) 139. https://doi.org/10.1617/s11527-023-02231-8.

[17] H.J.H. Brouwers, Particle-size distribution and packing fraction of geometric random packings, Phys. Rev. E 74 (2006) 031309. https://doi.org/10.1103/PhysRevE.74.031309.

[18] C. Hettiarachchi, W.K. Mampearachchi, Effect of surface texture, size ratio and large particle volume fraction on packing density of binary spherical mixtures, Granular Matter 22 (2019) 8. https://doi.org/10.1007/s10035-019-0978-3.

[19] EN 197-1:2011 - Cement - Composition, specifications and conformity criteria for common cements, (2011).

[20] EN 1097-6:2013 - Tests for mechanical and physical properties of aggregates - Determination of particle density and water absorption, (2013).

[21] O. Ahmadah, H. Bessaies-Bey, A. Yahia, N. Roussel, Effect of Morphological Characteristics on the Viscosity of Cementitious Materials: Optimization of the Rheological Behavior of Ternary Cements, SP 349 (2021) 533–540. https://doi.org/10.14359/51732770.

[22] F. Faleschini, M. Alejandro Fernández-Ruíz, M.A. Zanini, K. Brunelli, C. Pellegrino, E. Hernández-Montes, High performance concrete with electric arc furnace slag as aggregate: Mechanical and durability properties, Construction and Building Materials 101 (2015) 113–121. https://doi.org/10.1016/j.conbuildmat.2015.10.022.

[23] A. Santamaria, F. Faleschini, G. Giacomello, K. Brunelli, J.-T. San José, C. Pellegrino, M. Pasetto, Dimensional stability of electric arc furnace slag in civil engineering applications, Journal of Cleaner Production 205 (2018) 599–609. https://doi.org/10.1016/j.jclepro.2018.09.122.

[24] L. Evangelista, J. de Brito, Mechanical behaviour of concrete made with fine recycled concrete aggregates, Cement and Concrete Composites 29 (2007) 397–401. https://doi.org/10.1016/j.cemconcomp.2006.12.004.

[25] A. Schwartzentruber, C. Catherine, La méthode du mortier de béton équivalent (MBE)—Un nouvel outil d'aide à la formulation des bétons adjuvantés, Mat. Struct. 33 (2000) 475–482. https://doi.org/10.1007/BF02480524.

[26] Q. Deng, Y. Zhuang, W. Yang, K. Zhao, S. Zhang, Z. Duan, J. Xiao, Rheological properties of mortar with recycled fine aggregate: From the perspective of particle packing, Construction and Building Materials 465 (2025) 140237. https://doi.org/10.1016/j.conbuildmat.2025.140237.

[27] A. Perrot, T. Lecompte, H. Khelifi, C. Brumaud, J. Hot, N. Roussel, Yield stress and bleeding of fresh cement pastes, Cement and Concrete Research 42 (2012) 937–944. https://doi.org/10.1016/j.cemconres.2012.03.015.

[28] V.N. Nerella, M.A.B. Beigh, S. Fataei, V. Mechtcherine, Strain-based approach for measuring structural build-up of cement pastes in the context of digital construction, Cement and Concrete Research 115 (2019) 530–544. https://doi.org/10.1016/j.cemconres.2018.08.003.

[29] F. Faleschini, D. Trento, M.A. Zanini, C. Pellegrino, V. Ortega-López, A. Santamaria, Mechanical strength and environmental sustainability of EAF concrete, in: Life-Cycle of Structures and Infrastructure Systems, CRC Press, 2023: pp. 2455–2462. https://doi.org/10.1201/9781003323020-299.

[30] L. Martinie, P. Rossi, N. Roussel, Rheology of fiber reinforced cementitious materials: classification and prediction, Cement and Concrete Research 40 (2010) 226–234. https://doi.org/10.1016/j.cemconres.2009.08.032.

[31] A. Perrot, T. Lecompte, P. Estellé, S. Amziane, Structural build-up of rigid fiber reinforced cement-based materials, Mater Struct 46 (2013) 1561–1568. https://doi.org/10.1617/s11527-012-9997-9.

[32] D. Jiao, C. Shi, Q. Yuan, X. An, Y. Liu, H. Li, Effect of constituents on rheological properties of fresh concrete-A review, Cement and Concrete Composites 83 (2017) 146–159. https://doi.org/10.1016/j.cemconcomp.2017.07.016.

[33] Y. Keskin-Topan, H. Bessaies-Bey, L. Petit, N.-C. Tran, J.-B. d'Espinose de Lacaillerie, S. Rossignol, N. Roussel, Effect of maximum packing fraction of powders on the rheology of metakaolin-based geopolymer pastes, Cement and Concrete Research 179 (2024) 107482. https://doi.org/10.1016/j.cemconres.2024.107482.

[34] X. Chateau, G. Ovarlez, K.L. Trung, Homogenization approach to the behavior of suspensions of noncolloidal particles in yield stress fluids, Journal of Rheology 52 (2008) 489–506. https://doi.org/10.1122/1.2838254.

[35] J.M. Manso, J.J. Gonzalez, J.A. Polanco, Electric Arc Furnace Slag in Concrete, Journal of Materials in Civil Engineering 16 (2004) 639–645. https://doi.org/10.1061/(ASCE)0899-1561(2004)16:6(639).

[36] N. Rojas, M. Bustamante, P. Muñoz, K. Godoy, V. Letelier, Study of properties and behavior of concrete containing EAF slag as coarse aggregate, Developments in the Built Environment 14 (2023) 100137. https://doi.org/10.1016/j.dibe.2023.100137.

[37] C. Pellegrino, P. Cavagnis, F. Faleschini, K. Brunelli, Properties of concretes with Black/Oxidizing Electric Arc Furnace slag aggregate, Cement and Concrete Composites 37 (2013) 232–240. https://doi.org/10.1016/j.cemconcomp.2012.09.001.

[38] I. Arribas, A. Santamaría, E. Ruiz, V. Ortega-López, J.M. Manso, Electric arc furnace slag and its use in hydraulic concrete, Construction and Building Materials 90 (2015) 68–79. https://doi.org/10.1016/j.conbuildmat.2015.05.003.

[39] A. Santamaría, A. García-Llona, V. Revilla-Cuesta, I. Piñero, V. Ortega-López, Bending tests on building beams containing electric arc furnace slag and alternative binders and manufactured with energy-saving placement techniques, Structures 32 (2021) 1921–1933. https://doi.org/10.1016/j.istruc.2021.04.003.

[40] A. Santamaría, J.M. Romera, I. Marcos, V. Revilla-Cuesta, V. Ortega-López, Shear strength assessment of reinforced concrete components containing EAF steel slag aggregates, Journal of Building Engineering 46 (2022) 103730. https://doi.org/10.1016/j.jobe.2021.103730.

[41] C. Pellegrino, F. Faleschini, Experimental behavior of reinforced concrete beams with Electric arc furnace slag as recycled aggregate., ACI Materials Journal 110 (2013).

[42] J.-M. Lee, Y.-J. Lee, Y.-J. Jung, J.-H. Park, B.-S. Lee, K.-H. Kim, Ductile capacity of reinforced concrete columns with electric arc furnace oxidizing slag aggregate, Construction and Building Materials 162 (2018) 781–793. https://doi.org/10.1016/j.conbuildmat.2017.12.045.

[43] F. Faleschini, L. Hofer, M.A. Zanini, M. dalla Benetta, C. Pellegrino, Experimental behavior of beam-column joints made with EAF concrete under cyclic loading, Engineering Structures 139 (2017) 81–95. https://doi.org/10.1016/j.engstruct.2017.02.038.

[44] F. Faleschini, P. Bragolusi, M.A. Zanini, P. Zampieri, C. Pellegrino, Experimental and numerical investigation on the cyclic behavior of RC beam column joints with EAF slag concrete, Engineering Structures 152 (2017) 335–347. https://doi.org/10.1016/j.engstruct.2017.09.022.

[45] A. Mwafy, A. Elnashai, Importance of shear assessment of concrete structures detailed to different capacity design requirements, Engineering Structures 30 (2008) 1590–1604. https://doi.org/10.1016/j.engstruct.2007.10.015.

[46] A.S. Alqarni, A.S. Albidah, A.M. Alaskar, A.A. Abadel, The effect of coarse aggregate characteristics on the shear behavior of reinforced concrete slender beams, Construction and Building Materials 264 (2020) 120189. https://doi.org/10.1016/j.conbuildmat.2020.120189.

[47] P. Huber, T. Huber, J. Kollegger, Investigation of the shear behavior of RC beams on the basis of measured crack kinematics, Engineering Structures 113 (2016) 41–58. https://doi.org/10.1016/j.engstruct.2016.01.025.

[48] T. Huber, P. Huber, J. Kollegger, Influence of aggregate interlock on the shear resistance of reinforced concrete beams without stirrups, Engineering Structures 186 (2019) 26–42. https://doi.org/10.1016/j.engstruct.2019.01.074.

[49] J.C. Walraven, Aggregate interlock: A theoretical and experimental analysis, TU Delft, 1980. https://repository.tudelft.nl/record/uuid:c33a2890-f9c1-4176-929e-6988f0f23640 (accessed March 18, 2025).

[50] F.-I.F. for S. Concrete, Shear at the interface of precast and in situ concrete, FIB - International Federation for Structural Concrete, 1982.

[51] E. Cuenca, A. Conforti, L. Monfardini, F. Minelli, Shear transfer across a crack in ordinary and alkali activated concrete reinforced by different fibre types, Mater Struct 53 (2020) 24. https://doi.org/10.1617/s11527-020-1455-5.

[52] J.A. Hofbeck, I.O. Ibrahim, A.H. Mattock, Shear Transfer in Reinforced Concrete, JP 66 (1969) 119–128. https://doi.org/10.14359/7349.

[53] B.G. Fonteboa, F. Martínez, D. Carro, J. Eiras, Shear friction capacity of recycled concretes, Materiales de Construcción 60 (2010) 53–67. https://doi.org/10.3989/mc.2010.49708.

[54] J. Xiao, H. Xie, Z. Yang, Shear transfer across a crack in recycled aggregate concrete, Cement and Concrete Research 42 (2012) 700–709. https://doi.org/10.1016/j.cemconres.2012.02.006.

[55] C.G. Fakitsas, P.E.A. Papakonstantinou, P.D. Kiousis, A. Savva, Effects of Recycled Concrete Aggregates on the Compressive and Shear Strength of High-Strength Self-Consolidating Concrete, Journal of Materials in Civil Engineering 24 (2012) 356–361. https://doi.org/10.1061/(ASCE)MT.1943-5533.0000397.

[56] K.N. Rahal, W. Hassan, Shear strength of plain concrete made of recycled low-strength concrete aggregates and natural aggregates, Construction and Building Materials 311 (2021) 125317. https://doi.org/10.1016/j.conbuildmat.2021.125317.

[57] C. Sun, J. Xiao, D.A. Lange, Simulation study on the shear transfer behavior of recycled aggregate concrete, Structural Concrete 19 (2018) 255–268. https://doi.org/10.1002/suco.201600236.

[58] S.A. Waseem, B. Singh, Shear transfer strength of normal and high-strength recycled aggregate concrete – An experimental investigation, Construction and Building Materials 125 (2016) 29–40. https://doi.org/10.1016/j.conbuildmat.2016.08.022.

[59] J.C. Trindade, S.L.G. Garcia, T.N. Lacerda, T.L. Resende, Analysis of the shear behavior of reinforced recycled aggregate concrete beams based on shear transfer mechanisms, Engineering Structures 293 (2023) 116616. https://doi.org/10.1016/j.engstruct.2023.116616.

[60] T. Imjai, F. Kefyalew, P. Aosai, R. Garcia, B. Kim, H.M. Abdalla, S.N. Raman, A new equation to predict the shear strength of recycled aggregate concrete Z push-off specimens, Cement and Concrete Research 169 (2023) 107181. https://doi.org/10.1016/j.cemconres.2023.107181.

[61] L. Clerici, A. Piemonti, G. Plizzari, A. Conforti, Experimental Study on the aggregate interlock in concrete with EAF slag aggregates, in: SUM 2025 - 8th Multidisciplinary Symposium on Circular Economy and Urban Mining, CISA, Procida (NA), n.d.

[62] M. Yusuf, S. Sarhat, P. St.Onge, M. Green, Shear transfer strength of concrete made with recycled concrete aggregate after exposure to high temperatures, in: 2019.

[63] R.G. Bryan Barragan Luis Agullo, and Raul Zerbino, Shear Failure of Steel Fiber-Reinforced Concrete Based on Push-Off Tests, ACI Materials Journal 103 (2006). https://doi.org/10.14359/16608.

[64] M.E. Mathews, N. Anand, É. Lublóy, T. Kiran, Effect of elevated temperature on interfacial shear transfer capacity of self-compacting concrete, Case Studies in Construction Materials 15 (2021) e00753. https://doi.org/10.1016/j.cscm.2021.e00753.

[65] K.N. Rahal, A.-L. Al-Khaleefi, Shear-friction behavior of recycled and natural aggregate concrete-an experimental investigation, ACI Structural Journal 112 (2015) 725–734. https://doi.org/10.14359/51687748.

[66] Z. Fang, H. Jiang, A. Liu, J. Feng, Y. Li, Shear-friction behaviour on smooth interface between high-strength and lightweight concrete, Magazine of Concrete Research 72 (2020) 68–87. https://doi.org/10.1680/jmacr.17.00393.

[67] B.F. da Cunha, R.C. de Andrade Pinto, G. Savaris, Evaluation of self-consolidating concrete shear strength by means of push-off test, Magazine of Concrete Research 74 (2022) 879–888. https://doi.org/10.1680/jmacr.21.00067.
[68] EN 206:2013 - Concrete - Specification, performance, production and conformity, (2013).
[69] A. Santamaría, A. Orbe, M.M. Losañez, M. Skaf, V. Ortega-Lopez, J.J. González, Self-compacting concrete incorporating electric arc-furnace steelmaking slag as aggregate, Materials & Design 115 (2017) 179–193. https://doi.org/10.1016/j.matdes.2016.11.048.
[70] N.H. Roslan, M. Ismail, N.H.A. Khalid, B. Muhammad, Properties of concrete containing electric arc furnace steel slag and steel sludge, Journal of Building Engineering 28 (2020) 101060. https://doi.org/10.1016/j.jobe.2019.101060.
[71] P. Tamayo, J. Pacheco, C. Thomas, J. de Brito, J. Rico, Mechanical and Durability Properties of Concrete with Coarse Recycled Aggregate Produced with Electric Arc Furnace Slag Concrete, Applied Sciences 10 (2020). https://doi.org/10.3390/app10010216.
[72] K.N. Rahal, A.L. Khaleefi, A. Al-Sanee, An experimental investigation of shear-transfer strength of normal and high strength self compacting concrete, Engineering Structures 109 (2016) 16–25. https://doi.org/10.1016/j.engstruct.2015.11.015.
[73] ACI 318-19 Building Code Requirements for Structural Concrete and Commentary, American Concrete Institute, Farmington Hills, MI, 2019. https://doi.org/10.14359/51716937.
[74] Yang Yuguang, Walraven Joost, Uijl Joop den, Shear Behavior of Reinforced Concrete Beams without Transverse Reinforcement Based on Critical Shear Displacement, Journal of Structural Engineering 143 (2017) 04016146. https://doi.org/10.1061/(ASCE)ST.1943-541X.0001608.
[75] Y.D. Hamadi, P.E. Regan, Behaviour of normal and lightweight aggregate beams with shear cracks, The Structural Engineer 58B (1980) 71–79.
[76] F. Faleschini, D. Trento, M.A. Zanini, 8 - Steel slag aggregate in concrete, in: J. de Brito, F. Agrela, R.V. Silva (Eds.), The Path to Green Concrete, Woodhead Publishing, 2024: pp. 241–265. https://doi.org/10.1016/B978-0-443-19165-7.00006-X.
[77] EN 12390-3:2019 - Testing hardened concrete - Compressive strength of test specimens, (2019).
[78] EN 12390-6:2023 - Testing hardened concrete - Tensile splitting strength of test specimens, (2023).
[79] EN 12390-13:2021 - Testing hardened concrete - Determination of secant modulus of elasticity in compression, (2021).
[80] D. Kvočka, J. Šušteršič, A. Mauko Pranjić, A. Mladenović, Mass Concrete with EAF Steel Slag Aggregate: Workability, Strength, Temperature Rise, and Environmental Performance, Sustainability 14 (2022). https://doi.org/10.3390/su142315502.
[81] ACI 318-11 Building Code Requirements for Structural Concrete and Commentary, American Concrete Institute, Farmington Hills, MI, 2011.
[82] AASHTO LRFD Bridge Design Specifications, 9th Edition, American Association of State Highway and Transportation Officials (AASHTO), Washington, D.C., 2020.
[83] J. Sagaseta, R.L. Vollum, Influence of aggregate fracture on shear transfer through cracks in reinforced concrete, Magazine of Concrete Research 63 (2011) 119–137. https://doi.org/10.1680/macr.9.00191.
[84] A.H. Mattock, Shear friction and high-strength concrete, ACI Structural Journal 98 (2001) 50–59.
[85] K.N. Rahal, Shear-transfer strength of reinforced concrete, ACI Structural Journal 107 (2010) 419–426.
[86] Eurocode 2: Design of Concrete Structures - Part 1-1: General Rules and Rules for Buildings, European Committee for Standardization (CEN), Brussels, 2023.
[87] A.H. Mattock, W.K. Li, T.C. Wang, Shear transfer in lightweight reinforced concrete, Pcij 21 (1976) 20–39. https://doi.org/10.15554/pcij.01011976.20.39.
[88] L.F. Kahn, A.D. Mitchell, Shear Friction Tests with High-Strength Concrete, SJ 99 (2002) 98–103. https://doi.org/10.14359/11040.
[89] F. Faleschini, D. Trento, V. Ortega-López, M.A. Zanini, Shear transfer in fly ash concrete with electric arc furnace aggregates, Magazine of Concrete Research 75 (2023) 906–918. https://doi.org/10.1680/jmacr.22.00280.
[90] B.P. Sinha, K.H. Gerstle, L.G. Tulin, Stress-Strain Relations for Concrete Under Cyclic Loading, ACI Journal Proceedings 61 (1964). https://doi.org/10.14359/7775.
[91] Chen En-Sheng, Buyukozturk Oral, Constitutive Model for Concrete in Cyclic Compression, Journal of Engineering Mechanics 111 (1985) 797–814. https://doi.org/10.1061/(ASCE)0733-9399(1985)111:6(797).
[92] J. Xiao, H. Li, Z. Yang, Fatigue behavior of recycled aggregate concrete under compression and bending cyclic loadings, Construction and Building Materials 38 (2013) 681–688. https://doi.org/10.1016/j.conbuildmat.2012.09.024.
[93] S. Arora, S.P. Singh, Analysis of flexural fatigue failure of concrete made with 100% Coarse Recycled Concrete Aggregates, Construction and Building Materials 102 (2016) 782–791. https://doi.org/10.1016/j.conbuildmat.2015.10.098.

[94] X. Zhang, C. Wang, J. Wang, X. Liu, Y. Huang, L. Wang, Y. Ding, Experimental study on the compressive fatigue performance of nano-silica modified recycled aggregate concrete, Construction and Building Materials 447 (2024) 138161. https://doi.org/10.1016/j.conbuildmat.2024.138161.

[95] X. Hu, Q. Lu, Z. Xu, W. Zhang, S. Cheng, Compressive stress-strain relation of recycled aggregate concrete under cyclic loading, Construction and Building Materials 193 (2018) 72–83. https://doi.org/10.1016/j.conbuildmat.2018.10.137.

[96] P. Ge, Y. Song, J. Zhou, X. Ma, Study on stress–strain relationship and constitutive model of recycled aggregate concrete under axial cyclic compression, Structural Concrete 25 (2024) 3902–3938. https://doi.org/10.1002/suco.202300838.

[97] Z. Dai, X. Hu, S. Fu, Cyclic stress-strain relation of recycled aggregate concrete under confining pressure, Construction and Building Materials 468 (2025) 140402. https://doi.org/10.1016/j.conbuildmat.2025.140402.

[98] B. González-Fonteboa, F. Martínez-Abella, J. Eiras-López, S. Seara-Paz, Effect of recycled coarse aggregate on damage of recycled concrete, Mater Struct 44 (2011) 1759–1771. https://doi.org/10.1617/s11527-011-9736-7.

[99] B. González-Fonteboa, F. Martínez-Abella, M.F. Herrador, S. Seara-Paz, Structural recycled concrete: Behaviour under low loading rate, Construction and Building Materials 28 (2012) 111–116. https://doi.org/10.1016/j.conbuildmat.2011.08.010.

[100] S.P. Shah, S. Chandra, Critical Stress, Volume Change, and Microcracking of Concrete, ACI Journal Proceedings 65 (1968) 770–780. https://doi.org/10.14359/7512.

[101] D. Zheng, Q. Li, L. Wang, A microscopic approach to rate effect on compressive strength of concrete, Engineering Fracture Mechanics 72 (2005) 2316–2327. https://doi.org/10.1016/j.engfracmech.2005.01.012.

[102] S.P. Shah, G. Winter, Inelastic Behavior and Fracture of Concrete, ACI Journal Proceedings 63 (1966). https://doi.org/10.14359/7659.

[103] Karsan I. Demir, Jirsa James O., Behavior of Concrete Under Compressive Loadings, Journal of the Structural Division 95 (1969) 2543–2564. https://doi.org/10.1061/JSDEAG.0002424.

[104] B.Y. Bahn, C.-T.T. Hsu, Stress-Strain Behavior of Concrete under Cyclic Loading, ACI Materials Journal 95 (1998). https://doi.org/10.14359/363.

[105] D. Palermo, F.J. Vecchio, Compression Field Modeling of Reinforced Concrete Subjected to Revered Loading: Verification, ACI Structural Journal 101 (2004). https://doi.org/10.14359/13012.

[106] J.F. Sima, P. Roca, C. Molins, Cyclic constitutive model for concrete, Engineering Structures 30 (2008) 695–706. https://doi.org/10.1016/j.engstruct.2007.05.005.

[107] F. Aslani, S. and Nejadi, Cyclic Constitutive Model for High-Strength Concrete Confined by Ultra-High-Strength and Normal-Strength Transverse Reinforcements, Australian Journal of Structural Engineering 12 (2011) 159–172. https://doi.org/10.7158/13287982.2011.11465088.

[108] F. Aslani, R. Jowkarmeimandi, Stress–strain model for concrete under cyclic loading, Magazine of Concrete Research 64 (2012) 673–685. https://doi.org/10.1680/macr.11.00120.

[109] Z.H. Guo, Strength and deformation of concrete, Beijing: Tsinghua University Press 156 (1997) 156.

[110] J. Xiao, J. Li, Ch. Zhang, Mechanical properties of recycled aggregate concrete under uniaxial loading, Cement and Concrete Research 35 (2005) 1187–1194. https://doi.org/10.1016/j.cemconres.2004.09.020.

[111] H. Yang, J. Fang, J. Jiang, M. Li, J. Mei, Compressive stress–strain curve of recycled concrete under repeated loading, Construction and Building Materials 387 (2023) 131598. https://doi.org/10.1016/j.conbuildmat.2023.131598.

[112] B. Pomaro, F. Gramegna, R. Cherubini, V. De Nadal, V. Salomoni, F. Faleschini, Gamma-ray shielding properties of heavyweight concrete with Electric Arc Furnace slag as aggregate: An experimental and numerical study, Construction and Building Materials 200 (2019) 188–197. https://doi.org/10.1016/j.conbuildmat.2018.12.098.

[113] EN 12350-2:2019 - Testing fresh concrete - Slump test, (2019).

[114] A. Santamaría, V. Ortega-López, M. Skaf, J.A. Chica, J.M. Manso, The study of properties and behavior of self compacting concrete containing Electric Arc Furnace Slag (EAFS) as aggregate, Ain Shams Engineering Journal 11 (2020) 231–243. https://doi.org/10.1016/j.asej.2019.10.001.

[115] M.F.M. Zain, H.B. Mahmud, A. Ilham, M. Faizal, Prediction of splitting tensile strength of high-performance concrete, Cement and Concrete Research 32 (2002) 1251–1258. https://doi.org/10.1016/S0008-8846(02)00768-8.

[116] S. Bhanja, B. Sengupta, Influence of silica fume on the tensile strength of concrete, Cement and Concrete Research 35 (2005) 743–747. https://doi.org/10.1016/j.cemconres.2004.05.024.

[117] J.A. Carneiro, P.R.L. Lima, M.B. Leite, R.D. Toledo Filho, Compressive stress–strain behavior of steel fiber reinforced-recycled aggregate concrete, Cement and Concrete Composites 46 (2014) 65–72. https://doi.org/10.1016/j.cemconcomp.2013.11.006.

[118] B. Wu, Y. Yu, Z. Chen, X. Zhao, Shape effect on compressive mechanical properties of compound concrete containing demolished concrete lumps, Construction and Building Materials 187 (2018) 50–64. https://doi.org/10.1016/j.conbuildmat.2018.07.086.

[119] P. Sukontasukkul, P. Nimityongskul, S. Mindess, Effect of loading rate on damage of concrete, Cement and Concrete Research 34 (2004) 2127–2134. https://doi.org/10.1016/j.cemconres.2004.03.022.

[120] L. Rondi, G. Bregoli, S. Sorlini, L. Cominoli, C. Collivignarelli, G. Plizzari, Concrete with EAF steel slag as aggregate: A comprehensive technical and environmental characterisation, Composites Part B: Engineering 90 (2016) 195–202. https://doi.org/10.1016/j.compositesb.2015.12.022.

[121] S. Kilincarslan, I. Akkurt, C. Basyigit, The effect of barite rate on some physical and mechanical properties of concrete, Materials Science and Engineering: A 424 (2006) 83–86. https://doi.org/10.1016/j.msea.2006.02.033.

[122] M.A. Farooq, Y. Sato, T. Ayano, K. Niitani, Experimental and numerical investigation of static and fatigue behavior of mortar with blast furnace slag sand as fine aggregates in air and water, Construction and Building Materials 143 (2017) 429–443. https://doi.org/10.1016/j.conbuildmat.2017.03.147.

[123] M.A. Farooq, Y. Sato, K. Niitani, Experimental investigation of monotonic behavior and stress-strain models of AE and non-AE high strength concrete with BFS fine aggregates under freezing and thawing, Construction and Building Materials 249 (2020) 118679. https://doi.org/10.1016/j.conbuildmat.2020.118679.

3 RAW CRUSHED WIND TURBINE BLADES AS EFFECTIVE ADDITION FOR CONCRETE PRODUCTION

3.1 MOTIVATIONS

At the beginning of the Ph.D. program, the author conducted an extensive literature review, focused on the latest studies regarding the use of Raw Crushed Wind Turbine Blades (RCWTB) as a component in concrete production. This review led to the identification of some research gaps that may currently hinder the widespread adoption of RCWTB in the concrete industry. These gaps include:

4. Rheology
   Literature is already available on the workability of concrete incorporating Raw Crushed Wind Turbine Blade (RCWTB). Moreover, some previous works have already proposed consistent models to predict the flowability and yield stress of concretes containing conventional fibers, i.e. made from virgin raw materials. However, when it comes to recycled fiber, literature becomes much more limited. In this context, the prediction of flowability for concretes including recycled Glass Fiber Reinforced Polymer (GFRP) separated from RCWTB and whole RCWTB would be of great practical interest.
5. Interaction with recycled aggregates
   The inclusion of fibers enhances both the mechanical properties and durability of concrete by reducing its porosity and providing a diffuse reinforcement that helps confining the composite material. This beneficial effect is even more pronounced, in relative terms, when applied to concrete made with recycled aggregates. However, conventional fibers used in fiber-reinforced concrete are typically produced from virgin materials. When incorporated into recycled concrete, they can jeopardize the environmental advantages gained from using recycled aggregates. Therefore, utilizing recycled GFRP fibers recovered from Raw Crushed Wind Turbine Blades (RCWTB) presents a promising alternative, offering the potential to enhance the performance of recycled concrete while preserving its reduced carbon footprint.

The following subsections present results intended to address these identified research gaps.

The following papers on this topic have been already published by the Ph.D. candidate:

D. Trento, F. Faleschini, V. Revilla-Cuesta, V. Ortega-López, Improving the early-age behavior of concrete containing coarse recycled aggregate with raw-crushed wind-turbine blade, Journal of Building Engineering 92 (2024) 109815. https://doi.org/10.1016/j.jobe.2024.109815.

3.2 RHEOLOGY: YIELD STRESS CHARACTERIZATION

3.2.1 Introduction

In general, the behavior of fresh cementitious conglomerates is influenced by both the rheological properties of the cementitious paste and the aggregate particles [1,2]. The yield stress of the cement paste is principally governed by Van der Waals forces and the number of contact points between cement particles, as described by the well-known Yodel model [3,4]. In the case of mortars, the impact of aggregates on yield stress is generally related to the ratio between the sand volume fraction in the mixture and its loose packing fraction [5,6]. About fibers, it was demonstrated by Martinie et al. [7] that the aforementioned concepts also apply. However, fibers with a length significantly greater than their diameter exhibit a packing behavior that differs considerably from that of non-elongated inclusions. For rigid fiber, it was observed that a non-linear relationship exists between the fiber volume fraction (i.e. the ratio between the fiber volume fraction and the fiber maximum packing fraction) and the relative yield stress (i.e. the ratio between the yield stress of the paste containing fibers and the yield stress of the suspending reference paste) [7,8]. When it comes to flexible fibers, most of the previous principles still apply if the fibers do not interact physically or chemically with the cement paste. The challenge arises from the potential deformation of fibers within the cement matrix, which can alter their packing behavior. Martinie et al. [7] considered fiber deformation under the effect of the paste consistency in their work. Considering the fibers as bent like beams, they concluded that typical steel fibers can be considered rigid, while conventional polypropylene fibers are expected to be largely deformed [7].

In this section, the yield stress for cementitious pastes and mortars including Glass Fiber Reinforced Polymer (GFRP) separated from Raw Crushed Wind Turbine Blade (RCWTB) and whole RCWTB is measured and analyzed. The main goal is to deepen the knowledge of rheology for cementitious mixtures including RCWTB. The results are then discussed to determine whether yield stress of cementitious mixtures with RCWTB can be predicted considering GFRP as flexible fibers and roundish particles, e.g. balsa wood and polyurethane particles, as part of the aggregate.

3.2.2 Experimental program

3.2.2.1 Materials

The cement adopted in this experiment is a CEM II B-LL 32.5 R according to EN 197-1 [9], which includes clinker for 65-79% of the whole mass and limestone in the range 21-35%. Its granulometric distribution is displayed in Figure 3-2.

The aggregate used for this work is a conventional sand (Figure 3-1a), the granulometric distribution is shown in Figure 3-2. The particles have roundish shape, the water absorption and the apparent specific density are equal to 0.20% and 2630 kg/m^3, respectively. The specific surface was also estimated from the sieving distribution considering spherical shape of the particles, resulting in 4.04 m^2/kg.

RCWTB was made by non-selective crushing of sandwich panels from dismantled wind turbine blades. The resulting material shown in Figure 3-1b is a mix of long fibers, polyurethane, balsa wood, micro-fibers and small non-separable particles. The long fibers (Figure 3-1c), hereafter called Glass Fiber Reinforced Polymer (GFRP), are fiberglass composite formed of thread-like fibers bonded together with a polymer resin having an average length of approximately 13 mm and average diameter of 0.73 mm, comparable to some commercial fibers used in concrete [10]. Their tensile strength is about 270 MPa. Balsa wood and polyurethane appear roughly as spherical brown or green particles with an average size of 5 mm. The exceptionally low density of balsa wood justifies its use as a lightweight material in wind turbine blade manufacturing [11]. The micro-fibers tend to agglomerate into formations close to fluffs and consist of disintegrated fiberglass and coating gel. Furthermore, the so-called non-separable small particles consist of tiny fragments of polyurethane, fiberglass, and predominantly balsa wood, all agglomerated together. The physical characterization of RCWTB confirms its dual composition of fibers and particles, which can serve as fibers and aggregates in concrete, respectively. These characteristics should be considered when designing concrete mixes incorporating RCWTB. The RCWTB average density is equal to 1.63 kg/m^3, however GFRP occupies about 66.8% of the total mass.

a) *b)* *c)*

Figure 3-1. Materials employed in the experimental campaign: a) Sand; b) RCWTB; C) GFRP separated from RCWTB.

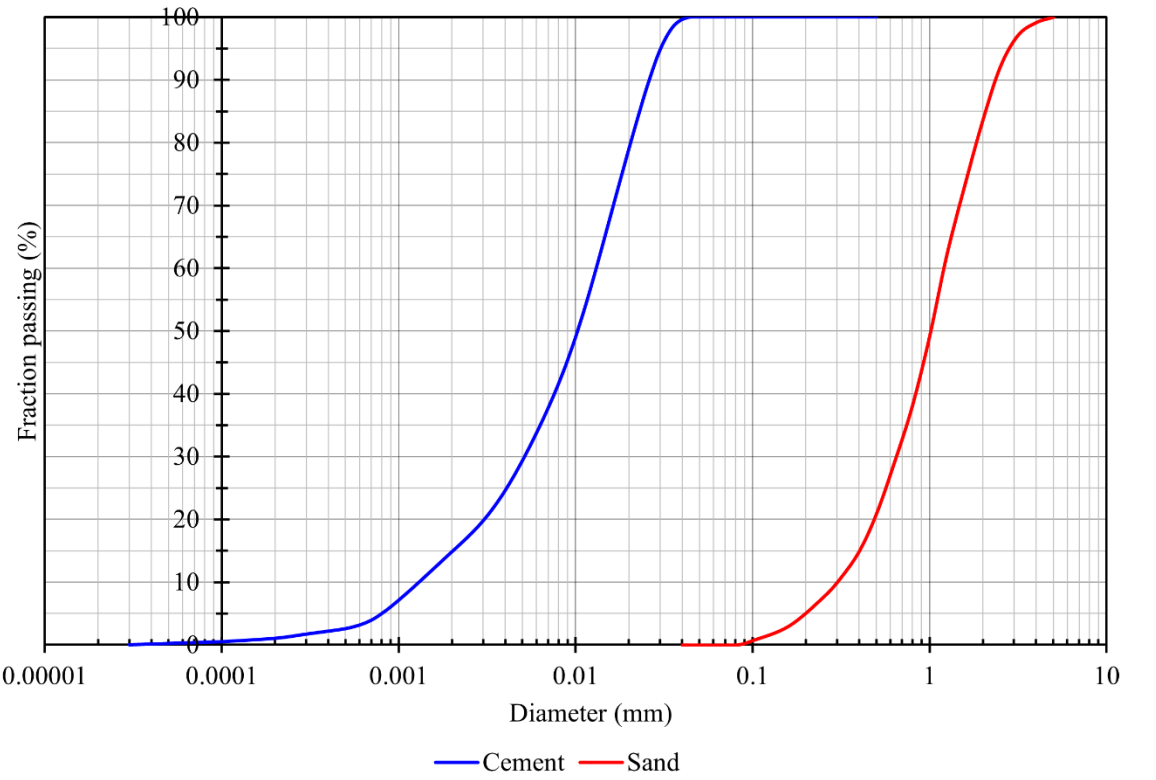

Figure 3-2. Granulometric distribution of cement and sand.

3.2.2.2 Mix design

Table 3-1 and Table 3-2 display the experimental matrix for the mortars prepared in this study. The aggregate volume fraction is 40% for all mortars, whereas water to cement ratio (W/C) was taken equal to either 0.4 or 0.5.

As a first trial, the GFRP contained into RCWTB was manually separated (Figure 3-1c) and mortars were cast including GFRP in volume 0.0, 0.5, 1.0, 1.5, 2.0 and 2.5%. According to Table 3-1 and Table 3-2, this group of mortars is called Mortar+GFRP series.

Another set of mortars was prepared including the whole RCWTB material, named Mortar+RCWTB series. In this circumstance the mix design is planned to include the same fiber volume as for GFRP series, considering all RCWTB components as part of the aggregate, except GFRP.

Some cementitious pastes named Cement Paste+GFRP were also made as being the cementitious paste related to the mortars of the Mortar+GFRP series. Thus, the corresponding fiber volumes for these cementitious pastes are slightly higher due to the aggregate absence.

3.2.2.3 Fabrication of the mixtures

Mortars were cast by mixing sand and cement for two minutes, followed by the addition of water and a further two-minutes mixing phase. Afterwards, GFRP or RCWTB were incorporated and mixed for one minute.

For cement paste, water and cement were mixed for two minutes. After that, GFRP was added into the cementitious pastes and blended for 1 minute.

Table 3-1. Experimental matrix of the cast mixtures with water/cement ratio equal to 0.4 (in kg/m^3).

	Cement Paste+GFRP					
Fiber volume (%)	**0.00%**	**0.83%**	**1.67%**	**2.50%**	**3.33%**	**4.17%**
Cement II/B-LL 32.5 R	818	811	805	798	791	784
Water	327	325	322	319	316	314
GFRP	0.0	10.2	20.4	30.6	40.8	51.0
	Mortar+GFRP					
Fiber volume (%)	**0.0%**	**0.5%**	**1.0%**	**1.5%**	**2.0%**	**2.5%**
Cement II/B-LL 32.5 R	818	811	805	798	791	784
Water	327	325	322	319	316	314
Sand	1052	1052	1052	1052	1052	1052
GFRP	0.0	10.2	20.4	30.6	40.8	51.0
	Mortar+RCWTB					
Fiber volume (%)	**0.0%**	**0.5%**	**1.0%**	**1.5%**	**2.0%**	**2.5%**
Cement II/B-LL 32.5 R	818	811	805	798	791	784
Water	327	325	322	319	316	314
Sand	1052	1047	1042	1037	1032	1027
GFRP (contained in RCWTB)	0.0	10.2	20.4	30.6	40.8	51.0
RCWTB	0.0	15.3	30.5	45.8	61.1	76.3

Table 3-2. Experimental matrix of the cast mixtures with water/cement ratio equal to 0.5 (in kg/m^3).

	Cement Paste+GFRP					
Fiber volume (%)	**0.00%**	**0.83%**	**1.67%**	**2.50%**	**3.33%**	**4.17%**
Cement II/B-LL 32.5 R	720	714	708	702	696	690
Water	360	357	354	351	348	345
GFRP	0.0	10.2	20.4	30.6	40.8	51.0
	Mortar+GFRP					
Fiber volume (%)	**0.0%**	**0.5%**	**1.0%**	**1.5%**	**2.0%**	**2.5%**
Cement II/B-LL 32.5 R	720	714	708	702	696	690
Water	360	357	354	351	348	345
Sand	1052	1052	1052	1052	1052	1052
GFRP	0.0	10.2	20.4	30.6	40.8	51.0
	Mortar+RCWTB					
Fiber volume (%)	**0.0%**	**0.5%**	**1.0%**	**1.5%**	**2.0%**	**2.5%**
Cement II/B-LL 32.5 R	720	714	708	702	696	690
Water	360	357	354	351	348	345
Sand	1052	1047	1042	1037	1032	1027
GFRP (contained in RCWTB)	0.0	10.2	20.4	30.6	40.8	51.0
RCWTB	0.0	15.3	30.5	45.8	61.1	76.3

3.2.2.4 Yield stress measurements

The yield stress measurements were performed using the Anton Paar Rheolab QC rheometer available at the University of Southern Brittany. The adopted procedure was already used in previous studies [12,13]. A constant strain rate of 0.01 s^{-1} was used to apply the torque stress. At this low shear rate, the influence of plastic viscosity can be neglected, enabling the yield stress to be determined from the measured maximum torque. The test duration was not established; instead, testing finished when the torque peak was reached to ensure accurate yield stress measurement. Two 4-blades Vane geometries were adopted: the former was used for most mixes, it has overall dimensions of 32 mm for both height and diameter, resulting in a Vane constant of 6.9×10^4 mm^3; the latter was employed just for those mortars having 0.4 water/cement ratio, it has overall dimensions of 18 mm for both height and diameter, resulting in a Vane constant of 1.2×10^4 mm^3.

For each mix a total of at least six measurements were taken, and the average yield stress was then calculated.

3.2.3 Results

In this subsection, the yield stress results are shown and compared for cementitious pastes and mortars including Glass Fibers Reinforced Polymer (GFRP) separated from Raw Crushed Wind Turbine Blade (RCWTB) and whole inclusions of RCWTB.

3.2.3.1 Effect of GRFP and RCWTB

The yield stress for cement pastes and mortars containing GFRP separated from RCWTB are shown in Figure 3-3, the results for mortars including whole inclusions of RCWTB are also displayed. As expected, higher GFRP additions lead to higher yield stress of the mixtures [14,15], in fact the presence of fibers hinders the flow of fine particles and increases the interfacial friction between fibers and aggregate [16–18].

The reference cementitious pastes (with 0% GFRP) exhibit yield stress of 55 Pa and 10 Pa for 0.4 W/C and 0.5 W/C ratios, respectively. Therefore, the yield stress grows almost linearly for higher GFRP fiber volume fraction, reaching values of 242 Pa for 0.4 W/C and 46 Pa for 0.5 W/C at 4.17% fiber volume fraction.

The reference mortar (with 0% GFRP) prepared with 40% sand over the total volume reached yield stress equal to 378 Pa and 109 Pa for 0.4 W/C and 0.5 W/C, respectively. In this case, the difference between GFRP and the whole RCWTB inclusion is not negligible. It is worth mentioning that for the series Mortar+RCWTB the fiber volume fraction graphed in the x-axis just counts the GFRP fibers contained in the RCWTB, whereas the other particles (i.e. polyurethane, balsa wood, micro-fibers and small non-separable particles) are deemed as part of the aggregate. The micro-fibers are also considered as part of the aggregate; this choice is mainly due to the fact they agglomerate in fluffs that do not separate and behave as dispersed fibers in the mixture. Consequently, the difference observed in Figure 3-3 between Mortar+GFRP and Mortar+RCWTB should be mainly attributed to the RCWTB components which are not GFRP fibers. Even if these constituents occupy a minor volume on the whole mixture (Table 3-1 and Table 3-2), their presence is significant due to some reasons: they have great sizes, indeed balsa wood and polyurethane have an average size of 5 mm; their density is quite different compared to sand and cement, balsa wood has a density of 330 kg/m^3 for example; the micro-fibers, even if agglomerated, might partially spread in the mix; balsa wood may absorb some free water, lowering the effective W/C ratio. As a result, a more limited yield stress growth is observed when just GFRP is added, rather than the whole RCWTB. For Mortar+GFRP series, the yield stress rise remains almost linear as for the cement paste, whereas an approximately quadratic trend can be observed for Mortar+RCWTB. Further, no yield stress increase was observed from 0.0% to 0.5% fiber volume fraction for 0.5 W/C mortars, probably the mixture is not stiff enough to activate the fibers in this range.

The relative yield stress was also calculated as the ratio between the experimental yield stress of the mixture containing fibers and the yield stress of the reference cementitious paste. Figure 3-4 shows the relative yield stress for each homogeneous group with the same W/C ratio and type of addition. It is interesting to observe the curves maintain almost the same slope while changing the W/C ratio.

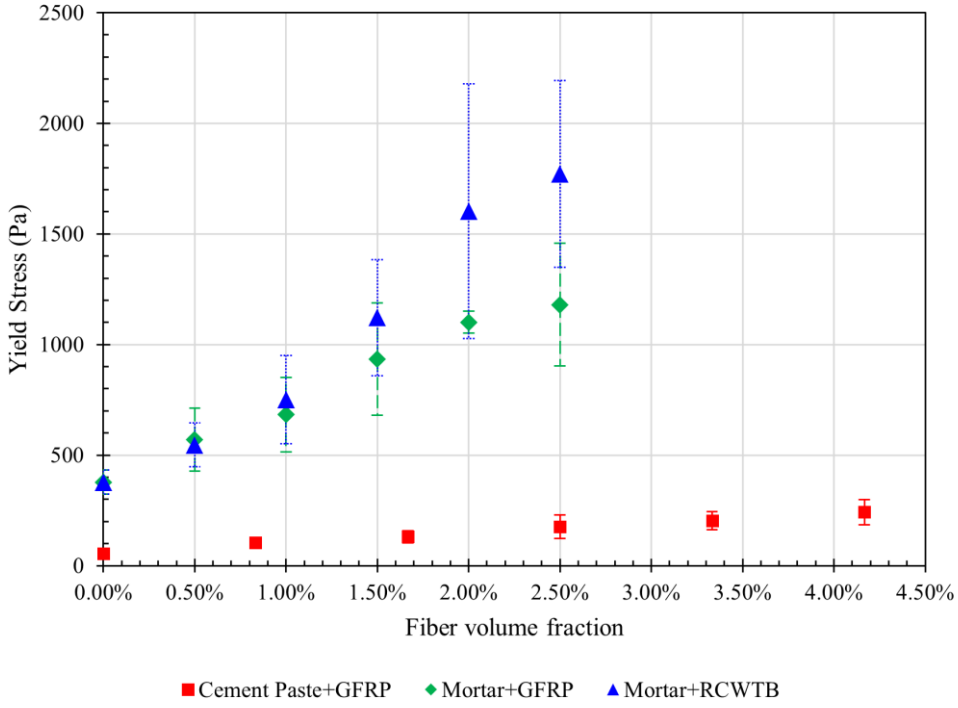

a)

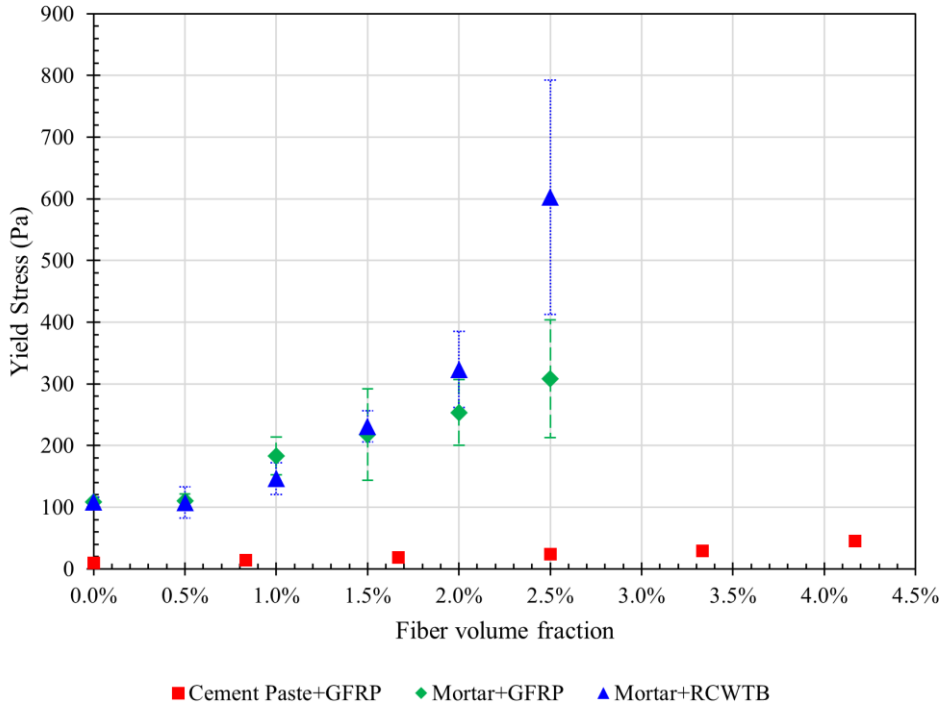

b)

Figure 3-3. Yield stress for the cementitious pastes and mortars prepared for this experimental campaign: a) W/C=0.4; b) W/C=0.5. Error bars indicate the standard deviation.

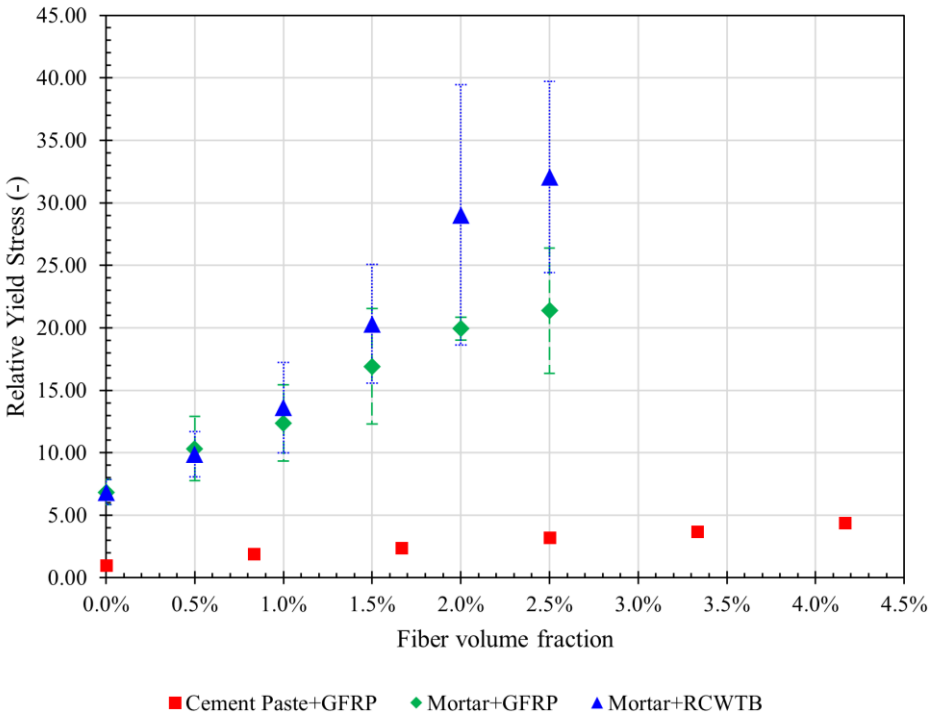

a)

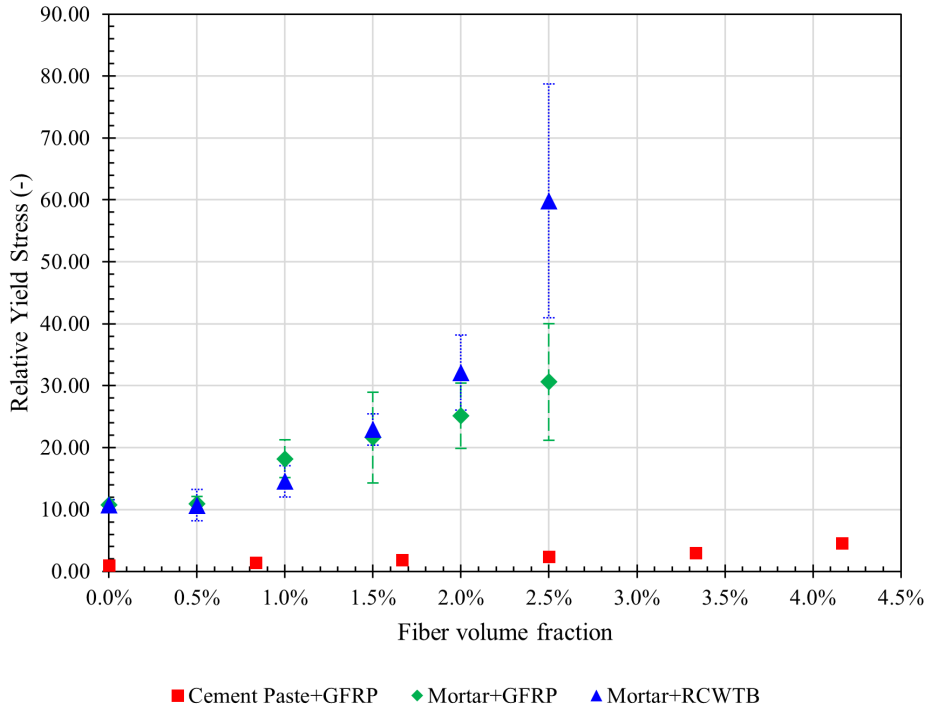

b)

Figure 3-4. Relative yield stress (i.e. ratio between the yield stress of the mixture containing fibers and the yield stress of the reference cement paste) for the cement pastes and mortars prepared in this work: a) W/C=0.4; b) W/C=0.5. Error bars indicate the standard deviation.

3.2.3.2 Effect of water/cement ratio

Mortars usually demonstrate an almost linear correlation between W/C ratio and workability [19,20], resulting in higher fluidity for higher W/C ratio. This observation can be largely verified even in this work for cementitious pastes and mortars containing GFRP or RCWTB.

Figure 3-5a displays the W/C ratio effect for cementitious pastes including GFRP separated from RCWTB. The trend is linear for both curves, i.e. 0.4 and 0.5 W/C, but the slope is different. As confirmation, the yield stress for the 0.4 W/C reference cement paste is 5.48 times higher than the 0.5 W/C counterpart, and this ratio appears to be almost constant, indeed the yield stress reaches 5.29 times higher value for the corresponding mixtures containing 4.17% fiber volume fraction.

Similar conclusions can be derived from Figure 3-5b for mortars including GFRP separated from RCWTB. In general, the trend appears to be linear, but with different slopes. In this case, the ratio between 0.4 and 0.5 W/C reference mortars yield stress is 3.48, and remains almost constant, in fact the same ratio for 2.5% fiber volume fraction reaches a value of 3.83.

Regarding mortars containing the whole RCWTB, whose results are presented in Figure 3-5c, the trend appears to be different from Figure 3-5b. In this case, the yield stress for the 0.4 W/C reference mortar is 3.48 times higher than the 0.5 W/C counterparts, while the yield stress attains 2.94 times higher value for the corresponding mixtures containing 2.5% fiber volume fraction. This observation confirms the trend is not linear in this case.

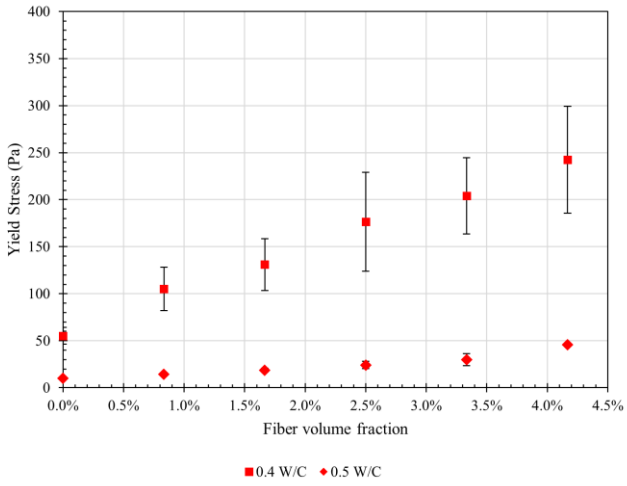

a)

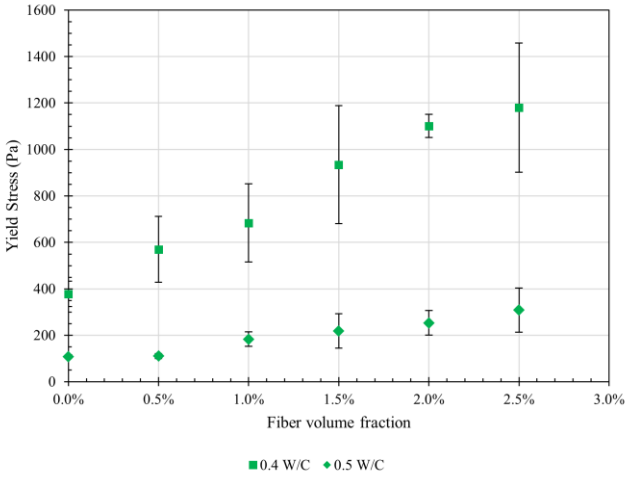

b)

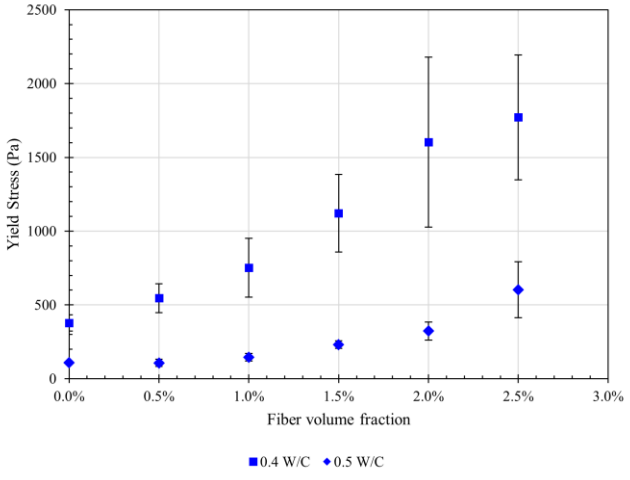

c)

Figure 3-5. Effect of the W/C ratio for: a) Cement Paste+GFRP; b) Mortar+GFRP; c) Mortar+RCWTB.

3.2.4 Analysis and discussion

The results presented in the previous section suggest that Glass Fiber Reinforced Polymer (GFRP) in Raw Crushed Wind Turbine Blade (RCWTB) can be treated as dispersed fibers into the cementitious mixture, whereas those components of RCWTB that do not have fiber-like appearance, such as balsa wood and polyurethane particles, can be considered as part of the aggregate.

In this subsection, a physical model proposed by Sultangaliyeva et al. [8] that predicts fibers conformation based on their elastic properties, geometry and the rheology of the surrounding cement-based material is applied and validated for RCWTB.

3.2.4.1 Analysis of the cementitious paste

In the case of rigid fibers with length L and diameter D, more direct mechanical contacts between fibers are noted when the fiber volume fraction is closer to the fiber volume fraction $1/R$, where R is the aspect ratio calculated as L/D. When the volume fraction reaches $1/R$, any motion must involve all adjacent fibers. Therefore, this is generally identified as the maximum packing fraction $_{fm}$ for rigid fibers. Thus, a relationship exists between the relative yield stress (i.e. ratio between the yield stress of the mixture containing fibers and the yield stress of the suspending reference paste) and the relative fiber volume fraction (i.e. ratio between the fiber volume fraction and the fiber maximum packing fraction) according to Equation 3-1:

$$\frac{\tau_0}{\tau_{00}} = \left(1 - \frac{\varphi_f}{\varphi_{fm}}\right)^{-2} \quad 3\text{-}1$$

Where τ_0/τ_{00} is the relative yield stress, φ_f indicates the fiber volume fraction within the mixture, and φ_{fm} is the fiber maximum packing fraction.

For flexible fibers, each fiber can be imagined as an elementary beam subjected to a linear load of $\tau_{00}D$, where τ_{00} is the yield stress of the cement paste/mortar stressing the fiber [7]. In this way, the maximum packing fraction of flexible fibers φ_{fm} should be proportional to Equation 3-2 [8]:

$$\varphi_{fm} \propto \left(\frac{E}{\tau_{00}}\right)^{-\frac{1}{5}} D^{\frac{2}{5}} L^{-\frac{1}{5}} \quad 3\text{-}2$$

Where E is the Young's Modulus, D is the diameter and L is the length of the flexible fiber.

In this section, Equation 3-3 is applied to predict the maximum packing fraction of GFRP according to the proportionality given in Equation 3-2:

$$\varphi_{fm} = a\left(\frac{E}{\tau_{00}}\right)^{-\frac{1}{5}} D^{\frac{2}{5}} L^{-\frac{1}{5}} \quad 3\text{-}3$$

Where a is a scaling factor that is calibrated according to the experimental data. All inputs of this formula are known or measured in previous works about the same GFRP contained in RCWTB. The average length and diameter were measured by Revilla-Cuesta et al. [21], resulting in values of approximately 13 mm and 0.73 mm for length and diameter, respectively; whereas the Young's Modulus was calculated in a more recent publication by Manso-Morato et al. [22], resulting in 25 GPa. It is worth noting that this value is relatively low compared to the approximately 210 GPa observed for steel fibers, for which the rigid fiber criterion applies [7]. Therefore, GFRP should be regarded as flexible.

Figure 3-6 graphs the theoretical model as for Equation 3-1 in dashed lines, whereas the experimental data are represented as dots. In Figure 3-6a, the GFRP fibers are considered stressed by the reference cement paste yield stress. Following this hypothesis, quite accurate predictions can be obtained up to about 0.5 fiber volume fraction, beyond this threshold the accuracy drops significantly, suggesting that fibers are not just stressed by the reference cement paste. Then, the GFRP fibers are considered as being stressed by the

overall mixture yield stress in Figure 3-6b. In this way, the predictions are much more accurate, especially for high fiber relative packing fraction.

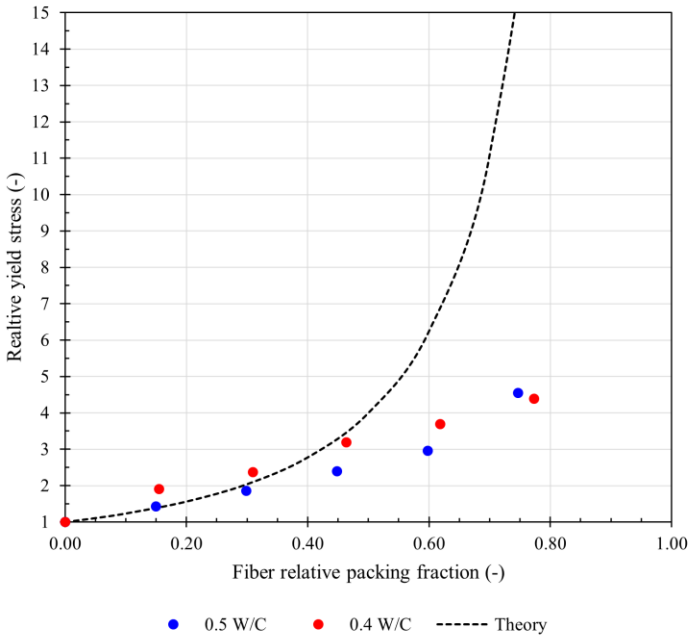

a)

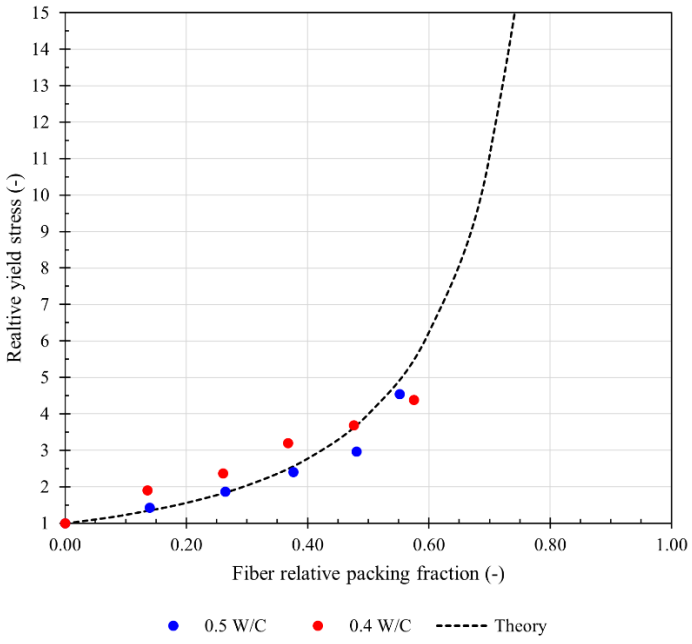

b)

Figure 3-6. Relative yield stress (i.e. ratio between the yield stress of the mixture containing fibers and the yield stress of the reference cement paste) as a function of the fiber relative packing fraction (i.e. ratio between the fiber volume fraction and the fiber maximum packing fraction) for cement pastes containing GFRP separated from RCWTB: a) GFRP fibers are considered as being deformed by the constitutive cement paste yield stress; b) GFRP fibers are considered as deformed by the overall mixture yield stress (paste and fibers).

3.2.4.2 Analysis of the mortars

In this subsection, the theory and principles applied in §3.2.4.1 for cementitious pastes are extended to mortars, therefore including the contribution of the aggregates.

3.2.4.2.1 Mortars containing GFRP separated from RCWTB

In mixtures containing fibers and aggregates, Equation 3-1 should be adjusted and extended to consider the contribution of the sand (Eq. 3-4):

$$\frac{\tau_0}{\tau_{00}} = \left(1 - \frac{\varphi_f}{\varphi_{fm}} - \frac{\varphi_s}{\varphi_{sm}}\right)^{-2} \quad 3\text{-}4$$

Where φ_s is sand volume fraction within the mixture, and φ_{sm} is the sand maximum packing fraction. The maximum packing fraction of the sand is measured as the loose packing fraction obtained through gravity flowing in a funnel located 5 cm above the top of the test container, which consists of a 2 liters cylinder. After weighing the filled container, the maximum packing fraction was calculated knowing the particle density. Following this approach, the sand used in this study demonstrates maximum packing fraction equal to 0.585.

Figure 3-7 shows the theoretical model as for Equation 3-4 in dashed lines, whereas the experimental data are displayed with dots. The total relative packing fraction in x-axis corresponds to the sum of the total relative packing fraction of both fiber and sand $\varphi_f/\varphi_{fm}+\varphi_s/\varphi_{sm}$. In Figure 3-7a, the GFRP fibers are counted as stressed by the reference cement paste yield stress. Following this assumption, the predictions are quite inaccurate, furthermore an experimental value is represented with total relative packing fraction higher than 1, which is meaningless from the physical point of view. The GFRP fibers are assumed as stressed by the yield stress of the reference mortar in Figure 3-7b. This means that fibers are considered strained uniquely by the reference cementitious paste and the sand. As expected, in this case the predictions are quite more accurate, especially for high total relative packing fraction. Though, the best predictions were found considering the GFRP fibers as stressed by the overall mixture yield stress, this means that each fiber is considered stressed by the cement paste, the sand and the other GFRP fibers (Figure 3-7c).

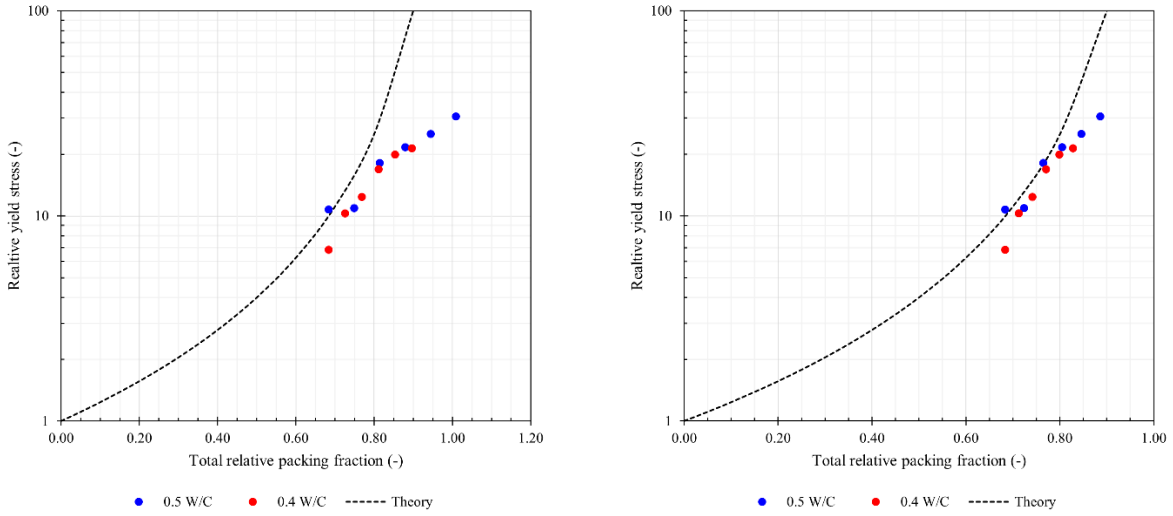

a)

b)

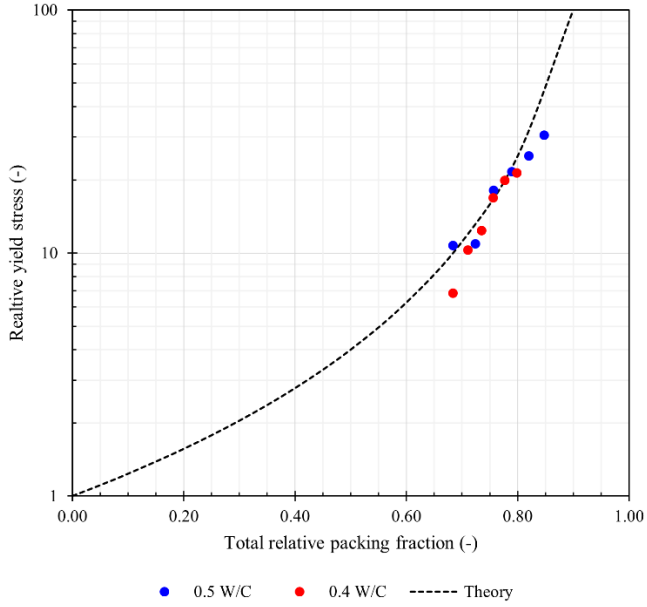

c)

Figure 3-7. Relative yield stress (i.e. ratio between the yield stress of the mortar containing fibers and the yield stress of the reference cement paste) as a function of the total relative packing fraction (i.e. the sum of the relative packing fraction of sand and fiber) for mortars containing GFRP separated from RCWTB: a) GFRP fibers are considered as being deformed by the constitutive cement paste yield stress; b) GFRP fibers are considered as deformed by the constitutive mortar yield stress (paste and sand); c) GFRP fibers are considered as deformed by the overall mixture yield stress (paste, sand and fibers).

3.2.4.2.2 Mortars containing whole RCWTB

The results found in the previous subsection §3.2.4.2.1 for mortars containing GFRP separated from RCWTB can be extended to whole RCWTB, even including aggregate-like particles like balsa wood and polyurethane particles. In this subsection, Equation 3-4 is employed to model the behavior of mortars incorporating whole RCWTB, whose particles that are not GFRP are considered part of the aggregate, like sand.

Figure 3-8a plots Equation 3-4 with a dashed line, while colorful dots are the experimental data. In this way, the RCWTB that are not GFRP are considered as sand in Equation 3-4. Here, GFRP fibers are deemed stressed by the overall mixture yield stress, this means that each fiber is stressed by the cement paste, the aggregates and the other GFRP fibers.

In Figure 3-8b, RCWTB particles that are not GFRP are treated separately from sand. These non-GFRP RCWTB particles are incorporated into Equation 3-4 through an additional term, with their maximum packing fraction measured in the same way as for sand. Further, GFRP fibers are assumed to be stressed according to the overall mixture yield stress.

The theoretical model shows great agreement with experimental data, which is noteworthy given that RCWTB is a recycled material and typically exhibits greater variability in physical properties than conventional fibers and aggregates made from virgin raw materials. The proportion of RCWTB with aggregate-like characteristics was found to be negligible in the total volume (Table 3-1 and Table 3-2, Mortar+RCWTB series) for the inputs in Equation 3-4, as shown in Figure 3-8. Therefore, treating the non-fiber-like RCWTB particles as part of the sand is a valid and reasonable simplification.

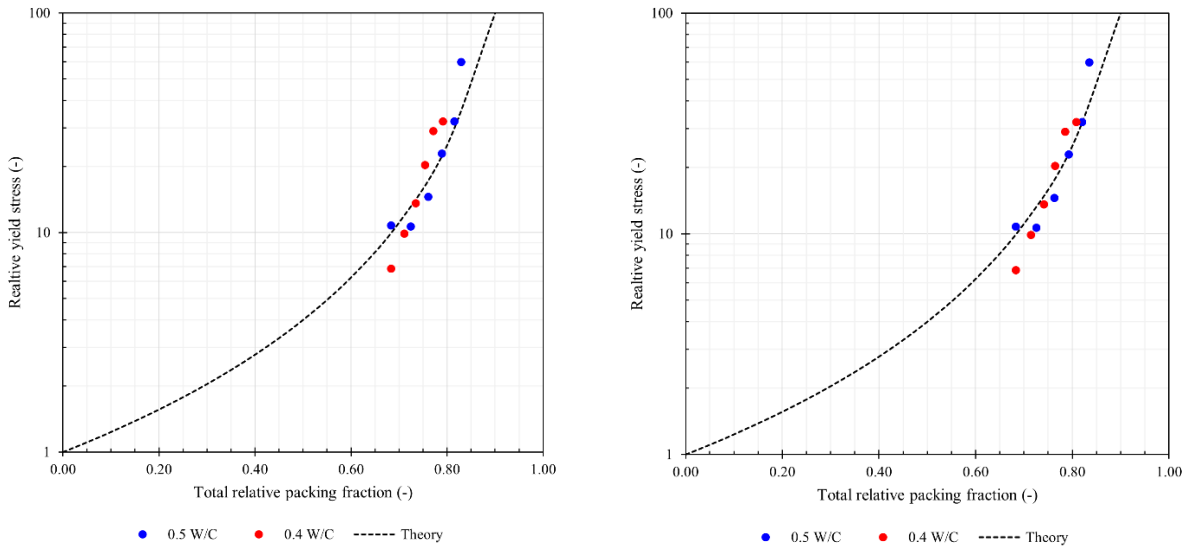

Figure 3-8. Relative yield stress (i.e. ratio between the yield stress of the mortar containing fibers and the yield stress of the reference cement paste) as a function of the total relative packing fraction (i.e. the sum of the relative packing fraction of aggregate and fiber) for whole RCWTB inclusions: a) GFRP fibers are considered as deformed by the overall mixture yield stress (paste, aggregate and fibers), whereas RCWTB aggregate-like particles are considered as part of the sand; b) GFRP fibers are considered as deformed by the overall mixture yield stress, whereas RCWTB aggregate-like particles are not considered as part of the sand.

3.2.5 Conclusions

In this study, the yield stress of cementitious pastes and mortars incorporating either Glass Fiber Reinforced Polymer (GFRP) extracted from Raw Crushed Wind Turbine Blades (RCWTB) or whole RCWTB was experimentally measured and theoretically modeled. The following conclusions were drawn:

- Increasing the content of GFRP fibers leads to a higher yield stress in the mixtures. This is attributed to the fibers inhibiting the mobility of fine particles and increasing interfacial friction between the fibers and aggregates.
- A notable distinction was observed between mortars containing only GFRP fibers and those incorporating the entire RCWTB. This difference is due to the presence of aggregate-like particles in the RCWTB, such as balsa wood and polyurethane particles, which have distinct physical characteristics compared to conventional aggregates. Consequently, the increase in yield stress is more pronounced when using whole RCWTB than when using GFRP alone.
- An approximately linear increase in yield stress was observed for mixes containing only GFRP fibers. In contrast, mortars including the full RCWTB exhibited a nearly quadratic increase.
- The predictive model employed demonstrated good accuracy in estimating the relative yield stress by considering the GFRP fibers as flexible entities when calculating their maximum packing fraction. Nevertheless, the highest agreement with experimental results was achieved when assuming that the GFRP fibers are subjected to the yield stress of the entire mixture, rather than just that of the reference cement paste or mortar.

3.3 IMPROVING RECYCLED AGGREGATE CONCRETE WITH RAW CRUSHED WIND TURBINE BLADE

3.3.1 Introduction

Despite its environmental benefits, the use of recycled aggregates as a replacement for conventional aggregates remains contained due to the typically inferior performance of the resulting concrete [23]. This performance degradation associated with recycled aggregates is evident across all concrete curing times [24], though it is particularly notable at early ages. This is because recycled aggregates tend to delay the development of concrete strength during the initial curing phase [25,26]. Additionally, their high deformability negatively affects strength development, especially while the cementitious matrix is still hardening [24]. These factors not only compromise mechanical performance but also contribute to increased plastic shrinkage, which promotes crack formation and weakens the long-term durability of the concrete [23].

Nonetheless, the properties of Recycled Aggregate Concrete (RAC) can be significantly enhanced through various strategies. These include the removal or strengthening of adhered mortar on the recycled aggregate surface [27–30], the incorporation of supplementary cementitious materials [31,32], and particularly, the addition of fibers, which offers several benefits to RAC [33–35]. Among these, fiber reinforcement stands out for its ability to clearly improve the tensile properties of RAC, which are generally poor due to weak bond between the cementitious matrix and the recycled aggregate [36]. Fibers also help controlling the initiation and propagation of micro-cracks, thereby enhancing RAC durability [37,38]. Furthermore, since recycled aggregates contain mortar fragments that contribute to shrinkage-induced cracking, fibers serve as rigid inclusions that constrain internal contraction, mitigating these effects [36].

Glass Fiber-Reinforced Polymer (GFRP) is a composite material consisting of glass fibers embedded within a polymeric epoxy resin matrix. Its use has expanded significantly in recent years across sectors such as construction, aerospace, and energy, owing to its excellent mechanical performance [39]. In 2017, the United States alone reported an annual consumption of nearly 2 million tons of GFRP materials [40]. This rapid growth in production and usage has led to a corresponding increase in GFRP composite waste generation [41].

In this context, wind turbine blades are predominantly composed of GFRP composites, except for the metallic hub connection. To improve mechanical performance and reduce weight, additional lightweight materials such as balsa wood and polymers are incorporated into a GFRP sandwich structure [42]. Blade surfaces are further treated with polymeric resin coatings, and polyvinyl chloride stiffeners may also be present [11]. The integration of these various materials complicates separation and recycling processes, making blade recycling a challenging research area. One viable recycling method involves the production of Raw-Crushed Wind-Turbine Blade (RCWTB), which is generated by crushing entire blades without prior separation of their components [43]. The resulting material comprises GFRP fibers mixed with nearly spherical particles of balsa wood and polyurethane [42].

In this subsection, RCWTB was included into concrete to mitigate the adverse effects of Coarse Recycled Aggregate (CRA), a topic not yet explored in existing scientific literature to the best of the author's knowledge. The specific objective was to review whether RCWTB can enhance the early-age performance of RAC, with a particular focus on shrinkage, compressive strength, and flexural strength under varying curing conditions. Early-age behavior was prioritized due to its susceptibility to the negative

impacts of recycled aggregates [24]. Therefore, the study aimed to determine whether RCWTB can contribute to a more favorable balance of these properties in CRA-based concrete at early stages.

3.3.2 Experimental methods

3.3.2.1 Materials

Cement CEM II/A-L 42.5 R, conforming to BS EN 197-1 [9], was used in this experimental program. This cement type incorporates limestone as a partial clinker replacement, with a replacement level ranging from 6% to 20%. Tap water from the municipal supply network in Burgos (Spain) was utilized for mixing. To attain adequate workability at a reduced water-to-cement ratio, two plasticizer admixtures were included. Both were based on modified polycarboxylates: one in a water-based formulation and the other in a standard form, selected for their synergistic interaction.

A total of five different aggregates were combined to obtain a well-graded mix. Their Saturated Surface-Dry (SSD) density and 24-hour Water Absorption (WA) were determined according to BS EN 1097-6 [44], and their particle size distributions are presented in Figure 3-9. The aggregate types included: three siliceous fractions 12/22 mm (SSD density: 2.60 kg/dm^3, WA: 0.55%), 4/12 mm (SSD density: 2.63 kg/dm^3, WA: 0.33%), and 0/4 mm (SSD density: 2.62 kg/dm^3, WA: 0.13%); a limestone sand with a 0/2 mm grading (SSD density: 2.66 kg/dm^3, WA: 0.10%); and a coarse recycled aggregate (CRA) in the 4/22 mm range (SSD density: 2.44 kg/dm^3, WA: 6.12%).

The CRA used in this study was obtained from crushed concrete elements originally made with siliceous aggregate and demonstrating a characteristic compressive strength of 45 MPa. Supplied by a Spanish company specialized in construction and demolition waste (C&DW), the CRA was over five years old at the time of use, ensuring that the shrinkage and strength development of the adhered mortar had already stabilized. In the laboratory, the material was carefully sieved and sorted to isolate only the coarse fraction between 4 and 22 mm.

The RCWTB was produced by crushing rectangular panels (20-30 cm per side) made of GFRP composite, balsa wood, and polymer layers using a knife mill, followed by sieving. The resulting material contained GFRP-composite fibers and roughly spherical particles of balsa wood and polyurethane. On average, the GFRP made up 66.8% of the RCWTB by weight, with mean dimensions of 13.1 mm in length and 0.73 mm in diameter, yielding an aspect ratio of about 18. The bulk density of the RCWTB is 1.63 kg/dm^3, as determined following BS EN 1097-6 [44].

Figure 3-10 depicts the aggregates and the RCWTB used in the experimental campaign.

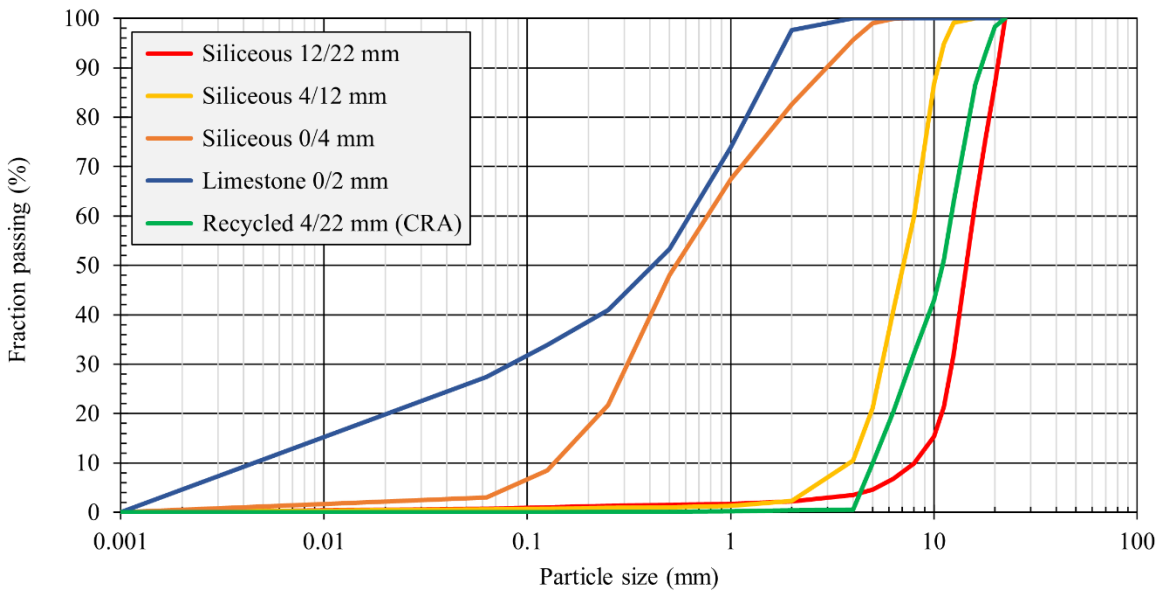

Figure 3-9. Granulometric distribution of the aggregates.

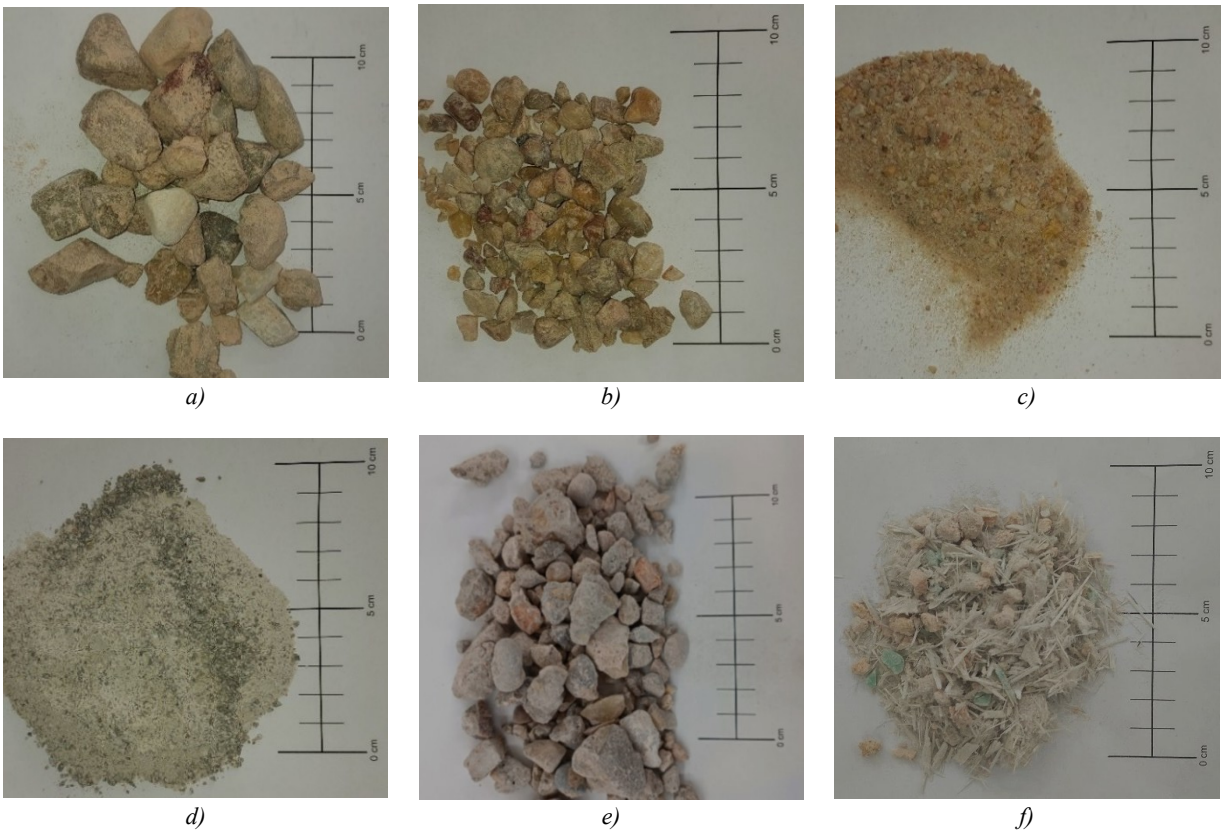

Figure 3-10. Materials employed in the experimental campaign: a) siliceous aggregate 12/22 mm; b) siliceous aggregate 4/12 mm; c) siliceous aggregate 0/4 mm; d) limestone aggregate 0/2 mm; e) CRA 4/22 mm; f) RCWTB.

3.3.2.2 Mix design

A total of six concrete mixtures were produced in this study. Three served as reference mixes, incorporating Coarse Recycled Aggregate (CRA) at replacement levels of 0%, 50%, and 100%, without the addition of Raw-Crushed Wind-Turbine Blade (RCWTB). The remaining three mixes included 6% RCWTB by total aggregate volume.

The mix design was designed according to the following considerations:

- The RCWTB content was fixed at 6% of the total aggregate volume, based on previous findings [42] indicating that this proportion leads to an improvement in the flexural strength of conventional concrete.
- CRA was included using a volume-based replacement approach. Due to its lower density compared to natural aggregates, the total aggregate mass was reduced in mixtures containing CRA.
- The cement dosage was maintained at a constant 320 kg/m^3 across all mixtures. However, the water content was slightly increased in the CRA-containing mixes to maintain a constant effective water-to-cement ratio, accounting for the higher water absorption of CRA. The total dosage of plasticizer was fixed at 1% of the cement mass in all cases.

Mix proportions are defined in Table 3-3. Concrete labels for each mix include two parts: the former indicates the CRA replacement level, and the latter whether RCWTB was incorporated.

Table 3-3. Mix design (in kg/m^3).

	0CRA/ 0RCWTB	***50CRA/ 0RCWTB***	***100CRA/ 0RCWTB***	***0CRA/ 6RCWTB***	***50CRA/ 6RCWTB***	***100CRA/ 6RCWTB***
Cement	320	320	320	320	320	320
Water	130	140	150	130	140	150
w/c ratio	0.41	0.44	0.47	0.41	0.44	0.47
Plasticizer 1	1.07	1.07	1.07	1.07	1.07	1.07
Plasticizer 2	2.13	2.13	2.13	2.13	2.13	2.13
Siliceous 12/22 mm	780	390	0	733	367	0
Siliceous 4/12 mm	555	277	0	522	261	0
Siliceous 0/4 mm	385	385	385	362	362	362
Limestone 0/2 mm	280	280	280	263	263	263
CRA 4/22 mm	0	623	1246	0	586	1171
RCWTB	0	0	0	75	75	75

3.3.2.3 Testing program

This study explores both the fresh and hardened properties of concrete mixtures. Two curing regimes, ambient and moist, were applied to describe the differences in strength development resulting from variations in cement hydration kinetics [45].

Fresh properties, including slump, fresh density, and air content, were measured during casting according to BS EN 12350-2 [46], BS EN 12350-6 [47], and BS EN 12350-7 [48], respectively. For each concrete mix, a set of specimens was prepared: fifteen cylinders (100×200 mm), fifteen prisms (75×75×275 mm), and three cubes (100×100×100 mm). Following casting and vibration, the specimens were covered with plastic sheets to prevent moisture loss and left to cure in a controlled laboratory environment (20±2 °C, 50±5% RH) for 24 hours.

Initial mechanical testing was conducted after 24 hours of curing, with three cylinders and three prisms tested for compressive and flexural strength, respectively. Subsequently, the remaining specimens were divided between two curing conditions: six cylinders and six prisms were placed in a moist curing chamber (20±2 °C, 90±5% RH), while the others were stored under ambient conditions (20 ± 2 °C, 60 ± 5% RH). Compressive and flexural strength were evaluated at 3 and 7 days for both curing environments, following BS EN 12390-3 [49] and BS EN 12390-5 [50], respectively. In addition, a predictive model was developed to estimate flexural strength based on compressive strength for the types of concrete studied. Hardened density was measured using the cubic samples after 1, 3, and 7 days of ambient curing, in accordance with BS EN 12390-7 [48].

Plastic shrinkage was monitored over the first three days of ambient curing using a custom testing setup developed by Ortega-López et al. [51]. Fresh concrete was poured into a 1 meter long channel with one end fixed and the other free to move during setting. A digital comparator, accurate to ±0.01 mm, was attached to the free end to track shrinkage-induced displacement.

To further understand the mechanical performance of the mixes, Scanning Electron Microscopy (SEM) and Energy Dispersive X-ray (EDX) analyses were conducted on fractured specimens. These analyses focused on the Interfacial Transition Zones (ITZs) between the RCWTB components and the cementitious matrix. SEM imaging, conducted with a JEOL JSM-6460LV microscope at up to 1000× magnification, was accompanied by EDX spectra to provide insight into the microstructural and chemical interactions [52,53].

Finally, a cost analysis was also carried out to evaluate the economic feasibility of using CRA and RCWTB in concrete production.

3.3.3 Results

3.3.3.1 Fresh properties

The results of the fresh concrete tests are summarized in Table 3-4. A general reduction in workability was observed with the substitution of natural coarse aggregate by Coarse Recycled Aggregate (CRA) and further reduced with the incorporation of Raw Crushed Wind Turbine Blade (RCWTB). This decrease can be attributed to the intrinsic features of recycled aggregates, which typically exhibit more angular shapes and rougher surface textures, leading to increased interparticle friction which hinders concrete flow [54]. Similarly, the inclusion of fibrous materials, such as those present in RCWTB, limits the mobility of the concrete components, further reducing workability [55]. These effects suggest that a higher water-to-cement ratio is necessary when using CRA in concrete mixes [56,57], and an even greater adjustment may be needed when RCWTB is included. This is demonstrated by the extremely low slump value of just 1 cm recorded for the 100CRA/6RCWTB mixture.

Mehdipour et al. [58] reported that incorporating 2% by volume of 12-mm glass fibers into concrete leads to a 40% reduction in workability, while increasing the fiber content to 3% results in a 75% decrease. In the present study, the estimated fiber content from the GFRP composite within the RCWTB additions was approximately 2.5% by volume, assuming an average fiber density of 2.04 kg/dm^3 [21]. The inclusion of RCWTB led to workability reductions of 0%, 25%, and 80% when combined with 0%, 50%, and 100% CRA, respectively. Although workability worsened with increasing CRA content, the observed values, up to 50% CRA, were still more promising than those reported by Mehdipour et al. [58], despite the use of recycled fibers in this study. It is also important to note that the presence of balsa wood and polyurethane particles in RCWTB likely contributed to the observed reduction in workability.

Fresh density decreased progressively with increasing CRA content and with the incorporation of RCWTB. This decline followed a near-linear trend due to the lower density and higher porosity of CRA attributable to the presence of adhered mortar [59]. Additionally, higher CRA replacement levels required increased water content, which further contributed to a more porous microstructure [60]. Similarly, RCWTB reduced fresh density due to the substantial density contrast between RCWTB components (~1.63 kg/dm^3) and conventional aggregates (~2.60 kg/dm^3), as previously observed by Revilla-Cuesta et al. [42].

Air content also followed a consistent trend, increasing with greater proportions of both CRA and RCWTB. The simultaneous incorporation of 100% CRA and 6% RCWTB resulted in an absolute increase of 1.7% in air content. This rise is primarily attributed to the rough surface texture and angular geometry of CRA, which promote air entrapment during mixing [54]. In addition, RCWTB contributes to elevated air retention due to the inclusion of fibers [61] and the presence of lightweight, porous materials such as balsa wood and polyurethane [62,63].

Table 3-4. Results of fresh tests.

	0CRA/ 0RCWTB	***50CRA/ 0RCWTB***	***100CRA/ 0RCWTB***	***0CRA/ 6RCWTB***	***50CRA/ 6RCWTB***	***100CRA/ 6RCWTB***
Slump (cm)	15	17	5	15	13	1
Fresh density (in kg/m^3)	2.46	2.37	2.33	2.39	2.32	2.29
Air content (% vol)	2.4	2.1	3.2	3.0	3.7	4.1

3.3.3.2 Hardened density

The hardened density results are presented in Table 3-5. As observed with fresh density, hardened density decreased with increasing levels of CRA replacement and RCWTB incorporation. These reductions can be attributed to the same factors discussed for fresh density, namely the lower density and higher porosity of both CRA and RCWTB components [64]. Additionally, all concrete mixes exhibited a slight decrease in weight over time, primarily due to ongoing water evaporation during the early stages of curing [65]. This effect was slightly more pronounced in mixtures containing RCWTB. It is worth noting that the cubic specimens used for hardened density measurements were cured under ambient conditions (20 ± 2 °C and 60 ± 5 % relative humidity), which further promoted moisture loss.

Table 3-5. Hardened density (in kg/m³).

	0CRA/ 0RCWTB	***50CRA/ 0RCWTB***	***100CRA/ 0RCWTB***	***0CRA/ 6RCWTB***	***50CRA/ 6RCWTB***	***100CRA/ 6RCWTB***
1 day	2.45	2.37	2.34	2.36	2.32	2.30
3 days	2.43	2.36	2.33	2.36	2.31	2.29
7 days	2.43	2.36	2.32	2.35	2.31	2.28

3.3.3.3 Plastic shrinkage

The results of the plastic shrinkage test are illustrated in Figure 3-11. Most shrinkage took place within the first 10 hours of curing, after which the rate of shrinkage gradually slowed down. All concrete mixtures displayed detectable shrinkage, with absolute values remaining below -0.7 mm/m after 72 hours of ambient curing, except for the 100CRA/0RCWTB mixture, which showed a significantly higher shrinkage of -1.07 mm/m at the same age. This elevated shrinkage is consistent with the known behavior of CRA, which typically increases shrinkage due to its higher flexibility and water absorption compared to natural aggregates [66]. Particularly, the inclusion of 50% CRA had a minor impact on plastic shrinkage, while the use of 100% CRA led to a substantial increase. After 72 hours, the 100CRA/0RCWTB mix displayed 70% more shrinkage than the 0CRA/0RCWTB reference, whereas the 50CRA/0RCWTB mix exhibited only a 3% increase.

The inclusion of RCWTB significantly mitigated plastic shrinkage. The GFRP-composite fibers present in RCWTB produced a bridging effect similar to that observed in conventional fiber-reinforced concretes using commercial fibers [67]. These fibers contributed to the formation of a more cohesive matrix, reducing the extent of expansion and contraction by acting as rigid inclusions within the cementitious network [68]. This shrinkage reduction was especially pronounced in mixtures with higher CRA content, likely due to enhanced mechanical interlocking between the GFRP fibers and the rough CRA surface [36]. For example, the addition of RCWTB to concrete containing 100% CRA reduced plastic shrinkage by 47% after 72 hours, whereas a more modest reduction of 21% was observed in concrete with natural aggregates only. Consequently, when 6% RCWTB was incorporated, variations in CRA content had a minimum effect on plastic shrinkage, indicating a stabilizing influence of the recycled fibers.

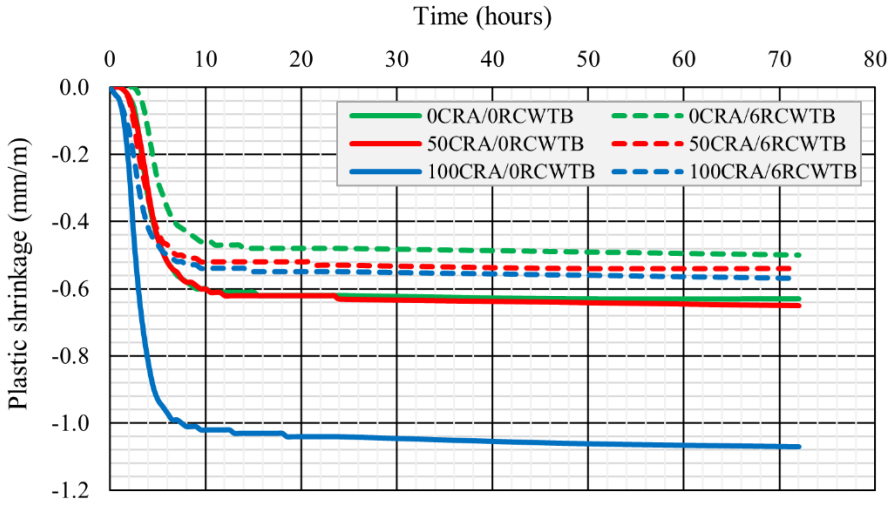

Figure 3-11.Plastic shrinkage: evolution over three days.

3.3.3.4 Mechanical properties

3.3.3.4.1 Compressive strength

The compressive strength results are given in Figure 3-12a for ambient curing and Figure 3-12b for moist curing. All concrete mixtures achieved compressive strengths beyond 40 MPa at 7 days under both curing conditions, confirming their suitability for structural use according to the European standard EN 1992-1-1 (Eurocode 2) [69].

As expected, the conventional 0CRA/0RCWTB concrete mix exhibited the highest compressive strength, consistent with existing literature indicating that the inclusion of both CRA and RCWTB tends to reduce compressive strength [42,70,71]. This can be attributed to the following factors:

- Coarse Recycled Aggregate (CRA): The strength reduction is primarily due to the presence of residual mortar on the surface of CRA, which is generally soft and highly porous. Additionally, concrete made with CRA features two distinct Interfacial Transition Zones (ITZs): the former between the natural aggregate and the old mortar, and the latter between the CRA and the new cementitious matrix [23]. These dual ITZs weaken the internal structure, as ITZs are known to be the most vulnerable zones in concrete, where cracks are likely to initiate and propagate [52,53].
- Raw Crushed Wind Turbine Blade (RCWTB): Likewise, RCWTB contributes to strength reduction due to the presence of low-adhesion components such as balsa wood and polyurethane, which weaken the quality of ITZs [72,73]. Moreover, the GFRP-composite fibers in RCWTB are more effective at enhancing flexural and deformational performance than compressive strength [74]. As a result, the addition of 6% RCWTB led to a 6% reduction in compressive strength in the mix with 0% CRA after 7 days of ambient curing. In mixes with 50% and 100% CRA, the strength was reduced by only 5%, suggesting a favorable interaction between RCWTB and CRA. A similar trend was observed under moist curing, with one notable exclusion: the mix containing 50% CRA experienced a 7% increase in compressive strength with the addition of 6% RCWTB. This improvement is likely a consequence of the synergistic interaction between the two recycled materials. A comparable positive effect of combining hybrid steel and polypropylene fibers in recycled aggregate concrete was previously demonstrated by He et al. [75]. Similar mechanical performance was achieved in this work using RCWTB, which is a recycled waste material.

Another relevant analyzed aspect is the strength evolution over time. Moist curing is widely recognized for enhancing strength by promoting cement hydration regardless of mix composition [76,77], a trend confirmed in this study. Interestingly, excluding the 0CRA/0RCWTB mix, the differences in compressive strength among mixes under ambient curing were more pronounced than for moist curing. Under moist conditions, the concrete mixes showed more uniform strength levels and clearer benefits from the inclusion of RCWTB, particularly in mixes containing CRA.

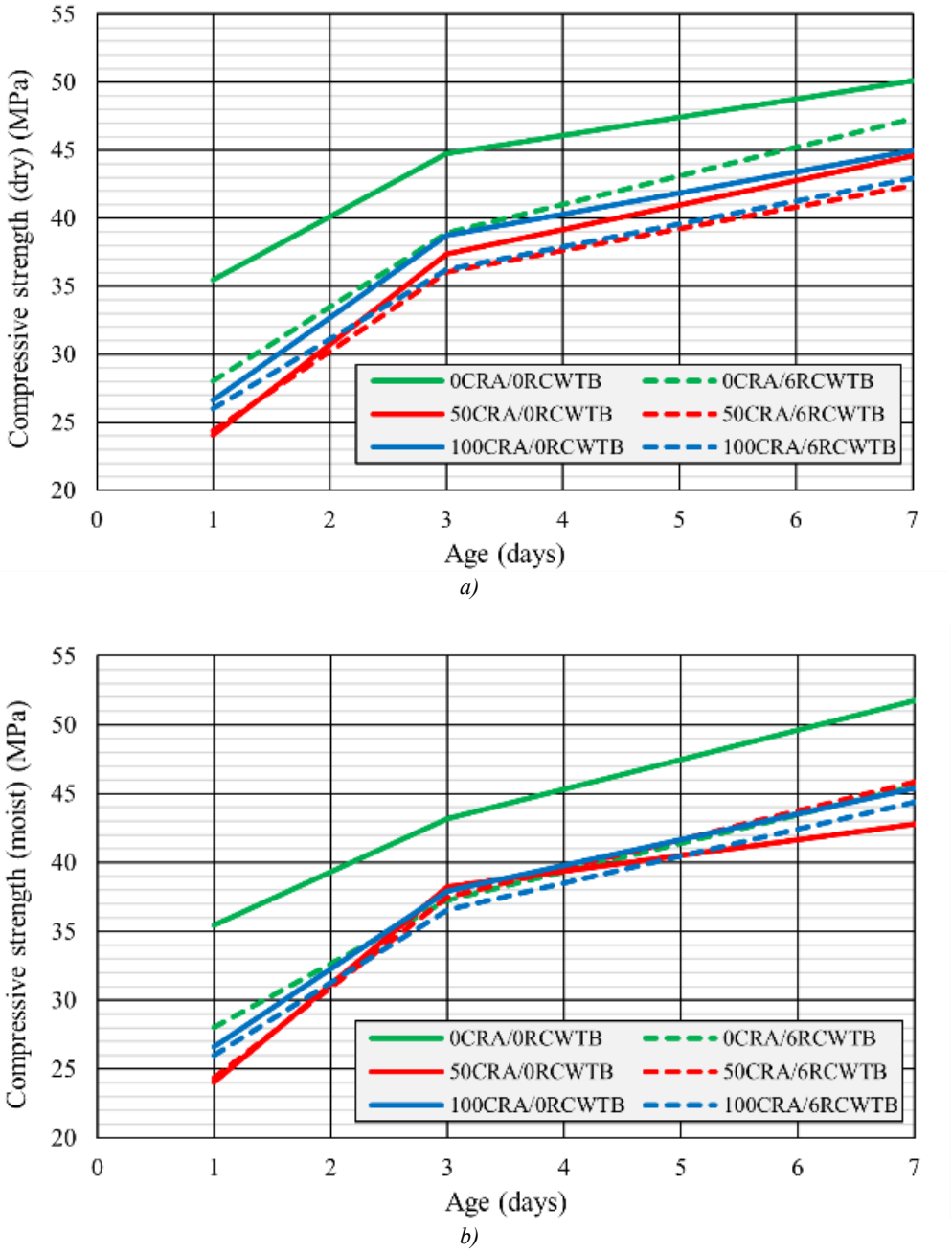

Figure 3-12. Compressive strength test results: a) evolution under ambient curing; b) evolution under moist curing.

3.3.3.5 Flexural strength

Flexural strength results are presented in Figure 3-13a and Figure 3-13b for ambient and moist curing, respectively. After 7 days of curing under both conditions, all concrete mixes achieved a minimum flexural strength of 4.5 MPa.

Examining the mixes without RCWTB, a clear deterioration of flexural strength was observed while increasing CRA content. The 0CRA/0RCWTB mix consistently demonstrated the highest strength across all curing ages and environments. The 50CRA/0RCWTB and 100CRA/0RCWTB mixes experienced similar flexural strength at 1 day; however, the 50% CRA mix showed a greater strength gain over time, resulting in a 7% higher flexural strength at 7 days. This reduction in flexural strength with higher CRA replacement is attributed to the same factors affecting compressive strength, i.e. weaker and more porous ITZs due to the presence of old mortar, and the increased water content required in mixes containing CRA [78].

Contrasting compressive strength, the inclusion of RCWTB had a positive impact on flexural strength. Although prior studies have shown that RCWTB does not substantially enhance the flexural strength of conventional concrete [42], the current results reveal a marked improvement when RCWTB is combined with 50% or 100% CRA. This effect is clearly proved in Figure 3-14a and Figure 3-14b, which shows strength developments at 3 and 7 days. After 7 days of ambient curing, the incorporation of 6% RCWTB led to increases in flexural strength of 2%, 11%, and 8% for concrete with 0%, 50%, and 100% CRA, respectively. Under moist curing, the gains were 1%, 13%, and 14%, respectively. The combination of 50% CRA and RCWTB was particularly advantageous, with the 50CRA/6RCWTB mix exceeding the flexural strength of both 0CRA mixes across all curing times and conditions.

These results suggest that RCWTB can effectively offset the negative impact of CRA on flexural strength, with further improvements observed under moist curing. The GFRP-composite fibers within RCWTB played a key role by providing a bridging mechanism across microcracks in the cementitious matrix [74]. Furthermore, the beneficial interaction between RCWTB and CRA is noteworthy, as the improvement was more pronounced when both materials were used together, an effect also reported in the literature for other types of fibers [36,38]. The weak bond between CRA and the cement paste increases the influence of the fibers to the concrete tensile behavior, as they help mitigating microcrack propagation in the ITZs [37]. The frictional interaction between the rough CRA particles and the GFRP-composite fibers may further enhance the bridging effect [28].

Xu et al. [79] reported flexural strength increases of 4.34%, 13.30%, and 37.85% for fiber volume fractions of 0.5%, 1.5%, and 2.5%, respectively, using macro-fibers derived from dismantled wind-turbine blades. Rodin et al. [80] also reported optimal strength gains at 5% fiber volume using recycled GFRP fibers from end-of-life turbine blades. In the present study, a similar improvement was achieved with 6% RCWTB by volume. Though, it is important to note that RCWTB includes not only GFRP fibers but also balsa wood and polyurethane particles, which can partially weaken the overall strengthening effect.

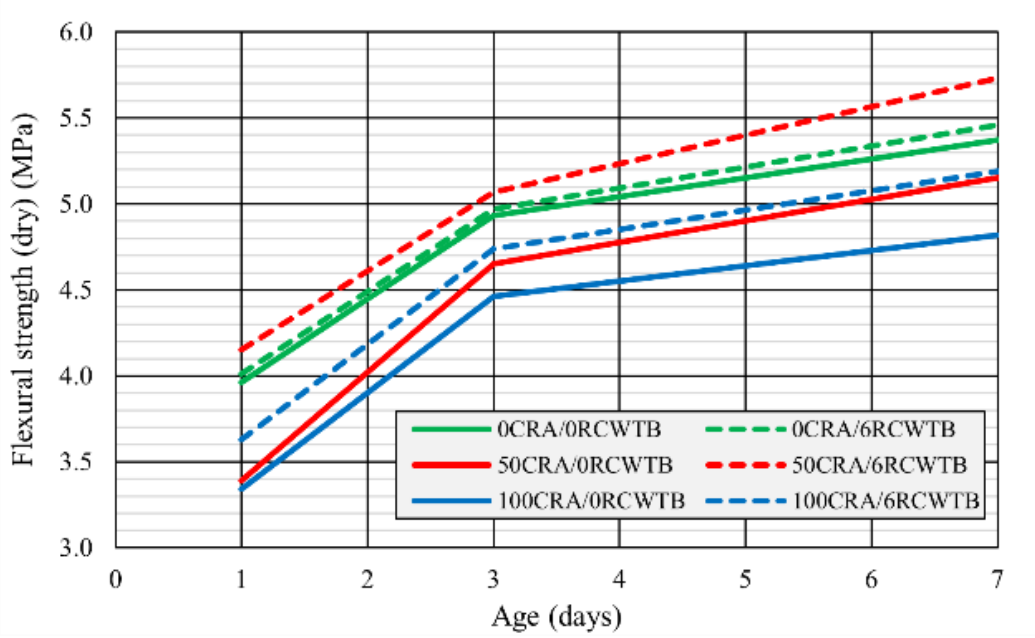

a)

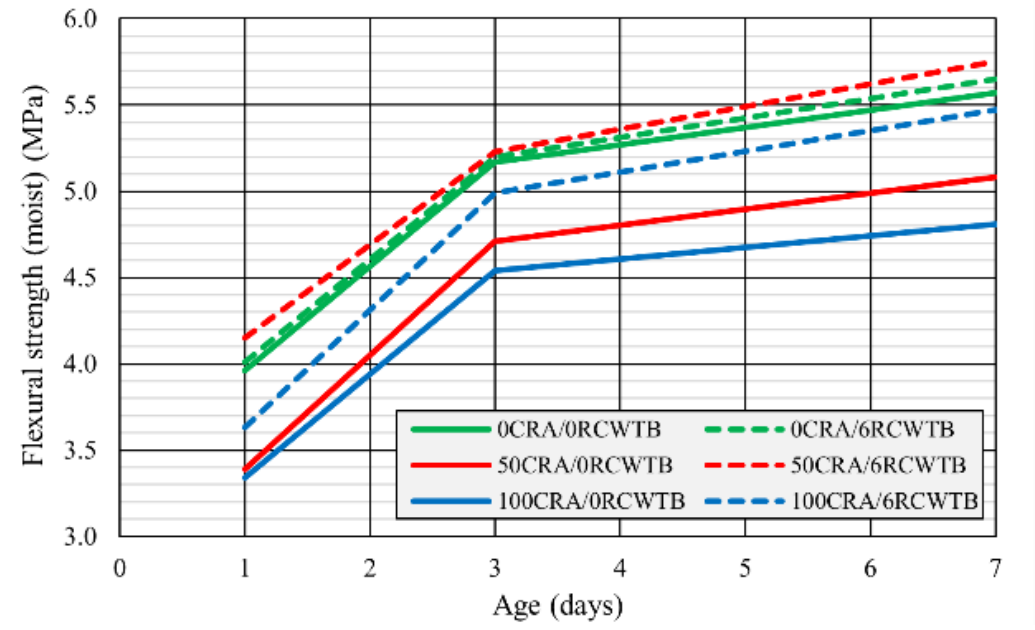

b)

Figure 3-13. Flexural strength test results: a) evolution under ambient curing; b) evolution under moist curing.

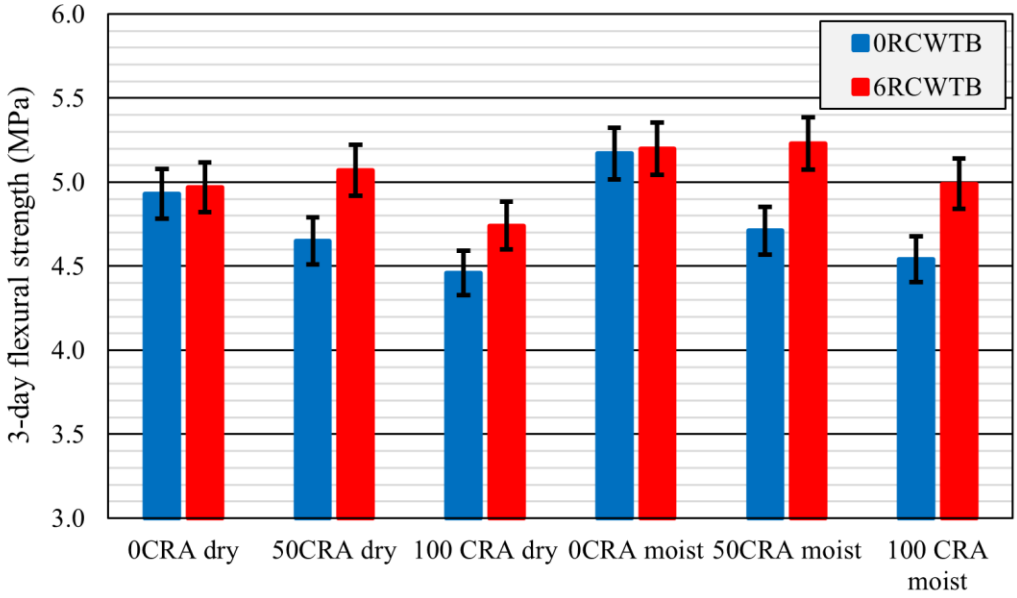

a)

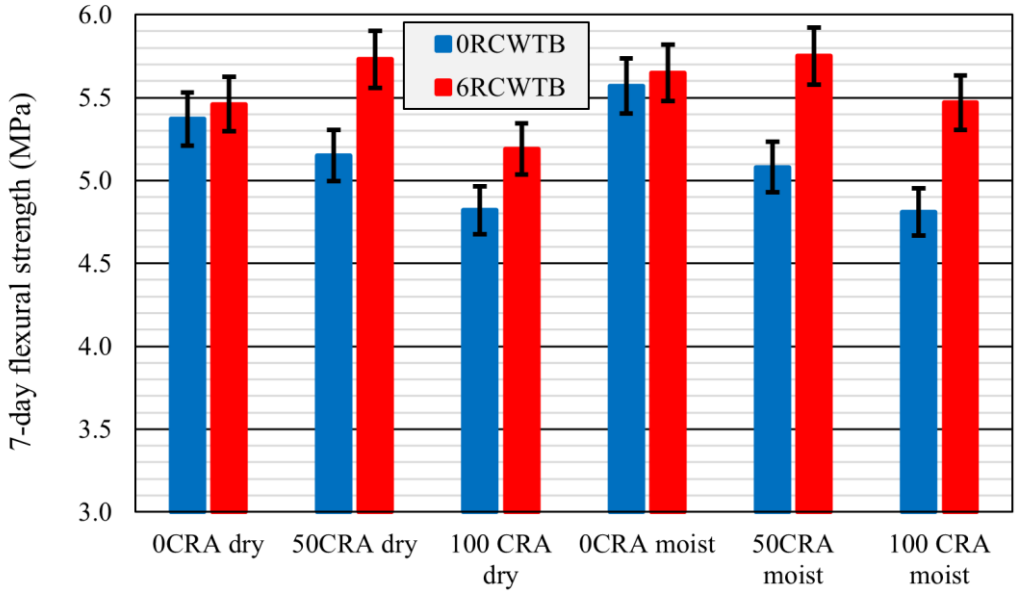

b)

Figure 3-14. Flexural strength test results: a) effect of RCWTB in 3-day flexural strength; b) effect of RCWTB in 7-day flexural strength.

3.3.3.6 Microstructural analysis

Microstructural analyses were carried out to gain deeper insights into the mechanisms underlying the early-age performance of concrete mixtures incorporating CRA and RCWTB. Figure 3-15 presents Scanning Electron Microscope (SEM) images of the Interfacial Transition Zones (ITZs) surrounding a GFRP-composite fiber and a polymeric particle. In addition, Figure 3-16 and Figure 3-17 display the corresponding Energy Dispersive X-ray (EDX) spectra for the same GFRP-composite fiber and polymeric particle, respectively.

Regarding the GFRP-composite fibers, SEM analysis revealed a strong bond with the cementitious matrix (Figure 3-15a), as the fiber ends remained well embedded after failure. This performance may be attributed to the irregular surface texture of the epoxy resin matrix within the GFRP fibers [21]. Moreover, small fragments of cementitious material were observed adhering to the surface of fibers that slipped and fractured during flexural testing (Figure 3-15a). These residual fragments were also detected in the EDX analysis (Figure 3-16), where elevated levels of calcium and silica were identified on the fiber surface, despite the GFRP and epoxy-based composition, suggesting a composition similar to the surrounding cementitious matrix. These findings help explain the observed improvements in both plastic shrinkage resistance and flexural strength when RCWTB was included into concrete containing CRA.

In contrast, the fibers had a less significant effect on compressive strength, allowing the influence of weaker components, particularly polyurethane particles, to become more pronounced [73]. These polyurethane inclusions exhibited poor bond at their ITZs, as shown in Figure 3-15b. A visible gap between the particles and the surrounding matrix suggested that sliding was possible under loading. Moreover, the polymeric particles did not fracture during testing, indicating weak adhesion to the matrix, fracture would have occurred if the bond had been stronger [52]. The corresponding EDX spectrum (Figure 3-17) confirmed this lack of matrix attachment, showing a dominance of carbon and oxygen elements typical of polymers, and a noticeable absence of cementitious constituents. This detachment behavior under load led to slight reductions in compressive strength.

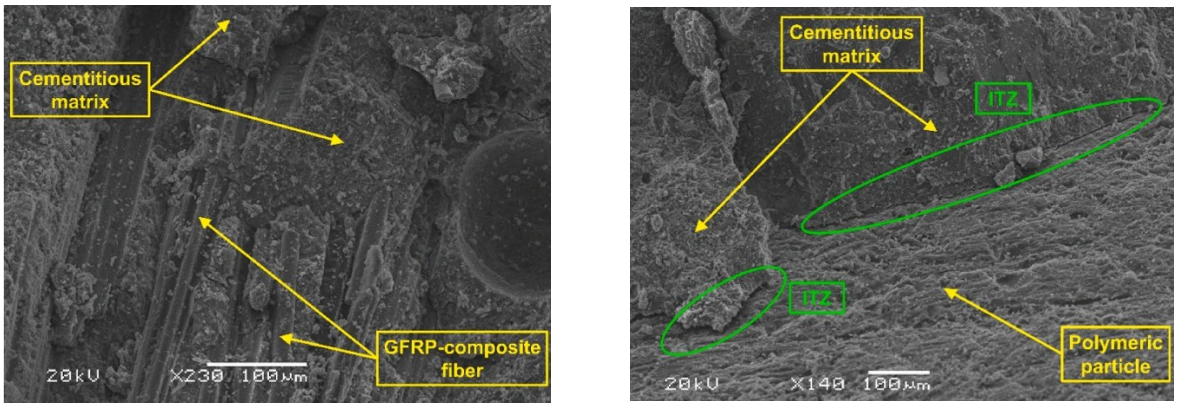

a) *b)*

Figure 3-15. SEM images of ITZs between RCWTB components and the cementitious matrix: a) GFRP-composite fiber; b) polymeric particle. Source: [81].

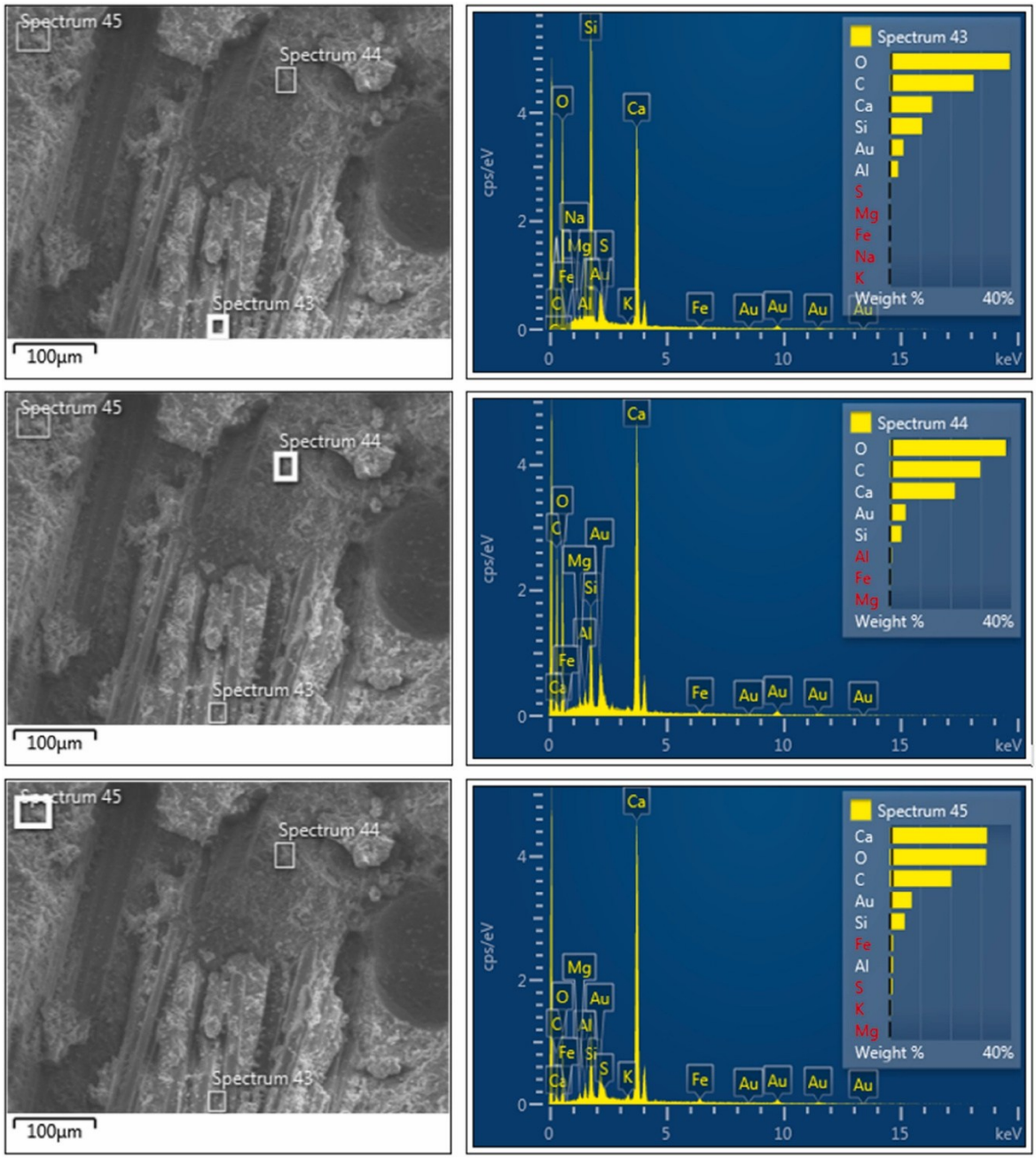

Figure 3-16. EDX spectra of a GFRP-composite fiber. Source: [81].

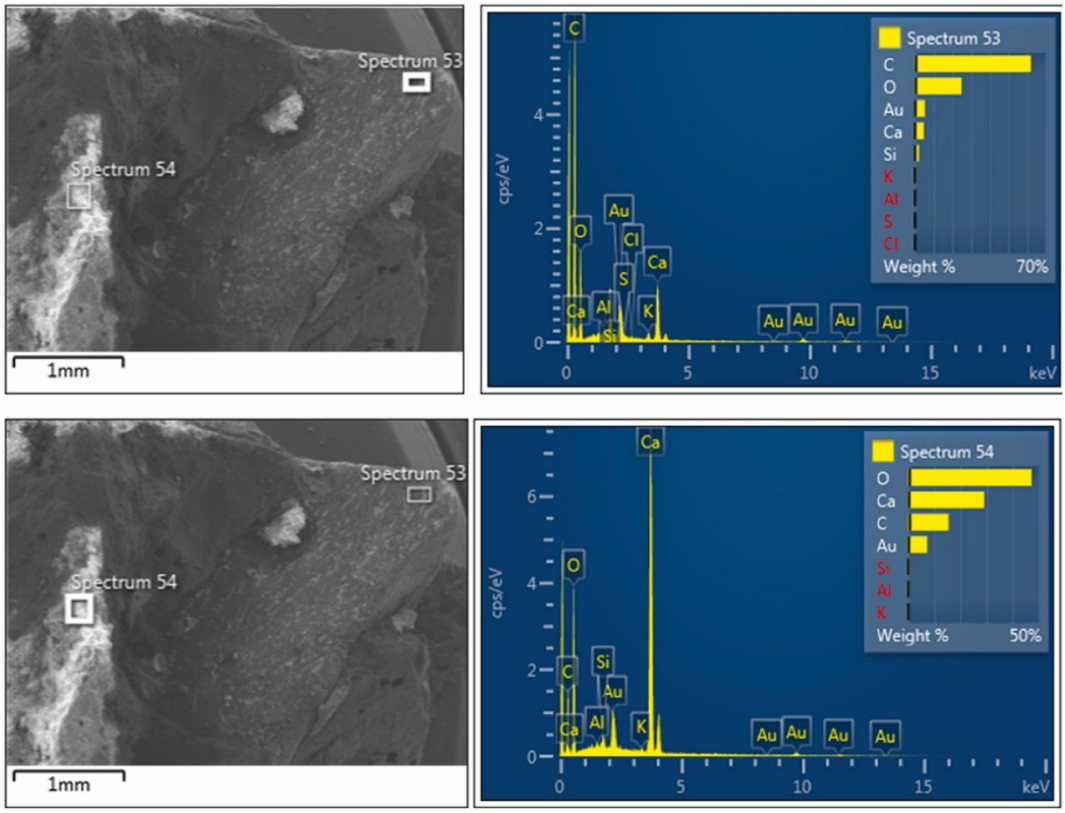

Figure 3-17. EDX spectra of a polymeric particle. Source: [81]

3.3.4 Analysis and discussion

3.3.4.1 Prediction of flexural strength

Predicting flexural strength based on compressive strength is highly useful for a wide range of structural design applications. However, when alternative constituents are used in concrete production, the correlation between these two strengths can differ significantly from that of conventional concrete. This subsection explores the relationship between compressive and flexural strengths to develop a predictive model for estimating early-age flexural strength.

The approach adopted for model development aligns with the methodology drawn in design standards such as BS EN 1992-1-1 (Eurocode 2) [69]. Compressive strength was used as the primary independent variable, and a logarithmic time-dependent factor was incorporated to enhance the model predictive accuracy. Initial analysis involved a simple regression, but this revealed autocorrelation in the residuals, making the initial models statistically invalid. To address this issue, the Cochrane-Orcutt method was applied, enabling a refined estimation of the error term through a linear modeling approach [82]. The resulting model is presented in Equation 3-5:

$$FS = 3.138 + 0.026 \times CS + 0.550 \times \ln(t) \qquad 3\text{-}5$$

Where *FS* represents the flexural strength of the concrete mix (in MPa), *CS* denotes the compressive strength (in MPa), and *t* is the age of the concrete (in days).

The developed model demonstrated strong performance, yielding an R^2 value of 88.26%, a Mean Absolute Error (MAE) of 0.251, and a Durbin-Watson statistic of 1.809. The R^2 coefficient reflects the proportion of variance in flexural strength explained by the model; in this case, the high value indicates a strong correlation with the experimental data. The MAE measures the average absolute difference between predicted and observed values, with low values confirming a close agreement with experimental results. The Durbin-Watson statistic, used to assess autocorrelation in the residuals, exceeded the critical threshold of 1.566, indicating no significant autocorrelation. Together, these metrics validate both the model predictive accuracy and the randomness of its residuals. Moreover, the maximum absolute deviation between predicted and experimental flexural strengths remained within 10%, as illustrated in Figure 3-18, further supporting the model reliability.

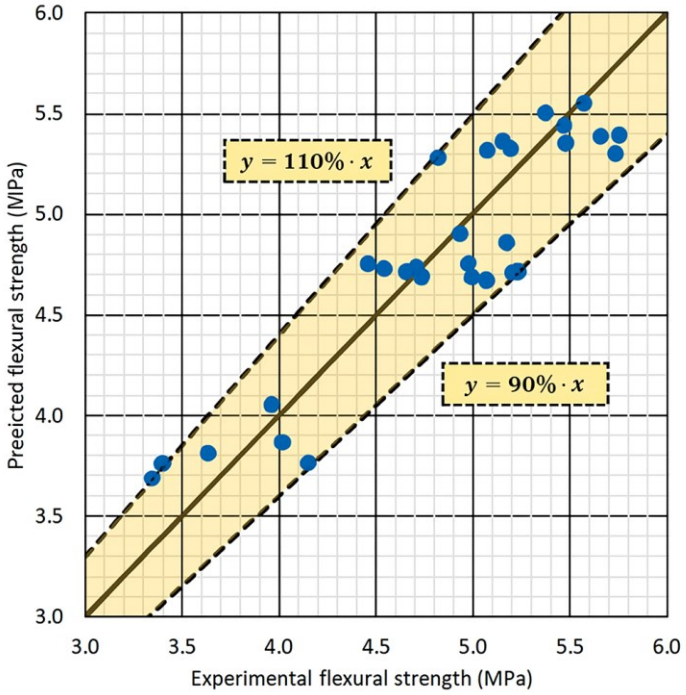

Figure 3-18. Comparison between experimental and predicted flexural strengths.

3.3.4.2 Economic analysis

For the concrete mixes examined in this study to be viable on a larger scale, they must also prove to be economically competitive [83]. For this reason, a cost analysis was carried out focusing exclusively on the cost of raw materials. Expenses related to transportation, energy consumption during mixing, and other operational factors were excluded. The aim is to provide a preliminary evaluation of how incorporating CRA and RCWTB affects concrete cost from the perspective of raw material supply.

In this context, the cost of each concrete mix was calculated by multiplying the unit cost of each constituent material by its quantity per cubic meter of concrete, as specified in Table 3-3 [84]. The pricing data for all raw materials (Table 3-6) were sourced from official Spanish price databases [85], given that the study was conducted in Spain, except for RCWTB, whose cost was estimated based on information provided by its producers. As shown in Figure 3-19, the incorporation of 50% CRA led to a cost reduction of approximately 4.2%, whereas the addition of 6% RCWTB reduced the cost by around 0.75%. Both waste materials contributed to lowering the overall cost of concrete, consistent with trends observed in the literature [83,84]. However, the more established industrial production of CRA and its higher replacement ratio in the mixes had a more pronounced impact on cost reduction.

Table 3-6. Cost of the concrete constituents.

Constituent	***Cost (€/kg)***
Cement	0.0962
Water	0.0006
Plasticizer 1	1.3700
Plasticizer 2	1.3700
Siliceous 12/22 mm	0.0068
Siliceous 4/12 mm	0.0067
Siliceous 0/4 mm	0.0085
Limestone 0/2 mm	0.0058
CRA 4/22 mm	0.0038
RCWTB	0.0052

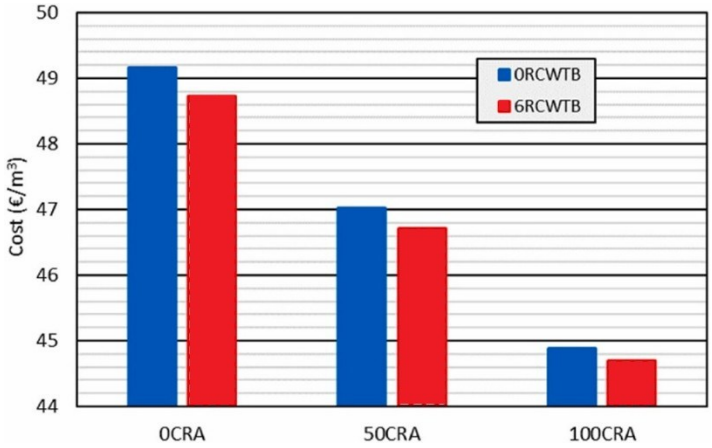

Figure 3-19. Cost of the concrete mixes.

3.3.5 Conclusions

In this subsection, a method to enhance the performance of recycled concrete incorporating Coarse Recycled Aggregate (CRA) is proposed by adding Raw Crushed Wind Turbine Blade (RCWTB), a composite waste material resulting from crushing wind turbine blades. The resulting RCWTB is primarily made of Glass Fiber Reinforced Polymer (GFRP), balsa wood, and polyurethane particles. RCWTB was introduced at dosages of 0% and 6% by volume, while CRA content varied from 0% to 100%. The main findings of the research are summarized as follows:

- The inclusion of CRA and RCWTB negatively affects workability and fresh density, while increasing air content. These changes are attributed to the angular shape and rough surface texture of CRA, as well as the fibrous nature of the GFRP material in RCWTB, which might hinder the flow of the fresh mix. Additionally, the lower density and higher porosity of both materials contributes to the reductions in fresh density and the increase of entrapped air.
- RCWTB is highly effective in reducing plastic shrinkage, especially in concrete containing higher CRA content. The GFRP-composite fibers act as micro-reinforcements that restrain early-age volumetric deformation. In fact, the addition of RCWTB to concrete with 100% CRA reduces plastic shrinkage over three days of ambient curing by 47%.
- All mixes incorporating CRA and RCWTB achieved compressive strengths above 40 MPa after 7 days, confirming their suitability for structural applications. However, a slight reduction in compressive strength was observed with RCWTB inclusion, primarily due to the suboptimal performance of GFRP fibers under compressive loading and weak bond of polyurethane particles with the cementitious matrix.
- All mixes reached a minimum flexural strength of 4.5 MPa after 7 days. RCWTB effectively mitigates the adverse effects of CRA on flexural performance, likely due to the bridging action and adequate bond of GFRP fibers within the cementitious matrix, as confirmed by scanning electron microscopy. This enhancement was more pronounced under moist curing. Notably, the mix containing 6% RCWTB and 50% CRA even exceeded the flexural strength of the reference mix without CRA, potentially due to enhanced fiber-aggregate interaction through mechanical interlocking with the rough CRA surface.
- A time-dependent predictive model based on the Cochrane-Orcutt method was successfully developed to estimate early-age flexural strength from compressive strength. This model effectively captured the behavior of concrete incorporating both CRA and RCWTB.

This research demonstrates that incorporating 6% RCWTB can significantly reduce plastic shrinkage and enhance the flexural strength of CRA-based concrete, particularly under moist curing, while maintaining adequate compressive strength. Additionally, RCWTB contributes to modest cost reductions in concrete production.

REFERENCES

[1] F. Mahaut, X. Chateau, P. Coussot, G. Ovarlez, Yield stress and elastic modulus of suspensions of noncolloidal particles in yield stress fluids, Journal of Rheology 52 (2008) 287–313. https://doi.org/10.1122/1.2798234.

[2] F. Mahaut, S. Mokéddem, X. Chateau, N. Roussel, G. Ovarlez, Effect of coarse particle volume fraction on the yield stress and thixotropy of cementitious materials, Cement and Concrete Research 38 (2008) 1276–1285. https://doi.org/10.1016/j.cemconres.2008.06.001.

[3] R.J. Flatt, P. Bowen, Yodel: A Yield Stress Model for Suspensions, Journal of the American Ceramic Society 89 (2006) 1244–1256. https://doi.org/10.1111/j.1551-2916.2005.00888.x.

[4] R.J. Flatt, P. Bowen, Yield Stress of Multimodal Powder Suspensions: An Extension of the YODEL (Yield Stress mODEL), Journal of the American Ceramic Society 90 (2007) 1038–1044. https://doi.org/10.1111/j.1551-2916.2007.01595.x.

[5] Z. Toutou, N. Roussel, Multi Scale Experimental Study of Concrete Rheology: From Water Scale to Gravel Scale, Mater Struct 39 (2006) 189–199. https://doi.org/10.1617/s11527-005-9047-y.

[6] H. Hafid, G. Ovarlez, F. Toussaint, P.H. Jezequel, N. Roussel, Effect of particle morphological parameters on sand grains packing properties and rheology of model mortars, Cement and Concrete Research 80 (2016) 44–51. https://doi.org/10.1016/j.cemconres.2015.11.002.

[7] L. Martinie, P. Rossi, N. Roussel, Rheology of fiber reinforced cementitious materials: classification and prediction, Cement and Concrete Research 40 (2010) 226–234. https://doi.org/10.1016/j.cemconres.2009.08.032.

[8] F. Sultangaliyeva, H. Carré, C. La Borderie, W. Zuo, E. Keita, N. Roussel, Influence of flexible fibers on the yield stress of fresh cement pastes and mortars, Cement and Concrete Research 138 (2020) 106221. https://doi.org/10.1016/j.cemconres.2020.106221.

[9] EN 197-1:2011 - Cement - Composition, specifications and conformity criteria for common cements, (2011).

[10] J. Manso-Morato, N. Hurtado-Alonso, V. Revilla-Cuesta, M. Skaf, V. Ortega-López, Fiber-Reinforced concrete and its life cycle assessment: A systematic review, Journal of Building Engineering 94 (2024) 110062. https://doi.org/10.1016/j.jobe.2024.110062.

[11] J. Joustra, B. Flipsen, R. Balkenende, Structural reuse of wind turbine blades through segmentation, Composites Part C: Open Access 5 (2021) 100137. https://doi.org/10.1016/j.jcomc.2021.100137.

[12] A. Perrot, T. Lecompte, H. Khelifi, C. Brumaud, J. Hot, N. Roussel, Yield stress and bleeding of fresh cement pastes, Cement and Concrete Research 42 (2012) 937–944. https://doi.org/10.1016/j.cemconres.2012.03.015.

[13] M. Barry, M. Clément, D. Rangeard, Y. Jacquet, A. Perrot, Manufactured crushed sand: packing fraction prediction and influence on mortar rheology, Mater Struct 56 (2023) 139. https://doi.org/10.1617/s11527-023-02231-8.

[14] R. Mandal, S.K. Panda, S. Nayak, Rheology of Concrete: Critical Review, recent Advancements, and future prospectives, Construction and Building Materials 392 (2023) 132007. https://doi.org/10.1016/j.conbuildmat.2023.132007.

[15] S. Gwon, M. Shin, Rheological properties of cement pastes with cellulose microfibers, Journal of Materials Research and Technology 10 (2021) 808–818. https://doi.org/10.1016/j.jmrt.2020.12.067.

[16] S. Das, Md. Habibur Rahman Sobuz, V.W.Y. Tam, A.S.M. Akid, N.M. Sutan, F.M.M. Rahman, Effects of incorporating hybrid fibres on rheological and mechanical properties of fibre reinforced concrete, Construction and Building Materials 262 (2020) 120561. https://doi.org/10.1016/j.conbuildmat.2020.120561.

[17] M. Tabatabaeian, A. Khaloo, A. Joshaghani, E. Hajibandeh, Experimental investigation on effects of hybrid fibers on rheological, mechanical, and durability properties of high-strength SCC, Construction and Building Materials 147 (2017) 497–509. https://doi.org/10.1016/j.conbuildmat.2017.04.181.

[18] D. Malaszkiewicz, Influence of polymer fibers on rheological properties of cement mortars, Open Engineering 7 (2017) 228–236. https://doi.org/10.1515/eng-2017-0029.

[19] P. Chindaprasirt, N. Buapa, H.T. Cao, Mixed cement containing fly ash for masonry and plastering work, Construction and Building Materials 19 (2005) 612–618. https://doi.org/10.1016/j.conbuildmat.2005.01.009.

[20] V.G. Haach, G. Vasconcelos, P.B. Lourenço, Influence of aggregates grading and water/cement ratio in workability and hardened properties of mortars, Construction and Building Materials 25 (2011) 2980–2987. https://doi.org/10.1016/j.conbuildmat.2010.11.011.

[21] V. Revilla-Cuesta, M. Skaf, V. Ortega-López, J.M. Manso, Raw-crushed wind-turbine blade: Waste characterization and suitability for use in concrete production, Resources, Conservation and Recycling 198 (2023) 107160. https://doi.org/10.1016/j.resconrec.2023.107160.

[22] J. Manso-Morato, N. Hurtado-Alonso, V. Revilla-Cuesta, R. Serrano-López, V. Ortega-López, Deformational and energy-absorption performance of low-strength structural concrete with joint additions of raw-crushed wind-turbine blade and coarse recycled aggregate, Emergent Mater. (2025). https://doi.org/10.1007/s42247-025-01060-5.

[23] B. Wang, L. Yan, Q. Fu, B. Kasal, A Comprehensive Review on Recycled Aggregate and Recycled Aggregate Concrete, Resources, Conservation and Recycling 171 (2021) 105565. https://doi.org/10.1016/j.resconrec.2021.105565.

[24] S. Tejas, D. Pasla, Assessment of mechanical and durability properties of composite cement-based recycled aggregate concrete, Construction and Building Materials 387 (2023) 131620. https://doi.org/10.1016/j.conbuildmat.2023.131620.

[25] A. Akhtar, A.K. Sarmah, Construction and demolition waste generation and properties of recycled aggregate concrete: A global perspective, Journal of Cleaner Production 186 (2018) 262–281. https://doi.org/10.1016/j.jclepro.2018.03.085.

[26] M.C. Collivignarelli, G. Cillari, P. Ricciardi, M.C. Miino, V. Torretta, E.C. Rada, A. Abbà, The Production of Sustainable Concrete with the Use of Alternative Aggregates: A Review, Sustainability 12 (2020). https://doi.org/10.3390/su12197903.

[27] L. Wang, J. Wang, X. Qian, P. Chen, Y. Xu, J. Guo, An environmentally friendly method to improve the quality of recycled concrete aggregates, Construction and Building Materials 144 (2017) 432–441. https://doi.org/10.1016/j.conbuildmat.2017.03.191.

[28] V.W.Y. Tam, M. Soomro, A.C.J. Evangelista, Quality improvement of recycled concrete aggregate by removal of residual mortar: A comprehensive review of approaches adopted, Construction and Building Materials 288 (2021) 123066. https://doi.org/10.1016/j.conbuildmat.2021.123066.

[29] J.A. Forero, J. de Brito, L. Evangelista, C. Pereira, Improvement of the Quality of Recycled Concrete Aggregate Subjected to Chemical Treatments: A Review, Materials 15 (2022) 2740. https://doi.org/10.3390/ma15082740.

[30] S. Jamil, J. Shi, M. Idrees, Effect of various parameters on carbonation treatment of recycled concrete aggregate using the design of experiment method, Construction and Building Materials 382 (2023) 131339. https://doi.org/10.1016/j.conbuildmat.2023.131339.

[31] N. Kisku, H. Joshi, M. Ansari, S.K. Panda, S. Nayak, S.C. Dutta, A critical review and assessment for usage of recycled aggregate as sustainable construction material, Construction and Building Materials 131 (2017) 721–740. https://doi.org/10.1016/j.conbuildmat.2016.11.029.

[32] C. Shi, Y. Li, J. Zhang, W. Li, L. Chong, Z. Xie, Performance enhancement of recycled concrete aggregate – A review, Journal of Cleaner Production 112 (2016) 466–472. https://doi.org/10.1016/j.jclepro.2015.08.057.

[33] F. Aslani, J. Kelin, Assessment and development of high-performance fibre-reinforced lightweight self-compacting concrete including recycled crumb rubber aggregates exposed to elevated temperatures, Journal of Cleaner Production 200 (2018) 1009–1025. https://doi.org/10.1016/j.jclepro.2018.07.323.

[34] K.J.N.S. Nitesh, S.V. Rao, P.R. Kumar, An experimental investigation on torsional behaviour of recycled aggregate based steel fiber reinforced self compacting concrete, Journal of Building Engineering 22 (2019) 242–251. https://doi.org/10.1016/j.jobe.2018.12.011.

[35] R. Chan, X. Liu, I. Galobardes, Parametric study of functionally graded concretes incorporating steel fibres and recycled aggregates, Construction and Building Materials 242 (2020) 118186. https://doi.org/10.1016/j.conbuildmat.2020.118186.

[36] W. Ahmed, C.W. Lim, Production of sustainable and structural fiber reinforced recycled aggregate concrete with improved fracture properties: A review, Journal of Cleaner Production 279 (2021) 123832. https://doi.org/10.1016/j.jclepro.2020.123832.

[37] D. Gao, L. Zhang, J. Zhao, P. You, Durability of steel fibre-reinforced recycled coarse aggregate concrete, Construction and Building Materials 232 (2020) 117119. https://doi.org/10.1016/j.conbuildmat.2019.117119.

[38] C.R. Meesala, Influence of different types of fiber on the properties of recycled aggregate concrete, Structural Concrete 20 (2019) 1656–1669. https://doi.org/10.1002/suco.201900052.

[39] S.A. Hadigheh, F. Ke, S. Kashi, 3D acid diffusion model for FRP-strengthened reinforced concrete structures: Long-term durability prediction, Construction and Building Materials 261 (2020) 120548. https://doi.org/10.1016/j.conbuildmat.2020.120548.

[40] A. Yazdanbakhsh, L.C. Bank, Y. Tian, Mechanical Processing of GFRP Waste into Large-Sized Pieces for Use in Concrete, Recycling 3 (2018) 8–0. https://doi.org/10.3390/recycling3010008.

[41] S. Karuppannan Gopalraj, T. Kärki, A review on the recycling of waste carbon fibre/glass fibre-reinforced composites: fibre recovery, properties and life-cycle analysis, SN Appl. Sci. 2 (2020) 433. https://doi.org/10.1007/s42452-020-2195-4.

[42] V. Revilla-Cuesta, J. Manso-Morato, N. Hurtado-Alonso, M. Skaf, V. Ortega-López, Mechanical and environmental advantages of the revaluation of raw-crushed wind-turbine blades as a concrete component, Journal of Building Engineering 82 (2024) 108383. https://doi.org/10.1016/j.jobe.2023.108383.

[43] V. Revilla-Cuesta, F. Faleschini, C. Pellegrino, M. Skaf, V. Ortega-López, Water transport and porosity trends of concrete containing integral additions of raw-crushed wind-turbine blade, Developments in the Built Environment 17 (2024) 100374. https://doi.org/10.1016/j.dibe.2024.100374.
[44] EN 1097-6:2013 - Tests for mechanical and physical properties of aggregates - Determination of particle density and water absorption, (2013).
[45] C.D. Atiş, F. Özcan, A. Kılıç, O. Karahan, C. Bilim, M.H. Severcan, Influence of dry and wet curing conditions on compressive strength of silica fume concrete, Building and Environment 40 (2005) 1678–1683. https://doi.org/10.1016/j.buildenv.2004.12.005.
[46] EN 12350-2:2019 - Testing fresh concrete - Slump test, (2019).
[47] EN 12350-6:2019 - Testing fresh concrete - Density, (2019).
[48] EN 12350-7:2019 - Testing fresh concrete - Air content. Pressure methods, (2019).
[49] EN 12390-3:2019 - Testing hardened concrete - Compressive strength of test specimens, (2019).
[50] EN 12390-5:2019 - Testing hardened concrete - Flexural strength of test specimens, (2019).
[51] Ortega-López Vanesa, Revilla-Cuesta Víctor, Santamaría Amaia, Orbe Aimar, Skaf Marta, Microstructure and Dimensional Stability of Slag-Based High-Workability Concrete with Steelmaking Slag Aggregate and Fibers, Journal of Materials in Civil Engineering 34 (2022) 04022224. https://doi.org/10.1061/(ASCE)MT.1943-5533.0004372.
[52] K.L. Scrivener, A.K. Crumbie, P. Laugesen, The Interfacial Transition Zone (ITZ) Between Cement Paste and Aggregate in Concrete, Interface Science 12 (2004) 411–421. https://doi.org/10.1023/B:INTS.0000042339.92990.4c.
[53] B.J. Zhan, D.X. Xuan, C.S. Poon, K.L. Scrivener, Characterization of interfacial transition zone in concrete prepared with carbonated modeled recycled concrete aggregates, Cement and Concrete Research 136 (2020) 106175. https://doi.org/10.1016/j.cemconres.2020.106175.
[54] J. Lavado, J. Bogas, J. de Brito, A. Hawreen, Fresh properties of recycled aggregate concrete, Construction and Building Materials 233 (2020) 117322. https://doi.org/10.1016/j.conbuildmat.2019.117322.
[55] D. Ravichandran, P.R. Prem, S.K. Kaliyavaradhan, P.S. Ambily, Influence of fibers on fresh and hardened properties of Ultra High Performance Concrete (UHPC)—A review, Journal of Building Engineering 57 (2022) 104922. https://doi.org/10.1016/j.jobe.2022.104922.
[56] R. Sri Ravindrarajah, Y.H. Loo, C.T. Tam, Recycled concrete as fine and coarse aggregates in concrete, Magazine of Concrete Research 39 (1987) 214–220. https://doi.org/10.1680/macr.1987.39.141.214.
[57] J. Montero, S. Laserna, Influence of effective mixing water in recycled concrete, Construction and Building Materials 132 (2017) 343–352. https://doi.org/10.1016/j.conbuildmat.2016.12.006.
[58] I. Mehdipour, N.A. Libre, M. Shekarchi, M. Khanjani, Effect of workability characteristics on the hardened performance of FRSCCMs, Construction and Building Materials 40 (2013) 611–621. https://doi.org/10.1016/j.conbuildmat.2012.11.051.
[59] R.V. Silva, J. de Brito, R.K. Dhir, Fresh-state performance of recycled aggregate concrete: A review, Construction and Building Materials 178 (2018) 19–31. https://doi.org/10.1016/j.conbuildmat.2018.05.149.
[60] Z. Lafhaj, M. Goueygou, A. Djerbi, M. Kaczmarek, Correlation between porosity, permeability and ultrasonic parameters of mortar with variable water / cement ratio and water content, Cement and Concrete Research 36 (2006) 625–633. https://doi.org/10.1016/j.cemconres.2005.11.009.
[61] A. Alsaif, Y.R. Alharbi, Strength, durability and shrinkage behaviours of steel fiber reinforced rubberized concrete, Construction and Building Materials 345 (2022) 128295. https://doi.org/10.1016/j.conbuildmat.2022.128295.
[62] N.V. Gama, A. Ferreira, A. Barros-Timmons, Polyurethane Foams: Past, Present, and Future, Materials 11 (2018). https://doi.org/10.3390/ma11101841.
[63] M. Borrega, P. Ahvenainen, R. Serimaa, L. Gibson, Composition and structure of balsa (Ochroma pyramidale) wood, Wood Sci Technol 49 (2015) 403–420. https://doi.org/10.1007/s00226-015-0700-5.
[64] Á. Salesa, J.A. Pérez-Benedicto, D. Colorado-Aranguren, P.L. López-Julián, L.M. Esteban, L.J. Sanz-Baldúz, J.L. Sáez-Hostaled, J. Ramis, D. Olivares, Physico – mechanical properties of multi – recycled concrete from precast concrete industry, Journal of Cleaner Production 141 (2017) 248–255. https://doi.org/10.1016/j.jclepro.2016.09.058.
[65] M. Bakhshi, B. Mobasher, M. Zenouzi, Model for Early-Age Rate of Evaporation of Cement-Based Materials, Journal of Engineering Mechanics 138 (2012) 1372–1380. https://doi.org/10.1061/(ASCE)EM.1943-7889.0000435.
[66] G. Bai, C. Zhu, C. Liu, B. Liu, An evaluation of the recycled aggregate characteristics and the recycled aggregate concrete mechanical properties, Construction and Building Materials 240 (2020) 117978. https://doi.org/10.1016/j.conbuildmat.2019.117978.
[67] J. Liu, F. Han, G. Cui, Q. Zhang, J. Lv, L. Zhang, Z. Yang, Combined effect of coarse aggregate and fiber on tensile behavior of ultra-high performance concrete, Construction and Building Materials 121 (2016) 310–318. https://doi.org/10.1016/j.conbuildmat.2016.05.039.

[68] N. Yousefieh, A. Joshaghani, E. Hajibandeh, M. Shekarchi, Influence of fibers on drying shrinkage in restrained concrete, Construction and Building Materials 148 (2017) 833–845. https://doi.org/10.1016/j.conbuildmat.2017.05.093.

[69] Eurocode 2: Design of Concrete Structures - Part 1-1: General Rules and Rules for Buildings, European Committee for Standardization (CEN), Brussels, 2023.

[70] R.V. Silva, J. de Brito, R.K. Dhir, The influence of the use of recycled aggregates on the compressive strength of concrete: a review, European Journal of Environmental and Civil Engineering 19 (2015) 825–849. https://doi.org/10.1080/19648189.2014.974831.

[71] N. Hurtado-Alonso, J. Manso-Morato, V. Revilla-Cuesta, V. Ortega-López, M. Skaf, Optimization of concrete containing wind-turbine wastes following mechanical, environmental and economic indicators, Cleaner Materials 16 (2025) 100317. https://doi.org/10.1016/j.clema.2025.100317.

[72] Md.J. Islam, Md. Shahjalal, N.M.A. Haque, Mechanical and durability properties of concrete with recycled polypropylene waste plastic as a partial replacement of coarse aggregate, Journal of Building Engineering 54 (2022) 104597. https://doi.org/10.1016/j.jobe.2022.104597.

[73] A. Al-Mansour, S. Chen, C. Xu, Y. Peng, J. Wang, S. Ruan, Q. Zeng, Sustainable cement mortar with recycled plastics enabled by the matrix-aggregate compatibility improvement, Construction and Building Materials 318 (2022) 125994. https://doi.org/10.1016/j.conbuildmat.2021.125994.

[74] J. Ahmad, R.A. González-Lezcano, A. Majdi, N. Ben Kahla, A.F. Deifalla, M.A. El-Shorbagy, Glass Fibers Reinforced Concrete: Overview on Mechanical, Durability and Microstructure Analysis, Materials 15 (2022). https://doi.org/10.3390/ma15155111.

[75] W. He, X. Kong, Y. Fu, C. Zhou, Z. Zheng, Experimental investigation on the mechanical properties and microstructure of hybrid fiber reinforced recycled aggregate concrete, Construction and Building Materials 261 (2020) 120488. https://doi.org/10.1016/j.conbuildmat.2020.120488.

[76] A.A. Ramezanianpour, V.M. Malhotra, Effect of curing on the compressive strength, resistance to chloride-ion penetration and porosity of concretes incorporating slag, fly ash or silica fume, Cement and Concrete Composites 17 (1995) 125–133. https://doi.org/10.1016/0958-9465(95)00005-W.

[77] F. López Gayarre, C. López-Colina Pérez, M.A. Serrano López, A. Domingo Cabo, The effect of curing conditions on the compressive strength of recycled aggregate concrete, Construction and Building Materials 53 (2014) 260–266. https://doi.org/10.1016/j.conbuildmat.2013.11.112.

[78] S. Seara-Paz, B. González-Fonteboa, F. Martínez-Abella, J. Eiras-López, Flexural performance of reinforced concrete beams made with recycled concrete coarse aggregate, Engineering Structures 156 (2018) 32–45. https://doi.org/10.1016/j.engstruct.2017.11.015.

[79] G.-T. Xu, M.-J. Liu, Y. Xiang, B. Fu, Valorization of macro fibers recycled from decommissioned turbine blades as discrete reinforcement in concrete, Journal of Cleaner Production 379 (2022) 134550. https://doi.org/10.1016/j.jclepro.2022.134550.

[80] H. Rodin, S. Nassiri, K. Englund, O. Fakron, H. Li, Recycled glass fiber reinforced polymer composites incorporated in mortar for improved mechanical performance, Construction and Building Materials 187 (2018) 738–751. https://doi.org/10.1016/j.conbuildmat.2018.07.169.

[81] D. Trento, F. Faleschini, V. Revilla-Cuesta, V. Ortega-López, Improving the early-age behavior of concrete containing coarse recycled aggregate with raw-crushed wind-turbine blade, Journal of Building Engineering 92 (2024) 109815. https://doi.org/10.1016/j.jobe.2024.109815.

[82] F. Golestaneh, I. Kazemi, Cross-section asymptotic for random-effects panel data models with autoregressive errors, Communications in Statistics - Simulation and Computation 53 (2024) 4554–4567. https://doi.org/10.1080/03610918.2022.2154799.

[83] S. Saha, D. Sau, T. Hazra, Economic viability analysis of recycling waste plastic as aggregates in green sustainable concrete, Waste Management 169 (2023) 289–300. https://doi.org/10.1016/j.wasman.2023.07.023.

[84] F.K. Alqahtani, I.S. Abotaleb, M. ElMenshawy, Life cycle cost analysis of lightweight green concrete utilizing recycled plastic aggregates, Journal of Building Engineering 40 (2021) 102670. https://doi.org/10.1016/j.jobe.2021.102670.

[85] Govern of Extremadura, Construction Prices Guide, (2023).

4 AGGREGATES RECOVERED FROM CONCRETE SLUDGE WASTE IN CEMENTITIOUS CONGLOMERATES

4.1 INTRODUCTION

Construction and Demolition Waste (C&DW) represents one of the largest solid waste burdens worldwide [1,2]. Nowadays, recycling C&DW to produce recycled aggregates is a widely adopted practice, as it helps saving natural aggregate resources and reducing environmental pollution [3,4].

However, other waste-like materials also have the potential for reuse in fresh concrete mixtures, although research and documented applications are more limited. From the perspective of concrete producers, there is a growing interest in developing solutions to recycle Concrete Sludge Waste (CSW) [5,6]. As a general definition, CSW, also known as returned concrete, refers to the leftover concrete remaining in the mixing truck, which is typically in a fresh state and contains a substantial amount of cement mortar [7].

This study examines the properties of CSW obtained directly from crushing hardened leftover concrete in mixing trucks, including waste generated during the cleaning process. The resulting material is an all-in aggregate in fraction 0-20 mm which can be directly employed as both fine and coarse aggregate. The main advantage of this recovery process lies in its simplicity, as it can be implemented at any Ready-Mix Concrete (RMC) plant with only the requirement of storage space and crushing equipment.

Existing literature includes studies on the use of CSW in fine fractions as a filler to improve packing [8]. However, to the authors' knowledge, limited research has been conducted on utilizing an all-in CSW like the one presented in this study for producing new concrete.

This section presents the results of an experimental campaign aiming to investigate the use of an all-in CSW as replacement for fine and coarse aggregates, evaluating its impact on workability, compressive strength, tensile strength, and Young's modulus.

4.2 EXPERIMENTAL METHODS

4.2.1 Materials

4.2.1.1 Cement paste

The cement employed in this study is classified as CEM II/A-LL 42.5 R, containing 80-94% clinker and 6-20% limestone, in accordance with EN 197-1 [9]. Mixing was performed using tap water provided from the municipal supply of Padova, Italy, which is free of harmful contaminants. To attain the required consistency, a formaldehyde-free superplasticizer based on non-sulphonated acrylic polymers was also added.

4.2.1.2 Aggregates

To optimize the mix design, a selection of aggregates was used, including a natural sand (NA 0-4), two conventional gravels (NA 4-8 and NA 8-16), and an all-in Concrete Sludge Waste (CSW 0-20), as illustrated in Figure 4-1. The physical properties of these aggregates, e.g. particle density and water absorption, were determined according to EN 1097-6 [10] and are summarized in Table 4-1. Their grading curves are presented in Figure 4-2.

It is important to mention that the NA 0-4 and NA 8-16 aggregates typically exhibit smooth surfaces and rounded shapes due to their alluvial origin. In contrast, the intermediate fraction NA 4-8, produced from crushed rocks, also has a smooth surface but with a more angular shape.

The CSW 0-20 aggregate used in this study is a 0-20 mm all-in material derived from the crushing of hardened leftover concrete and residues generated during the equipment cleaning process. Consequently, it comprises both fine and coarse particles with residual adhered mortar, along with a powdery, predominantly carbonated cementitious paste. The fines content of CSW 0-20 was determined to be 6.88%, following the procedure outlined in EN 933-1 [11].

Table 4-1. Physical properties of the aggregates.

Aggregate type	**Shape**	ρ_a **(Mg/m^3)**	ρ_{rd} **(Mg/m^3)**	ρ_{ssd} **(Mg/m^3)**	***WA* (%)**
		Apparent Particle density	Oven-dried particle density	SSD particle density	Water absorption
NA 0-4	Roundish	2.644	2.467	2.534	2.714
NA 4-8	Sharp	2.782	2.680	2.717	1.367
NA 8-16	Roundish	2.769	2.679	2.711	1.212
CSW 0-20	Sharp	2.748	2.222	2.413	8.691

Figure 4-1. Aggregates employed in this work: a) NA 0-4; b) NA 4-8; c) NA 8-16; d) CSW 0-20.

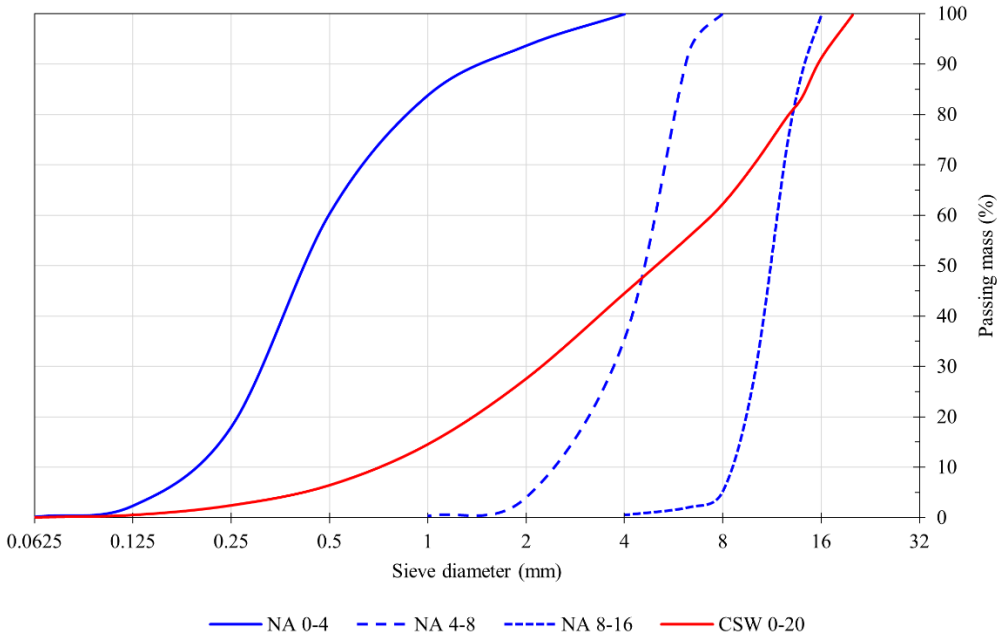

Figure 4-2. Aggregate grading curves.

4.2.2 Mix design

The concrete mixtures developed for this experimental campaign are shown in Table 4-2 and Table 4-3. The first series (Set 1) includes mixes with varying replacement ratios of Concrete Sludge Waste (CSW 0-20), while maintaining a constant cementitious paste composition, as shown in Table 4-2. Based on the outcomes of Set 1, a selection of these mixtures was further refined to improve some specific properties. These optimized formulations, grouped in Set 2, are presented in Table 4-3.

Set 1 comprises mixtures with CSW 0-20 aggregate replacement levels ranging from 0% to 100% in volume. Cement and water dosages were kept constant at 330 kg/m^3 and 155 kg/m^3, respectively, resulting in a water-to-cement ratio (w/c) equal to 0.47. This calculation assumes that all aggregates are in a saturated surface dry condition when included in the mixture. A superplasticizer was incorporated at a dosage of 1% by the weight of cement. Aggregate grading for all mixes was designed according to the modified Bolomey curve, accounting for all solid components, including both cement and aggregates. It is worth noting that the mixture labeled 100CSW contains a minor quantity of natural sand, added solely to adjust the grading curve.

In Set 2, mixtures containing 10%, 30% and 100% CSW 0-20 were selected for optimization. These three replacement ratios were not chosen arbitrarily but were determined by practical and regulatory considerations. According to the Italian criteria for public works, known as Criteri Ambientali Minimi (CAM) [12], ready-mixed concrete and pre-mixed concrete must contain a minimum of 5% by weight of recycled, recovered, or by-product materials. This percentage is calculated based on the dry weight of such materials relative to the total weight of the concrete, excluding both free and absorbed water. Only materials that remain in the final product are counted toward this requirement. Mixes incorporating 10% CSW 0-20 in the total aggregate mass yield approximately 8.5% recycled content by weight of the finished concrete (excluding water), thereby falling within the CAM criteria. These mixtures are of particular interest for the Italian market, as they offer comparable performance to conventional concretes while satisfying sustainability requirements. Conversely, mixture with 100% CSW 0-20 represents the highest level of recycled aggregate utilization, effectively minimizing the use of virgin raw materials. While not intended for structural use, mixes incorporating 100% CSW 0-20 are promising for non-structural applications where performance demands are less stringent. Instead, the mixture with 30% CSW 0-20 is a compromise between performance optimization and reduced raw material consumption. Thus, the optimized mixtures 10CSW2 and 30CSW2 were designed to offer improved workability and compressive strength relative to their Set 1 counterparts. Instead, 100CSW2 was formulated for non-structural use with the goal of enhancing overall quality while prioritizing a reduced environmental impact over mechanical strength.

Table 4-2. Mix design for Set 1 (in kg/m^3).

	REF	***10CSW***	***20CSW***	***30CSW***	***40CSW***	***50CSW***	***100CSW***
Cement II/A-LL 42.5R	330	330	330	330	330	330	330
W/C ratio	0.47	0.47	0.47	0.47	0.47	0.47	0.47
Water	155	155	155	155	155	155	155
NA 0-4	654	674	598	524	449	374	224
NA 4-8	590	531	472	413	354	295	-
NA 8-16	685	530	471	412	353	294	-
CSW 0-20	-	194	389	583	778	972	1710
Superplasticizer	3.3 (1%)	3.3 (1%)	3.3 (1%)	3.3 (1%)	3.3 (1%)	3.3 (1%)	3.3 (1%)

Table 4-3. Mix design Set 2 (in kg/m³).

	10CSW2	***30CSW2***	***100CSW2***
Cement II/A-LL 42.5R	360	360	330
W/C ratio	0.50	0.50	0.61
Water	180	180	202
NA 0-4	533	412	219
NA 4-8	467	363	-
NA 8-16	651	506	-
CSW 0-20	184	552	1666
Superplasticizer	5.4 (1.5%)	5.4 (1.5%)	4.0 (1.2%)

4.2.3 Testing program

This study investigates both the fresh and hardened properties of concrete. Fresh consistency was evaluated using the slump test according to EN 12350-2 [13]. For each concrete mix, a series of cylindrical specimens (100×200 mm) was cast, and fresh density was measured in this stage. After casting and compacting the concrete into molds, the specimens were covered with plastic sheets and kept in a controlled laboratory environment for 24 hours to minimize moisture loss.

After 24 hours, the specimens were demolded and transferred to a moist curing chamber. Compressive strength tests were carried out at 7 (1 test) and 28 days (at least 3 tests) in accordance with EN 12390-3 [14]. Prior to testing, hardened density was also determined using the same specimens. At 28 days, the elastic modulus (2 tests) and splitting tensile strength (2 tests) were also measured for mixtures containing up to 40% CSW 0-20, following EN 12390-13 [15] and EN 12390-6 [16], respectively. These mixes were selected because structural applications are more promising in mixture including up to 40% CSW 0-20. The microstructure was also analyzed through the Scanning Electron Microscope (SEM) for some characteristic mixtures of the Set 1.

In addition, leaching tests were conducted on cylindrical concrete specimens from the REF and 10CSW2 mixtures, according to EN 15863 [17]. Unlike granular leaching methods, typically performed in batch or dynamic modes, the monolithic test evaluates contaminant release from materials in their end-use form. While the granular approach is based on pre-defined aggregate grading, the monolith test reflects real-world performance of concrete. For each mixture, two leaching tests were performed on cylindrical samples that had been cut in half, resulting in a total of four specimens. The leaching tests reached 28 days of time interval according to EN 15863 [17]. As prescribed by the standard, the ratio between the volume of the leaching solution and the specimen exposed surface area (L/A) was maintained at 8±2 mL/cm^2. In this case, with an exposed surface area of 464 cm^2 and 3.8 liters of deionized water, the L/A ratio was 8.19. This test is classified as a semi-dynamic tank leaching procedure, where specimens are immersed in the leaching solution for sequential time intervals. After each interval, the leachate is collected, the solution is renewed, and testing continues. The collected leachates were analyzed for both major cations and trace elements. Additionally, cyanides, Chemical Oxygen Demand (COD), and pH were evaluated in accordance with the standards M.U. 2251 [18], EN 1484 [19] and ISO 10523 [20], respectively. The selection of these parameters is intended to align with the requirements outlined in DM 5/2/1998, n. 22 [21], which sets the regulatory limits for leaching tests on granular materials.

4.3 RESULTS

Table 4-4 and Table 4-5 sum up the results for slump test, fresh density ρ_{fc}, hardened density ρ_c, compressive strength at 7-days of curing $f_{c,7}$ and compressive strength at 28-days of curing f_c.

Table 4-4. Results for fresh properties, density and compressive strength of the Set 1 mixtures.

	REF	***10CSW***	***20CSW***	***30CSW***	***40CSW***	***50CSW***	***100CSW***
Slump (cm)	23.5	6.0	4.0	3.0	3.5	0.5	0.5
ρ_{fc} *(kg/m³)*	2301	2323	2364	2313	2307	2258	2161
ρ_c *(kg/m³)*	2259	2322	2353	2322	2305	2278	2132
$f_{c,7}$ *(MPa)*	24.99	28.15	33.64	29.82	28.96	26.60	17.92
f_c *(MPa)*	29.05	31.90	39.16	34.58	33.10	30.88	25.49

Table 4-5. Results for fresh properties, density and compressive strength of the Set 2 mixtures.

	10CSW2	***30CSW2***	***100CSW2***
Slump (cm)	26.0	3.5	13.5
ρ_{fc} *(kg/m³)*	2415	2379	1912
ρ_c *(kg/m³)*	2402	2396	1903
$f_{c,7}$ *(MPa)*	32.06	38.92	8.97
f_c *(MPa)*	37.69	43.61	9.07

4.3.1 Set 1

4.3.1.1 Fresh properties and density

Figure 4-3 presents the influence of replacing natural aggregates with CSW 0-20 on slump, fresh density, and hardened density.

The slump results revealed a marked reduction in workability as the proportion of CSW 0-20 increased. At 0% replacement, the concrete exhibited a high slump of 23.5 cm, indicating excellent workability. However, introducing just 10% CSW 0-20 in place of natural aggregates led to a sharp slump decrease to approximately 6 cm. Beyond a 40% replacement level, the slump dropped to nearly 0 cm and remained unchanged up to full replacement. This pronounced decline in workability is likely attributed to the fine particle content and high water absorption of CSW 0-20, even when used in a saturated surface dry condition.

The fresh density of concrete initially exhibited a slight increase with the incorporation of CSW 0-20, peaking at around 2364 kg/m^3 for the 20% replacement mix. However, with further increases in CSW 0-20 content, a gradual reduction in fresh density was observed, reaching 2161 kg/m^3 at 100% replacement. This downward trend is likely due to the lower specific gravity of CSW 0-20 compared to natural aggregates, combined with potential changes in mix compaction and entrained air content.

A similar pattern emerged in the hardened density results. The highest hardened density was recorded at 20% CSW 0-20 replacement, reaching 2353 kg/m^3. As the replacement level increased further, the hardened density progressively declined, reaching a minimum of 2132 kg/m^3 at 100% CSW 0-20

replacement. As for fresh density, this reduction may be attributed to greater internal porosity and a less compact microstructure caused by the higher content of concrete sludge waste.

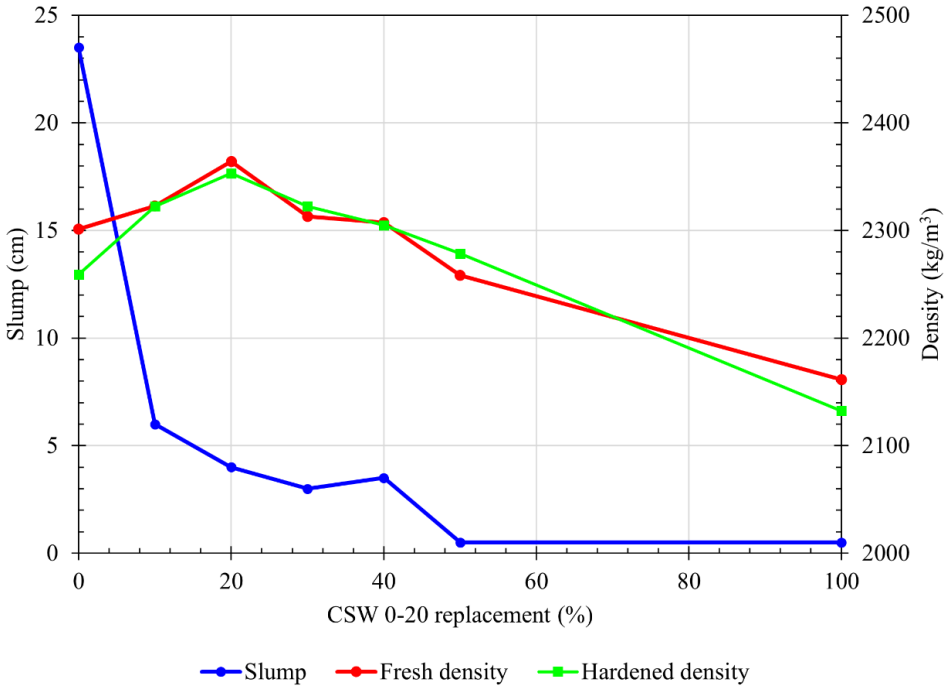

Figure 4-3. Slump and densities of the Set 1 mixtures.

4.3.1.2 Mechanical properties

4.3.1.2.1 Compressive strength

Figure 4-4 illustrates the average compressive strength measured after 7- and 28-days of curing across a range of CSW 0-20 replacement levels from 0% to 100%. Error bars for 28-days compressive strength indicate the standard deviation of the results, no bars are plotted for 7-days compressive strength since a single test was performed at that curing time.

The results indicate that both 7-day and 28-day compressive strengths increased with the addition of CSW 0-20 up to a certain replacement level, after which strength began to decline. At 7 days, the control mix (REF) achieved a compressive strength of 24.99 MPa. Strength values increased with higher CSW 0-20 content, peaking at 33.64 MPa with a 20% replacement. Beyond this point, compressive strength gradually decreased, reaching 17.92 MPa at 100% replacement.

A similar pattern was observed at 28 days. The initial compressive strength at 0% CSW 0-20 was 29.05 MPa, increasing to a maximum of 39.16 MPa at 20% replacement. As the CSW 0-20 content increased further, compressive strength steadily declined, falling to 25.49 MPa at full replacement.

The strength improvement observed up to the 20% replacement level can likely be attributed to enhanced particle packing, with the fine particles in the CSW 0-20 acting as micro-filler that improves the concrete matrix. However, exceeding this threshold led to a significant reduction in mechanical performance, indicating a limit to the beneficial effects of CSW 0-20 in concrete mixtures.

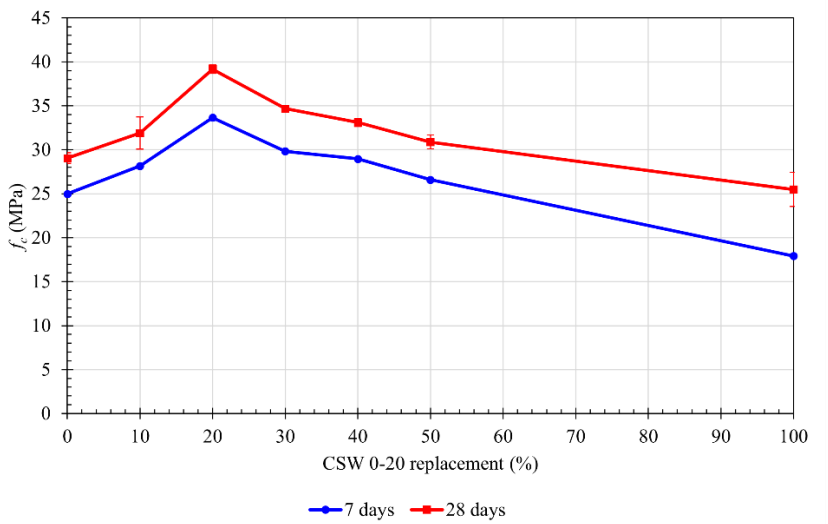

Figure 4-4. Compressive strength of the Set 1 mixtures. Error bars indicate the standard deviation.

4.3.1.2.2 Elastic Modulus

Figure 4-5 presents the average Elastic modulus E and splitting tensile strength f_{ct} after 28 days of curing for Set 1 mixtures containing up to 40% CSW 0-20. These mixes were chosen as they are more promising for structural applications. The left y-axis of the graph denotes the elastic modulus E, while the right y-axis corresponds to the splitting tensile strength f_{ct}.

As illustrated in the figure, the elastic modulus of concrete increases with the inclusion of CSW 0-20 up to a replacement level of 20%. At 0% replacement, the elastic modulus E was 25.51 GPa. With a 10% CSW 0-20 substitution, E grew to 27.12 GPa, reaching its maximum value of 30.34 GPa at 20% replacement. However, at 40% replacement, the modulus declined to 25.47 GPa. These results suggest that incorporating CSW 0-20 up to approximately 20% can enhance the stiffness of concrete, potentially due to a denser microstructure or improved compaction. Beyond this threshold, however, the excess CSW 0-20 content may begin to negatively impact the matrix, resulting in reduced mechanical performance.

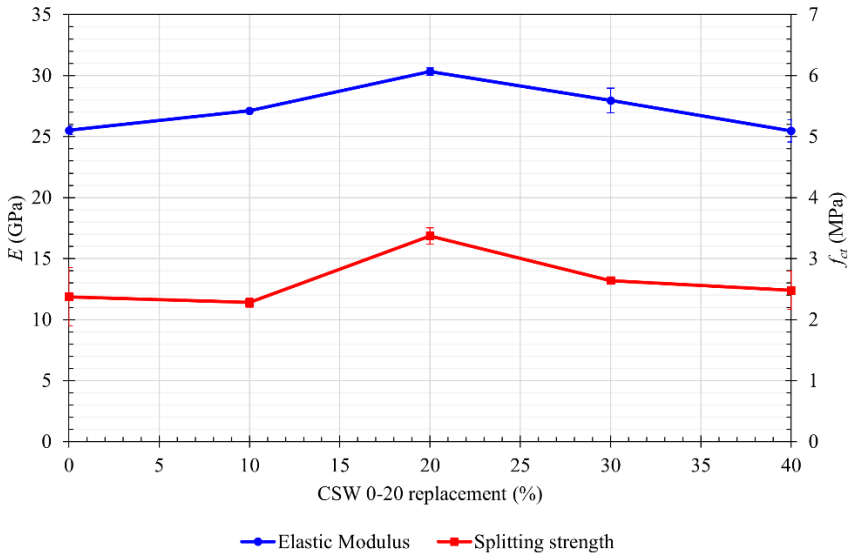

Figure 4-5. Elastic Modulus E and splitting strength f_{ct} for Set 1 mixtures. Error bars indicate the standard deviation.

4.3.1.2.3 Splitting strength

In terms of splitting tensile strength f_{ct}, the values remain relatively stable across the different replacement levels, with minor variations (Figure 4-5).

At 0% CSW 0-20, the splitting tensile strength is 2.37 MPa. This value remained nearly unchanged up to 10% replacement level, then increased to 3.37 MPa at 20%, before decreasing to 2.64 and 2.48 MPa at 30% and 40% replacements, respectively. This trend suggests that the inclusion of CSW 0-20 does not significantly compromise the concrete tensile performance. On the contrary, moderate replacement levels may even offer a slight improvement, potentially due to enhanced bond between the cement paste and the fine particles present in the concrete sludge waste.

4.3.1.3 Microstructural analysis

According to the mechanical tests, the best performance was obtained for the 20% CSW 0-20 replacement ratio. The reasons behind this result are probably related to mixed design physics. Packing and filler effects likely peak at about 20% CSW 0-20: sufficient fines to fill micro-voids and densify paste-aggregate skeleton without overwhelming the system with high-absorption, angular fines. However, this hypothesis should be verified within the cementitious paste and the Interfacial Transition Zone (ITZ).

For this reason, some photos were taken at the Scanning Electron Microscope (SEM) for mixtures REF, 20CSW, 30CSW and 100CSW. These scans are shown in Figure 4-6.

In the first photo (Figure 4-6a), the microstructure of REF is presented. An aggregate particle is visible on the left, while the cementitious paste on the right exhibits several pores, the largest of which, captured in this image, has a diameter of approximately 200 μm. The ITZ, i.e. the zone between cement past and aggregate, does not show optimal bond. In the second picture (Figure 4-6b), 20CSW is presented. The grey, smooth surface shown in the lower-right region corresponds to an aggregate particle. Notably, the cement paste exhibits a reduced pore content and smaller pore sizes. Furthermore, a well-bonded interface between the cement paste and the aggregate can be observed. The third photo (Figure 4-6c) illustrates the microstructure of the 30CSW concrete. A large aggregate particle is visible on the right side. In this case, a good bond is observed in the interfacial transition zone (ITZ); however, several pores with diameters ranging from approximately 10 to 60 μm are present, indicating a less compact microstructure compared to the 20CSW mixture. The last picture (Figure 4-6d) depicts the 100CSW concrete microstructure. In the lower part, a macro void of few millimeters is present, which is not totally captured in this photo.

As an outcome, the concretes microstructure confirms the hypothesis that 20% CSW 0-20 replacement ratio allows optimizing the compaction through micro-voids filling.

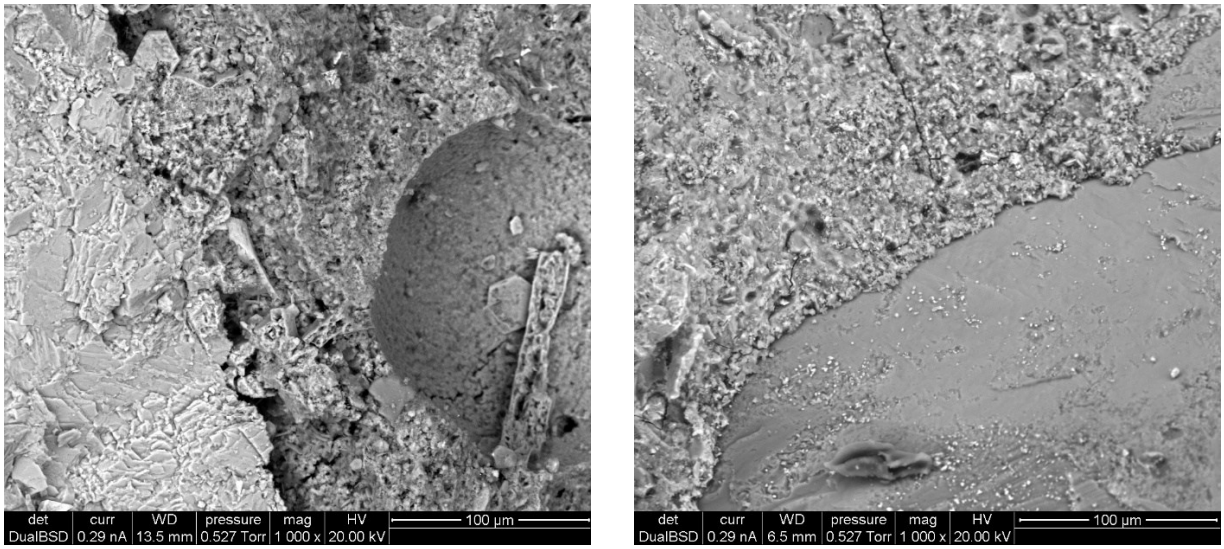

a) *b)*

c) *d)*

Figure 4-6. SEM images of the mixtures: a) REF; b) 20CSW; c) 30CSW; d) 100CSW.

4.3.2 Set 2

4.3.2.1 Improving mixture with 10% CSW 0-20

This section outlines the mechanical performance enhancements achieved by optimizing the 10CSW mixture (Set 1), which includes 10% CSW 0-20 as a replacement for natural aggregate. The original formulation, labeled 10CSW, was refined into 10CSW2 by increasing the cement content, slightly raising the water-to-cement (w/c) ratio, and increasing the superplasticizer dosage.

In terms of fresh properties, the slump experienced a noteworthy rise from 6 cm in the original mix to 26 cm in 10CSW2. Both fresh and hardened densities also increased by approximately 80-90 kg/m^3. As shown in Table 4-8, compressive strength at 7 days improved from 28.15 MPa in 10CSW to 32.06 MPa in 10CSW2. At 28 days, the strength rose from 31.90 MPa to 37.69 MPa, marking a significant gain of 5.79 MPa. Similarly, the elastic modulus at 28 days increased from 27.12 GPa to 30.06 GPa, showing an enhancement of 2.94 GPa. The splitting tensile strength also improved, rising from 2.28 MPa to 3.05 MPa.

These improvements indicate that the modified proportions in the 10CSW2 mix, particularly the increased water and superplasticizer content, effectively reduced internal voids and enhanced compaction. As expected, the most significant gains were observed in workability and compressive strength, which are closely linked to the quality of the cementitious matrix. In contrast, *E* showed more modest changes, as it is more influenced by the aggregate characteristics.

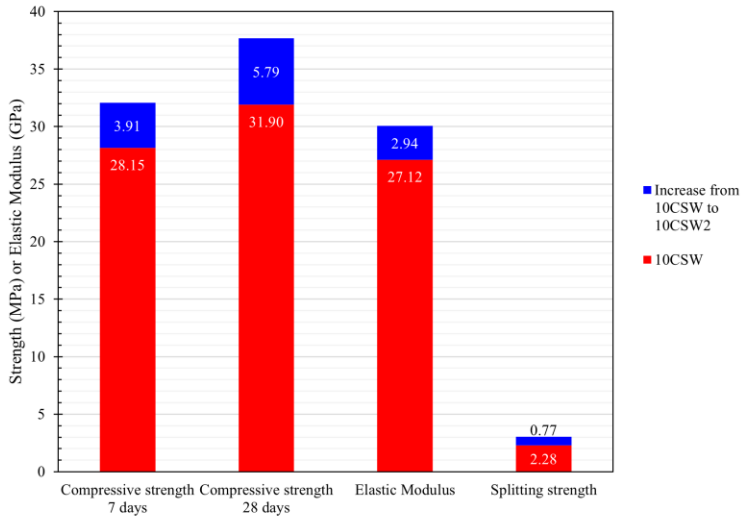

Figure 4-7. Improvement recorded in the mixture optimization for 10% CSW 0-20.

4.3.2.2 Improving mixture with 30% CSW 0-20

This section reports the mechanical performance improvements obtained by optimizing the 30CSW mixture (Set 1), containing 30% CSW 0-20 as a replacement for natural aggregate. The reference mix (30CSW) was modified to produce 30CSW2 through an increased cement content, a slightly higher water-to-cement ratio, and a greater superplasticizer dosage.

In the fresh state, slump did not change substantially, as it increased from 3 cm to 3.5 cm, while fresh and hardened densities rose by approximately 60 and 90 kg/m^3, respectively. Mechanical testing confirmed significant gains: compressive strength improved from 29.82 MPa to 38.92 MPa at 7 days, and from 34.68

MPa to 43.61 MPa at 28 days. The elastic modulus at 28 days increased from 27.96 GPa to 32.80 GPa, and splitting tensile strength rose from 2.64 MPa to 3.23 MPa.

These enhancements are attributed to the modified mix proportions, particularly the higher cement dosage and higher packing obtained thanks to the fine fraction of the all-in CSW 0-20, which can help filling micro-voids.

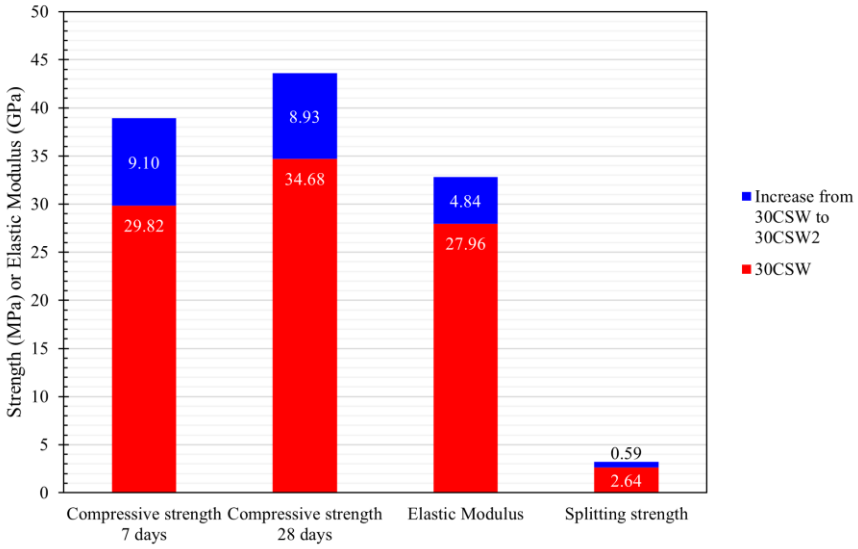

Figure 4-8. Improvement recorded in the mixture optimization for 30% CSW 0-20.

4.3.2.3 Improving mixture with 100% CSW 0-20

The optimization of the mixture containing 100% CSW (0-20 mm) was aimed at improving workability to enhance its suitability for non-structural applications. Currently, fully recycled aggregate mixes are not widely used in structural applications due to existing standards that recommend much lower replacement ratios [12].

In this context, the original 100CSW mix (Set 1) was modified to make 100CSW2 by increasing the amounts of water and superplasticizer. The cement content was kept constant at 330 kg/m^3 to minimize the carbon footprint rather than maximize mechanical performance, in line with its intended non-structural use.

Regarding fresh properties, the slump significantly improved: from 0.5 cm in 100CSW to 13.5 cm in 100CSW2. However, both fresh and hardened densities decreased by approximately 240 kg/m^3. Compressive strength also declined, with the 100CSW2 mix reaching 8.97 MPa at 7 days, i.e. a reduction of 8.95 MPa compared to the original 100CSW mix. It is worth mentioning that 100CSW2 targets a different objective, aiming for a mixture prioritizing fresh performance and reduced environmental impact rather than enhancing mechanical properties.

Table 4-6 and Figure 4-9 summarize the main features and properties of the mixtures with the same CSW 0-20 replacement ratio in Set 1 and Set 2.

Table 4-6. Comparison between Set 1 and Set 2 for mixtures with the same replacement ratio.

	10CSW	***10CSW2***	***30CSW***	***30CSW2***	***100CSW***	***100CSW2***
Cement dosage	330	360	330	360	330	330
W/C ratio	0.47	0.50	0.47	0.50	0.47	0.61
ρ_{fc} *(kg/m^3)*	2323	2415	2313	2379	2161	1912
ρ_c *(kg/m^3)*	2322	2402	2322	2396	2132	1903
$f_{c,7}$ *(MPa)*	28.15	32.06	29.82	38.92	17.92	8.97
f_c *(MPa)*	31.90	37.69	34.68	43.61	25.49	9.07

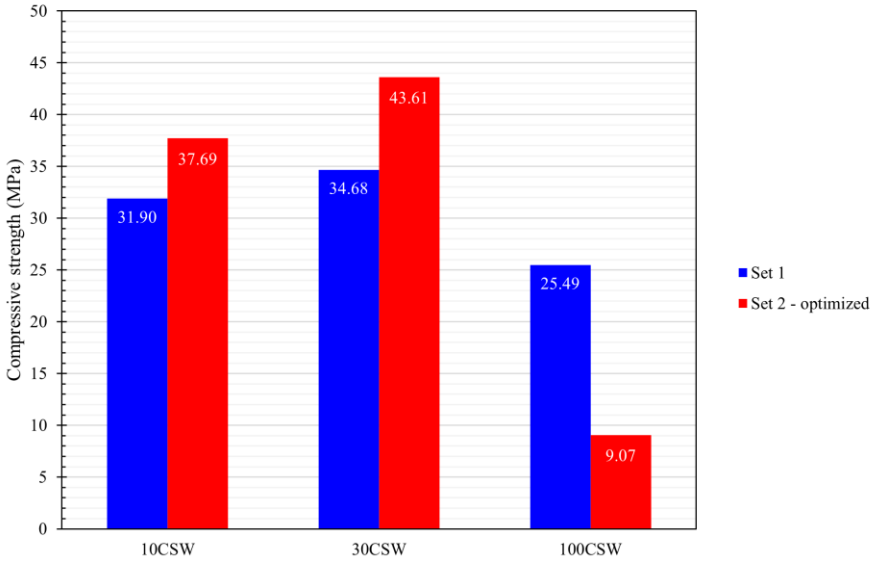

Figure 4-9. Compressive strength (28-days) comparison between Set 1 and Set 2 for mixtures with the same replacement ratio.

4.3.3 Leaching tests

Table 4-7 and Table 4-8 summarize the concentration of metals and anions on the leaching liquid over time according to the procedure described in EN 15863 [17], the Chemical Oxygen Demand (COD) and pH of the leaching agent were also measured considering the standards EN 1484 [19] and ISO 10523 [20]. For each cylinder two tests were performed. In this report, the test result with the maximum concentration of constituents is selected and shown for each mixture.

All constituents and values are below the limits provided by the Italian standard DM 5/2/1998, n. 22 [21].

Table 4-7. Results of the leaching test on REF.

	Duration from the start of the test								***Limits DM 5/2/98, n. 22*** [21]
	6h	***1d***	***2d 6h***	***4d***	***9d***	***16d***	***36d***	***64d***	
	Duration of the time interval								
	6h	***18h***	***1d 6h***	***1d 18h***	***5d***	***7d***	***20d***	***28d***	
METALS (µg/L)									
arsenic (As)	<0.2	<0.2	<0.2	<0.2	<0.2	<0.2	<0.2	<0.2	50
barium (Ba)	3.2	10.4	14.0	15.8	21.8	18.7	18.5	21.2	1000
beryllium (Be)	<0.5	<0.5	<0.5	<0.5	<0.5	<0.5	<0.5	<0.5	10
cadmium (Cd)	<0.16	<0.16	<0.16	<0.16	<0.16	<0.16	<0.16	<0.16	5
cobalt (Co)	<0.05	<0.05	<0.05	<0.05	<0.05	<0.05	<0.05	<0.05	250
chromium (Cr)	4.8	8.5	5.8	4.5	4.7	3.9	6.5	3.4	50
copper (Cu)	1.2	1.8	0.9	1.0	<0.5	<0.5	<0.5	<0.5	50
nickel (Ni)	0.4	0.2	0.1	<0.1	<0.1	<0.1	<0.1	<0.1	10
lead (Pb)	<0.2	<0.2	<0.2	<0.2	<0.2	<0.2	<0.2	<0.2	50
selenium (Se)	<1	<1	<1	<1	<1	<1	<1	<1	10
vanadium (V)	<0.5	1.7	2.7	3.6	5.6	6.4	12.5	7.8	250
zinc (Zn)	<1.5	<1.5	<1.5	<1.5	<1.5	<1.5	<1.5	<1.5	3000
mercury (Hg)	<0.03	<0.03	<0.03	<0.03	<0.03	<0.03	<0.03	<0.03	1
ANIONS (mg/L)									
fluorides	<0.1	<0.1	<0.1	<0.1	<0.1	<0.1	<0.1	<0.1	1.5
chlorides	0.26	0.24	0.14	<0.1	<0.1	0.22	0.21	0.25	200
nitrates	0.26	<0.1	<0.1	<0.1	<0.1	0.45	0.69	0.35	50
sulfates	<1	1.1	1.5	<1	1.1	2.85	5.92	4.43	250
cyanides	<0.01	<0.01	<0.01	<0.01	<0.01	<0.01	<0.01	<0.01	0.05
COD (mg/L)									
COD	<1	<1	<1	<1	7	3	3	<1	30
pH									
pH	9.36	10.10	10.20	10.00	9.96	9.60	9.00	7.98	5.5-12

Table 4-8. Results of the leaching test on 10CSW2.

	Duration from the start of the test								***Limits DM 5/2/98, n. 22*** [21]
	6h	***1d***	***2d 6h***	***4d***	***9d***	***16d***	***36d***	***64d***	
	Duration of the time interval								
	6h	***18h***	***1d 6h***	***1d 18h***	***5d***	***7d***	***20d***	***28d***	
METALS (µg/L)									
arsenic (As)	<0.2	<0.2	<0.2	<0.2	<0.2	<0.2	<0.2	<0.2	50
barium (Ba)	3.5	27.0	53.7	75.2	108.3	118.7	155.7	147.1	1000
beryllium (Be)	<0.5	<0.5	<0.5	<0.5	<0.5	<0.5	<0.5	<0.5	10
cadmium (Cd)	<0.16	<0.16	<0.16	<0.16	<0.16	<0.16	<0.16	<0.16	5
cobalt (Co)	0.06	0.08	0.08	0.14	0.15	0.13	0.20	0.10	250
chromium (Cr)	1.3	0.8	0.7	0.7	1.1	1.0	1.5	1.1	50
copper (Cu)	1.4	1.9	1.3	1.4	0.8	<0.5	1.6	0.6	50
nickel (Ni)	0.7	0.1	0.1	0.1	0.2	0.2	0.1	<0.1	10
lead (Pb)	<0.2	<0.2	<0.2	<0.2	<0.2	1.8	<0.2	<0.2	50
selenium (Se)	<1	<1	<1	<1	<1	<1	<1	<1	10
vanadium (V)	1.2	0.9	0.8	0.9	1.3	1.6	2.5	1.9	250
zinc (Zn)	<1.5	<1.5	<1.5	<1.5	<1.5	<1.5	2.1	<1.5	3000
mercury (Hg)	<0.03	<0.03	<0.03	<0.03	<0.03	<0.03	<0.03	<0.03	1
ANIONS (mg/L)									
fluorides	<0.1	<0.1	<0.1	<0.1	<0.1	<0.1	<0.1	<0.1	1.5
chlorides	0.13	0.25	0.39	0.27	0.27	0.37	0.52	0.28	200
nitrates	0.33	<0.1	<0.1	<0.1	<0.1	0.53	0.58	4.54	50
sulfates	<1	<1	<1	<1	<1	1.75	3.28	2.79	250
cyanides	<0.01	<0.01	<0.01	<0.01	<0.01	<0.01	<0.01	<0.01	0.05
COD (mg/L)									
COD	<1	<1	<1	10	10	8	3	1	30
pH									
pH	9.50	10.41	10.72	10.78	11.01	11.03	11.00	8.85	5.5-12

4.3.3.1 Metals

The graph in Figure 4-10 illustrates the leaching patterns of barium (Ba), chromium (Cr), and vanadium (V) which are the most relevant ones as they usually are the most readily leached elements in cement and concrete matrices.

Barium concentrations are significantly higher in the 10CSW2 mixture compared to the REF sample. The 10CSW2 mix exhibits a sharp early increase, peaking at 156 µg/L by day 20, while the REF mixture follows a similar but much lower trajectory, stabilizing below 30 µg/L. The elevated Ba levels in 10CSW2 leachate are attributed to the substantial presence of cement particles, originating both from the new binder and from the recycled concrete content of the CSW 0-20 aggregate. Literature often reports that barium can precipitate as barium sulfate [22]; however, the relatively low sulfate concentrations observed may have limited this stabilization process, reducing the potential for Ba fixation in a crystalline form.

Chromium, assessed as total Cr (sum of Cr(III) and Cr(VI)), showed the lowest leaching levels among the metals tested. Both mixtures maintained Cr concentrations below 10 µg/L throughout the test, with a slight increase noted after 7 days. Overall, Cr levels were slightly lower in the 10CSW2 mix. This may suggest a more refined pore structure in 10CSW2, which can reduce leaching. As surface wash-off is a key mechanism in Cr release, improving concrete properties, such as reducing the water-to-cement ratio and increasing strength, can significantly limit its mobility [23]. Additionally, in both mixtures, chromium leaching follows the pH trend, peaking between days 2 and 5 when alkalinity is at its highest, consistent with the known pH-dependent solubility of heavy metals [24].

Vanadium concentrations remained low in both mixtures, with 10CSW2 consistently exhibiting slightly lower values than REF. In the REF sample, vanadium levels rose to 12.5 µg/L by day 20 before gradually decreasing. In contrast, the 10CSW2 mix maintained stable concentrations, staying below 10 µg/L. While vanadium behavior in cement-based systems is not fully understood, it is known to form oxyanions under alkaline conditions, though not all species are effectively immobilized within the matrix [25]. The lower vanadium leaching in 10CSW2 may be linked to its higher average pH compared to REF, which appears to influence vanadium solubility.

4.3.3.2 Anions

Figure 4-11 presents the leaching results for chlorides, nitrates, and sulfates. It is well-established that anion leaching is influenced by pH levels, and this experimental test confirms that higher alkalinity generally increases the leachability of these compounds. Among the anions examined, sulfates exhibited the highest leaching levels.

In the REF mixture, sulfate concentrations steadily rise from the beginning of the test, reaching a peak of 5.92 mg/L at 20 days of time interval, followed by a slight decline toward the end. Conversely, the 10CSW2 mixture shows a delayed response, with sulfate levels beginning to increase at 7 days of time interval and peaking at 3.28 mg/L by day 20, before gradually decreasing.

Nitrate leaching behavior also differs between the two mixtures. In the REF sample, nitrate concentrations remain relatively low and stable throughout, peaking at 0.69 mg/L before slowly diminishing. In contrast, the 10CSW2 sample starts with nitrate levels similar to REF but shows a sharp increase after 20 days of time interval, ultimately reaching 4.54 mg/L by the end of the test, differently from the REF behavior.

Chloride concentrations in both mixtures remain low and stable over time, not exceeding 0.55 mg/L. While 10CSW2 exhibits slightly higher chloride levels than REF in the early stages, the difference is minimal.

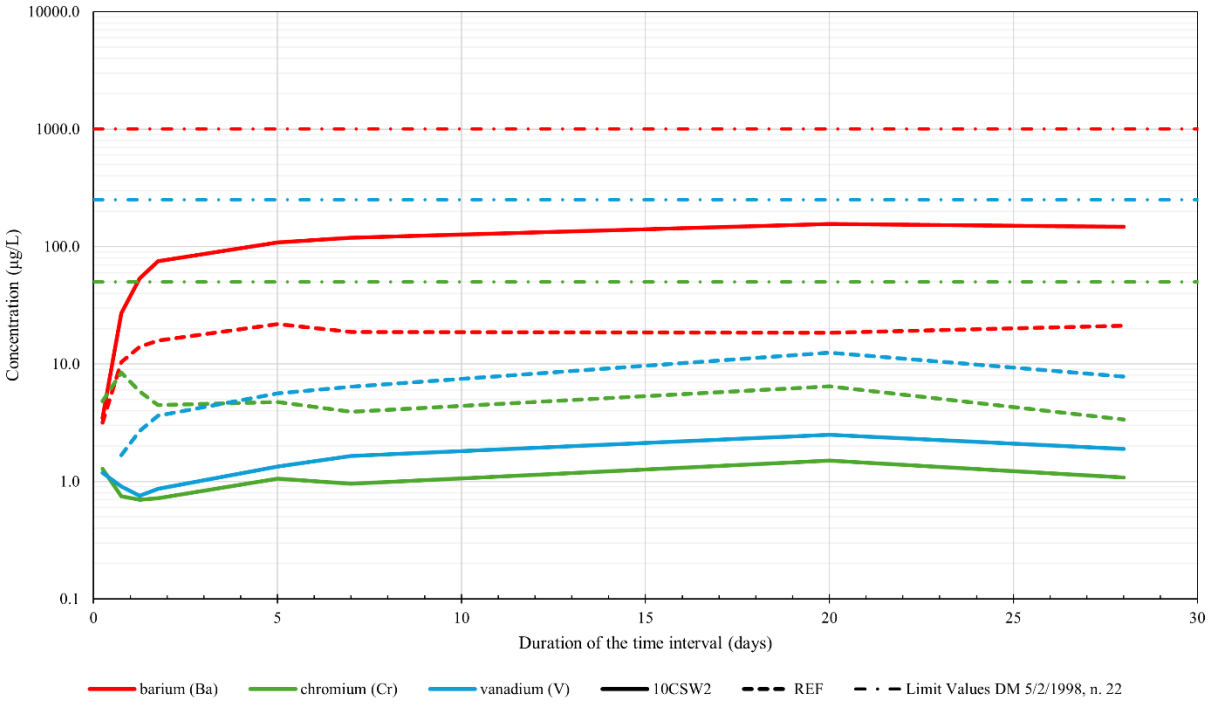

Figure 4-10. Concentration of metals in the leachate.

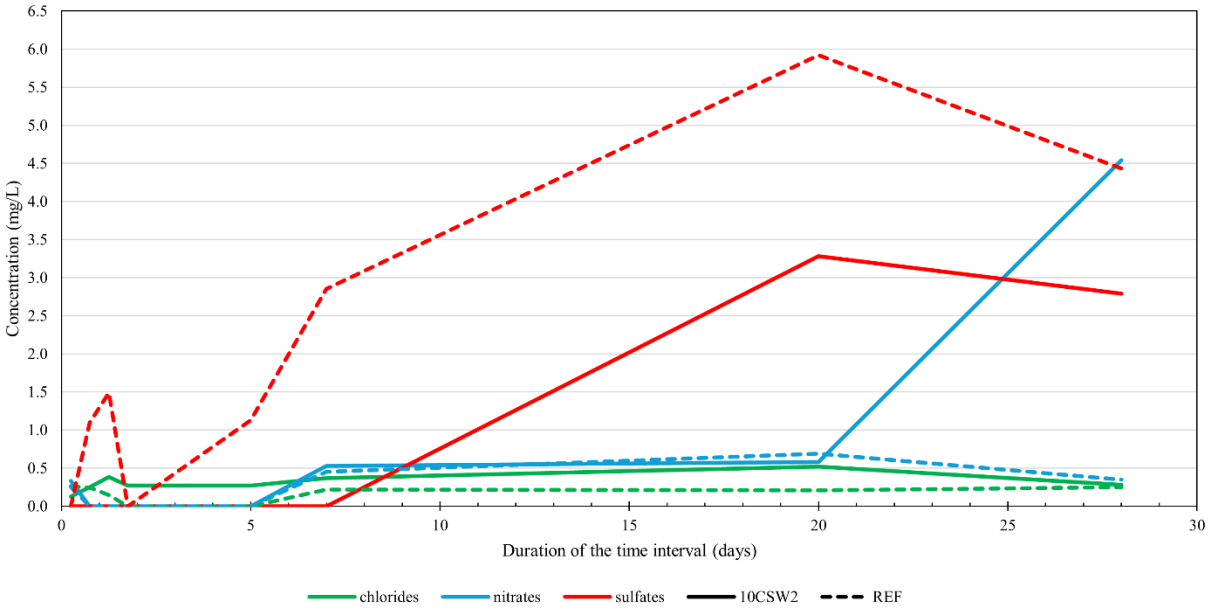

Figure 4-11. Concentration of anions in the leachate.

4.3.3.3 Chemical Oxygen Demand

Figure 4-12 displays the results of the leaching test measuring the evolution of Chemical Oxygen Demand (COD), a crucial parameter in environmental chemistry used to assess the concentration of organic matter in water or leachate. COD represents the total amount of oxygen needed to chemically oxidize both biodegradable and non-biodegradable organic compounds into carbon dioxide and water. Elevated COD levels indicate a higher presence of organic substances, which could negatively affect water quality and environmental safety.

At the beginning of the test, both the REF and 10CSW2 concrete samples show minimal COD values, suggesting very limited organic leaching in the early phase. However, by day 5, the 10CSW2 mixture exhibits a sharp increase, peaking at 10 mg/L, whereas the REF sample shows only a modest rise. After this peak, COD levels in 10CSW2 steadily decline, dropping below 5 mg/L by day 20 and continuing to decrease slightly thereafter. Throughout the test period, the REF mixture maintains consistently lower COD levels, gradually decreasing toward zero by the end.

Importantly, all COD values recorded during the test remain within the acceptable limits established by Italian regulation DM 5/2/1998, n. 22 [21].

4.3.3.4 pH

Figure 4-13 illustrates the average pH levels in the leachate for both REF and 10CSW2 samples. The observed pH trends align with those typically reported for monolithic concrete specimens undergoing aqueous leaching. These trends reflect the chemical evolution of the system over time, influenced by processes such as leaching, ongoing hydration, and carbonation:

- Initial Phase (first week): A noticeable increase in pH occurs, primarily due to the dissolution of alkaline hydroxides within the matrix, particularly calcium hydroxide ($Ca(OH)_2$), along with sodium and potassium hydroxides (NaOH and KOH), which are commonly present in Portland cement. Continued hydration also contributes to the accumulation of alkaline species in the leachate, often resulting in pH values exceeding 11 or 12.
- Intermediate Phase (7 to 20 days): The pH either stabilizes or continues to rise gradually. At this stage, carbonation is still limited, allowing the pH to remain relatively stable or slightly increase.
- Final Phase (after 20 days): A marked decrease in pH is often observed, primarily due to the onset of carbonation. In this process, calcium hydroxide and other alkaline components react with atmospheric CO_2 to form carbonates, such as calcium carbonate ($CaCO_3$), thereby reducing the concentration of free hydroxide ions in solution. Additionally, the formation of a carbonated surface layer can inhibit further OH^- release. In some cases, particularly in matrices with lower alkalinity or the presence of sulfate or phosphate ions, acidic or neutral species may also leach out, contributing to the pH drop.

This progression reflects a shift from an early stage dominated by the release of alkaline substances to a later stage where neutralization and carbonation processes begin to dominate, significantly altering the chemical environment of the solid-liquid system.

Notably, the average pH in the 10CSW2 mix is slightly higher than in the REF sample, suggesting a greater concentration of hydroxide ions (OH^-), which are the primary drivers of pH in concrete. This elevated pH in the CSW 0-20 mix indicates that incorporating this recycled aggregate does not impair, and may even enhance, resistance to carbonation. Nevertheless, dedicated testing should be conducted to more definitively assess the carbonation resistance of the 10CSW2 mixture.

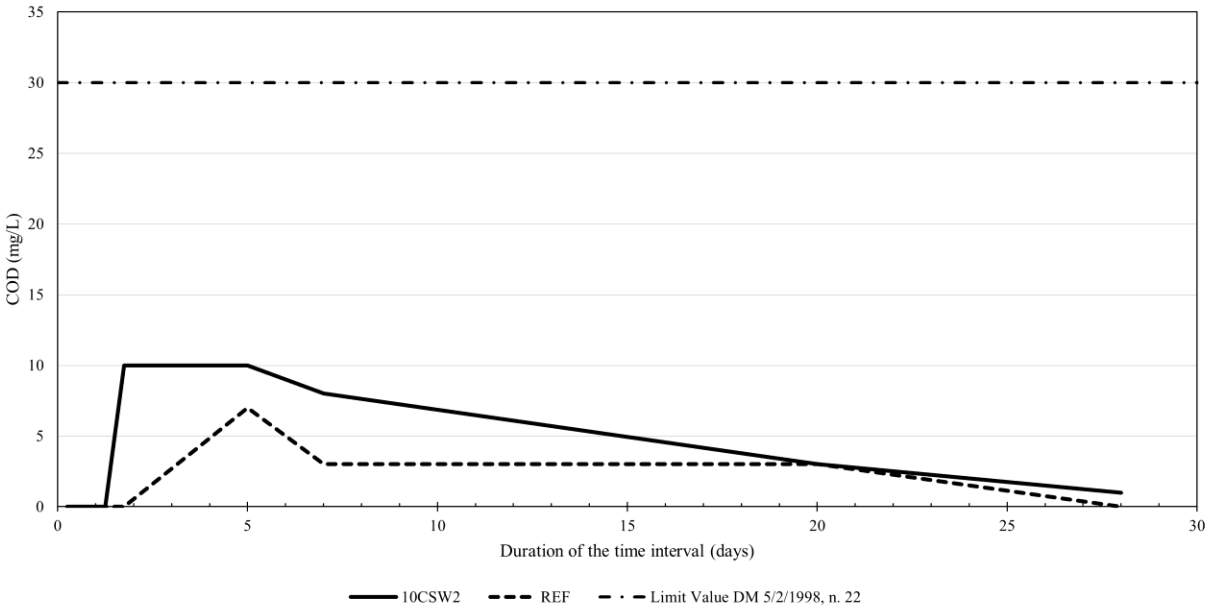

Figure 4-12. Chemical Oxygen Demand (COD) in the leachate.

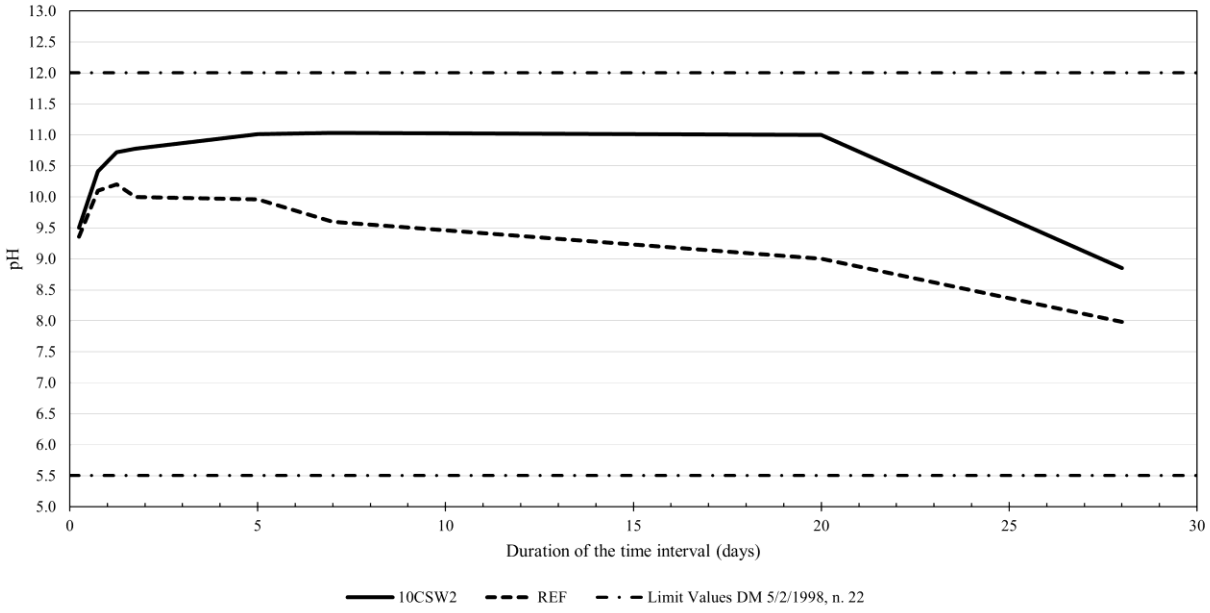

Figure 4-13. pH in the leachate.

4.4 CONCLUSIONS

This work focuses on the use of Concrete Sludge Waste as all-in fraction 0-20 (CSW 0-20) to replace conventional fine and coarse aggregate for concrete production.

The experimental campaign involved two sets of concrete mixtures (Set 1 and Set 2). Set 1 focused on mixes with varying replacement levels (0-100%) of CSW 0-20 aggregate, keeping the cementitious paste composition constant (330 kg/m^3 cement, 155 kg/m^3 water, w/c ratio of 0.47). Set 2 included optimized versions of the 10CSW, 30CSW and 100CSW mixes, aiming to enhance workability and performance. Slump drop, fresh density and hardened density were measured while compressive strength was tested on cylindrical samples at 7 and 28 days of curing. Elastic modulus and splitting tensile strength were also assessed on some selected mixtures. Furthermore, leaching tests were performed on cylindrical sample of the optimized 10% CSW 0-20 (10CSW2) and the reference mixture (REF). At the end of this study, the following conclusions can be drawn:

- Increasing the replacement level of CSW 0-20 aggregate from 0% to 100% led to a noticeable reduction in slump and density, but a modest peak in density was observed at 20% CSW 0-20 content.
- Compressive strength improved with CSW 0-20 replacement up to 20%, reaching a peak value of 39.16 MPa at 28 days. Beyond this level, strength declined, likely due to the inferior mechanical properties of CSW compared to conventional aggregates. The reasons behind this result are probably related to packing and filler effects which seem to peak at about 20% CSW 0-20, as confirmed by the microstructural analysis.
- The modulus of elasticity increased with CSW 0-20 content up to 20%, reaching 30.34 GPa, indicating enhanced stiffness resulting from better particle packing. However, it declined for higher replacement levels.
- Splitting strength remained relatively consistent across all replacement levels, with peak observed at 20% CSW, suggesting that tensile performance was not adversely affected.
- Adjustments to cement content, water dosage, and admixture proportions in the 10% CSW and 30% CSW mixes (mixtures 10CSW2 and 30CSW2) resulted in improved workability and significant gains in both compressive strength and stiffness, enhancing the overall performance of both fresh and hardened concrete.
- The 10CSW2 mix exhibited slightly higher leaching of metals compared to the reference concrete, particularly during the first 10 days, after which metal concentrations stabilized or decreased slightly.
- Slightly elevated nitrate leaching was observed in the later stages for the 10CSW2 mix. Sulfate leaching was lower than that of the reference concrete, while chloride leaching remained consistently low and similar in both mixes.
- COD values in the leachate of the 10CSW2 concrete were higher than the reference, though still well below the regulatory threshold of 30 mg/L, indicating acceptable environmental performance.
- The leachate from concrete with CSW 0-20 showed a slightly higher pH, suggesting an increased presence of OH^- ions. This indicates that carbonation resistance was not compromised, and may even be enhanced, by the inclusion of CSW as a partial aggregate replacement.

REFERENCES

[1] K. Chen, J. Wang, B. Yu, H. Wu, J. Zhang, Critical evaluation of construction and demolition waste and associated environmental impacts: A scientometric analysis, Journal of Cleaner Production 287 (2021) 125071. https://doi.org/10.1016/j.jclepro.2020.125071.

[2] B. Wang, L. Yan, Q. Fu, B. Kasal, A Comprehensive Review on Recycled Aggregate and Recycled Aggregate Concrete, Resources, Conservation and Recycling 171 (2021) 105565. https://doi.org/10.1016/j.resconrec.2021.105565.

[3] J. Lavado, J. Bogas, J. de Brito, A. Hawreen, Fresh properties of recycled aggregate concrete, Construction and Building Materials 233 (2020) 117322. https://doi.org/10.1016/j.conbuildmat.2019.117322.

[4] M. Nedeljković, J. Visser, B. Šavija, S. Valcke, E. Schlangen, Use of fine recycled concrete aggregates in concrete: A critical review, Journal of Building Engineering 38 (2021) 102196. https://doi.org/10.1016/j.jobe.2021.102196.

[5] J. Vieira Martins, M.T. Paulino Aguilar, D.C. Silva Garcia, W.J. dos Santos, Management and characterization of concrete wastes from concrete batching plants in Belo Horizonte – Brazil, Journal of Materials Research and Technology 20 (2022) 1157–1171. https://doi.org/10.1016/j.jmrt.2022.07.136.

[6] S. Adomako, C.J. Engelsen, L.T. Døssland, T. Danner, R.T. Thorstensen, Technical and environmental properties of recycled aggregates produced from concrete sludge and excavation materials, Case Studies in Construction Materials 19 (2023) e02498. https://doi.org/10.1016/j.cscm.2023.e02498.

[7] G. Ferrari, M. Miyamoto, A. Ferrari, New sustainable technology for recycling returned concrete, Construction and Building Materials 67 (2014) 353–359. https://doi.org/10.1016/j.conbuildmat.2014.01.008.

[8] J.V. Martins, D.C.S. Garcia, M.T.P. Aguilar, W.J. dos Santos, Influence of replacing Portland cement with three different concrete sludge wastes, Construction and Building Materials 303 (2021) 124519. https://doi.org/10.1016/j.conbuildmat.2021.124519.

[9] EN 197-1:2011 - Cement - Composition, specifications and conformity criteria for common cements, (2011).

[10] EN 1097-6:2013 - Tests for mechanical and physical properties of aggregates - Determination of particle density and water absorption, (2013).

[11] EN 933-1:2012 - Tests for geometrical properties of aggregates - Determination of particle size distribution: Sieving method, (2012).

[12] Decreto 23 giugno 2022. Criteri ambientali minimi per l'affidamento del servizio di progettazione ed esecuzione dei lavori di interventi edilizi, Ministero della Transizione Ecologica, Rome, 2022.

[13] EN 12350-2:2019 - Testing fresh concrete - Slump test, (2019).

[14] EN 12390-3:2019 - Testing hardened concrete - Compressive strength of test specimens, (2019).

[15] EN 12390-13:2021 - Testing hardened concrete - Determination of secant modulus of elasticity in compression, (2021).

[16] EN 12390-6:2023 - Testing hardened concrete - Tensile splitting strength of test specimens, (2023).

[17] EN 15863:2015 - Characterization of waste - Leaching behaviour test for basic characterization: Dynamic monolithic leaching test with periodic leachant renewal, under fixed conditions, (2015).

[18] MU 2251:2008 - Qualità dell'acqua: determinazione dei cianuri liberi e totali - Metodo mediante decomposizione dei cianocomplessi, distillazione e misura finale con: test in cuvetta, cromatografia ionica, flow injection (fia), (2008). https://pubblicazioni.unichim.it/dettaglio/63.

[19] EN 1484:1997 - Water analysis - Guidelines for the determination of total organic carbon (TOC) and dissolved organic carbon (DOC), (1997).

[20] ISO 10523:2008 - Water quality - Determination of pH, (2008).

[21] Decreto Ministeriale 5 febbraio 1998. Individuazione dei rifiuti non pericolosi sottoposti alle procedure semplificate di recupero ai sensi degli articoli 31 e 33 del decreto legislativo 5 febbraio 1997, n. 22, Ministero dell'Ambiente, Rome, 1998.

[22] A. Vollpracht, W. Brameshuber, Binding and leaching of trace elements in Portland cement pastes, Cement and Concrete Research 79 (2016) 76–92. https://doi.org/10.1016/j.cemconres.2015.08.002.

[23] A. Król, Mechanisms Accompanying Chromium Release from Concrete, Materials 13 (2020). https://doi.org/10.3390/ma13081891.

[24] H.A. Van der Sloot, J. Dijkstra, P. Seignette, O. Hjelmar, G. Spanka, Characterization leaching tests as basis of reference for quality control and decisions on acceptability of alternative materials in construction, in: Energy Research Centre of the Netherlands, Wascon Conference, Lyon, 2009.

[25] M. Pourbaix, Atlas of electrochemical equilibria in aqueous solutions, NACE (1966).

References

5 SUMMARY, CONCLUSIONS AND FUTURE DEVELOPMENTS

5.1 SUMMARY

Concrete plays a major role for the building industry, because of its versatility, excellent performance and reduced price. In fact, it is the most widely used construction material. The concrete great demand in the construction industry is also an environmental concern linked to its components. Sand and gravel extraction for the building industry carries significant environmental consequences due to the massive scale of its consumption in construction. The growing demand for Natural Aggregates (NA) has been forcing industry to consider alternative materials. The possibility of using waste and by-products as aggregates to reduce the environmental impact of concrete is well-documented. Whereas research has been exploring this path extensively, large-scale applications of these practices remain a challenge.

At the beginning of the Ph.D. program, some recovered aggregates were selected and analyzed to define the research gaps which might hinder their extensive application.

Electric Arc Furnace Slag (EAFS) is a by-product generated during the refining of molten steel in Electric Arc Furnace. When EAFS is included in concrete as coarse fraction of the aggregate, superior performance is usually observed, however some research lacks were observed concerning rheology, shear transfer performance, and axial cyclic loading. Rheology was studied on fresh mortars containing EAFS in fine fraction (0-4 mm) at replacement levels of 0%, 20%, 40%, 60%, 80%, and 100%. Instead, shear transfer was studied on push-off (S-shaped) samples. When loaded vertically, this geometry allows stress concentration in the middle plane. In the first experimental campaign, samples were cast without clamping steel to focus on the cohesion effect mechanism, which is independent from the reinforcement ratio. Following this experimental campaign, other samples were cast including clamping steel to study completely the shear transfer mechanism. Cyclic axial compression was also analyzed on cylindrical samples with incremental solicitations until failure. Tests were performed on mixtures after 28 days and 6 years of curing.

The properties of recycled concrete are usually worse than those attained by the conventional counterparts. This is due to the features of the aggregates recovered from Construction & Demolition Waste (C&DW) which are made of virgin aggregates and portions of attached mortars that increase water absorption and lower the average particle density. For these reasons, recycled concrete usually demonstrates poorer mechanical properties, lower workability and higher shrinkage. In this dissertation a method is proposed to effectively reduce the plastic shrinkage by adding Raw Crushed Wind Turbine Blade (RCWTB) in the mix, a material obtained from crushing decommissioned wind turbine blades. Further, rheology, and specifically yield stress, was studied on mortars including RCWTB.

Concrete Sludge Waste (CSW), also known as returned concrete, indicates the leftover concrete remaining in the mixing truck, which is typically in a fresh state and contains a substantial amount of cement mortar. In this dissertation, an all-in recovered aggregate in fraction 0-20 mm obtained directly from crushed CSW is adopted to produce recycled concrete. The main advantage of this recovery process lies in

its simplicity, as it can be implemented at any Ready-Mix Concrete (RMC) plant with only the requirement of storage space and crushing equipment.

5.2 CONCLUSIONS

At the end of this dissertation, experimental observations demonstrate promising results which help to solve the identified research gaps.

The second chapter of this dissertation focuses on conglomerates containing Electric Arc Furnace Slag (EAFS) as partial or total aggregate replacement. In the presented experimental campaigns, EAFC gains compressive strength against the conventional counterparts (≈+30–40% at 28 days in multiple campaigns), but yield stress increases far more strongly (≈×4.5 at 100% EAFS in mortars). The mechanisms differ: in fresh state, angular/rough EAFS raises interparticle friction and intrinsic viscosity η, while in hardened state compressive strength responds to aggregate strength, Interfacial Transition Zone (ITZ) quality and matrix composition.

- Rheology was studied for fresh mortars containing fine EAFS at replacement levels of 0%, 20%, 40%, 60%, 80%, and 100%. The results demonstrate yield stress depends on the geometry of the particles. EAFS particles exhibit rough surface and lower flatness compared to the conventional aggregates adopted in this experimental campaign, indicating more uniform and isotropic dimensions across the three axes. Thus, the yield stress increased with rising EAFS content, which increased the intrinsic viscosity and resistance to flow in the mortar mixtures. Further, yield stress was modelled using Yodel and Trung-Ovarlez-Chateau equations, the predictions align well with the experimental values.
- Shear transfer was analyzed on concrete totally replacing the coarse fraction of the aggregate with EAFS. As expected, the concrete containing EAFS (EAFC) demonstrated higher shear strength than Natural Aggregate Concrete (NAC) in push-off tests, with all specimens failing in a brittle manner and differences noted in crack propagation along the shear interface. EAFC failure mainly involved aggregate crushing, while NAC exhibited cracking through or around aggregates. However, the fracture surfaces in EAFC were notably rough, featuring angular and irregular textures that eased multiple contact points and enhanced shear resistance through macro-scale aggregate interlock. Traditional shear friction models underestimated EAFC performance, proving conservative results but offering a higher safety margin compared to NAC.
- Under cyclic loading, results were comparable to monotonic loading in terms of strength, and EAFC maintained a steeper stress-strain curve over time. The constitutive models proposed and calibrated in this work effectively predict the stress-strain behavior under cyclic loading for both NAC and EAFS concrete. Furthermore, the simplified model, i.e. assuming linear and overlapping unloading/reloading branches, proved to be effective for practical applications, offering comparable predictive performance with reduced complexity.

The third chapter concerns the use of Raw Crushed Wind Turbine Blades (RCWTB) as effective addition to improve concrete mechanical properties.

- Rheology was analyzed on mixtures including Glass Fiber Reinforced Polymer (GFRP) separated from RCWTB or whole RCWTB. Yield stress increases with higher GFRP fiber content due to reduced particle mobility and higher interfacial friction. Mortars with whole RCWTB show greater yield stress increases than those with only GFRP, due to the presence of irregular, aggregate-like particles. The predictive model showed strong accuracy in estimating relative yield stress by treating GFRP fibers as flexible when determining their maximum packing fraction. However, the best alignment with experimental data was achieved when the fibers were assumed to experience the yield stress of the entire mixture, rather than that of the reference cement paste or mortar alone.

- The addition of RCWTB in recycled concrete containing Coarse Recycled Aggregate (CRA) demonstrated to be an effective method to improve mechanical and fresh performance. Indeed, RCWTB is highly efficient in reducing plastic shrinkage. GFRP works as fibers that restrain early-age volumetric deformation. Furthermore, RCWTB effectively mitigates the adverse effects of CRA on flexural performance, likely due to the bridging action and bond of GFRP fibers within the cementitious matrix, as confirmed by scanning electron microscope images.

Finally, the fourth chapter focuses on the use of Concrete Sludge Waste (CSW) as aggregate replacement for concrete production.

- CSW was employed in aggregate fraction 0-20 as all-in replacement for both sand and gravel. Results demonstrate that replacing natural aggregate with up to 20% CSW 0-20 improved compressive strength, stiffness, and fresh properties, with optimal performance observed at about 20% replacement. Adjustments to cement content, water dosage, and admixture proportions in the 10% CSW and 30% CSW mixes resulted in improved workability and significant gains in both compressive strength and stiffness, enhancing the overall performance of both fresh and hardened concrete. Environmental performance remained acceptable and within the limits of the Italian regulation.

5.3 FUTURE DEVELOPMENTS

This dissertation aimed to solve research gaps in the mechanical and rheological properties of cementitious conglomerates containing recovered aggregates. Although the results obtained help solve some specific research lacks, other aspects still need to be deepened and extended.

Electric Arc Furnace Slag (EAFS) is obtained as by-product in the homonymous furnace. Its properties depend on the type of furnace, type of steel used to feed the furnace, additional materials used. Hence, the physical properties of the EAFS may change for each steel-making company. Thus, a detailed analysis of the EAFS physical properties based on the production process would be of great interest for ensuring consistent and predictable performance. Further, EAFS concrete still demonstrates some research lacks in durability, in fact EAFS may contain in some cases free lime (CaO) and free periclase (MgO) which might be responsible for expansion phenomena. The author plans to perform in the next years some expansion tests according to standard EN 1744-1: in this method a steam flux interacts with the EAFS, allowing for accelerated swelling. Research on EAFS and concrete with EAFS is quite abundant in the literature, however the main limit for its extensive application is related to the regulation. Though there are some timid experiences, the reluctance of stakeholders and the lack of specific recognition in the standards make its reliable employment more challenging.

The use of Raw Crushed Wind Turbine Blade (RCWTB) as inclusion for concrete production strongly depends on the geographical location, making it more viable in those countries that rely significantly on the wind energy, e.g. Denmark, Spain and the Netherlands. The beneficial effect of the Glass Fiber Reinforced Polymer (GFRP) is partially jeopardized by the co-presence of balsa wood and polyurethane. Hence, the mechanical or physical separation of GFRP from the other constituents should be further studied, hence adopting solely the GFRP as concrete incorporation.

The study here presented on the use of Concrete Sludge Waste (CSW) for concrete production is just a first step in the possible reuse of this kind of waste. Hence, alternative recycling methods should be considered, considering economic and environmental compatibility. Further, a scaling-up in a ready-mix concrete plant would be of great interest to analyze the feasibility of CSW recycling at a large-scale level.